ISSN: 3082-849X (Online)
Volume 2 · Issue 1
March 2026

Engineering Science in ADDITIVE MANUFACTURING

Engineering Science in Additive Manufacturing (ESAM) aims to collate the cutting-edge research and review articles in additive manufacturing that highlight the engineering science

ACCSCIENCE PUBLISHING

Engineering Science in Additive Manufacturing

Online ISSN: 3082-849X

Engineering Science in Additive Manufacturing (ESAM) aims to collate the cutting-edge research and review articles in additive manufacturing that highlight the engineering science. The journal covers all fundamentals of additive manufacturing, including its principles and applications. The journal publishes articles that acknowledge the significant development in the field and its disruptive nature in the industry. ESAM provides a platform for publishing articles that advance the in-depth understanding of additive manufacturing. The journal also welcomes papers that employ theories, numerical methods and/or simulations that demonstrate relevance to the additive manufacturing community.

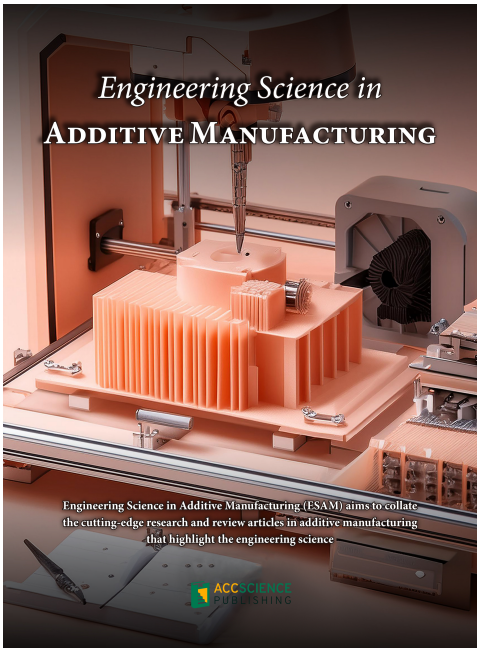

About the Publisher

AccScience Publishing is a publishing company based in Singapore. We publish a range of high-quality, open-access, peer-reviewed journals and books from a broad spectrum of disciplines.

Contact Us

Managing Editor
esam.office@accscience.sg

AccScience Publishing
2 Venture Drive, #07-06 Vision Exchange,Singapore 608526.

Volume 2 • Issue 1 • March 2026
ISSN 3082-849X (online)

ENGINEERING SCIENCE IN ADDITIVE MANUFACTURING

Editor-in-Chief
Swee Leong Sing
National University of Singapore, Singapore

ACCSCIENCE PUBLISHING
Access Science Without Barriers

ENGINEERING SCIENCE IN ADDITIVE MANUFACTURING

ISSN: 3082-849X (online)

Editorial and Production Credits

Publisher: AccScience Publishing
Managing Editor: Shirley Lu
Production Editor: Sharmila Velapasamy
Article Layout and Typeset: Sinjore Technologies (India)

For all advertising queries, contact esam.office@accscience.sg.

Supplementary file

Supplementary files of articles can be obtained at https://accscience.com/journal/ESAM/2/1.

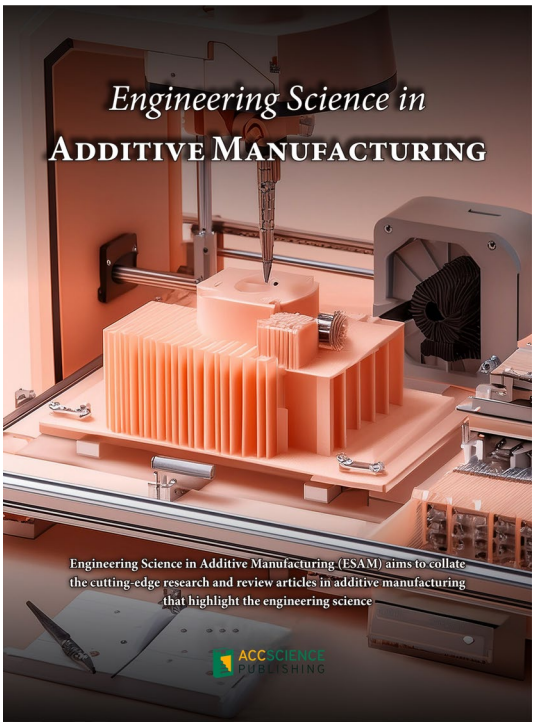

Disclaimer

AccScience Publishing is not liable to the statements, perspectives, and opinions contained in the publications. The appearance of advertisements in the journal shall not be construed as a warranty, endorsement, or approval of the products or services advertised and/or the safety thereof. AccScience Publishing disclaims responsibility for any injury to persons or property resulting from any ideas or products referred to in the publications or advertisements. AccScience Publishing remains neutral with regard to jurisdictional claims in published maps and institutional affiliations.

Engineering Science in Additive Manufacturing

Editorial Board

ACCSCIENCE PUBLISHING

Volume 2 | Issue 1 | March 2026

Engineering Science in Additive Manufacturing

https://accscience.com/journal/ESAM

CONTENTS

REVIEW ARTICLES

1 **An interdisciplinary review of the development and applications of embedded three-dimensional printing technology**
Shengyu Gao, Hanyu Yang, Zhengnan Sun, Liang Zhou, Aiwu Zhou, Xiaosheng Zhang, Yi Zhang

2 **Microstructure-controlled strengthening mechanisms and strategies in additively manufactured aluminum alloys: A review**
Yingming Zhang, Tianai Huang, Xin He, Xiaoming Wang

PERSPECTIVE ARTICLE

3 **Why semiconductor additive manufacturing is challenging—and what comes next**
Ali Ghasemi, Swee Leong Sing

ORIGINAL RESEARCH ARTICLES

4 **Understanding melt pool characteristics as a means for reducing build layout quality variations in laser-based powder bed fusion: An approach toward spatial parameter compensations**
Jaivindra Singh, J. P. Oliveira, Hunter Taylor, Jesus Rivas, Jorge Mireles, Oscar Garcia, Ryan Wick

5 **Dual-wavelength photoinhibition-aided vat photopolymerization (PinVPP) of bio-based polymers and functional hydrogels**
Yousra Bensouda, Xiayun Zhao

ACCSCIENCE PUBLISHING

Engineering Science in Additive Manufacturing

REVIEW ARTICLE

An interdisciplinary review of the development and applications of embedded three-dimensional printing technology

Shengyu Gao[1†], Hanyu Yang[1†], Zhengnan Sun[1], Liang Zhou[1], Aiwu Zhou[1], Xiaosheng Zhang[1*], and Yi Zhang[1,2*]

[1]Integrated Microsystems Laboratory, School of Integrated Circuit Science and Engineering, University of Electronic Science and Technology of China, Chengdu, Sichuan, China

[2]Tianfu Jiangxi Laboratory, Chengdu, Sichuan, China

Abstract

Embedded three-dimensional (3D) printing (EMB3D), also termed immersion 3D printing, overcomes the inherent limitations of extrusion-based methods by providing *in situ* support during deposition, thereby preventing structural collapse and enabling the fabrication of complex architectures from soft- or low-viscosity inks. This technology significantly enhances shape fidelity and expands the application of 3D printing in soft material systems. This review systematically examines the development, principles, classifications, and material properties of EMB3D, with a strong emphasis on its cross-disciplinary applications. While notable biomedical advances, such as tissue engineering, vascularized constructs, and patient-specific anatomical models, are thoroughly discussed, this review also highlights emerging uses in flexible electronics, soft robotics, and customized functional materials. By integrating the latest research and identifying underexplored avenues, this review offers a forward-looking perspective on the challenges and future trends of EMB3D, serving as a comprehensive and authoritative reference for researchers and engineers across multiple fields.

Keywords: Additive manufacturing; Embedded three-dimensional printing; Immersion three-dimensional printing; Soft materials; Low-viscosity inks; Soft robotics

1. Introduction

With the rapid evolution of modern manufacturing and increasing demand for complex architectures in soft materials, three-dimensional (3D) printing[1-4] has established itself as a transformative force. It drives innovation through unparalleled design freedom, high customizability, and unique fabrication capabilities. Extrusion-based 3D printing,[5-8] despite its significant potential across numerous fields, encounters substantial challenges when processing soft materials, especially those with low viscosity. Issues such as poor interlayer adhesion, structural collapse, and deformation critically limit the broader adoption of this technology in pivotal areas such as biomedicine, soft robotics, and flexible electronics, where the demand for fabricating with soft materials is rapidly growing.

[†]These authors contributed equally to this work.

***Corresponding authors:**
Xiaosheng Zhang (zhangxs@uestc.edu.cn);
Yi Zhang (yi_zhang@uestc.edu.cn)

Citation: Gao S, Yang H, Sun Z, *et al*. An interdisciplinary review of the development and applications of embedded three-dimensional printing technology. *Eng Sci Add Manuf*. 2026;2(1):025470032. doi: 10.36922/ESAM025470032

Received: November 19, 2025

Revised: December 9, 2025

Accepted: December 17, 2025

Published online: January 5, 2026

Embedded 3D printing (EMB3D),[9-12] also referred to as immersion 3D printing, effectively mitigates these limitations by utilizing a support bath. This bath provides *in situ* mechanical support for the deposited ink during the printing process, thereby preventing structural collapse and deformation and ensuring high dimensional stability and printing accuracy. Crucially, EMB3D significantly enhances the shape fidelity and resolution of structures fabricated from soft, low-viscosity materials.[13] These distinctive advantages have unlocked new application frontiers for 3D printing with soft materials.

As EMB3D technology has progressed, numerous review articles have been published. Most have focused on specific technical aspects,[14-16] biomedical applications,[11,17-21] parametric interactions,[9,22] or the selection of support baths and inks.[23-25] This review distinguishes itself by providing a comprehensive examination of a broad range of EMB3D applications. It aims to illuminate its cross-disciplinary potential and technical benefits, extending beyond the well-documented biomedical sphere to encompass emerging fields such as flexible electronics and the creation of customized functional materials. Furthermore, the review critically assesses future prospects and challenges.

This review provides a comprehensive analysis of EMB3D (Figure 1), beginning with an overview of its historical development, operational principles, classification systems, and key material properties. It proceeds to deliver a cross-disciplinary assessment of EMB3D applications, with particular emphasis on biomedicine, flexible electronics, and tailored functional materials. By exploring understudied applications and research avenues, this work expands the scope of EMB3D technology while integrating the latest discoveries to present a current perspective on the field's landscape and future path. The review also addresses critical challenges that impede real-world deployment across diverse domains, providing valuable insights to guide future innovation. Through its interdisciplinary, application-focused analysis that highlights both biomedical and non-biomedical applications, this review serves as a valuable resource for researchers, engineers, and professionals seeking to explore the potential of EMB3D.

2. Overview of embedded three-dimensional printing technology

2.1. Historical development of embedded three-dimensional printing

EMB3D originated as an extension of extrusion-based 3D printing to overcome limitations in fabricating complex structures, particularly with soft materials. The introduction of a support bath enabled stable and accurate deposition by providing *in situ* mechanical support. Gratson *et al.*[40] pioneered the foundational concept of EMB3D in 2004, establishing the framework for subsequent technological advancements.

Between the mid-2010s and early 2020s, EMB3D underwent rapid evolution. Wu *et al.*[26] developed omnidirectional printing (ODP), a method for printing 3D biomimetic microvascular networks within a hydrogel support bath. This work laid the groundwork for techniques such as freeform reversible embedding of suspended hydrogels (FRESH). In 2015, Hinton *et al.*[30] successfully printed a complex chicken heart model using FRESH, demonstrating high-fidelity fabrication of intricate 3D structures. Since then, FRESH has been widely adopted for constructing various tissue and organ models, including vascular networks and neural constructs. Research during this period focused on optimizing support bath materials—transitioning from granular to continuous-phase systems, such as Pluronic F-127—and bioinks, including alginate, gelatin, and hyaluronic acid, which offer excellent biocompatibility and rheological properties. EMB3D applications were initially concentrated in the biomedical field.

Since the 2020s, EMB3D has expanded its disciplinary scope into materials science, food science, flexible electronics, and soft robotics. It is now used to fabricate composite materials, architecturally complex food structures in edible gels, and to integrate soft sensors and actuators. Commercialization has accelerated, with companies such as BioBot Scientific introducing desktop EMB3D, thereby lowering entry barriers and expanding the technology's applicability across multiple fields. These developments underscore EMB3D's growing impact as a versatile manufacturing platform.

2.2. Classification of embedded three-dimensional printing strategies

EMB3D strategies are primarily categorized into four distinct approaches based on the role and fate of the support medium and the ink: sacrificial support bath, sacrificial ink, combined sacrificial support bath, and permanent co-curing.

2.2.1. Sacrificial ink

In contrast to sacrificial support baths, which provide a stabilizing environment for ink deposition, sacrificial inks serve as temporary structural materials that are selectively removed after printing to create internal features such as microchannels, cavities, or interconnected networks. This approach enables the fabrication of complex architectures that would otherwise be unattainable through conventional layering techniques (Figure 2A).

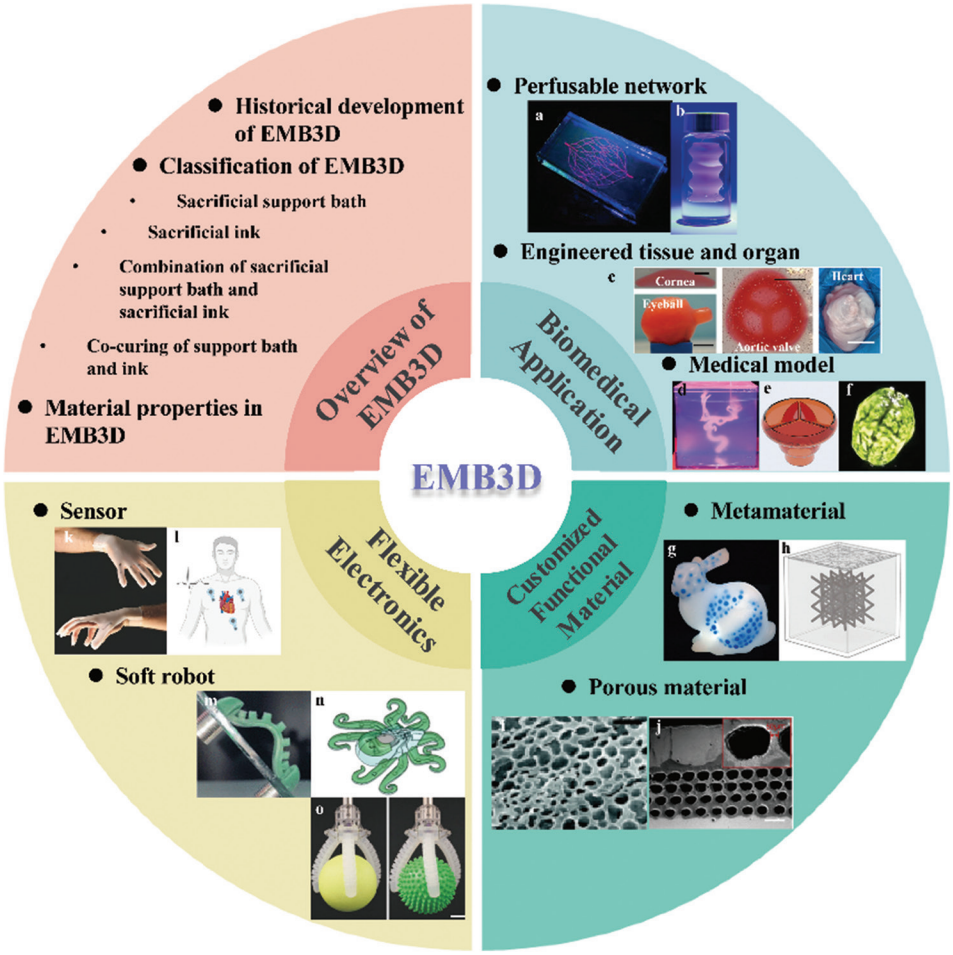

Figure 1. Overview of embedded three-dimensional (3D) printing (EMB3D) technology and its cross-disciplinary applications. (A) Perfusable vascular network. Reprinted with permission from Wu *et al.*[26] Copyright © 2011, WILEY-VCH Verlag GmbH & Co. (B) Model trachea implants. Reprinted with permission from O'Bryan *et al.*[27] Copyright © 2017, The American Association for the Advancement of Science. (C) Tissue and organ equivalents. Adapted from Zhang *et al.*[28] (D) Brain aneurysm model and (E) heart valve model. Reprinted with permission from Duraivel *et al.*[29] Copyright © 2023, The American Association for the Advancement of Science. (F) Brain model. Reprinted with permission from Hinton *et al.*[30] Copyright © 2015, The American Association for the Advancement of Science. (G) Silicone composite fabrication. Adapted from Zehnder *et al.*[31] (H) Complex 3D lattice. Reprinted with permission from Weeks *et al.*[32] Copyright © 2022, Wiley-VCH GmbH. (i) Controlled porous materials. Reprinted with permission from Karyappa *et al.*[33] Copyright © 2019, Royal Society of Chemistry. (J) Ceramic body with microchannels. Adapted from Zhou *et al.*[34] (K) Glove with embedded sensors. Reprinted with permission from Muth *et al.*[35] Copyright © 2014, WILEY-VCH Verlag GmbH & Co. (l) Electrocardiogram recording setup. Reprinted with permission from Hui *et al.*[36] Copyright © 2022, Springer Nature. (M) Magnetic soft robot. Reprinted with permission from Zhang *et al.*[37] Copyright © 2021, IEEE. (N) Octopus-shaped soft robot. Reprinted with permission from Wehner *et al.*[38] Copyright © 2016, Macmillan Publishers Limited. (O) Soft somatosensitive actuator. Reprinted with permission from Truby *et al.*[39] Copyright © 2018, WILEY-VCH Verlag GmbH & Co.

A prominent example of this strategy is found in the work of Lee *et al.*,[53] who utilized the FRESH method to fabricate collagen-based constructs that mimic components of the human heart. The technique achieved multiscale structural fidelity, preserving fine anatomical details essential for physiological function.

In the domain of vascularized tissue engineering, Kolesky *et al.*[44] employed Pluronic F-127 as a sacrificial ink printed within a gelatin methacryloyl (GelMA) matrix. The fugitive ink was subsequently removed by cooling to 4°C, resulting in perfusable microchannels as narrow as 100 μm. These microvascular networks supported endothelial cell lining and nutrient perfusion, demonstrating utility in constructing biologically relevant tissue models.[44]

Beyond biomedical applications, sacrificial inks have been leveraged in soft electronics and robotics. Muth *et al.*[35] formulated a composite ink comprising carbon grease and Pluronic F-127, which was embedded within a silicone elastomer. Dissolution of the Pluronic phase in cold water yielded embedded microcavities, forming the basis of a

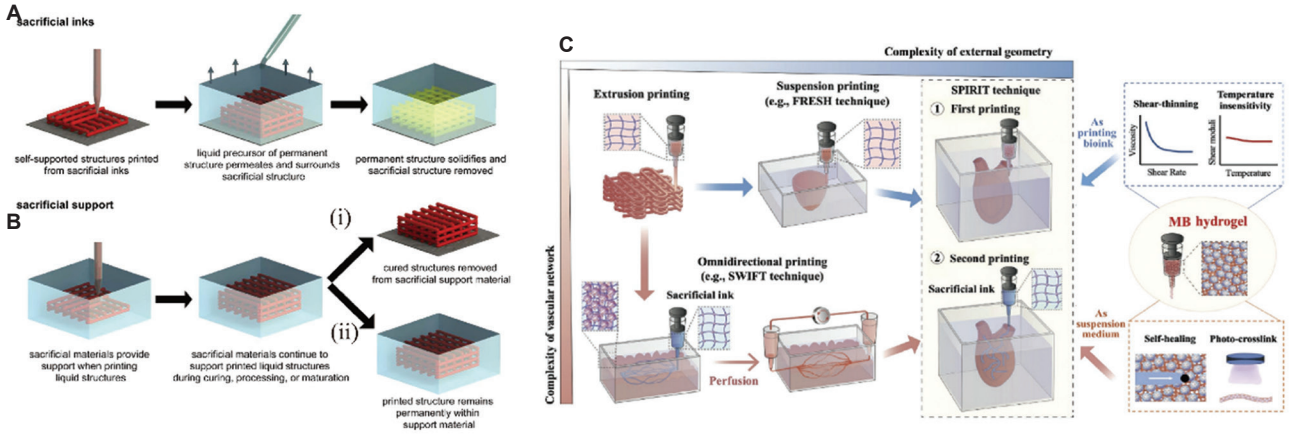

Figure 2. Classification of embedded three-dimensional printing strategies. (A) Schematic of the sacrificial ink approach, where a fugitive ink is deposited and later removed to create internal channels or cavities. (B) Two variations of support-based strategies: (i) Sacrificial support bath, where ink is deposited into a temporary medium that is removed after curing; (ii) permanent co-curing, where both the ink and support bath are solidified together into a unified structure. Reprinted from O'Bryan *et al.*[40] Copyright © 2017, The M printing in a reversible ink template (SPIRIT) strategy, which combines a sacrificial support bath and a sacrificial ink for sequential printing of complex organ constructs with internal vasculature. Reprinted from Fang *et al.*[41] Copyright © 2023, Wiley-VCH GmbH.
Abbreviations: FRESH: Freeform reversible embedding of suspended hydrogels; MB: Microgel-based biphasic; SWIFT: Sacrificial writing into functional tissue.

monolithic three-layer sensor capable of detecting strain and pressure. This method allowed a seamless integration of sensing elements within elastomeric matrices, circumventing interfacial adhesion issues common in multi-material assembly.[35]

Further refining the approach, Shin *et al.*[42] developed a gelatin microparticle-based sacrificial ink that liquefies at 37°C. When printed within a GelMA precursor, the ink promoted the interdiffusion of the photoinitiator, enabling the crosslinking of a surrounding shell before thermal removal. This process yielded self-supporting, endothelialized channels with inner diameters as small as 300 μm, exhibiting high structural integrity and luminal continuity.[42]

Collectively, these studies highlight the versatility of sacrificial ink strategies across a range of applications, from biomimetic tissue constructs to embedded soft sensors. Ongoing research aims to enhance printing resolution, optimize ink removal efficiency, and improve functional integration, further broadening the scope of EMB3D in advanced manufacturing.

2.2.2. Sacrificial support bath

In the sacrificial support bath strategy, liquid ink is extruded into a temporary support medium that provides mechanical confinement during printing and curing. Once the ink solidifies, the support bath is removed, yielding the freestanding printed structure. This approach is particularly well-suited for soft or low-viscosity inks that lack self-supporting ability (Figure 2B).

A notable application of sacrificial support baths in high-temperature processing is demonstrated by Zhou *et al.*,[34] who employed a thermoreversible Pluronic F-127 hydrogel as a self-healing matrix for embedding steel and graphite inks within an alumina-loaded slurry. The Pluronic bath exhibited yield stress at room temperature, enabling shape retention, while its shear-thinning behavior facilitated smooth nozzle traversal. Subsequent drying and high-temperature sintering (up to 1,450°C) decomposed the Pluronic matrix and any sacrificial graphite, resulting in dense alumina ceramics that incorporated steel reinforcements or intricate microchannel networks.

In bioprinting, sacrificial support baths have enabled the fabrication of delicate tissue constructs. Hinton *et al.*[30] developed the FRESH technique, which uses a gelatin microparticle slurry to support the printing of soft hydrogels such as collagen and alginate. The gelatin support is removed by incubation at 37°C, leaving behind complex anatomical architectures, such as heart valves and vascular networks, with high fidelity and minimal structural damage.

Carbopol-based microgel suspensions have also been widely adopted as sacrificial supports due to their tunable yield stress and biocompatibility. O'Bryan *et al.*[41] showed that carbopol gels can sustain the printing of cell-laden hydrogels while preserving cell viability and construct integrity. The support can be readily removed via aqueous dilution, making it ideal for sensitive biological applications.[40]

More recently, ethanol–gel systems have been explored for their rapid solidification and low interfacial tension. Karyappa *et al.*[46] used an ethanol gel to support the printing of polylactic acid/dichloromethane solutions, achieving high-resolution suspended and helical architectures. The gel's rapid recovery post-printing ensured shape retention in complex geometries.

These examples underscore the versatility of sacrificial support baths across material systems. Successful implementation depends critically on tailoring the support's rheology (yield stress, shear-thinning) and removal mechanism (thermal, dissolution, or degradation) to the ink properties and target application.

2.2.3. Permanent co-curing of support bath and ink

Distinct from the sacrificial strategies described above, co-curing approaches intentionally solidify both the support bath and the ink into a single, permanent matrix. In this scenario, the support medium is formulated with reactive groups that can participate in the cross-linking or photopolymerization process of the ink, thereby transforming the originally fluid surroundings into an integral, load-bearing, or functional layer after curing. Since no subsequent removal step is required, co-curing is especially advantageous for creating bulk-soft devices where the interface between "ink" and "support" must be mechanically seamless or where delicate micro-features would collapse during wash-out (Figure 2B).

Greenwood *et al.*[13] first demonstrated this concept for low-stiffness silicone parts: A fumed-silica-thickened silicone oil served as the support bath, while an ultraviolet-initiated silicone ink was printed inside. Localized exposure to 405 nm light triggered simultaneous chain extension in both the extruded filament and the bath region immediately adjacent to the nozzle path. After full cure, the former "support" became a continuous elastomeric block with a spatially programmed modulus (≈20 kPa) and an elongation at break greater than 200%. The absence of a liquefaction/removal stage eliminated the residual swelling problem that is frequently observed when Pluronic or gelatin baths are washed out, and reduced the overall fabrication time by ~30%.

Recent work has extended co-curing to tough hydrogel systems. Hui *et al.*[36] printed silver-hydrogel conductive traces within an alginate–polyacrylamide double-network bath. A one-step thermal cycle (60°C, 30 min) initiated the radical polymerization of the bath and the ink, producing a monolithic, stretchable (≈1,800% strain) and highly conductive (1.4×10^3 S/cm) composite. Impedance spectroscopy showed that the interfacial resistance between trace and matrix was below 1 Ω cm^2, confirming molecular-scale integration.

Despite these advantages, co-curing demands strict rheological and chemical matching. The gel-point, curing kinetics, and optical clarity of the bath must be tuned so that the nozzle can still move without tearing the matrix, and sufficient light or thermal energy reaches the full depth of the part. Ongoing efforts focus on spatio-temporally controlled initiation (e.g., two-photon or microwave-assisted curing) and on orthogonal chemistries that decouple nozzle shear response from cross-link density. If these challenges are solved, co-curing could become the preferred fabrication route for EMB3D of robust, multi-material, and multi-functional soft machines.

2.2.4. Combination of sacrificial support bath and sacrificial ink

The combination of sacrificial support bath and sacrificial ink represents a synergistic strategy that leverages the advantages of both approaches to fabricate highly complex, multi-material, or hollow structures in a single integrated process. This method typically involves depositing a sacrificial ink within a sacrificial support bath, followed by simultaneous or sequential curing and removal steps, enabling the creation of intricate internal features, such as vascular networks, microchannels, or multi-material interfaces, without the need for post-printing assembly (Figure 2C).

A prominent example of this combined approach is the embedded extrusion-volumetric printing process introduced by Tisato *et al.*[43] In this technique, a photopolymerizable support bath is used to stabilize the deposition of an embedded ink through EMB3D. The system supports two modes: Positive embedded extrusion-volumetric printing, where both the ink and support bath are photopolymerizable and cure simultaneously during volumetric printing to form multi-material structures; and negative embedded extrusion-volumetric printing, where a non-polymerizable sacrificial ink is deposited and later flushed out to form hollow microchannels. This approach overcomes the limitations of traditional volumetric printing in achieving multi-material or micro-scale channel features, demonstrating the ability to fabricate structures such as helical actuators and microfluidic chips with channel diameters as small as 119 μm.

Similarly, the sequential printing in a reversible ink template (SPIRIT) strategy, developed by Fang *et al.*,[41] utilizes a microgel-based biphasic bioink that functions both as a printable ink and a self-supporting suspension medium. In SPIRIT, the first printing step defines the external geometry of a tissue construct (e.g., a ventricle) within a sacrificial support bath (e.g., carbopol or gelatin microparticles). The second step involves printing

a sacrificial ink (e.g., gelatin or Pluronic F-127) into the uncrosslinked construct to form internal vascular networks. After crosslinking, both the support bath and sacrificial ink are removed, yielding a perfusable, complex organ model with high structural fidelity and biological functionality.

These integrated strategies highlight the potential of combining sacrificial elements to achieve unprecedented design freedom and functional complexity. Key considerations include the rheological compatibility between the ink and support bath, the kinetics of crosslinking, and the efficiency of removal processes. Future developments may focus on optimizing material formulations and print protocols to further enhance resolution, scalability, and biocompatibility for applications in biomedicine, soft robotics, and advanced materials.

2.3. Material properties in embedded three-dimensional printing

2.3.1. Support bath materials

The selection of an appropriate support bath is crucial in EMB3D, as it directly influences printing resolution, structural fidelity, and integrity. Support baths are broadly classified into two categories based on their microstructure: continuous phase and discontinuous phase (Table 1).

Continuous phase support baths consist of homogeneous materials, such as viscous biofunctional polymer solutions that often incorporate extracellular matrix (ECM) macromolecules, including collagen, laminin, hyaluronic acid, and fibronectin. These materials exhibit favorable rheological behavior, undergoing smooth and reversible solid–liquid transitions under localized shear stress. This enables the printing nozzle to traverse and deposit ink with minimal resistance, while the rapid recovery of the bath to a solid state under static or low-shear conditions stabilizes the deposited structures. By mitigating adverse effects from surface tension, gravity, and particle diffusion, continuous phase baths enhance printing stability and reproducibility.

In contrast, discontinuous phase support matrices comprise discrete particles or microgels—such as carbopol microgel particles[45,46]—that form a heterogeneous internal architecture. Both types of support baths offer distinct advantages; the choice depends on specific printing objectives and application contexts.

Rheological properties are paramount for achieving high-fidelity EMB3D. Support baths typically require shear-thinning behavior and sufficient yield stress to support printed structures while permitting nozzle movement. The composition of the bath governs its rheology, and consequently, its print quality. Tuning the proportions of constituent materials allows optimization of these properties.

The Herschel–Bulkley model (Equation [1]) effectively describes the rheological behavior of support baths:

$$\tau = \tau_y + k\gamma^n \quad (1)$$

where τ is the shear stress, τ_y is the yield stress, k is the consistency index, n is the flow behavior index, and γ is the shear rate. This model is particularly suitable for characterizing materials at low shear rates.

The Oldroyd number (Od), is defined as Equation (2):

$$Od = \frac{\tau_y d}{KU} \quad (2)$$

where d is the nozzle diameter, and U is the printing speed. It quantifies the size of the yielded region within the support bath during the printing process. A higher Od corresponds to a smaller yield zone, which reduces deformation of the surrounding matrix and improves printing precision.[47]

In a study by Grosskopf *et al.*,[48] the rheology of polydimethylsiloxane-based support baths was systematically modified by varying the content of SE 1700. Increasing the SE 1700 concentration raised both the yield stress $\tau_{y,matrix}$ and elastic modulus G'_{matrix} of the bath. For instance, a formulation with 33 wt% SE 1700 exhibited a yield stress of 1.3 ± 0.3 Pa, whereas at 80 wt%, the value increased to 123.7 ± 14 Pa. These rheological adjustments directly influenced yielding behavior and printing fidelity. Furthermore, pronounced shear-thinning—exemplified by the 66 wt% SE 1700 bath—effectively suppressed crack formation during printing, thereby enhancing structural integrity and print quality.

2.3.2. Ink materials

Ink materials are pivotal for constructing 3D structures in EMB3D, as they directly determine printability, structural fidelity, and the functionality of the resulting structures. Based on composition and curing mechanisms, inks are classified into several categories, each with distinct characteristics and applications.

Photocurable inks, such as Silopren UV Electro-225-1 and GelMA, rapidly polymerize under light to achieve high-resolution structures like heart valves and corneal equivalents.[13,28,29] Fused deposition inks, such as polylactic acid and acrylonitrile butadiene styrene, are cost-effective thermoplastics suited for scaffolds, albeit with lower precision.[33] Powder-based inks (e.g., alumina, steel)

Table 1. A comprehensive summary of support bath materials in embedded three-dimensional printing

Category	Support bath material	Key characteristics	Targeted applications
Continuous	Pluronic F-127[34]	Thermoreversible, self-healing hydrogel; shear-thinning	Complex multi-material architectures with high shape fidelity
	Nanoclay-Pluronic F-127 nanocomposite[28]	Thermosensitive yield-stress fluid; ultraviolet transparent; reusable; biocompatible	Precision biomedical constructs: cornea, heart valves, heart models
	Pluronic F-127/ H-hydroxypropyl methylcellulose composite[49]	Easy preparation; rapid removal; bioink compatible; biocompatible	Liver bioprinting with perfusable vascular networks
	Ecoflex 00-30[31,35,37,39]	Ultra-soft elastomer; high elasticity (≤900% elongation); cyclic durability	Stretchable soft sensors and robotic actuators
	Ecoflex 00-10[39]	Soft (Shore-00 10); shear-thinning; thixotropic	Internal geometries in soft robotics and biomedical devices
	SortaClear 40[39]	High durometer (Shore-A 40); rigid yet flexible	Soft robotic grippers and manipulators with force output
	Ethanol[33,50]	Low viscosity; fast solvent diffusion and solidification	Micron-scale structures for microfluidics and sensors
	Paraffin wax matrix[51]	High thermal stability (≤180°C); supports metal inks; inert	Metallic structures: microelectrodes, electron microscope components, scaffolds
	AMULIT[29]	Ultra-low interfacial tension; sub-micron feature capability; ultraviolet inert	Silicone structures: aneurysm models, heart valves
	SMP ink (tBA/AUD)[52]	Photocurable shape-memory polymer; self-supporting; programmable recovery	Shape-memory structures for soft robots and biomedical devices
	Silicone oil/fumed silica[13]	Tunable shear-thinning; balances mobility and support; silicone compatible.	Silicone components: biomechanical models, flexible electronics
	Water[33]	Low viscosity; high surface tension; non-toxic; fast solidification.	Water-soluble inks for drug delivery and cell scaffolds
	DMF[33]	High viscosity; low vapor pressure; controlled diffusion; hydrophobic polymer compatible	Slow solidification for uniform tissue engineering scaffolds
	Dimethyl sulfoxide[33]	High viscosity; low vapor pressure; broad compatibility; minimal ink degradation	Bioinks requiring slow diffusion, e.g., protein hydrogels
Discontinuous	Gelatin microparticles[30,44,53]	Reversible phase transition; uniform particles; biocompatible and biodegradable	Heart models and tendon/ligament tissue constructs
	Ethanol gel[50]	Localized flow; fast structural recovery; enables freeform fabrication	Freeform structures: microfluidic coils, MEMS
	Alginate polyacrylamide hydrogel[36]	Yield-stress fluid; shear-thinning; cures to soft, stretchable hydrogel	Flexible electronics: strain sensors, inductors, electrodes
	Granular silicone microgel[32]	Solvent-free; shear-thinning and yield-stress; easy part retrieval	Polymer lattices and composites with clean retrieval

Abbreviations: AMULIT: Additive manufacturing at ultralow interfacial tension; AUD: Aliphatic urethane diacrylate; DMF: N, N-dimethylformamide; SMP: Shape memory polymer; tBA: tert-Butyl acrylate.

require post-printing sintering and are used in ceramic composites.[34] Bioinks, including cell-laden collagen and alginate, enable the fabrication of living tissues but demand stringent control over printing conditions.[49,54] Metal inks, such as silver nanoparticle ink, produce conductive features for electronics, though they often involve high-temperature processing.[51]

Specialized functional inks are also employed: carbon conductive grease serves as a sensing element,[35,52] Pluronic F-127 acts as a fugitive material,[39] and ionic liquids like 1-ethyl-3-methylimidazolium ethyl sulfate create conductive sensors.[39] The selection of an ink must account for its rheology, curing kinetics, and compatibility with the support bath. A summary of common EMB3D ink materials is provided in Table 2.

2.3.3. Matching of support bath and ink

The successful implementation of EMB3D heavily relies on the optimal matching between the support bath and the ink. This matching is governed by several critical factors,

Table 2. A comprehensive summary of ink materials in embedded three-dimensional printing

Category	Ink material	Key characteristics	Typical applications
Solvent-induced phase separation	PLA/DCM[50]	Shear-thinning; rapid ethanol-induced solidification; tunable porosity; low-temperature processing	Tissue engineering scaffolds (e.g., vascular grafts, bone)
	Acrylonitrile butadiene styrene[33]	Soluble in various solvents; forms porous structures	Applications requiring high mechanical strength
	PLA[33]	Biodegradable; suitable for biomedical applications	Biocompatible scaffolds
	Polycaprolactone[33]	Low melting point; suitable for low-temperature processing	Tissue engineering and drug delivery
	Alumina[34]	High hardness and melting point; biocompatible	Ceramic composites
	Steel[34]	High strength and density	Reinforcement in ceramic composites
	Graphite[34]	Low density; high electrical conductivity	Microchannel arrays
Photopolymerization	Silopren UV Electro-225-1[13,29]	High precision; suitable for complex silicone structures	Heart valves; vocal fold models
	MoldStar[31]	Platinum-cure silicone; moderate stiffness	Stiffness-tuning dopant
	GelMA[28,44,49]	Photocrosslinkable; biocompatible; cell-compatible	Cell-laden matrices; corneal structures
	NaAlg/PEGDA[28]	Tunable mechanics; dual crosslinking (photo/ionic)	Cornea; eyeball; heart valve models
Thermal crosslinking	Gelest ExSil 100[29]	Tunable mechanical properties to mimic tissues	Brain aneurysm models
	Epoxy resin-based ink[32]	Thermoset; tunable rheology	Lattice structures
	Flexible epoxy ink[32]	Flexibilizer-modified; tunable mechanics	Multi-material lattices
Chemical crosslinking	Silver flakes in support matrix[36]	High conductivity; covalent bonding with matrix; stretchable	Soft sensors; electrodes; wireless devices
	NdFeB magnetic particles in a support matrix[37]	Magnetic responsiveness	Magnetic soft robots
	EMIM-ES with fumed silica[39]	Shear-thinning; non-volatile; non-permeating	Soft actuators with sensing
	Ecoflex 00-30[13]	Low stiffness; biocompatible	Soft robots; biomechanical models
	Sylgard 184[13]	High stiffness; widely applicable	Structural silicone parts
	Collagen[54]	Enhanced bonding through EDC/NHS; tunable mechanics	Tendon repair; muscle-tendon interfaces
Ionic crosslinking sintering	Alginate[54]	Calcium chloride crosslinking; biocompatible; low strength	Soft robotics; cardiac/muscle tissues
	Silver nanoparticle ink[51]	High-resolution; high-temperature sintering	Three-dimensional metal structures (springs, antennas)
	Copper nanoparticle ink[51]	High-resolution; high-temperature sintering	Metallic microstructures
	Alumina nanoparticle ink[51]	High-resolution; high-temperature sintering	Ceramic microstructures
Other/functional	Carbon conductive grease[35,52]	Shear-thinning; high yield stress; conductive	Embedded sensors
	Pluronic F-127[39]	Sacrificial; forms removable channels	Fugitive ink for vasculature
	Water (with xanthan gum)[31]	Incompressible; viscosity-enhanced	Matrix softening dopant

Abbreviations: DCM: Dichloromethane; EDC/NHS: 1-ethyl-3-(3-dimethylaminopropyl) carbodiimide/N-hydroxysuccinimide; EMIM-ES: 1-ethyl-3-methylimidazolium ethyl sulfate; GelMA: Gelatin methacryloyl; NaAlg/PEGDA: Sodium alginate/polyethylene glycol diacrylate; NdFeB: Neodymium–iron–boron; PLA: Polylactic acid.

including interfacial tension, diffusion-driven interfacial instability, charge-driven interfacial instability, and, for photo-crosslinkable inks, the optical properties and distribution of photoinitiators. A thorough understanding and control of these interactions are essential prerequisites for achieving high-fidelity prints with complex geometries.

Interfacial tension plays a pivotal role in determining the stability of the ink within the support bath. When the interfacial tension is high, the ink filaments tend to break into droplets due to Rayleigh–Plateau instability, leading to poor print resolution. Conversely, low interfacial tension promotes filament stability, enabling the printing of fine

features. For instance, Duraivel *et al.*[29] demonstrated that printing silicone-based inks into aqueous support baths with high interfacial tension resulted in filament breaking into spherical droplets. In contrast, using silicone oil-based support baths with ultralow interfacial tension enabled the printing of continuous and stable filaments with high resolution (Figure 3A). This highlights the importance of selecting support bath and ink pairs with matched chemical properties to minimize interfacial tension.

Diffusion-driven interfacial instability arises when molecular diffusion between the ink and support bath occurs faster than the ink's solidification kinetics. This is particularly problematic for small-molecule inks in aqueous support baths, where rapid diffusion can cause ink spreading, swelling, or dissolution, degrading the printed structure. To mitigate this, oil-based support baths can be used to slow down diffusion, allowing sufficient time for the ink to solidify. For example, in immersion precipitation 3D printing (ip3DP), Karyappa *et al.*[33] utilized non-solvent baths to control the solidification of polymeric inks through phase separation, achieving porous structures with high fidelity (Figure 3B). Similarly, Lei *et al.*[45] emphasized the importance of matching the diffusion rates to prevent interfacial instability. The use of viscous support baths, such as those containing high polymer concentrations, can further suppress diffusion and enhance print accuracy.

Charge-driven interfacial instability occurs due to electrostatic interactions between the ink and support bath,

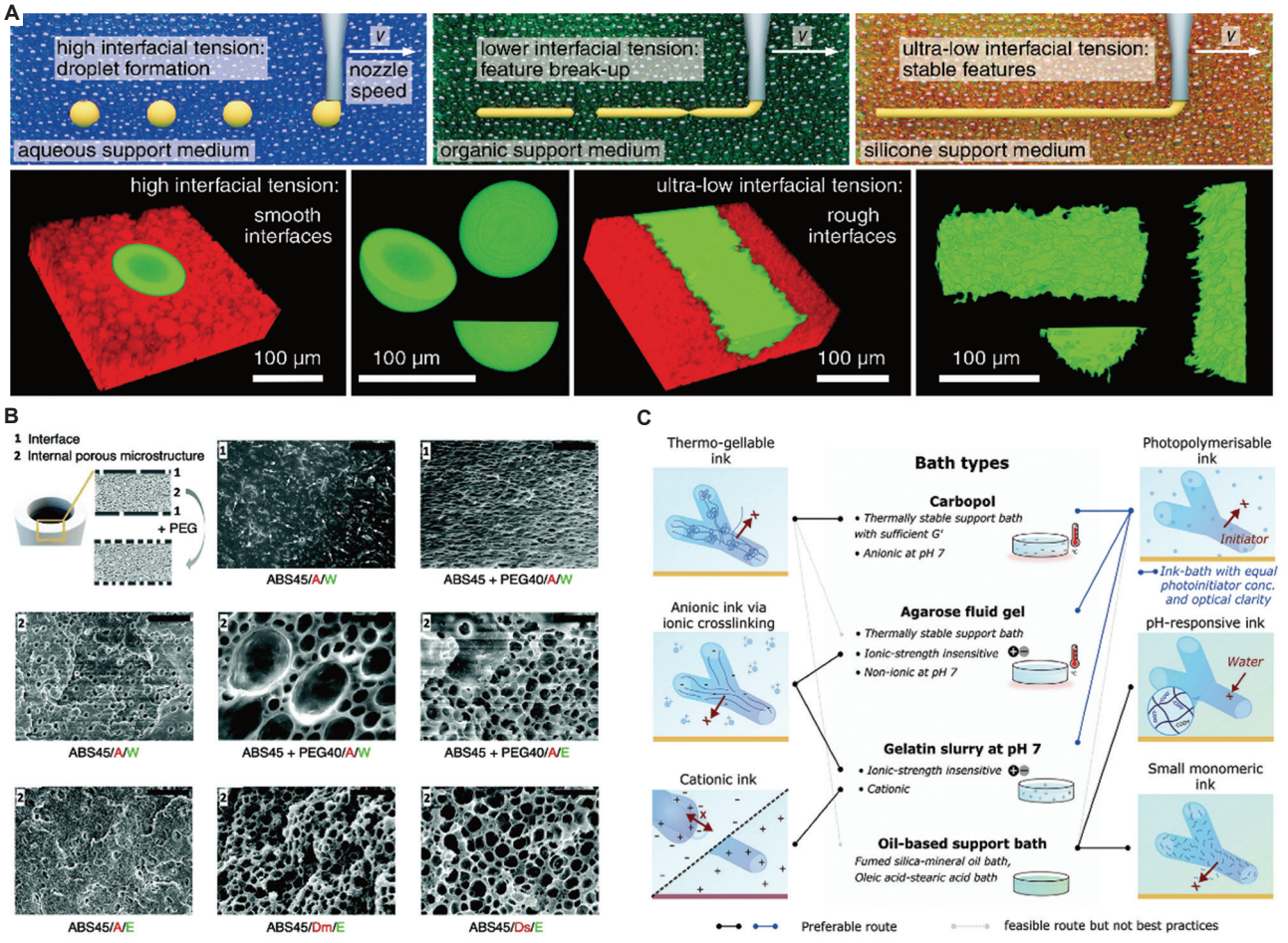

Figure 3. Key factors influencing the fidelity of embedded three-dimensional printing through support bath–ink interactions. (A) Interfacial tension governs filament stability: high tension leads to droplet breakup, while ultralow tension enables continuous printing of fine features. Scale bar: 100 µm. Reprinted with permission from Duraivel *et al.*[29] Copyright © 2023, The American Association for the Advancement of Science. (B) Diffusion-induced phase separation and microstructure control in immersion precipitation 3D printing, illustrating the effects of porogens and solvents on internal and interfacial porosity. Scale bar: 2 µm. Reprinted with permission from Karyappa *et al.*[33] Copyright © 2019, Royal Society of Chemistry. (C) Guidance for selecting support baths based on hydrogel ink properties, emphasizing matching photoinitiator concentration and optical clarity for optimal printability. Adapted from Lei *et al.*[45]
Abbreviation: PEG: Polyethylene glycol.

especially when using polyelectrolyte-based materials. For instance, printing anionic hydrogels into cationic support baths can lead to ink dragging, aggregation, or precipitation, resulting in poor print quality. To address this, neutral support baths, such as agarose gels or gelatin slurries, are often employed to minimize electrostatic interactions (Figure 3C). Hui *et al.*[36] reported the use of alginate–polyacrylamide support baths for printing conductive silver–hydrogel inks, where charge compatibility was crucial for maintaining structural integrity.

For photo-crosslinkable inks, the optical transparency of the support bath and the distribution of photoinitiators are critical factors. High optical transparency ensures uniform light penetration for effective crosslinking throughout the printed structure. If the support bath is opaque, light scattering can reduce the curing efficiency, leading to incomplete crosslinking.[55,56] Moreover, the photoinitiator concentration must be optimized in both the ink and support bath to prevent diffusion-related issues. If photoinitiators are only present in the ink, they may diffuse into the support bath, reducing the local concentration and requiring longer exposure times. Studies have shown that matching the photoinitiator type and concentration between the ink and support bath can improve crosslinking efficiency and print resolution.[13,36] For example, in the co-curing approach by Greenwood *et al.*,[13] both the ink and support bath contained photoinitiators, enabling simultaneous curing and seamless integration.

In summary, achieving high-quality EMB3D requires careful consideration of the physicochemical interactions between the support bath and ink. By minimizing interfacial tension, controlling diffusion, neutralizing charge interactions, and optimizing photo-crosslinking conditions, researchers can exploit the full potential of EMB3D for fabricating complex 3D structures. Table 3 provides a comprehensive overview of successful support bath-ink combinations, serving as a valuable guide for material selection in various applications.

2.4. Comparison with other extrusion-based technologies

EMB3D is differentiated from other extrusion-based methods by its core innovation: a yield stress support bath that provides *in situ* stabilization. This section contrasts EMB3D with three principal extrusion techniques to delineate its unique niche.

Direct ink writing (DIW) relies on the viscoelasticity of inks to maintain structural integrity during deposition. While enabling multi-material and functional printing, DIW is fundamentally constrained by the need for rapid solidification or high ink storage modulus, making it unsuitable for low-viscosity or soft materials that lack cohesive strength.[57,58] EMB3D circumvents this limitation by decoupling structural support from ink rheology, allowing the freeform deposition of fluidic materials that would otherwise flow or collapse.

Fused deposition modeling extrudes and fuses thermoplastic filaments, excelling in the production of robust, durable parts. Its material scope, however, is largely confined to engineering polymers with melt-processing characteristics, precluding the use of elastomers, hydrogels, or living cells.[59,60] EMB3D's support bath environment is inherently compatible with these soft and biologically active materials, opening avenues in biomedical and soft robotic applications where elasticity and biocompatibility are essential.

Conventional extrusion bioprinting often employs viscous bioinks to mitigate deformation, yet struggles with gravitational sagging and poor resolution when fabricating delicate features such as vascular networks.[61] The omnidirectional support in EMB3D effectively counters these forces, enabling high-fidelity fabrication of overhanging structures, internal cavities, and perfusable channels that are critical for advanced tissue models.

In summary, as shown in Table 4, EMB3D not only incrementally improves upon existing extrusion methods but also introduces a distinct paradigm. By providing transient, programmable mechanical support, it uniquely addresses the challenge of shape fidelity for soft matter, thereby expanding the functional and material frontiers of additive manufacturing.

3. Biomedical applications of embedded three-dimensional printing

The pursuit of functional tissue fabrication through extrusion-based bioprinting remains challenging due to the inherent structural complexity and biochemical heterogeneity of native tissues. Effective bioprinting requires bioinks that exhibit excellent printability, cytocompatibility, and biomimetic properties. While biopolymer hydrogels are widely used for their tunable mechanical and physicochemical traits—enabling replication of the ECM with high cell viability—conventional methods struggle to maintain structural integrity during printing. EMB3D addresses these limitations by utilizing a support bath that provides *in situ* stabilization, enabling the fabrication of high-fidelity, complex structures from low-viscosity precursors without the need for external supports or orientation constraints.[19,45] Support baths range from viscous fluids to particulate and solid gels, each tailored to specific bioink requirements. EMB3D is particularly

Table 3. A comprehensive summary of support bath-ink combinations in embedded three-dimensional printing

Support bath material	Ink material	Features	Applications
Ethanol	PLA/DCM solution (7.5–30% w/w)[50]	Rapid solvent diffusion enables solidification within seconds; requires precise control of printing parameters to prevent ink spreading	Fabrication of tissue engineering scaffolds, microfluidic devices, and customizable biodegradable structures
Ethanol-based gel	PLA/DCM solution (≥15% w/w)[50]	Exhibits shear-thinning and yield stress; supports freeform fabrication with rapid recovery post-printing	Ideal for complex suspended structures, flexible electronics, and drug delivery systems
Ecoflex 00-30	Carbon conductive grease[35]	High elasticity and stretchability; conductive ink with shear-thinning behavior	Highly stretchable soft sensors
	NdFeB magnetic particles mixed with a support matrix[37]	Non-Newtonian support bath with magnetic-responsive ink	Magnetically driven soft robots
	Mixture of EMIM-ES and fumed silica nanoparticles[39]	Intermediate durometer combined with conductive ionic gel for complex internal structures	Soft robotic actuators with integrated sensing capabilities
	MoldStar[31]	Ecoflex as a compliant matrix and MoldStar as a stiff dopant; tunable mechanical properties	Fabrication of composite silicone materials with adjustable stiffness
	Water[31]	Ecoflex matrix with water as an inviscid dopant; enables tunable stiffness	Composite silicone materials with modified mechanical properties
SortaClear 40	Mixture of EMIM-ES and fumed silica nanoparticles[39]	High durometer support combined with conductive ionic gel	Soft robotic actuators requiring robust structural support
Ecoflex 00-10	Mixture of EMIM-ES and fumed silica nanoparticles[39]	Highly extensible support bath with conductive ionic gel	Soft robotic actuators with complex internal geometries
Paraffin wax matrix	Silver nanoparticle ink[51]	High thermal stability and appropriate yield stress; enables high-resolution printing and sintering	Fabrication of three-dimensional metal structures, such as micro-spring arrays and BCC lattices
	Copper nanoparticle ink[51]	Similar thermal properties and yield stress; supports high-resolution metal printing	Production of micro-springs and other metallic components
	Alumina nanoparticle ink[51]	High thermal stability and yield stress; suitable for high-temperature sintering	Manufacturing of micro-springs and ceramic-metal composites
AMULIT (inverse emulsion)	Polydimethylsiloxane inks (e.g., Gelest ExSil 100 and Silopren UV Electro-225-1)[29]	Ultralow interfacial tension allows printing of features as small as 8 μm; excellent mechanical properties	Complex silicone structures, such as brain aneurysm models and functional heart valves
Alginate–polyacrylamide	Silver flakes mixed with support matrix[36]	Yield stress fluid behavior; high conductivity and covalent crosslinking with the support	Strain sensors, inductors, biomedical electrodes, and wireless powering devices
SMP ink (tBA/AUD)	Carbon conductive grease[52]	Self-supporting structure with embedded sensors; compatible with complex geometries	Smart hinges with integrated strain sensors
A mixture of silicone oil and fumed silica	UV Electro 225-1[13]	Support bath cures during printing, bonding with ink for uniform support	Silicone parts with complex internal structures.
	Ecoflex 00-30[13]	Rheological properties support low-viscosity inks, achieving high geometric fidelity	Soft biomechanical models and robots
	Sylgard 184[13]	High strength and stability support printing of high-stiffness inks	Silicone structures requiring high mechanical strength
Gelatin microparticles	Alginate[54]	Supports complex geometries; stable printing of low-strength hydrogels	Bioprinting of heart models and vascular structures
	Collagen[54]	Enhanced mechanical properties via chemical crosslinking; cell-friendly	Cardiac ventricles and tendon tissue engineering

(Cont'd...)

Table 3. ***(Continued)***

Support bath material	Ink material	Features	Applications
Granular silicone microgel	Epoxy resin-based ink[32]	Temporary support during printing; cured epoxy separated post-printing	Complex three-dimensional lattice structures, including periodic and stochastic designs
	Flexible epoxy ink[32]	Co-printed with rigid epoxy to create multi-material lattices with anisotropic properties	Programmable mechanical responses in multi-material architectures
Water	Acrylonitrile butadiene styrene[33]	Rapid solidification; forms porous structures	Applications requiring high mechanical strength
Ethanol	PLA[33]	Biodegradable; rapid solidification	Biocompatible scaffolds
DMF	Polycaprolactone[33]	Low melting point; suitable for low-temperature processing	Tissue engineering and drug delivery
Pluronic F-127	Alumina[34]	High viscosity and self-healing properties	Ceramic structure fabrication
	Steel[34]	High viscosity supports high-density structures	Reinforcement of ceramic composites
	Graphite[34]	Low viscosity; supports complex microchannels	Microfluidic devices
Nanoclay-Pluronic F-127 nanocomposite	NaAlg/PEGDA[28]	Thermosensitive support bath; photocrosslinkable and ionically crosslinkable ink	High-precision printing of complex structures like eyeballs and heart valves
	GelMA[28]	High transparency ink; enables printing of transparent structures	Cornea and eyeball models with smooth surface finish
Composed of Pluronic F-127 and H-hydroxypropyl methylcellulose	GelMA[28]	Biocompatible support media; photocrosslinkable and cell-compatible ink	Liver tissue constructs with vascular networks and hepatospheroids

Abbreviations: AMULIT: Additive manufacturing at ultralow interfacial tension; AUD: Aliphatic urethane diacrylate; BCC: Body-centered cubic; DCM: Dichloromethane; DMF: N, N-dimethylformamide; EDC/NHS: 1-ethyl-3-(3-dimethylaminopropyl) carbodiimide/N-hydroxysuccinimide; EMIM-ES: 1-ethyl-3-methylimidazolium ethyl sulfate; GelMA: Gelatin methacryloyl; NaAlg/PEGDA: Sodium alginate/polyethylene glycol diacrylate; NdFeB: Neodymium–iron–boron; PLA: Polylactic acid; SMP: Shape memory polymer; tBA: tert-Butyl acrylate.

Table 4. Comparative overview of embedded three-dimensional printing and other extrusion-based three-dimensional printing technologies

Parameters	Embedded three-dimensional printing	Direct ink writing	Fused deposition modeling	Conventional extrusion bioprinting
Support mechanism	Yield stress bath (*in situ*)	None or passive substrate	None	None or temporary scaffolds
Typical material viscosity	Low to high (soft materials dominant)	Medium to high	High (thermoplastics)	Medium to high
Structural support	Omnidirectional, prevents collapse	Limited, relies on ink self-support	None, relies on rapid solidification	Limited, prone to sagging
Primary advantage	High fidelity with soft/ low-viscosity inks	Multi-material, functional composites	Mechanical strength, cost efficiency	Biocompatibility, cell compatibility
Main limitation	Post-printing bath removal and clean up	Collapse of low-viscosity structures	Limited to thermoplastics	Poor resolution with low-viscosity inks
Representative applications	Soft robotics, vascularized tissues, and customized functional materials	Electronics, structural composites	Prototypes, mechanical components	Tissue scaffolds, organ models

well-suited for applications that require precise spatial and compositional control, such as tissue engineering, drug screening, and regenerative medicine. One of its most promising applications lies in the fabrication of perfusable vascular networks, which are essential for sustaining cellular viability in engineered tissues.

3.1. Fabrication of perfusable vascular networks

The fabrication of perfusable, vascular-like networks is a cornerstone in engineering clinically relevant tissues, as these conduits are indispensable for nutrient delivery, gas exchange, and metabolic waste removal in thick, cellularized constructs.[62-66] While extrusion-based

3D printing allows for the customization of channel architectures,[67,68] its layer-by-layer approach often results in structural weaknesses at the interfaces and surface roughness that compromise lumen integrity and fluidic performance.[69-71] EMB3D circumvents these limitations by providing omnidirectional support during deposition, enabling the direct writing of continuous and complex vascular features within a stabilizing matrix.

Early demonstrations of this capability include the omnidirectional printing technique by Wu *et al.*,[26] which employed a fugitive Pluronic F-127 ink printed into a photopolymerizable support bath to create 3D biomimetic microvascular networks with channel diameters ranging from 200 to 600 μm (Figure 4A). A key innovation of this approach was the use of a physically supportive yet chemically permissive reservoir that stabilized the printed fugitive ink during patterning and was subsequently rendered permanent through cross-linking, after which the ink was evacuated to yield patent microchannels.

However, such sacrificial ink strategies typically generate bare conduits lacking a built-in, vessel-like wall. To address this, subsequent research has focused on forming defined, cohesive tubular walls around the sacrificial templates. Strategies leveraging interfacial phenomena have shown particular promise. For instance, the co-assembly of oppositely charged polyelectrolytes at the ink–bath interface can spontaneously form a thin membrane,[72] albeit this method is inherently material-specific. Diffusion-controlled gelation, where an initiator diffuses from a sacrificial core into a gelable support bath, can produce denser, multilayered walls,[73] yet its reliance on sequential manual immersion limits resolution and scalability for intricate, small-diameter networks.

A significant advancement was achieved with the development of the gelation of uniform interfacial diffusant in the EMB3D (GUIDE-3DP) method by Shin *et al.*[42] (Figure 4B). This technique strategically uses a sacrificial ink laden with a gel initiator. On printing, the initiator diffuses radially into the surrounding gel-precursor support bath, triggering a localized cross-linking reaction that forms a seamless, tubular shell with tunable thickness. By controlling parameters such as printing speed, pressure, initiator concentration, and diffusion time, the inner and outer diameters of the resulting vessel can be independently and precisely defined. The GUIDE-3DP platform has been validated by fabricating endothelial cell-lined channels and complex, multi-branched vascular networks that faithfully mimic native anatomical and physiological features.

Further expanding the design space, the SPIRIT strategy, as proposed by Fang *et al.*,[41] combines sacrificial support baths and inks in a sequential printing process to engineer organ-scale constructs, such as ventricles, that incorporate intricate, hierarchical, and perfusable vascular trees within a defined external geometry (Figure 4C). Complementing these approaches, Senior *et al.*[74] demonstrated the use of an agarose particulate gel as a support bath to fabricate large, bifurcated vascular constructs and osteochondral-mimicking structures with perfusable channels up to 25 mm in height, showcasing the ability to maintain architectural fidelity in mechanically graded scaffolds (Figure 4D). In a similar vein, O'Bryan *et al.*[27] employed a self-assembled micro-organogel to 3D print silicone-based, perfusable vascular networks (Figure 4E). They successfully fabricated a complex, branched construct in which a single inlet channel diverged into multiple patent outlets, supporting high-flow-rate fluid perfusion post-curing.

Collectively, these EMB3D-derived methodologies have fundamentally transformed the landscape of vascularized tissue engineering. They provide a versatile and robust toolkit for creating perfusable, hierarchically branched, and biologically functional vascular networks that are critical for the development of viable, implantable tissue constructs and physiologically representative *in vitro* models.

3.2. Bioprinting of engineered tissues and organs

The on-demand fabrication of 3D vascularized tissues represents a pivotal advancement for tissue engineering,[75] drug screening,[76] and organ repair.[77-79] Successful replication of native tissues requires the integration of key components: cells, ECM, and a functional vascular network. The absence of perfusable microvasculature—critical for nutrient transport and waste removal—has long impeded the development of viable volumetric tissues.[80,81]

Three-dimensional printing has emerged as a promising strategy to address these challenges.[82] While early approaches focused on constructing cell-free scaffolds or molds for post-fabrication cell seeding,[83-86] direct bioprinting (or bioprinting) of cell-laden constructs enables more precise spatial control.[69,87] However, conventional methods often fail to incorporate implantable vascular networks, limiting the scale and functionality of engineered tissues.

EMB3D offers a transformative solution by enabling the fabrication of complex, vascularized structures within a supportive matrix. A landmark study by Kolesky *et al.*[44] demonstrated the co-printing of vasculature, multiple cell types, and ECM using a custom multi-head bioprinter. They employed a fugitive ink comprising Pluronic F-127 to create perfusable channels and GelMA as a biocompatible ECM analog, achieving heterogeneous tissue constructs with programmable architecture.

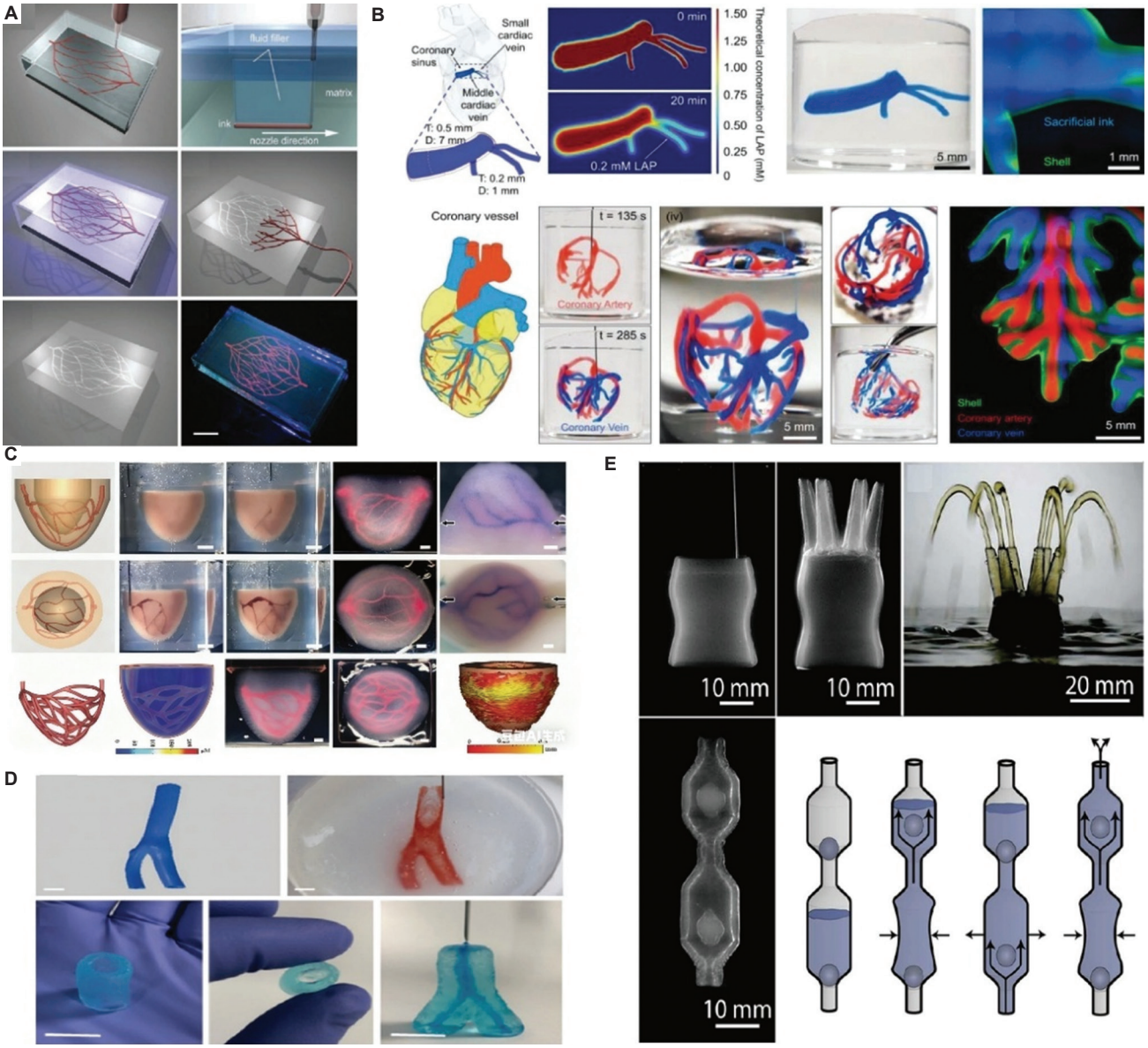

Figure 4. Embedded three-dimensional (3D) printing strategies for fabricating perfusable vascular networks and organ-scale constructs. (A) Schematic and fluorescent image of a 3D biomimetic microvascular network fabricated by omnidirectional printing of a fugitive ink within a photopolymerizable hydrogel support bath. Scale bar: 10 mm. Reprinted with permission from Wu *et al.*[26] Copyright © 2011, WILEY-VCH Verlag GmbH & Co. (B) Complex perfusable networks fabricated via the gelation of uniform interfacial diffusant in embedded 3D printing method, enabling controlled shell thickness and multi-material channel structures. Scale bars: 1 mm, 5 mm. Reprinted from Shin *et al.*[42] Copyright © 2023, Wiley-VCH GmbH. (C) SPIRIT strategy for fabricating a ventricle construct with an embedded hierarchical vascular network. Reprinted with permission from Fang *et al.*[41] Scale bar: 2 mm. Copyright © 2023, Wiley-VCH GmbH. (D) Tubular and branched vascular structures fabricated using suspended layer additive manufacturing within a gellan-based support bath. Scale bar: 10 mm. Adapted from Senior *et al.*[74] (E) 3D-printed silicone-based perfusable networks and functional pumps fabricated within a self-assembled micro-organogel support matrix. Scale bars: 10 mm, 20 mm. Reprinted with permission from O'Bryan *et al.*[27] Copyright © 2017, The American Association for the Advancement of Science.

Beyond achieving vascularization, the *de novo* reconstruction of human organs from autologous sources represents a paramount long-term objective in tissue engineering.[88,89] Engineered tissues and organs not only offer a solution to the global organ shortage,[90,91] but also hold great promise in surgical planning,[92] education,[93] and disease modeling.[94] Traditional strategies involve seeding cells onto biomaterial scaffolds[95,96] or decellularized

natural organs,[97,98] yet replicating the complex structures, heterogeneous components, and physiological functions of native tissues remains challenging.

The advent of 3D bioprinting, particularly extrusion-based methods due to their broad material compatibility and low cost,[99,100] offers a promising solution. Among the primary bioprinting strategies—inkjet,[101,102] material extrusion,[103,104] and vat photopolymerization[105]—embedded 3D bioprinting is a key advancement for extrusion-based techniques. This approach involves printing bioinks into a yield stress support bath, which provides ubiquitous physical support, enabling the fabrication of engineered tissue and organ equivalents with complex structures.[74,106]

Human tissues and organs typically exhibit functional features across multiple length scales. For instance, the cornea possesses submicron surface roughness,[106,107] while the overall eyeball and aortic valve are tens of millimeters in size, with key features like the optic nerve sheath diameter[108] and leaflet thickness[109] being only a few millimeters. The heart, one of the largest organs, measures over 10 cm in diameter. Despite significant successes with embedded printing methods,[30,53,88,110-112] particulate gels,[91,95,104,113-117] nanoclay-assisted printing,[90,103,118] and other techniques,[27,74,94,97,100,106,119-124] the achievable feature sizes have been limited to hundreds of micrometers to tens of millimeters. This limitation stems partly from the constrained processability of existing yield-stress fluids, whose inadequate flow characteristics hinder the *in situ* replenishment of the support bath. Consequently, the achievable printing scale and feature resolution are governed by a combination of nozzle geometry, ink rheology, and cellular concentration.

To achieve high-fidelity replication of human tissues and organs possessing multi-scale anatomical features, Zhang *et al.*[28] devised a multiscale embedded printing strategy. This approach employed a stimulus-responsive, yield stress support bath material engineered to undergo liquefaction at 4°C, thereby enabling its on-demand replenishment throughout the printing process. Furthermore, the implementation of a dynamic layer height control technique was critical for fabricating corneal constructs with exceptionally smooth surface topographies. This method successfully fabricated homogeneous and heterogeneous human eye analogs and aortic valve structures (Figure 5A). Notably, the multiscale embedded printing strategy successfully overcame previous size and resolution barriers, as evidenced by the printing of a full-scale human heart (Figure 5B) via a short nozzle and cyclic bath addition.

The versatility of EMB3D is further demonstrated by its application in creating functional and implantable organ analogs. Building on prior work showing the therapeutic potential of 3D liver assemblies,[125,126] Jiang *et al.*[53] fabricated transplantable hepatic constructs via EMB3D.[49] They utilized a novel support bath, termed the omnidirectional print embedding network, which was designed to ease preparation and removal, thereby safeguarding delicate vascular networks.[127] The bioprinted transplantable hepatic constructs, featuring integrated venous networks (Figure 5C), promoted endogenous neovascularization upon implantation, marking a significant advance toward viable organ replacement. In a complementary approach for structural organs, Lee *et al.*[53] employed the FRESH technique to bioprint a tri-leaflet heart valve from collagen that functioned under pulsatile flow, as well as a neonatal-scale human heart model that replicated the intricate internal anatomy (Figure 5D).

These collective advances underscore the capacity of EMB3D to generate biologically relevant tissues and organs with complex geometry and functionality. Continued innovation in bioink formulation, support bath design,[127] and multi-material printing will further accelerate the translation of engineered tissues into regenerative medicine and disease modeling.

3.3. Patient-specific anatomical models for surgical planning

EMB3D enables the fabrication of high-fidelity, patient-specific anatomical models for surgical planning by accurately replicating complex internal and external structures derived from medical imaging data. These models offer surgeons tangible, biomimetic tools for preoperative simulation, thereby enhancing procedural precision and clinical outcomes.

Hinton *et al.*[30] demonstrated the capability of EMB3D using the FRESH technique to create complex anatomical models. They printed an embryonic chicken heart model, scaled up to ~2.5 cm, based on confocal microscopy data, which retained internal trabecular structures as validated by multiphoton microscopy and dark-field imaging (Figure 6A). In addition, a human brain model from magnetic resonance imaging data, scaled down to 3 cm, captured intricate cortical folds, with key regions such as the frontal lobe, temporal lobe, and cerebellum delineated using alginate and contrast-enhanced dye (Figure 6B). These models demonstrate EMB3D's capability to produce structures with sub-millimeter resolution, thereby overcoming the limitations of traditional manufacturing.

Duraivel *et al.*[29] advanced this application with the additive manufacturing at ultralow interfacial tension technology, employing a reverse emulsion support bath with ultralow interfacial tension to prevent deformation

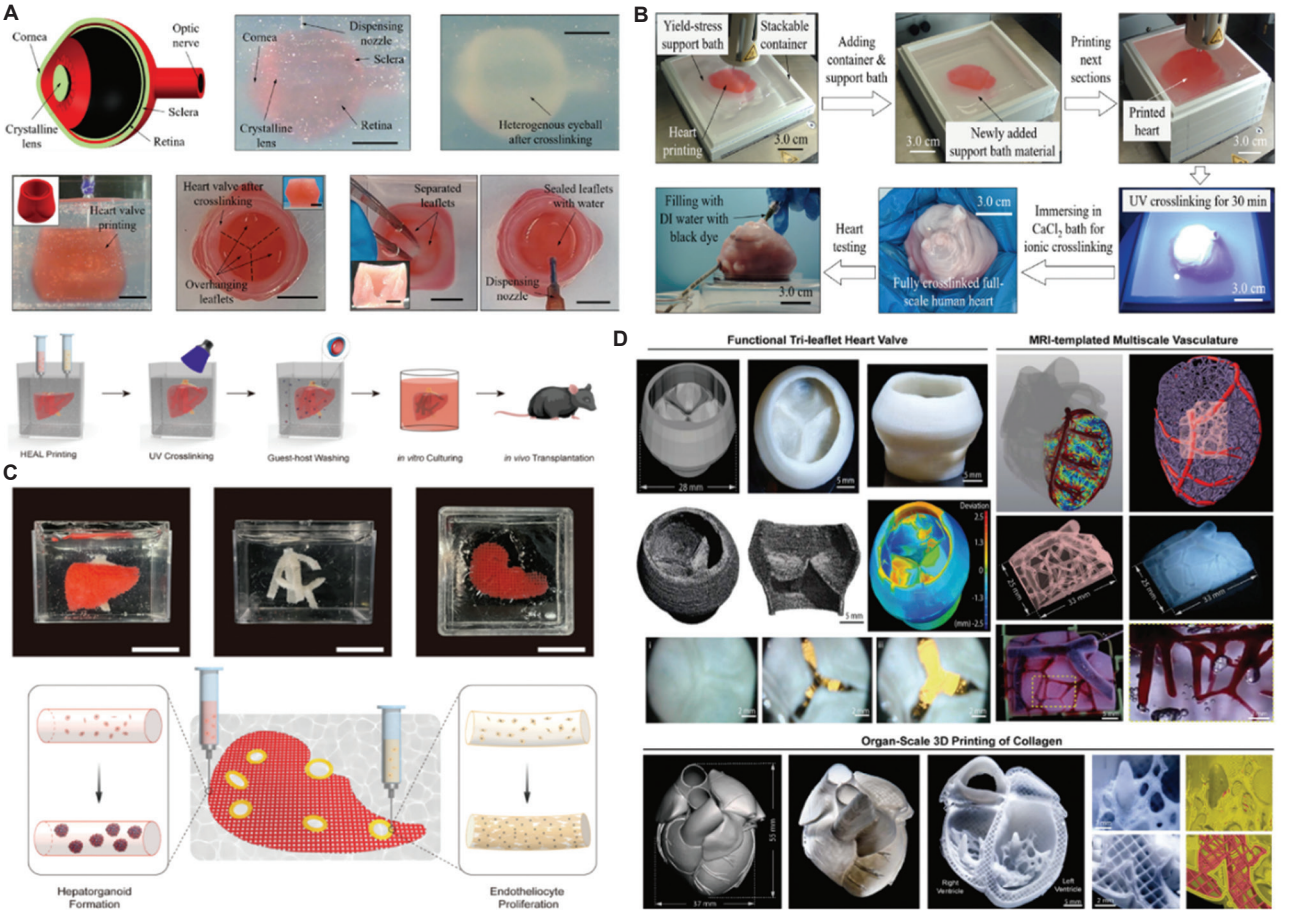

Figure 5. Embedded three-dimensional (3D) printing of engineered human tissue and organ equivalents. (A) Multiscale printing of heterogeneous eyeball and aortic valve structures, demonstrating high anatomical fidelity. Scale bar: 10 mm. (B) A full-scale human heart printed via the multiscale embedded printing strategy, demonstrating chamber perfusion. Scale bar: 3 cm. Adapted from Zhang *et al.*[28] (C) Bioprinted transplantable hepatic constructs with integrated vascular network, illustrating *in vivo* regenerative potential. Scale bar: 20 mm. Adapted from Jiang *et al.*[49] (D) FRESH-bioprinted collagen-based tri-leaflet heart valve and neonatal-scale human heart with multiscale vasculature. Scale bars: 2 mm, 5 mm. Reprinted with permission from Lee *et al.*[53] Copyright © 2019, The American Association for the Advancement of Science.
Abbreviations: FRESH: Freeform reversible embedding of suspended hydrogels; MRI: Magnetic resonance imaging.

during silicone printing. This method facilitated the creation of a patient-specific brain aneurysm model featuring interconnected hollow tubes, with computed tomography imaging confirming structural accuracy and a deviation of ±1 mm from the original design. The team also fabricated a functional tri-leaflet aortic heart valve model with a 250 μm wall thickness, which exhibited realistic hemodynamic behavior under simulated cardiac cycle conditions (Figure 6C). These models provide superior tactile feedback and mechanical robustness, making them ideal for surgical training and testing biomedical devices.

In summary, EMB3D-derived patient-specific anatomical models bridge the gap between medical imaging and physical realization, providing unparalleled accuracy for surgical planning. Ongoing enhancements in material versatility and printing resolution will further broaden their clinical utility.

4. Embedded three-dimensional printing for flexible electronics and soft robotics

4.1. Soft sensors

The rapid development of wearable electronics has spurred growing interest in stretchable strain sensors embedded within soft, conformal substrates. While conventional fabrication techniques, such as photolithography and microchannel molding, face constraints in scalability, cost, and durability, EMB3D offers a promising alternative. For instance, Muth *et al.*[35] employed EMB3D to fabricate strain sensors by extruding carbon conductive grease into an Ecoflex 00-30 support bath,

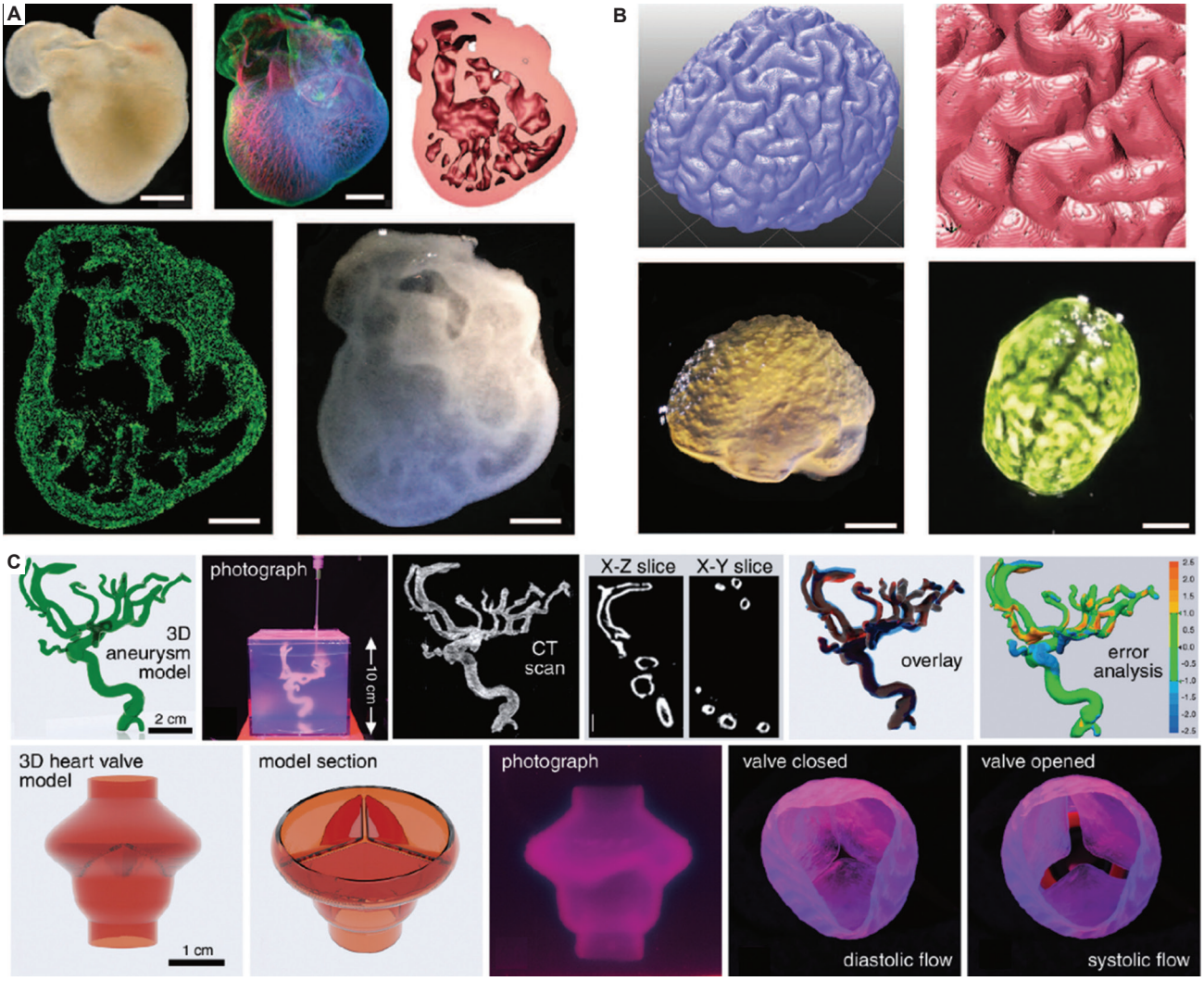

Figure 6. Patient-specific anatomical models fabricated via embedded three-dimensional (3D) printing for surgical planning. (A) Embryonic chick heart with internal trabeculation printed by FRESH. Scale bar: 1 mm. (B) Human brain model with cortical folds printed from MRI data. Scale bar: 1 cm. Reprinted with permission from Hinton *et al.*[30] Copyright © 2015, The American Association for the Advancement of Science. (C) Brain aneurysm and aortic valve models printed via AMULIT, enabling functional flow simulation. Scale bars: 1 cm, 2 cm. Reprinted with permission from Duraivel *et al.*[29] Copyright © 2023, The American Association for the Advancement of Science.

Abbreviations: AMULIT: Additive manufacturing at ultralow interfacial tension; CT: Computed tomography; FRESH: Freeform reversible embedding of suspended hydrogels; MRI: Magnetic resonance imaging.

whose rheological properties were tailored to enable stable printing. The ink retained structural integrity during deposition and curing, yielding monolithic, highly elastic devices capable of withstanding elongations up to 900%. This approach enabled the direct printing of sophisticated sensor architectures, including a glove-integrated array for monitoring finger motion and a multilayer biaxial strain–pressure sensor (Figure 7A). By adjusting rheological parameters and print paths, EMB3D allows extensive customization in sensor design, thereby supporting applications in wearable technology, human–machine interfaces, and soft robotics.

Beyond gesture recognition, EMB3D has also been applied in health monitoring systems. Hui *et al.*[36] developed a method using a curable alginate–polyacrylamide double-network hydrogel as a support bath and a conductive silver–hydrogel ink with a segregated structure. This configuration provided high electrical conductivity (1.4×10^3 S/cm) and seamless integration between the printed circuit and the hydrogel matrix. After printing on a customized DIW platform, thermal curing simultaneously solidified the support bath and the embedded circuits. The resulting functional devices included reproducible strain sensors tolerant of up to 800% strain, compressible

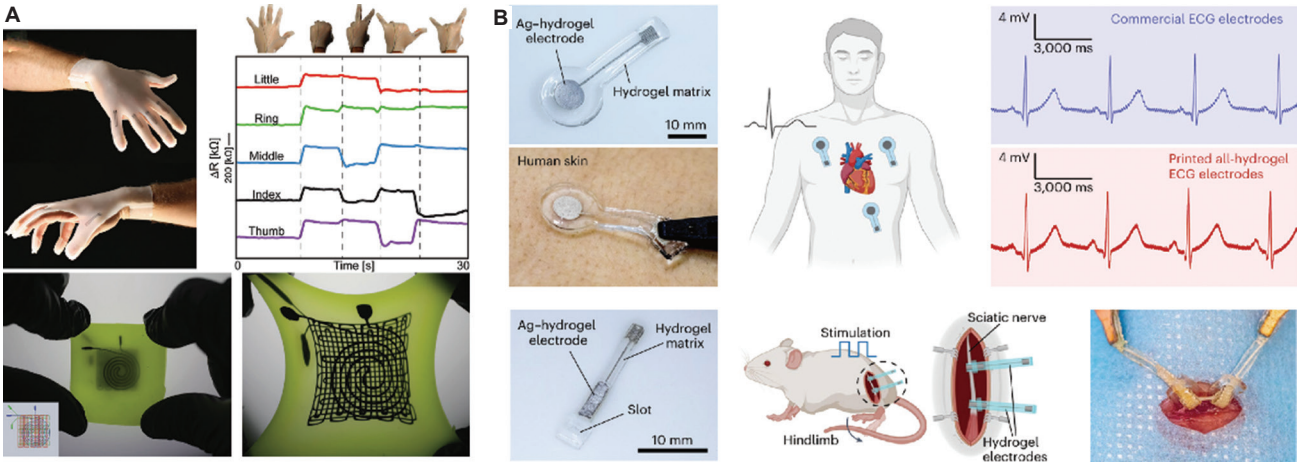

Figure 7. Soft sensors fabricated through embedded three-dimensional printing. (A) Stretchable strain sensors integrated into a glove and a multilayer biaxial sensor. Reprinted with permission from Muth *et al.*[35] Copyright © 2014, WILEY-VCH Verlag GmbH & Co. (B) Hydrogel-based electrocardiogram (ECG) electrodes and nerve-stimulating devices for biomedical monitoring. Scale bar: 10 mm. Reprinted with permission from Hui *et al.*[36] Copyright © 2022, Springer Nature.

inductors, and all-hydrogel electrodes. These hydrogel-based electrodes demonstrated superior performance in electrocardiogram resolution and efficacy in sciatic nerve stimulation compared to conventional commercial electrodes. This strategy facilitates the fabrication of biocompatible, stretchable sensors well-suited for next-generation wearable and implantable health monitoring systems (Figure 7B).

4.2. Functional soft robots

EMB3D has emerged as a pivotal manufacturing technology for fabricating functional soft robots with complex internal geometries and integrated functionalities, thereby overcoming the limitations of traditional methods, such as molding and manual assembly. By enabling the direct integration of sensors, actuators, control systems, and power sources within soft matrices, EMB3D facilitates the creation of highly autonomous and multifunctional robotic systems.

In one notable demonstration, Zhang *et al.*[37] developed a magnetically driven soft robot using EMB3D, where a neodymium–iron–boron particle-Ecoflex composite ink was printed into an Ecoflex 00-30 support bath. This approach allowed the creation of an inchworm-like robot with embedded magnetic domains, capable of controlled crawling on various surfaces, including aluminum, glass, and polyvinyl chloride, with vertical climbing success rates up to 85% and adaptable performance on sloped substrates (Figure 8A). The robot's locomotion was driven by external magnetic fields, highlighting the potential of EMB3D for embedding responsive functional elements directly into elastomeric structures.

Advancing beyond magnetic actuation, Wehner *et al.*[38] pioneered an entirely soft, autonomous robot—the "octobot"—by combining EMB3D with molding and soft lithography. The octobot featured an embedded microfluidic network comprising pneumatic actuators, fuel reservoirs, and catalytic reaction chambers, all printed within an uncured silicone support bath using fugitive and catalytic inks. After curing, the sacrificial ink was removed, forming hollow channels that enabled pneumatic actuation. The system was powered by the catalytic decomposition of hydrogen peroxide into oxygen gas, which pressurized the microfluidic network to drive rhythmic actuation (Figure 8B). This work demonstrated the capability of EMB3D to seamlessly integrate fluidic control and energy conversion systems within soft, continuous structures, enabling autonomous operation without rigid components.

Further expanding the functional scope, Truby *et al.*[39] introduced soft somatosensitive actuators fabricated through multi-material EMB3D. These devices incorporated embedded ionic liquid-based sensors, including curvature, inflation, contact, and thermal sensors, within a layered elastomeric matrix. The sensor ink, composed of 1-ethyl-3-methylimidazolium ethyl sulfate and fumed silica, exhibited suitable rheology and electrical properties for seamless printing. A multi-step printing process was used to define sensor networks and pneumatic channels within dorsal, actuator, and anterior support baths. When assembled into a soft gripper, the soft somatosensitive actuators provided real-time proprioceptive and haptic feedback, enabling differentiated responses to object geometry, temperature,

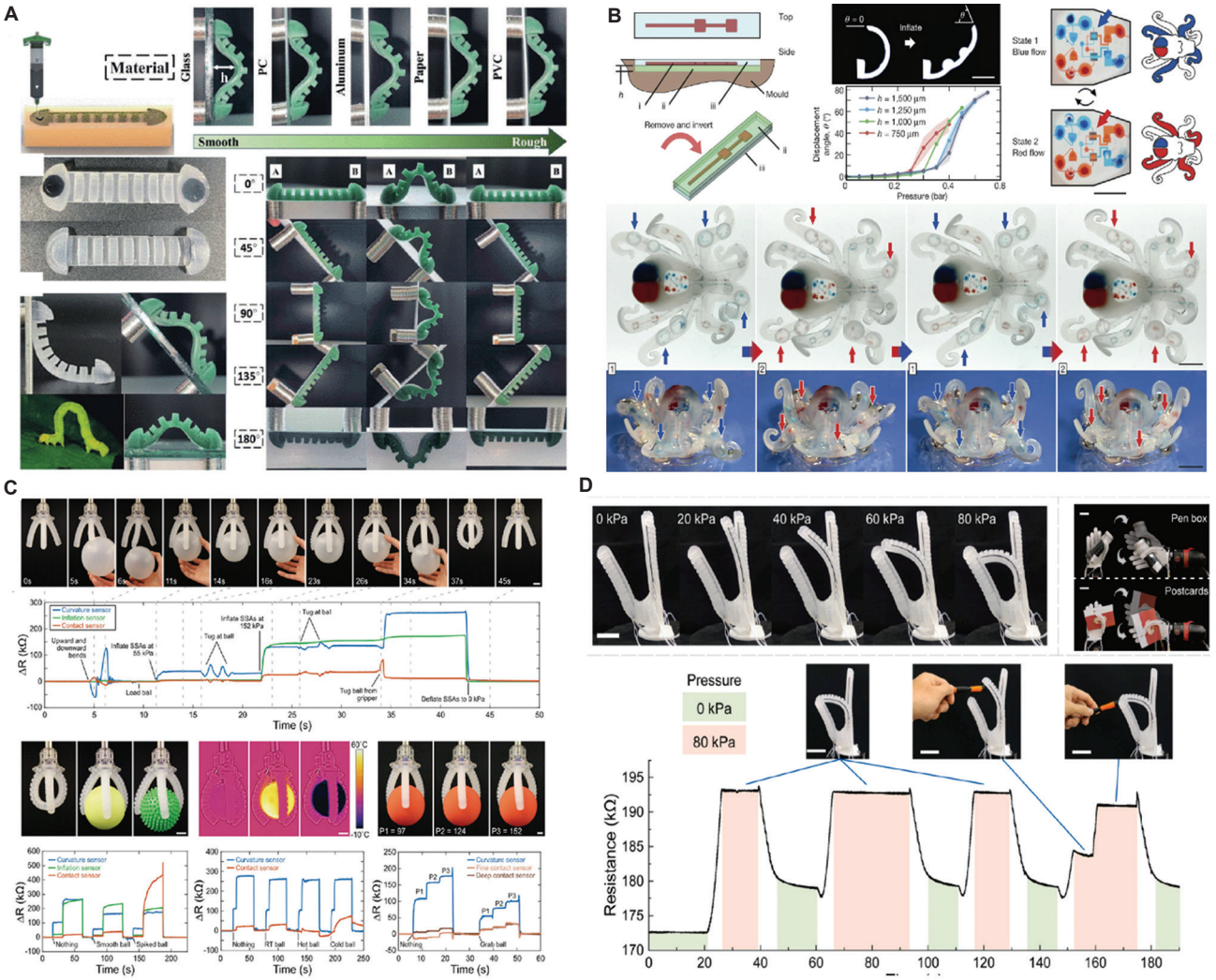

Figure 8. Functional soft robots fabricated through embedded three-dimensional printing. (A) Magnetically driven inchworm robot capable of surface crawling and vertical climbing, fabricated by printing a neodymium–iron–boron-Ecoflex composite ink into an Ecoflex support bath. Reprinted with permission from Zhang *et al.*[37] Copyright © 2021, IEEE. (B) Fully soft, autonomous "octobot" with embedded microfluidic network for pneumatic actuation, powered by catalytic decomposition of hydrogen peroxide. Scale bar: 10 mm. Reprinted with permission from Wehner *et al.*[38] Copyright © 2016, Macmillan Publishers Limited. (C) Soft somatosensitive gripper with embedded curvature, contact, and thermal sensors providing real-time feedback during object manipulation. Scale bar: 20 mm. Reprinted with permission from Truby *et al.*[39] Copyright © 2018, WILEY-VCH Verlag GmbH & Co. (D) Sensorized compliant fishtail and pneumatic humanoid hand with integrated strain sensors, fabricated via multi-material embedded printing. Scale bar: 50 mm. Reprinted with permission from Li *et al.* [128] Copyright © 2024, Elsevier B.V.

and grip pressure. This exemplifies how EMB3D can encode sophisticated sensing and actuation capabilities into monolithic soft systems (Figure 8C).

Recently, Li *et al.*[129] developed a one-step, silicone-based multi-material EMB3D printing method for fabricating multifunctional soft robots. This approach, which involves direct printing of diluted platinum catalyst ink into a removable silicone oil matrix, offers virtually unlimited printable time and enhanced ink utilization. A sensorized compliant fishtail with embedded strain sensors and a pneumatic humanoid hand with integrated sensing capabilities were fabricated. The strain sensors exhibited excellent linearity (R^2 = 0.99), repeatability, and stability, while the robotic hand demonstrated effective grasping under pneumatic actuation (Figure 8D). This approach simplifies the design and manufacturing process, enhancing integration and functionality for soft robotics.

Collectively, these advances highlight the transformative impact of EMB3D on soft robotics. By enabling the freeform fabrication of intricate, multifunctional architectures, this technology paves the way for a new generation of autonomous, adaptive, and sensor-rich soft machines.

5. Embedded three-dimensional printing for fabrication of customized functional materials

5.1. Architected metamaterials and composites

EMB3D is revolutionizing the fabrication of architected metamaterials and composites by providing unparalleled control over their internal architecture and multi-material composition. This capability enables the creation of structures with bespoke mechanical properties that extend beyond the intrinsic characteristics of their constituent materials.

A key application of EMB3D is the fabrication of complex polymer lattices with tailored performance. As exemplified by Weeks *et al.*,[32] computational design can be seamlessly integrated with EMB3D to automate the printing of intricate periodic and stochastic lattices comprising hundreds of struts. Their graph-theoretic automated Eulerian path optimization algorithm generates efficient, collision-free print paths, which are executed by extruding viscoelastic epoxy inks into a supportive silicone microgel bath. This approach allows for the systematic fabrication of multi-material lattices, demonstrating how print path and orientation can be leveraged to program anisotropic mechanical responses (Figure 9A).

Beyond designing structural forms, EMB3D permits the *in situ* engineering of a material's bulk properties. Zehnder *et al.*[31] pioneered this concept by creating a "metasilicone" composite, where immiscible liquid dopants are injected as spherical inclusions into a silicone matrix during printing (Figure 9B). These inclusions, stabilized by interfacial tension, act as mechanical modifiers, enabling macroscopic stiffness to be tuned from a 25% reduction to a 95% increase. This strategy exemplifies how EMB3D can create materials with spatially graded properties for applications like surgical simulators and soft robotics.

EMB3D has played a pivotal role in developing fiber-reinforced hydrogel composites, thereby overcoming the inherent weakness of soft hydrogels. Sun *et al.* demonstrated this by embedding high-strength fibers, such as electrochemically aligned collagen, into 3D hydrogel constructs using a multi-head FRESH bioprinter (Figure 9C).[54] This reinforcement strategy resulted in a dramatic enhancement of mechanical properties, with the

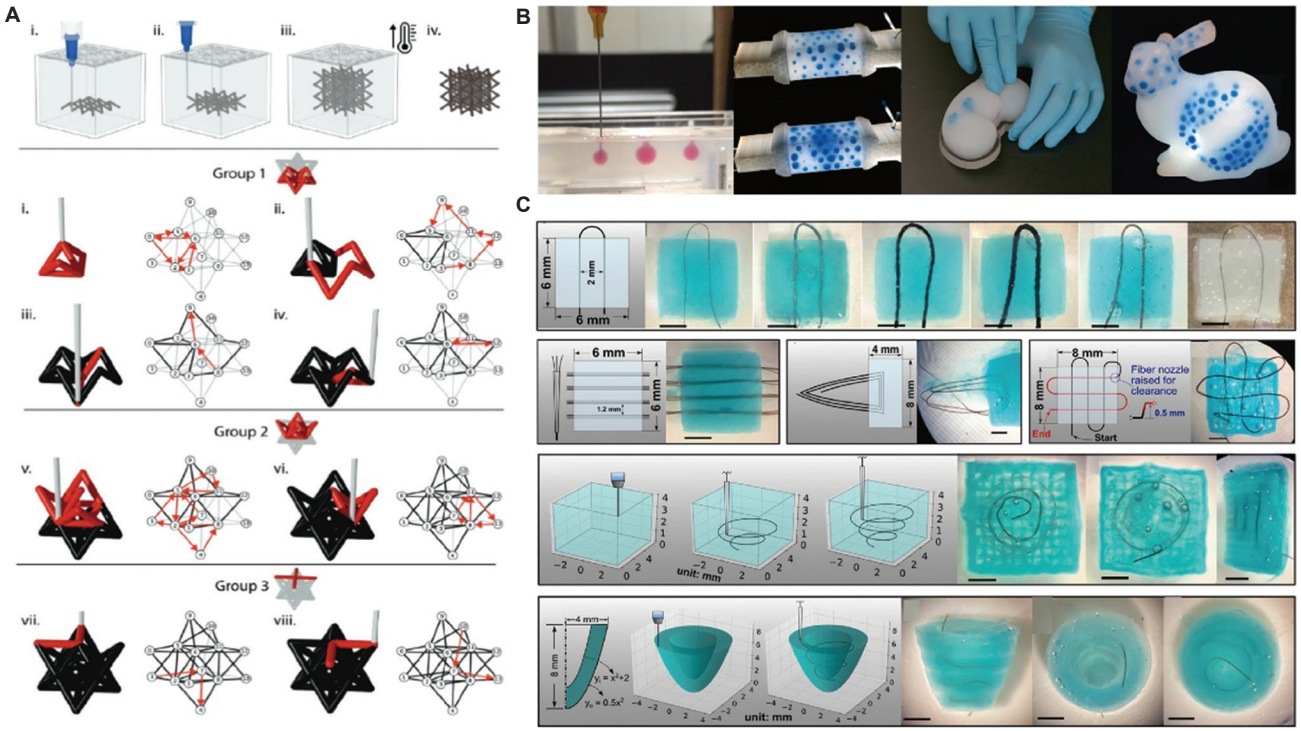

Figure 9. Fabrication of architected metamaterials and composites via embedded three-dimensional printing. (A) Automated Eulerian route optimization for graph-based print path planning of periodic and stochastic polymer lattices within a silicone microgel support bath. Reprinted with permission from Weeks *et al.*[32] Copyright © 2022, Wiley-VCH GmbH. (B) Injection of immiscible liquid dopants into a silicone matrix during printing to create "metasilicone" composites with tunable macroscopic stiffness. Adapted from Zehnder *et al.*[31] (C) Multi-head freeform reversible embedding of suspended hydrogel bioprinting of high-strength fiber-reinforced hydrogel composites for applications such as tendon-mimetic constructs and soft strain sensors. Scale bar: 2 mm. Reprinted with permission from Sun *et al.*[54] Copyright © 2021, American Chemical Society.

tensile modulus and strength increasing nearly sevenfold and fivefold, respectively. The technique enabled the fabrication of functional architectures from tendon-mimetic constructs to soft strain sensors, showcasing its potential for creating robust biohybrid systems.

In summary, EMB3D serves as a versatile manufacturing platform for a new generation of architected metamaterials and composites. By enabling synergistic control over geometry, composition, and property gradation, it unlocks possibilities for lightweight, strong, and functionally intelligent materials.

5.2. Ceramic and metallic structures

EMB3D technology has been successfully applied to the fabrication of high-performance ceramic composites and microscale metallic structures, overcoming the inherent challenges associated with processing these hard and dense materials. Zhou *et al.*[34] demonstrated the fabrication of microstructured multi-material ceramic composites by printing dense, particle-laden inks (e.g., steel, graphite) within an alumina-loaded Pluronic F-127 hydrogel support bath (Figure 10A). This self-healing bath provides the necessary yield stress to support denser inks and fully recovers after passing through the nozzle. After drying and high-temperature sintering (up to 1,450°C), which burns out the polymeric support, dense, defect-free alumina ceramic parts are formed. This approach enables the creation of fracture-resistant composites, such as steel-reinforced aluminum oxide with significantly enhanced toughness, and complex functional features,

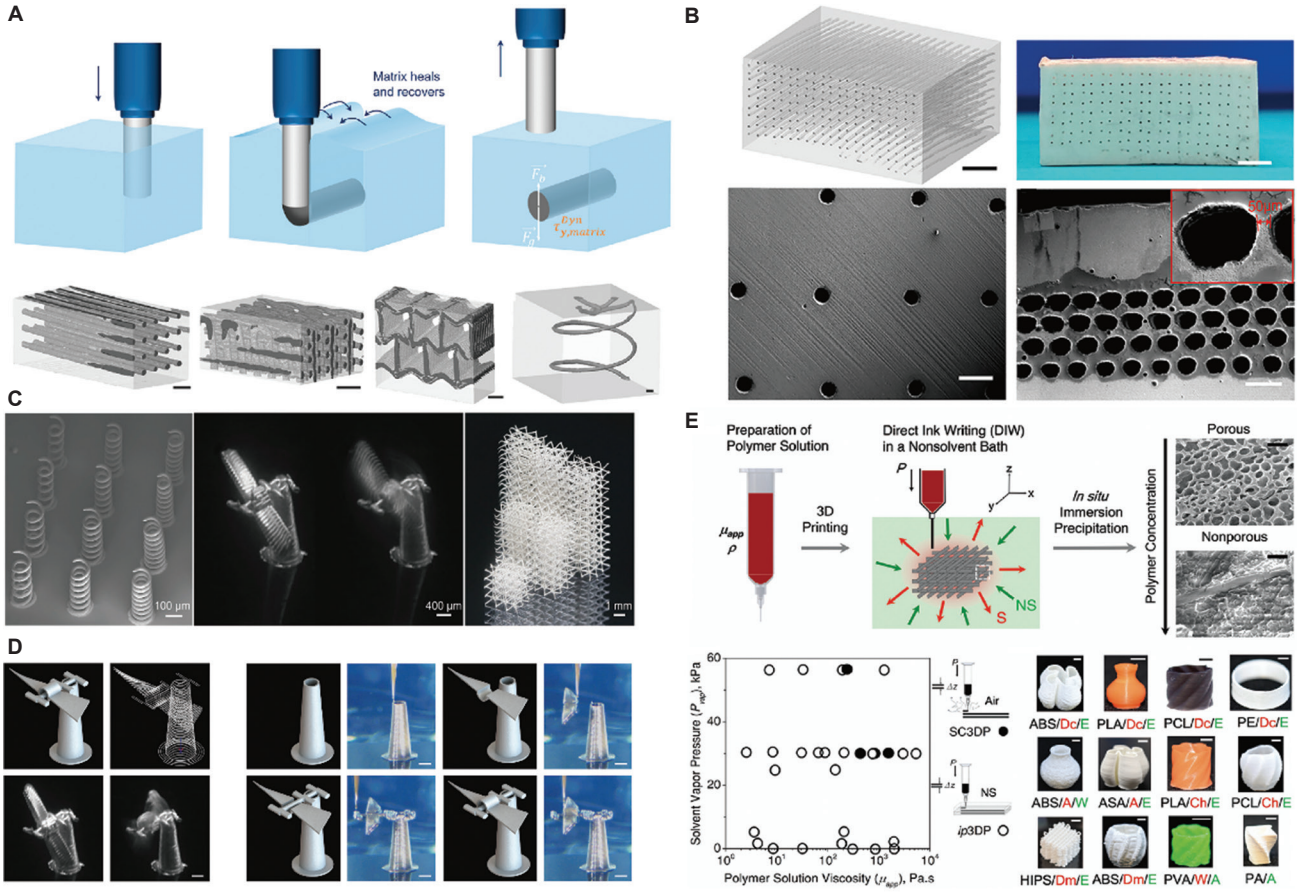

Figure 10. Fabrication of ceramic composites, metallic structures, and porous materials via embedded three-dimensional (3D) printing. (A) Embedded printing process and examples of multi-material ceramic composites, including steel fiber arrays, woodpile structures, auxetic architectures, and spiral microchannels, within a Pluronic F-127 support bath. Scale bar: 1 mm. (B) Sacrificial printing of graphite filaments for thermal management in aluminum oxide cubes with embedded microchannel networks. Scale bar: 5 mm and 500 μm for the top two and for the bottom two images, respectively. Adapted from Zhou *et al.*[34] (C) Embedded writing and embedded sintering of complex 3D silver architectures, including micro-spring arrays and rotatable windmill structures, within a paraffin wax matrix. Scale bars: 100 μm, 400 μm, 3 mm. (D) Functional 3D silver devices: WR10 pyramidal horn antenna for millimeter-wave applications and interpenetrating windmill with rotatable blades. Scale bar: 400 μm. Reprinted with permission from Wang *et al.*[51] Copyright © 2024, Wiley-VCH GmbH. (E) Overview of immersion precipitation 3D printing (ip3DP) and representative porous structures fabricated from various polymer–solvent–non-solvent systems. Scale bar: 2 μm and 4 mm for the top right and for the bottom right images, respectively. Reprinted with permission from Karyappa *et al.*[33] Copyright © 2019, Royal Society of Chemistry.

such as embedded microchannel networks, for thermal management, formed by the sacrificial printing of graphite inks (Figure 10B).

Concurrently, achieving high resolution in metallic structure fabrication has been realized via the embedded writing and embedded sintering technique.[51] This method involves printing a silver nanoparticle ink into a thermally stable paraffin wax support bath, followed by a two-step sintering process. Crucially, optimization of the bath's rheology and interfacial tension enables the direct writing of 3D metallic structures with exceptional resolution, down to ~7 μm. This capability facilitates the creation of complex functional motifs, such as 3D micro-spring arrays, body-centered cubic lattices, and a rotatable silver windmill (Figure 10C). Furthermore, the method demonstrates practical applicability in functional devices, exemplified by a WR10 pyramidal horn antenna exhibiting excellent radiofrequency performance (Figure 10D). The embedded writing and embedded sintering technique, also applicable to copper and alumina, pave the way for customized metallic components in electromagnetic metamaterials and 3D micro-electromechanical systems.

5.3. Porous materials via immersion precipitation printing

Controlled fabrication of porous architectures is vital for energy, catalytic, and biomedical applications. Karyappa *et al.*[33] developed ip3DP, an EMB3D approach that exploits solvent–non-solvent phase inversion to solidify polymeric inks directly within a non-solvent bath. This method bypasses the rheological and evaporative limitations of solvent-cast 3D printing by utilizing low-vapor-pressure solvents (e.g., water, N,N-dimethylformamide, dimethyl sulfoxide), thereby broadening material compatibility (Figure 10E). During printing, polymer solutions are extruded layer by layer into the bath, where instantaneous precipitation forms 3D constructs with tunable pore architectures governed by the ink composition, including polymer concentration and pore-forming additives. Resulting structures exhibit tailored porosity across diverse material systems. As a versatile EMB3D variant, ip3DP enables the creation of complex, graded porous scaffolds, positioning it as a promising platform for advanced functional materials and biomedical devices.

6. Current challenges and prospective solutions

While EMB3D has dramatically expanded the frontiers of soft material fabrication, its broader adoption in precision manufacturing and clinical translation remains tempered by several persistent technical challenges that demand systematic attention. A critical limitation stems from the fundamental reliance on material compatibility between the ink and the support bath. Interfacial instabilities—driven by mismatched chemical polarity, excessive interfacial tension, or unfavorable diffusion kinetics—can lead to poor filament definition, unintended porosity, or delamination, directly impacting the reliability of printed constructs. Addressing these interfacial challenges requires moving beyond empirical formulation toward predictive design. The integration of computational fluid dynamics to simulate flow and diffusion, coupled with machine learning models trained on large material datasets, can forecast compatibility issues. Concurrently, the development of novel amphiphilic compatibilizers and the adoption of orthogonal curing schemes (e.g., combining photopolymerization with ionic crosslinking) can decouple the printing stability from the final material's functional properties, thereby widening the accessible material palette.

Beyond material compatibility, achieving high resolution and consistent feature fidelity remains a significant hurdle. The theoretical resolution limit, governed by the nozzle diameter, is often compromised by the "plowing" effect of the nozzle through the support medium and the subsequent elastic recovery of the bath, which can distort delicate features. Innovations in dynamic nozzle design,[130] such as those utilizing localized shear-thinning or acoustic focusing to precondition the bath, are emerging. These can be combined with support baths engineered for ultra-short recovery times and tailored yield stress profiles, such as nanoclay-reinforced hydrogels or densely packed microgel systems. Such advances aim to bridge the gap between digital design and as-printed geometry, enabling the replication of sub-micron features in soft matter. Moreover, the post-processing stage presents its own complexities. The extraction of sacrificial supports from intricate, tortuous internal channels can be incomplete or mechanically damaging, while residual stress in co-cured systems may induce warping or cracking. The emergence of stimuli-responsive support materials—designed to liquefy or degrade upon a precise thermal, photonic, or chemical trigger—offers a pathway to gentle and complete removal, thereby preserving the structural integrity of complex final constructs.

A perhaps more profound challenge lies in the inherent opacity and lack of real-time control in the EMB3D process. Unlike conventional open-air printing, EMB3D operates within an occlusive medium, rendering traditional vision-based monitoring ineffective. This "blind" fabrication process makes real-time defect detection, correction, and quality assurance nearly impossible, posing a

substantial barrier to standardization, reproducibility, and scalability.[16] The integration of advanced *in situ* metrology is therefore a critical research frontier. Techniques such as high-frequency ultrasonic imaging,[131] optical coherence tomography,[132] or embedded force and impedance sensors can provide non-destructive, layer-by-layer feedback. Coupling this sensor data with closed-loop control algorithms that dynamically adjust printing parameters (e.g., pressure, speed, curing dose) would transform EMB3D from a skilled, open-loop craft into a reliable, automated, and intelligent manufacturing platform.

The integration of artificial intelligence and machine learning offers a transformative pathway to address many of the aforementioned challenges in 3D printing.[129,133,134] Data-driven models can predict printable material formulations by learning from databases of rheological, chemical, and interfacial properties, thereby reducing the trial-and-error typically associated with ink-support matching. Beyond material design, machine learning plays a pivotal role in enhancing the digital modeling stage—for instance, by enabling automatic, high-precision segmentation of anatomical structures from medical images, which significantly improves the fidelity of patient-specific 3D reconstructions and accelerates the preparation of printable models.[135] In process optimization, machine learning algorithms can analyze real-time sensor data (e.g., viscosity, pressure, or optical coherence tomography images) to dynamically adjust printing parameters, compensating for bath heterogeneity or nozzle wear. Furthermore, artificial intelligence-enabled defect detection systems—trained on images or acoustic signatures of flawed prints—can identify irregularities such as filament breakup, incomplete curing, or layer misalignment, enabling closed-loop correction during fabrication.[136-138] As EMB3D matures, the synergy between computational intelligence and embedded printing will not only enhance reproducibility and scalability but also unlock autonomous, adaptive manufacturing systems capable of fabricating complex, multi-functional structures with minimal human intervention.

7. Conclusion

EMB3D has established itself as a paradigm-shifting advancement in additive manufacturing, particularly for processing soft and low-viscosity materials that are challenging to fabricate using conventional extrusion-based methods. By introducing real-time, *in situ* structural support during the deposition process, EMB3D effectively mitigates issues such as structural collapse and deformation, thereby enabling the creation of intricate, high-fidelity architectures across various disciplines. As synthesized in this review, we have systematically delineated the evolutionary trajectory of EMB3D, deciphered its underlying physical/chemical working mechanisms, and established its material science foundations. Furthermore, we have highlighted its disruptive applications in high-impact fields: in biomedicine, this includes vascularized tissue constructs with physiological relevance and patient-specific anatomical models for surgical planning; in soft robotics, it encompasses compliant actuators and soft sensors with tunable mechanical responses; and in functional materials, it enables the design of architected metamaterials with exotic mechanical or optical properties. Collectively, these applications underscore EMB3D's unparalleled versatility and its potential to redefine innovation in additive manufacturing-enabled manufacturing.

Looking ahead, several critical research avenues must be prioritized to fully harness EMB3D's capabilities and expand its technological frontier. First, the development of next-generation functional feedstocks—with tailored properties such as enhanced biocompatibility (for long-term *in vivo* applications), tunable mechanical robustness (from ultra-soft to tough elastomers), and multi-stimuli responsiveness (e.g., to temperature, light, or magnetic fields)—will be instrumental in unlocking new application spaces. Concurrently, advancing printing resolution and dimensional precision remains a high-priority objective; this will require refined control over material rheological behavior (e.g., shear-thinning kinetics) and nozzle dynamics (e.g., flow rate stabilization and tip-positioning accuracy), as well as the integration of in-process monitoring (e.g., optical coherence tomography) for real-time defect correction. Another promising direction is the realization of multi-material EMB3D printing, which aims to fabricate heterogeneous structures with spatially localized functionality (e.g., regions with conductive, biodegradable, and structural properties in a single construct). However, this goal necessitates rigorous optimization of material compatibility, interfacial bonding strength, and synchronized cross-linking kinetics to avoid phase separation or delamination.

Moreover, post-processing methodologies—including controlled drying (to mitigate shrinkage), precision sintering (for ceramic/metal-based constructs), and site-specific chemical modification (to tailor surface functionality)—exert a decisive influence on the final performance, reliability, and longevity of EMB3D-printed structures. Innovations in these areas are crucial for minimizing defects and enhancing functional integration. As EMB3D continues to mature, its adoption is likely to extend beyond current domains into sectors such as aerospace, energy, and consumer electronics, where

customized, high-performance components are in growing demand.

In conclusion, EMB3D represents a dynamic, interdisciplinary platform with significant implications for the future of manufacturing. Its continued evolution will depend on synergistic collaborations across material science, mechanical engineering, biomedical engineering, and computer science—efforts that will drive technical refinements in feedstock design, process control, and post-processing. By addressing current limitations and expanding its application scope, EMB3D is well-positioned to enable new paradigms in digital fabrication, soft matter engineering, and biomedical device design, ultimately contributing to the broader vision of personalized, on-demand manufacturing.

Acknowledgments

None.

Funding

This study was supported by the Natural Science Foundation of Sichuan Province (Yi Zhang; No.: 2025ZNSFSC0464), the National Key Research and Development Program of China (Xiaosheng Zhang; No.: 2022YFB3206100), the National Natural Science Foundation of China (Yi Zhang; No.: 62271107), the Key R&D Program of Mianyang (Xiaosheng Zhang; No.: 2023ZYDF019), and the Fundamental Research Funds for the Central Universities (Yi Zhang; No.: ZYGX2022YGRH007).

Conflict of interest

The authors declare that they have no competing interests.

Author contributions

Conceptualization: Shengyu Gao, Zhengnan Sun, Liang Zhou, Aiwu Zhou

Funding Acquisition: Xiaosheng Zhang, Yi Zhang

Supervision: Xiaosheng Zhang, Yi Zhang

Writing–original draft: Shengyu Gao, Hanyu Yang

Writing–review & editing: Hanyu Yang, Zhengnan Sun, Liang Zhou, Aiwu Zhou

Ethics approval and consent to participate

Not applicable.

Consent for publication

Not applicable.

Availability of data

Not applicable.

References

1. Urbonaite G, Kibirkstis E, Miliunas V. *3D Print Technologies Analysis*. Berlin: Springer; 2013. p. 244-247.
2. Guo L, Qiu JX. Combination of cloud manufacturing and 3D printing: Research progress and prospect. *Int J Adv Manuf Technol*. 2018;96(5-8):1929-1942.

   doi: 10.1007/s00170-018-1717-3
3. Lv JJ, Jia CZ, Yang JC, Zhang YF. Status of 3D printing technology for metal materials. *Adv Eng Res*. 2017;128:256-259.
4. Shahrubudin N, Lee TC, Ramlan R. An overview on 3D printing technology: Technological, materials, and applications. *Proced Manuf*. 2019;35:1286-1296.

   doi: 10.1016/j.promfg.2019.06.089
5. Placone JK, Engler AJ. Recent advances in extrusion-based 3D printing for biomedical applications. *Adv Healthc Mater*. 2018;7(8)1701161.

   doi: 10.1002/adhm.201701161
6. Ning L, Chen X. A brief review of extrusion-based tissue scaffold bio-printing. *Biotechnol J*. 2017;12(8)1600671.

   doi: 10.1002/biot.201600671
7. Dávila JL, D'Avila MA. Rheological evaluation of Laponite/alginate inks for 3D extrusion-based printing. *Int J Adv Manuf Technol*. 2019;101(1-4):675-686.

   doi: 10.1007/s00170-018-2876-y
8. Ren LQ, Zhou XL, Song ZY, *et al.* Process parameter optimization of extrusion-based 3D metal printing utilizing PW-LDPE-SA binder system. *Materials (Basel)*. 2017;10(3)305.

   doi: 10.3390/ma10030305
9. Wu Y, Yang X, Gupta D, *et al.* Dissecting the interplay mechanism among process parameters toward the biofabrication of high-quality shapes in embedded bioprinting. *Adv Funct Mater*. 2024;34(21):2313088.

   doi: 10.1002/adfm.202313088
10. Bas J, Dutta T, Llamas Garro I, Velázquez-González JS, Dubey R, Mishra SK. Retracted: Embedded sensors with 3D printing technology: Review. *Sensors (Basel)*. 2024;24(6):1955.

    doi: 10.3390/s24061955
11. McCormack A, Highley CB, Leslie NR, Melchels FPW. 3D printing in suspension baths: Keeping the promises of bioprinting afloat. *Trends Biotechnol*. 2020;38(6):584-593.

    doi: 10.1016/j.tibtech.2019.12.020
12. Zhao J, He N. A mini-review of embedded 3D printing: Supporting media and strategies. *J Mater Chem B*. 2020;8(46):10474-10486.

    doi: 10.1039/d0tb01819h

13. Greenwood TE, Hatch SE, Colton MB, Thomson SL. 3D printing low-stiffness silicone within a curable support matrix. *Addit Manuf*. 2021;37:101681.

doi: 10.1016/j.addma.2020.101681

14. Shiwarski DJ, Hudson AR, Tashman JW, Feinberg AW. Emergence of FRESH 3D printing as a platform for advanced tissue biofabrication. *APL Bioeng*. 2021;5(1):010904.

doi: 10.1063/5.0032777

15. Bakirci E, Asghari Adib A, Ashraf SF, Feinberg AW. Advancing extrusion-based embedded 3D bioprinting via scientific, engineering, and process innovations. *Biofabrication*. 2025;17(2):023002.

doi: 10.1088/1758-5090/adb7c3

16. Deng X, Qi C, Meng S, *et al.* AllXaqueous embedded 3D printing for freeform fabrication of biomimetic 3D constructs. *Adv Mater*. 2024;36(50):e2406825.

doi: 10.1002/adma.202406825

17. Öztürk-Öncel MÖ, Leal-Martínez BH, Monteiro RF, Gomes ME, Domingues RMA. A dive into the bath: Embedded 3D bioprinting of freeform *in vitro* models. *Biomater Sci*. 2023;11(16):5462-5473.

doi: 10.1039/d3bm00626c

18. Hua W, Mitchell K, Raymond L, *et al.* Fluid bath-assisted 3D printing for biomedical applications: From pre- to postprinting stages. *ACS Biomater Sci Eng*. 2021;7(10):4736-4756.

doi: 10.1021/acsbiomaterials.1c00910

19. Zeng X, Meng Z, He J, *et al.* Embedded bioprinting for designer 3D tissue constructs with complex structural organization. *Acta Biomater*. 2022;140:1-22.

doi: 10.1016/j.actbio.2021.11.048

20. Yogeshwaran S, Goodarzi Hosseinabadi H, Gendy DE, Miri AK. Design considerations and biomaterials selection in embedded extrusion 3D bioprinting. *Biomater Sci*. 2024;12(18):4506-4518.

doi: 10.1039/d4bm00550c

21. Budharaju H, Sundaramurthi D, Sethuraman S. Embedded 3D bioprinting - an emerging strategy to fabricate biomimetic & large vascularized tissue constructs. *Bioact Mater*. 2024;32:356-384.

doi: 10.1016/j.bioactmat.2023.10.012

22. Karyappa R, Zhang D, Zhu Q, Ji R, Suwardi A, Liu H. Newtonian liquid-assisted material extrusion 3D printing: Progress, challenges and future perspectives. *Addit Manuf*. 2024;79:103903.

doi: 10.1016/j.addma.2023.103903

23. Duraivel S, Subramaniam V, Chisolm S, *et al.* Leveraging ultra-low interfacial tension and liquid-liquid phase separation in embedded 3D bioprinting. *Biophys Rev (Melville)*. 2022;3(3):031307.

doi: 10.1063/5.0087387

24. Zhou K, Sun Y, Yang J, Mao H, Gu Z. Hydrogels for 3D embedded bioprinting: A focused review on bioinks and support baths. *J Mater Chem B*. 2022;10(12):1897-1907.

doi: 10.1039/d1tb02554f

25. Wu Q, Song K, Zhang D, *et al.* Embedded extrusion printing in yield-stress-fluid baths. *Matter*. 2022;5(11):3775-3806.

doi: 10.1016/j.matt.2022.09.003

26. Wu W, Deconinck A, Lewis JA. Omnidirectional printing of 3D microvascular networks. *Adv Mater*. 2011;23(24):H178-H183.

doi: 10.1002/adma.201004625

27. O'Bryan CS, Bhattacharjee T, Hart S, *et al.* Self-assembled micro-organogels for 3D printing silicone structures. *Sci Adv*. 2017;3(5):e1602800.

doi: 10.1126/sciadv.1602800

28. Zhang C, Hua W, Mitchell K, *et al.* Multiscale embedded printing of engineered human tissue and organ equivalents. *Proc Natl Acad Sci U S A*. 2024;121(9):e2313464121.

doi: 10.1073/pnas.2313464121

29. Duraivel S, Laurent D, Rajon DA, *et al.* A silicone-based support material eliminates interfacial instabilities in 3D silicone printing. *Science*. 2023;379(6638):1248-1252.

doi: 10.1126/science.ade4441

30. Hinton TJ, Jallerat Q, Palchesko RN, *et al.* Three-dimensional printing of complex biological structures by freeform reversible embedding of suspended hydrogels. *Sci Adv*. 2015;1(9):e1500758.

doi: 10.1126/sciadv.1500758

31. Zehnder J, Knoop E, Bächer M, Thomaszewski B. Metasilicone: Design and fabrication of composite silicone with desired mechanical properties. *ACM Trans Graphics*. 2017;36(6):1-13.

doi: 10.1145/3130800.3130881

32. Weeks RD, Truby RL, Uzel SGM, Lewis JA. Embedded 3D printing of multimaterial polymer lattices via graph-based print path planning. *Adv Mater*. 2022;35(5):e2206958.

doi: 10.1002/adma.202206958

33. Karyappa R, Ohno A, Hashimoto M. Immersion precipitation 3D printing (ip3DP). *Mater Horiz*. 2019;6(9):1834-1844.

doi: 10.1039/c9mh00730j

34. Zhou S, Tirichenko IS, Zhang X, *et al.* Embedded 3D printing of microstructured multi-material composites. *Matter*. 2024;7(2):668-684.

doi: 10.1016/j.matt.2023.10.031

35. Muth JT, Vogt DM, Truby RL, *et al.* Embedded 3D printing of strain sensors within highly stretchable elastomers. *Adv Mater*. 2014;26(36):6307-6312.

doi: 10.1002/adma.201400334

36. Hui Y, Yao Y, Qian Q, *et al.* Three-dimensional printing of soft hydrogel electronics. *Nat Electron*. 2022;5(12):893-903.

doi: 10.1038/s41928-022-00887-8

37. Zhang W, Li J, Liu H, Jin G. *Research on Embedded 3D Printing for Magnetic Soft Robots*. United States: IEEE; 2021.

38. Wehner M, Truby RL, Fitzgerald DJ, *et al.* An integrated design and fabrication strategy for entirely soft, autonomous robots. *Nature*. 2016;536(7617):451-455.

doi: 10.1038/nature19100

39. Truby RL, Wehner M, Grosskopf AK, *et al.* Soft somatosensitive actuators via embedded 3D printing. *Adv Mater*. 2018;30(15):e1706383.

doi: 10.1002/adma.201706383

40. O'Bryan CS, Bhattacharjee T, Niemi SR, *et al.* Three-dimensional printing with sacrificial materials for soft matter manufacturing. *MRS Bull*. 2017;42(08):571-577.

doi: 10.1557/mrs.2017.167

41. Fang Y, Guo Y, Wu B, *et al.* Expanding embedded 3D bioprinting capability for engineering complex organs with freeform vascular networks. *Adv Mater*. 2023;35(22):e2205082.

doi: 10.1002/adma.202205082

42. Shin S, Brunel LG, Cai B, *et al.* Gelation of uniform interfacial diffusant in embedded 3D printing. *Adv Funct Mater*. 2023;33(50):2307435.

doi: 10.1002/adfm.202307435

43. Tisato S, Vera G, Song Q, Nekoonam N, Helmer D. Additive manufacturing of multi-material and hollow structures by embedded extrusion-volumetric printing. *Nat Commun*. 2025;16(1):6730.

doi: 10.1038/s41467-025-62057-6

44. Kolesky DB, Truby RL, Gladman AS, Busbee TA, Homan KA, Lewis JA. 3D bioprinting of vascularized, heterogeneous cell-laden tissue constructs. *Adv Mater*. 2014;26(19):3124-3130.

doi: 10.1002/adma.201305506

45. Lei IM, Zhang D, Gu W, Liu J, Zi Y, Huang YYS. Soft hydrogel shapeability via supportive bath matching in embedded 3D printing. *Adv Mater Technol*. 2023;8(15):230001

doi: 10.1002/admt.202300001

46. Graziano R, Preziosi V, Uva D, *et al.* The microstructure of carbopol in water under static and flow conditions and its effect on the yield stress. *J Colloid Interface Sci*. 2021;582(Pt B):1067-1074.

doi: 10.1016/j.jcis.2020.09.003

47. Webb B, Doyle BJ. Parameter optimization for 3D bioprinting of hydrogels. *Bioprinting*. 2017;8:8-12.

doi: 10.1016/j.bprint.2017.09.001

48. Grosskopf AK, Truby RL, Kim H, Perazzo A, Lewis JA, Stone HA. Viscoplastic matrix materials for embedded 3D printing. *ACS Appl Mater Interfaces*. 2018;10(27):23353-23361.

doi: 10.1021/acsami.7b19818

49. Jiang Z, Jin B, Liang Z, *et al.* Liver bioprinting within a novel support medium with functionalized spheroids, hepatic vein structures, and enhanced post-transplantation vascularization. *Biomaterials*. 2024;311:122681.

doi: 10.1016/j.biomaterials.2024.122681

50. Karyappa R, Liu H, Zhu Q, Hashimoto M. Printability of poly(lactic acid) ink by embedded 3D printing via immersion precipitation. *ACS Appl Mater Interfaces*. 2023;15(17):21575-21584.

doi: 10.1021/acsami.3c00149

51. Wang J, Shou J, Liu D, *et al.* 3D printing of metals with subing μm resolution. *Small*. 2024;20:e2406518.

doi: 10.1002/smll.202406518

52. Raymond L, Bandala E, Hua W, *et al.* Hybrid 3D printing of functional smart hinges. *Machines*. 2023;11(7):686.

doi: 10.3390/machines11070686

53. Lee A, Hudson AR, Shiwarski DJ, *et al.* 3D bioprinting of collagen to rebuild components of the human heart. *Science*. 2019;365(6452):482-487.

doi: 10.1126/science.aav9051

54. Sun W, Tashman JW, Shiwarski DJ, Feinberg AW, Webster-Wood VA. Long-fiber embedded hydrogel 3D printing for structural reinforcement. *ACS Biomater Sci Eng*. 2022;8(1):303-313.

doi: 10.1021/acsbiomaterials.1c00908

55. Sun Y, Yu K, Nie J, *et al.* Modeling the printability of photocuring and strength adjustable hydrogel bioink during projection-based 3D bioprinting. *Biofabrication*. 2021;13(3):035032.

doi: 10.1088/1758-5090/aba413

56. Yu K, Zhang X, Sun Y, *et al.* Printability during projection-based 3D bioprinting. *Bioact Mater*. 2022;11:254-267.

doi: 10.1016/j.bioactmat.2021.09.021

57. Antanitta SV, Patadiya J, Kandasubramanian B. Biopolymer-chitin products by direct ink writing (DIW): A review. *Hybrid Adv*. 2024;5:100115.

doi: 10.1016/j.hybadv.2023.100115

58. Li C, Feng C, Zhang L, Zhang L, Wang L. Direct ink writing of polymer-based materials-a review. *Polym Eng Sci*.

2024;65(2):431-454.

doi: 10.1002/pen.27038

59. Cano-Vicent A, Tambuwala MM, Hassan SS, *et al.* Fused deposition modelling: Current status, methodology, applications and future prospects. *Addit Manuf*. 2021;47:102378.

doi: 10.1016/j.addma.2021.102378

60. Ali S, Deiab I, Pervaiz S. State-of-the-art review on fused deposition modeling (FDM) for 3D printing of polymer blends and composites: Innovations, challenges, and applications. *Int J Adv Manuf Technol*. 2024;135(11-12):5085-5113.

doi: 10.1007/s00170-024-14820-0

61. Qin Y, Fan L, Zhan L, *et al.* Biofabrication: Bioprinting process, printing materials, and the frontier applications in biomedicine. *Addit Manuf Front*. 2024;3(4):200175.

doi: 10.1016/j.amf.2024.200175

62. Hendow EK, Guhmann P, Wright B, Sofokleous P, Parmar N, Day RM. Biomaterials for hollow organ tissue engineering. *Fibrogenesis Tissue Repair*. 2016;9(1):3.

doi: 10.1186/s13069-016-0040-6

63. Ahookhosh K, Pourmehran O, Aminfar H, Mohammadpourfard M, Sarafraz MM, Hamishehkar H. Development of human respiratory airway models: A review. *Eur J Pharm Sci*. 2020;145:105233.

doi: 10.1016/j.ejps.2020.105233

64. O'Connor C, Brady E, Zheng Y, Moore E, Stevens KR. Engineering the multiscale complexity of vascular networks. *Nat Rev Mater*. 2022;7(9):702-716.

doi: 10.1038/s41578-022-00447-8

65. Schaupper M, Jeltsch M, Rohringer S, Redl H, Holnthoner W. Lymphatic vessels in regenerative medicine and tissue engineering. *Tissue Eng Part B Rev*. 2016;22(5):395-407.

doi: 10.1089/ten.teb.2016.0034

66. Göhner C, Svensson-Arvelund J, Pfarrer C, *et al.* The placenta in toxicology. Part IV. *Toxicol Pathol*. 2014;42(2):345-351.

doi: 10.1177/0192623313482206

67. Hull SM, Brunel LG, Heilshorn SC. 3D bioprinting of cell-laden hydrogels for improved biological functionality. *Adv Mater*. 2022;34(2):e2103691.

doi: 10.1002/adma.202103691

68. Seymour AJ, Westerfield AD, Cornelius VC, Skylar-Scott MA, Heilshorn SC. Bioprinted microvasculature: Progressing from structure to function. *Biofabrication*. 2022;14(2):022002.

doi: 10.1088/1758-5090/ac4fb5

69. Norotte C, Marga FS, Niklason LE, Forgacs G. Scaffold-free vascular tissue engineering using bioprinting. *Biomaterials*. 2009;30(30):5910-5917.

doi: 10.1016/j.biomaterials.2009.06.034

70. Tabriz AG, Hermida MA, Leslie NR, Shu W. Three-dimensional bioprinting of complex cell laden alginate hydrogel structures. *Biofabrication*. 2015;7(4):045012.

doi: 10.1088/1758-5090/7/4/045012

71. Li C, Ouyang L, Armstrong JPK, Stevens MM. Advances in the fabrication of biomaterials for gradient tissue engineering. *Trends Biotechnol*. 2021;39(2):150-164.

doi: 10.1016/j.tibtech.2020.06.005

72. Yang Z, Zhang W, Wu S, *et al.* Slot-die coating large-area formamidinium-cesium perovskite film for efficient and stable parallel solar module. *Sci Adv*. 2021;7(18):eabg3749.

doi: 10.1126/sciadv.abg3749

73. Ouyang L, Highley CB, Sun W, Burdick JA. A generalizable strategy for the 3D bioprinting of hydrogels from nonviscous photo-crosslinkable inks. *Adv Mater*. 2017;29(8):1604983.

doi: 10.1002/adma.201604983

74. Senior JJ, Cooke ME, Grover LM, Smith AM. Fabrication of complex hydrogel structures using suspended layer additive manufacturing (SLAM). *Adv Funct Mater*. 2019;29(49):1904845.

doi: 10.1002/adfm.201904845

75. Langer R, Vacanti JP. Tissue engineering. *Science*. 1993;260(5110):920-926.

doi: 10.1126/science.8493529

76. Pan Y, Hu N, Wei X, *et al.* 3D cell-based biosensor for cell viability and drug assessment by 3D electric cell/matrigel-substrate impedance sensing. *Biosens Bioelectr*. 2019;130:344-351.

doi: 10.1016/j.bios.2018.09.046

77. Atala A, Kasper FK, Mikos AG. Engineering complex tissues. *Sci Transl Med*. 2012;4(160):160rv12.

doi: 10.1126/scitranslmed.3004890

78. Mironov V, Boland T, Trusk T, Forgacs G, Markwald RR. Organ printing: Computer-aided jet-based 3D tissue engineering. *Trends Biotechnol*. 2003;21(4):157-161.

doi: 10.1016/s0167-7799(03)00033-7

79. Mironov V, Visconti RP, Kasyanov V, Forgacs G, Drake CJ, Markwald RR. Organ printing: Tissue spheroids as building blocks. *Biomaterials*. 2009;30(12):2164-2174.

doi: 10.1016/j.biomaterials.2008.12.084

80. Zandonella C. T-ray specs. *Nature*. 2003;424(6950):721-722.

doi: 10.1038/424721a

81. Radisic M, Yang L, Boublik J, *et al.* Medium perfusion enables

engineering of compact and contractile cardiac tissue. *Am J Physiol Heart Circ Physiol*. 2004;286(2):H507-H516.

doi: 10.1152/ajpheart.00171.2003

82. Derby B. Printing and prototyping of tissues and scaffolds. *Science*. 2012;338(6109):921-926.

doi: 10.1126/science.1226340

83. Hollister SJ. Porous scaffold design for tissue engineering. *Nat Mater*. 2005;4(7):518-524.

doi: 10.1038/nmat1421

84. Hutmacher DW. Scaffolds in tissue engineering bone and cartilage. *Biomaterials*. 2000;21(24):2529-2543.

doi: 10.1016/s0142-9612(00)00121-6

85. Reiffel AJ, Kafka C, Hernandez KA, *et al.* High-fidelity tissue engineering of patient-specific auricles for reconstruction of pediatric microtia and other auricular deformities. *PLoS One*. 2013;8(2):e56506.

doi: 10.1371/journal.pone.0056506

86. Cohen DL, Malone E, Lipson H, Bonassar LJ. Direct freeform fabrication of seeded hydrogels in arbitrary geometries. *Tissue Eng*. 2006;12(5):1325-1335.

doi: 10.1089/ten.2006.12.1325

87. Mannoor MS, Jiang Z, James T, *et al.* 3D printed bionic ears. *Nano Lett*. 2013;13(6):2634-2639.

doi: 10.1021/nl4007744

88. Shen EM, McCloskey KE. Affordable, high-resolution bioprinting with embedded concentration gradients. *Bioprinting*. 2021;21:e00113.

doi: 10.1016/j.bprint.2020.e00113

89. Caneparo C, Brownell D, Chabaud S, Bolduc S. Genitourinary tissue engineering: Reconstruction and research models. *Bioengineering (Basel)*. 2021;8(7):99.

doi: 10.3390/bioengineering8070099

90. Jin Y, Chai W, Huang Y. Printability study of hydrogel solution extrusion in nanoclay yield-stress bath during printing-then-gelation biofabrication. *Mater Sci Eng C Mater Biol Appl*. 2017;80:313-325.

doi: 10.1016/j.msec.2017.05.144

91. Lee S, Sani ES, Spencer AR, Guan Y, Weiss AS, Annabi N. Human-recombinant-elastin-based bioinks for 3D bioprinting of vascularized soft tissues. *Adv Mater*. 2020;32(45):e2003915.

doi: 10.1002/adma.202003915

92. Tejo-Otero A, Buj-Corral I, Fenollosa-Artés F. 3D printing in medicine for preoperative surgical planning: A review. *Ann Biomed Eng*. 2020;48(2):536-555.

doi: 10.1007/s10439-019-02411-0

93. Shopova D, Yaneva A, Bakova D, *et al.* (Bio)printing in personalized medicine-opportunities and potential benefits. *Bioengineering (Basel)*. 2023;10(3):287.

doi: 10.3390/bioengineering10030287

94. Bao G, Jiang T, Ravanbakhsh H, *et al.* Triggered micropore-forming bioprinting of porous viscoelastic hydrogels. *Mater Horiz*. 2020;7(9):2336-2347.

doi: 10.1039/d0mh00813c

95. Savoji H, Davenport Huyer L, Mohammadi MH, *et al.* 3D printing of vascular tubes using bioelastomer prepolymers by freeform reversible embedding. *ACS Biomater Sci Eng*. 2020;6(3):1333-1343.

doi: 10.1021/acsbiomaterials.9b00676

96. Huang J, Xiong J, Wang D, *et al.* 3D bioprinting of hydrogels for cartilage tissue engineering. *Gels*. 2021;7(3):144.

doi: 10.3390/gels7030144

97. Noor N, Shapira A, Edri R, Gal I, Wertheim L, Dvir T. 3D printing of personalized thick and perfusable cardiac patches and hearts. *Adv Sci (Weinh)*. 2019;6(11):1900344.

doi: 10.1002/advs.201900344

98. Scarrit ME, Pashos NC, Bunnell BA. A review of cellularization strategies for tissue engineering of whole organs. *Front Bioeng Biotechnol*. 2015;3:43.

doi: 10.3389/fbioe.2015.00043

99. Wang P, Sun Y, Li D, *et al.* Extrusion-based 3D co-printing: Printing material design and novel workflow for fabricating patterned heterogeneous tissue structures. *Mater Design*. 2023;227:111737.

doi: 10.1016/j.matdes.2023.111737

100. Rocca M, Fragasso A, Liu W, Heinrich MA, Zhang YS. Embedded multimaterial extrusion bioprinting. *SLAS Technol*. 2018;23(2):154-163.

doi: 10.1177/2472630317742071

101. Gudapati H, Dey M, Ozbolat I. A comprehensive review on droplet-based bioprinting: Past, present and future. *Biomaterials*. 2016;102:20-42.

doi: 10.1016/j.biomaterials.2016.06.012

102. Zhou D, Chen J, Liu B, Zhang X, Li X, Xu T. Bioinks for jet-based bioprinting. *Bioprinting*. 2019;16:e00060.

doi: 10.1016/j.bprint.2019.e00060

103. Jin Y, Xiong R, Antonelli PJ, *et al.* Nanoclay suspension-enabled extrusion bioprinting of three-dimensional soft structures. *J Manuf Sci Eng*. 2021;143(12):1-29.

doi: 10.1115/1.4051010

104. Jin Y, Compaan A, Bhattacharjee T, Huang Y. Granular gel support-enabled extrusion of three-dimensional alginate and cellular structures. *Biofabrication*. 2016;8(2):025016.

doi: 10.1088/1758-5090/8/2/025016

105. Elkhoury K, Zuazola J, Vijayavenkataraman S. Bioprinting the future using light: A review on photocrosslinking reactions, photoreactive groups, and photoinitiators. *SLAS Technol*. 2023;28(3):142-151.

doi: 10.1016/j.slast.2023.02.003

106. Hassan S, Gomez-Reyes E, Enciso-Martinez E, *et al.* Tunable and compartmentalized multimaterial bioprinting for complex living tissue constructs. *ACS Appl Mater Interfaces*. 2022;14(46):51602-51618.

doi: 10.1021/acsami.2c12585

107. Gros-Otero J, Ketabi S, Cañones-Zafra R, *et al.* Corneal stromal roughness after VisuMax and intralase femtosecond laser photodisruption: An atomic force microscopy study. *PLoS One*. 2021;16(5):e0252449.

doi: 10.1371/journal.pone.0252449

108. Kim DH, Jun JS, Kim R. Measurement of the optic nerve sheath diameter with magnetic resonance imaging and its association with eyeball diameter in healthy adults. *J Clin Neurol*. 2018;14(3):345-350.

doi: 10.3988/jcn.2018.14.3.345

109. Sapp MC, Fares HJ, Estrada AC, Grande-Allen KJ. Multilayer three-dimensional filter paper constructs for the culture and analysis of aortic valvular interstitial cells. *Acta Biomater*. 2015;13:199-206.

doi: 10.1016/j.actbio.2014.11.039

110. Mirdamadi E, Tashman JW, Shiwarski DJ, Palchesko RN, Feinberg AW. FRESH 3D bioprinting a full-size model of the human heart. *ACS Biomater Sci Eng*. 2020;6(11):6453-6459.

doi: 10.1021/acsbiomaterials.0c01133

111. Jeon O, Lee YB, Hinton TJ, Feinberg AW, Alsberg E. Cryopreserved cell-laden alginate microgel bioink for 3D bioprinting of living tissues. *Mater Today Chem*. 2019;12:61-70.

doi: 10.1016/j.mtchem.2018.11.009

112. Spencer AR, Shirzaei Sani E, Soucy JR, *et al.* Bioprinting of a cell-laden conductive hydrogel composite. *ACS Appl Mater Interfaces*. 2019;11(34):30518-30533.

doi: 10.1021/acsami.9b07353

113. Abdollahi S, Davis A, Miller JH, Feinberg AW. Expert-guided optimization for 3D printing of soft and liquid materials. *PLoS One*. 2018;13(4):e0194890.

doi: 10.1371/journal.pone.0194890

114. Bhattacharjee T, Zehnder SM, Rowe KG, *et al.* Writing in the granular gel medium. *Sci Adv*. 2015;1(8):e1500655.

doi: 10.1126/sciadv.1500655

115. Hinton TJ, Hudson A, Pusch K, Lee A, Feinberg AW. 3D printing PDMS elastomer in a hydrophilic support bath via freeform reversible embedding. *ACS Biomater Sci Eng*. 2016;2(10):1781-1786.

doi: 10.1021/acsbiomaterials.6b00170

116. Ning L, Mehta R, Cao C, *et al.* Embedded 3D bioprinting of gelatin methacryloyl-based constructs with highly tunable structural fidelity. *ACS Appl Mater Interfaces*. 2020;12(40):44563-44577.

doi: 10.1021/acsami.0c15078

117. Zhou K, Feng M, Mao H, Gu Z. Photoclick polysaccharide-based bioinks with an extended biofabrication window for 3D embedded bioprinting. *Biomater Sci*. 2022;10(16):4479-4491.

doi: 10.1039/d2bm00632d

118. Jin Y, Compaan A, Chai W, Huang Y. Functional nanoclay suspension for printing-then-solidification of liquid materials. *ACS Appl Mater Interfaces*. 2017;9(23):20057-20066.

doi: 10.1021/acsami.7b02398

119. Mendes BB, Gómez-Florit M, Hamilton AG, *et al.* Human platelet lysate-based nanocomposite bioink for bioprinting hierarchical fibrillar structures. *Biofabrication*. 2019;12(1):015012.

doi: 10.1088/1758-5090/ab33e8

120. Skylar-Scott MA, Uzel SGM, Nam LL, *et al.* Biomanufacturing of organ-specific tissues with high cellular density and embedded vascular channels. *Sci Adv*. 2019;5(9):eaaw2459.

doi: 10.1126/sciadv.aaw2459

121. Jeon O, Lee YB, Jeong H, *et al.* Individual cell-only bioink and photocurable supporting medium for 3D printing and generation of engineered tissues with complex geometries. *Mater Horiz*. 2019;6(8):1625-1631.

doi: 10.1039/c9mh00375d

122. Wu Y, Wenger A, Golzar H, Tang X. 3D bioprinting of bicellular liver lobule-mimetic structures via microextrusion of cellulose nanocrystal-incorporated shear-thinning bioink. *Sci Rep.* 2020;10(1):20648.

doi: 10.1038/s41598-020-77146-3

123. Choi YJ, Jun YJ, Kim DY, *et al.* A 3D cell printed muscle construct with tissue-derived bioink for the treatment of volumetric muscle loss. *Biomaterials*. 2019;206:160-169.

doi: 10.1016/j.biomaterials.2019.03.036

124. Afghah F, Altunbek M, Dikyol C, Koc B. Preparation and characterization of nanoclay-hydrogel composite support-bath for bioprinting of complex structures. *Sci Rep.* 2020;10(1):5257.

doi: 10.1038/s41598-020-61606-x

125. Luo M, Lai J, Zhang E, *et al.* Rapid self-assembly mini-livers protect mice against severe hepatectomy-induced liver failure. *Adv Sci (Weinh)*. 2024;11(21):e2309166.

doi: 10.1002/advs.202309166

126. Yang H, Sun L, Pang Y, *et al.* Three-dimensional bioprinted hepatorganoids prolong survival of mice with liver failure. *Gut*. 2021;70(3):567-574.

doi: 10.1136/gutjnl-2019-319960

127. Okubo M, Iohara D, Anraku M, Higashi T, Uekama K, Hirayama F. A thermoresponsive hydrophobically modified hydroxypropylmethylcellulose/cyclodextrin injectable hydrogel for the sustained release of drugs. *Int J Pharm*. 2020;575:118845.

doi: 10.1016/j.ijpharm.2019.118845

128. Li Y, Wu Z, Chen Y, *et al.* Multi-material embedded 3D printing for one-step manufacturing of multifunctional components in soft robotics. *Addit Manuf*. 2024;85:104178.

doi: 10.1016/j.addma.2024.104178

129. Zhang X, Chu D, Zhao X, *et al.* Machine learning-driven 3D printing: A review. *Appl Mater Today*. 2024;39:102306.

doi: 10.1016/j.apmt.2024.102306

130. Kang SW, Mueller J. Multiscale 3D printing via active nozzle size and shape control. *Sci Adv*. 2024;10(23):eadn7772.

doi: 10.1126/sciadv.adn7772

131. Yang T, Jin Y, Smith LM, Dahotre NB, Neogi A. Real-time *in-situ* ultrasound monitoring of soft hydrogel 3D printing with subwavelength resolution. *Commun Eng*. 2024;3(1):162.

doi: 10.1038/s44172-024-00318-w

132. Zvagelsky R, Mayer F, Beutel D, Rockstuhl C, Gomard G, Wegener M. Towards *in-situ* diagnostics of multi-photon 3D laser printing using optical coherence tomography. *Light Adv Manuf*. 2022;3(3):39.

doi: 10.37188/lam.2022.039

133. Sun X, Zhou K, Demoly F, Zhao RR, Qi HJ. Perspective: Machine learning in design for 3D/4D printing. *J Appl Mech*. 2024;91(3):030801.

doi: 10.1115/1.4063684

134. Ukwaththa J, Herath S, Meddage DP. A review of machine learning (ML) and explainable artificial intelligence (XAI) methods in additive manufacturing (3D printing). *Mater Today Commun*. 2024;41:110294.

doi: 10.1016/j.mtcomm.2024.110294

135. Wang X, Li Y, Liang Z, Du R, Song T. High-fidelity, personalized cardiac modeling via AI-driven 3D reconstruction and embedded silicone rubber printing. *Exp Biol Med (Maywood)*. 2025;250:10756.

doi: 10.3389/ebm.2025.10756

136. Sani AR, Zolfagharian A, Kouzani AZ. Automated defects detection in extrusion 3D printing using YOLO models. *J Intellig Manuf*. 2024.

doi: 10.1007/s10845-024-02543-8

137. Brion DAJ, Pattinson SW. Generalisable 3D printing error detection and correction via multi-head neural networks. *Nat Commun*. 2022;13(1):4654.

doi: 10.1038/s41467-022-31985-y

138. Armin E, Ebrahimian S, Sanjari M, Saidi P, Pourreza HR. Defect detection in 3D printing: A review of image processing and machine vision techniques. *Int J Adv Manuf Technol*. 2025;140(3-4):2103-2128.

doi: 10.1007/s00170-025-16382-1

ACCSCIENCE PUBLISHING

Engineering Science in Additive Manufacturing

REVIEW ARTICLE

Microstructure-controlled strengthening mechanisms and strategies in additively manufactured aluminum alloys: A review

Yingming Zhang, Tianai Huang, Xin He, and Xiaoming Wang*

School of Engineering Technology, Purdue University, West Lafayette, Indiana, United States of America

Abstract

Laser powder bed fusion (LPBF) has emerged as an important but challenging route for producing high-strength aluminum alloys. However, existing studies often treat individual alloy systems or specific defects in isolation, which obscures the overall links between microstructural evolution, strengthening mechanisms, and strengthening strategies. This review addresses that gap by establishing a comprehensive, mechanism-based framework for the rational design of LPBF processing and aluminum alloys. We organize the discussion around a systematic causal chain linking microstructure, strengthening mechanisms, and strengthening strategies. The strengthening contributions are classified into five categories: Grain-boundary, solid-solution, precipitation, dislocation, and load-bearing strengthening. On this basis, we distill three transferable classes of practical strategies—process optimization, alloy design, and post-heat treatment—and clarify how they tailor high strength across different alloy families. The resulting mechanism-based framework links LPBF processing conditions, microstructures, strengthening mechanisms, and strengthening strategies in a unified manner. It provides a common reference for researchers and practitioners designing high-strength LPBF-processed aluminum alloys and highlights key directions where further quantitative and mechanistic studies are needed.

Keywords: Laser powder bed fusion; Aluminum alloys; Microstructural evolution; Strengthening mechanisms; Strengthening strategies

***Corresponding author:**
Xiaoming Wang
(wang1747@purdue.edu)

Citation: Zhang Y, Huang T, He X, Wang X. Microstructure-controlled strengthening mechanisms and strategies in additively manufactured aluminum alloys: A review. *Eng Sci Add Manuf*. 2026;2(1):025490033. doi: 10.36922/ESAM025490033

Received: December 6, 2025

Revised: December 23, 2025

Accepted: December 29, 2025

Published online: January 9, 2026

1. Introduction

Aluminum alloys have a low density and relatively high mechanical performance, making them suitable for lightweight structural applications.[1] In recent years, additive manufacturing (AM) has been increasingly used to produce aluminum-alloy components because it can quickly build complex shapes, support customized designs, and reduce material waste. These advantages are particularly important for critical parts in aircraft and vehicles.[2,3] As one of the main AM processes, laser powder bed fusion (LPBF) is now widely used to process aluminum alloys, providing stable processing conditions and enabling the efficient fabrication of complex parts.[4,5]

Over the past decade, LPBF of aluminum alloys has been discussed in a number of review papers. In general, these contributions can be grouped into three categories. The first category is process-oriented or defect-oriented reviews that cover several aluminum alloy systems and summarize how processing parameters influence densification, porosity, lack of fusion, and hot cracking, while only briefly describing microstructural details and specific strengthening mechanisms.[1,6,7] The second category focuses on one or a few specific alloy systems, such as AlSi10Mg, and establishes microstructure–property maps within those alloys; however, the discussion of strengthening mechanisms is fragmented and not easily transferred to other alloy families.[8-10] The third category focuses on high-strength or newly developed aluminum alloys and their printability, emphasizing alloy design concepts, crack sensitivity, and processing windows.[11,12] These reviews mainly address which alloys can be processed by LPBF and how to reduce defects, rather than systematically dissecting which strengthening mechanisms are exploited under LPBF conditions.

In this context, the present review approaches LPBF-processed aluminum alloys from a different angle. Instead of extending a specific alloy family or process window, we focus on the chain "microstructure → strengthening mechanisms → strengthening strategies." We first summarize the characteristic microstructures that commonly develop in LPBF-processed aluminum alloys under given melt-pool thermal and solidification conditions and discuss how these microstructural features relate to macroscopic mechanical properties. On this basis, we group the strengthening contributions in LPBF-processed aluminum alloys into five categories—grain boundary strengthening, solid solution strengthening, precipitation strengthening, dislocation strengthening, and load-bearing strengthening—and examine the conditions under which these mechanisms are activated during LPBF. Finally, drawing on existing experimental studies and alloy-design efforts, we consolidate the previously scattered experience into three transferable classes of strengthening strategies: Process optimization, alloy design, and post-heat treatment. The intention is to provide a mechanism-based framework that can be used as a common reference when designing high-strength LPBF-processed aluminum alloys across different alloy families.

In this review, we mainly draw on peer-reviewed journal papers on LPBF of aluminum-based alloys that report both microstructural characterization and mechanical properties in the as-built and/or heat-treated condition. Where appropriate, we also refer to work on related laser-based AM processes, on other alloy systems, and on classical literature about solidification and strengthening, when these are needed to clarify microstructural evolution or the underlying mechanisms.

The remainder of this review is organized as follows. Section 2 outlines the main AM routes for aluminum alloys. Section 3 discusses microstructural evolution during LPBF and its influence on mechanical properties. Section 4 depicts the classification of the strengthening mechanisms into five categories and relates each category to specific microstructural features. Section 5, based on recent research findings, summarizes three strengthening strategies: Process parameter optimization, alloy design, and post-heat treatment. The final section summarizes the main conclusions and highlights directions for future research. Overall, this review provides a theoretical foundation and practical guidance for the design and manufacture of high-strength LPBF-processed aluminum alloys. For clarity, Figure 1 summarizes the framework adopted in this review, linking LPBF processing conditions, characteristic microstructures, and the associated strengthening mechanisms and strategies.

2. Overview of aluminum alloys AM process

In AM, the resulting thermal cycles govern solidification, underpinning microstructural evolution.[13] This section offers a review of fundamental metal AM methods, followed by a focused discussion of the LPBF process for aluminum alloys.

2.1. An introduction to metal AM

Laser-based metal AM (LAM) has become an important method for producing metallic parts in high-performance applications.[14,15] Among LAM techniques, LPBF and directed energy deposition (DED) are currently the most widely used processes.

As shown in Figure 2A, DED uses a coaxial powder feeding method. Metal powder is carried through a nozzle into a laser-generated melt pool, where it fuses with the substrate or with previously deposited tracks. Material is added directly onto the surface, which allows relatively fast fabrication of large metallic parts.[2] However, its dimensional accuracy is limited, so it is mainly used for structures with relatively simple geometries.

In the LPBF process (Figure 2B), a powder layer is spread beforehand. The laser spot and scan path can be controlled precisely, and the powder layer is thin and relatively uniform, so LPBF can produce parts with good dimensional accuracy and comparatively smooth surfaces.[16] Its capability to realize complex geometries has made it one of the most widely studied AM routes for aluminum alloys. Accordingly, this review focuses on LPBF and discusses

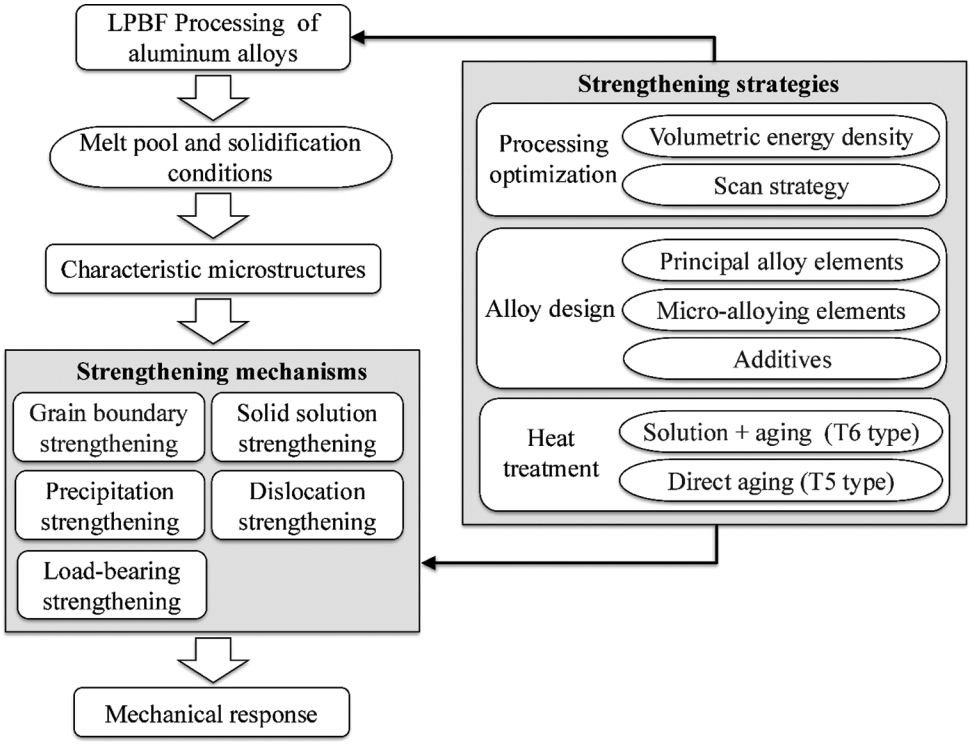

Figure 1. Schematic framework adopted in this review. Image created by the authors.

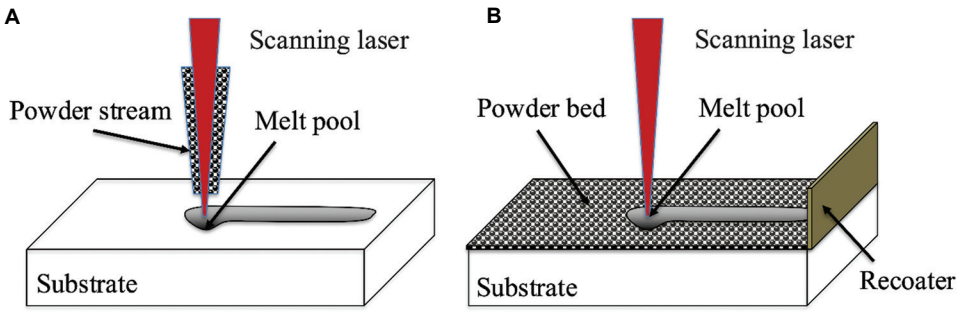

Figure 2. Schematic illustration of additive manufacturing processes: (A) Directed energy deposition and (B) laser powder bed fusion. Image created by the authors.

its process characteristics, microstructural evolution, and strategies for improving mechanical properties.

2.2. An introduction to LPBF process for aluminum alloys

Figure 3 shows a typical LPBF system. The system typically comprises a fiber laser, a beam expansion and scanning system, a sealed build chamber, powder delivery and recoating devices, and an atmosphere control system. During building, a thin layer of aluminum alloy powder is first uniformly spread on the substrate by the recoater. Under a high-purity inert gas atmosphere, the laser beam scans the powder layer along a predetermined path to melt it. After each scan, a fresh layer of powder is spread over the previously solidified layer; repeating this sequence gradually builds up the three-dimensional component. Processing variables such as laser power, scanning speed, layer thickness, and hatch distance control the local heat and solidification conditions.[17]

Figure 4 illustrates the local material response during LPBF of aluminum alloys. A tightly focused laser spot moves rapidly across the powder layer on the build platform, causing the irradiated region to undergo a sharp temperature rise, significantly exceeding the material's melting point, while generating extremely high thermal gradients. At this moment, the powder particles melt quickly and form a shallow, short-lived liquid pool. When

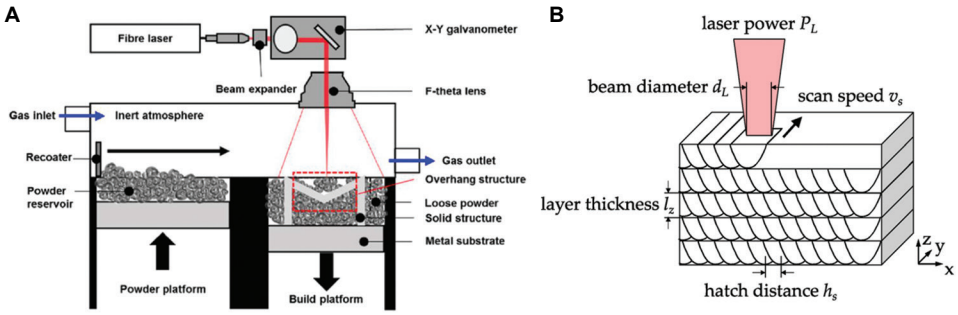

Figure 3. Overview of a typical laser powder bed fusion (LPBF) system and the key processing parameters. (A) Schematic of a typical LPBF system.[18] (B) Main process parameters. Reproduced from Ellendt *et al.*[17]

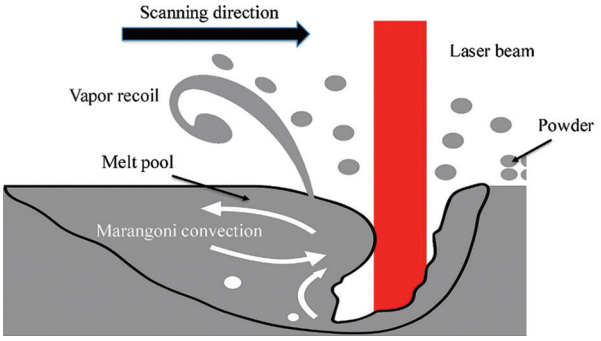

Figure 4. The local material response during laser powder bed fusion. Image created by the authors.

the laser spot moves away, the local liquid pool freezes within a very short time. Solidification, therefore, takes place far from equilibrium and is coupled with Marangoni convection and vapor recoil. As the scanning beam passes over adjacent layers, regions of the part are reheated several times. This repeated thermal cycling produces a complex thermal history, which in turn has a strong effect on shaping the final solidified microstructure.[19]

2.3. Aluminum alloy families and research status in LPBF

In LPBF studies, aluminum alloys are typically discussed in terms of processability and application-driven requirements. The literature most frequently focuses on Al–Si casting-type alloys (*e.g.*, AlSi10Mg), high-strength wrought families (Al–Cu [2xxx], Al–Mg–Si [6xxx], and Al–Zn–Mg [7xxx]), as well as Al–Mg (5xxx) alloys. For strength-oriented work, a common starting point is to establish a reproducible baseline that links process windows and scan strategies to density and defect modes; AlSi10Mg is frequently adopted because dense builds can be produced over comparatively broad parameter ranges, providing a stable baseline to evaluate strength gains from process optimization and post-processing routes before moving to more crack-sensitive wrought compositions.[20-22] When the focus shifts to higher-strength wrought compositions, the literature typically addresses build integrity before pushing strength: Cracking suppression and porosity reduction are recurrent milestones, and representative studies often combine composition modification (e.g., microalloying or powder modification) with scan/parameter optimization to obtain crack-free or crack-suppressed builds in 6xxx/7xxx alloys.[23-26] For Mg-containing alloys, reported work highlights an additional constraint—composition stability during melting/solidification—since Mg volatilization can shift melt pool chemistry and narrow viable processing windows; accordingly, strength-focused studies tend to emphasize parameter-window control and defect suppression to maintain a stable strength–ductility balance.[27,28]

3. Characteristic microstructural features in LPBF-processed aluminum alloys

In LPBF, the microstructure of aluminum alloys is mainly controlled by the intense, localized heating and cooling from the laser and by the layer-by-layer build process. This section explains how these factors shape the typical microstructural features of LPBF-processed aluminum alloys and outlines the main formation mechanisms.

3.1. Melt pool characteristics: Thermal gradient and solidification rate

In LPBF, laser processing parameters (*e.g.*, power and scan speed) control how much energy is delivered to the material, while the substrate and the previously solidified layers act as effective heat sinks. Together, these factors determine the melt-pool shape and its temperature field, and thus the local thermal gradient (G) and solidification rate (R). Both G and R are key parameters governing the solidification process and are widely used to characterize the solidification microstructure.[29]

Chouhan *et al.*[30] numerically investigated the distributions of G and R in LPBF. As illustrated in Figure 5,

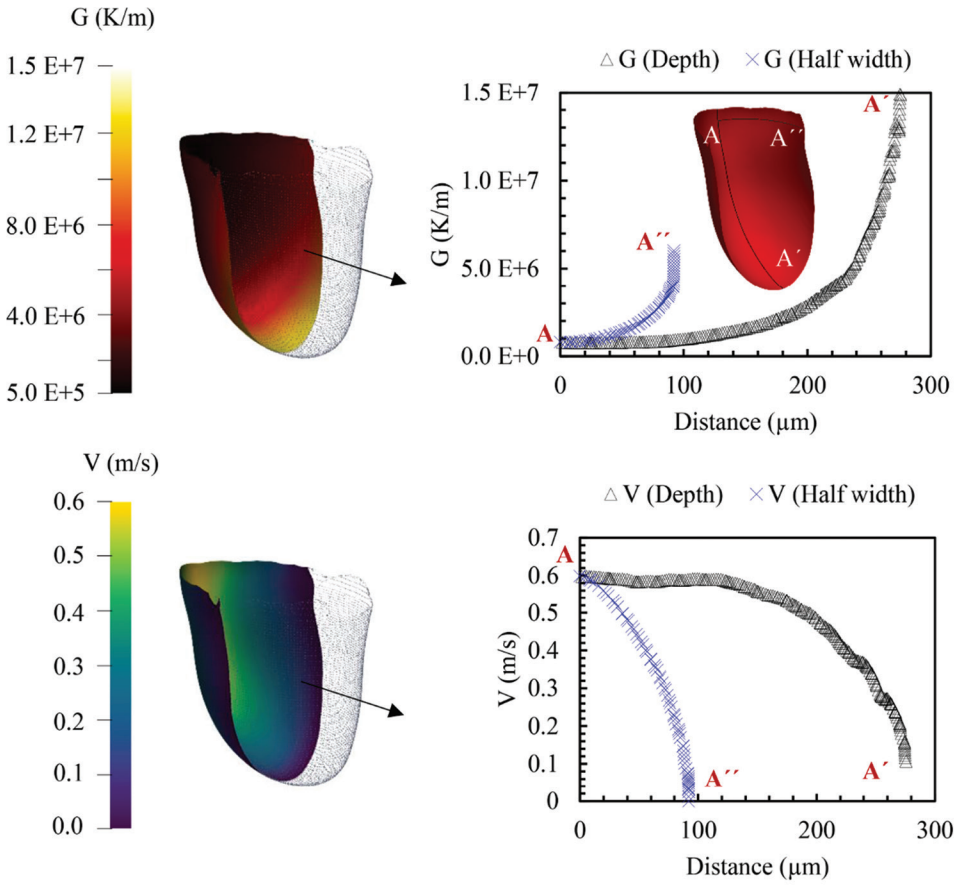

Figure 5. Numerical results for thermal gradient (G) and solidification rate (R) along the solid–liquid boundary of the melt pool. Reproduced from Chouhan *et al.*[30]

G is highest near the bottom of the pool (close to the laser–substrate interaction zone) and lowest at the trailing edge of the pool (away from the laser track). In contrast, the interface R reaches its maximum at the trailing edge of the melt pool and its minimum at the pool bottom.

3.2. Effect of G/R ratio and cooling rate on solidification morphology

The thermal gradient (G) and solidification rate (R) are often used together to describe the solidification conditions. Based on previous work, a G–R diagram can be constructed (Figure 6).[31,32] The ratio G/R mainly indicates the growth mode: When G/R is high, the front tends to be planar, and as G/R decreases, it changes to cellular, then columnar dendritic, and finally equiaxed dendritic. The product G·R corresponds to the cooling rate and is linked to the feature size of the microstructure; higher G·R (faster cooling) generally produces a finer microstructure.

From the previous section, we know that G and R vary from the bottom of the pool to the top surface. These (G, R) pairs can be plotted on the G–R diagram, where different

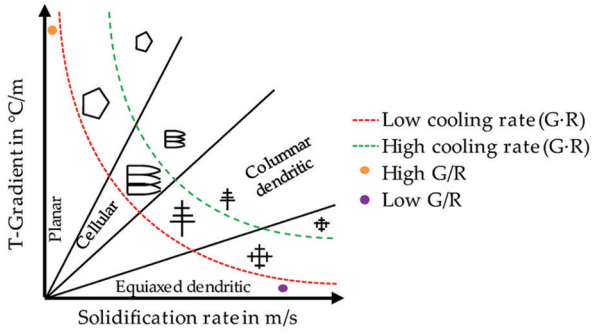

Figure 6. A G–R map depicting varying thermal gradient (G) and solidification rate (R) within a melt pool in laser powder bed fusion. Reproduced from Rasch *et al.*[33]

regions correspond to distinct solidification modes and cooling rates. Different locations within the melt pool exhibit different solidification morphologies.

Van Cauwenbergh *et al.*[34] examined how local values of G and R affect the melt-pool microstructure in LPBF-processed AlSi10Mg. As shown in Figure 7A-C, the vectors G and R

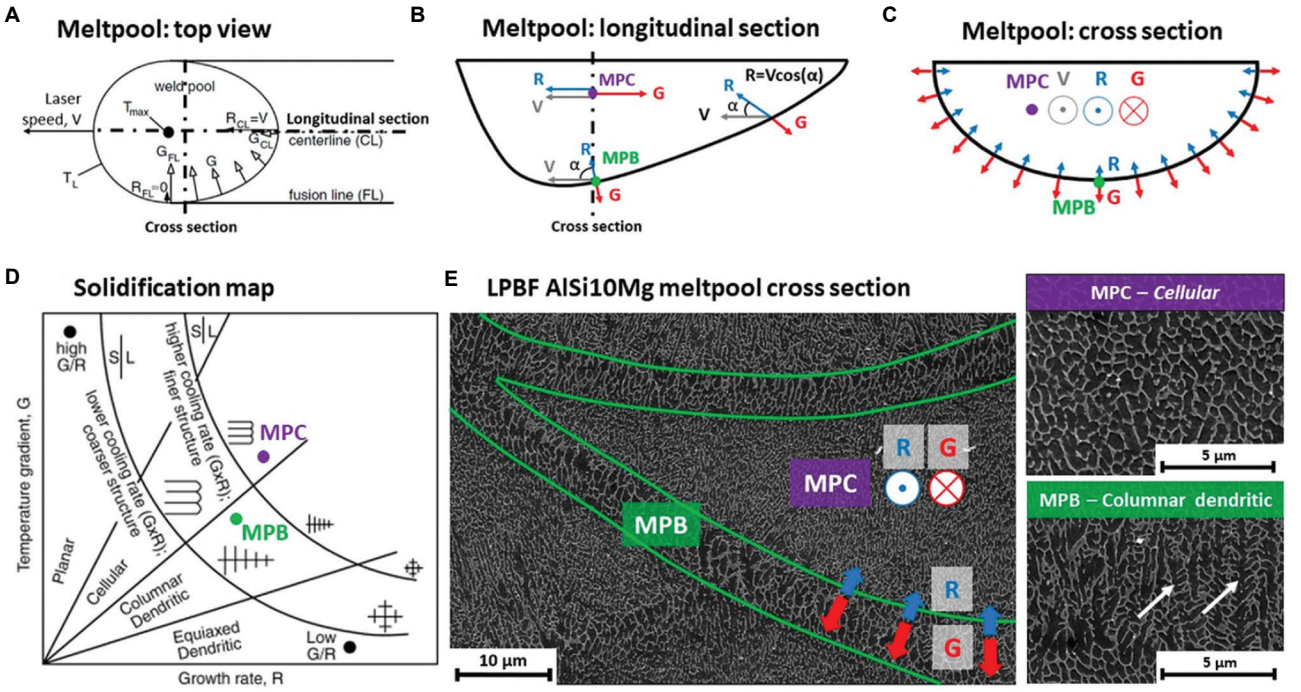

Figure 7. Melt pool schematics. (A) Melt pool top view; (B) melt pool longitudinal section; (C) melt pool cross-section; (D) solidification map; (E) SEM image of LPBF AlSi10Mg (AB), showing cellular features at the MPC and columnar dendritic structures at the MPB. Reproduced from van Cauwenbergh *et al.*[34]
Abbreviations: G: Thermal gradient; LPBF: Laser powder bed fusion; MPB: Melt-pool boundary; MPC: Melt-pool center; R: Solidification rate.

show changes in both magnitude and orientation when moving from the melt-pool center (MPC) toward the melt-pool boundary (MPB). In the MPC region, the cooling rate G·R is relatively high, and the dominant G and R vectors are almost parallel to the laser scan direction; the large R values, close to the scan speed, favor the formation of fine cellular structures. Closer to the MPB, heat loss into the surrounding material lowers the cooling rate, and the G and R vectors become weaker and more dispersed. As summarized in the solidification map (Figure 7D), the growth mode there shifts from cellular toward columnar dendritic, and the resulting microstructure is noticeably coarser (Figure 7E).

3.3. Formation of typical microstructures in as-built state

For aluminum alloys, the crystallization process within the melt pool is inherently complex due to the multi-component nature of the alloys. As an illustrative example, Mair *et al.*[35] examined LPBF processing of Al-4.60Cu-4.10Ti-0.70Ag-0.24Mg (wt%) powder, thereby revealing the associated microstructural evolution.

3.3.1. Laser–powder interaction

When the high-power laser scans over the powder, a small melt pool forms (Figure 8A). At the center of a melt pool, continuous laser heating makes the temperature rise above the melting point of aluminum.

3.3.2. Formation of columnar grains

At the edges of the melt pool, the liquid metal contacts with the previously solidified layer or the substrate, and these interfaces act as preferred sites for new grains. In these boundary zones, the temperature gradient is high, and the local thermal undercooling is relatively small, so solidification tends to start there and advance toward the pool center, giving rise to columnar grains (Figure 8B). Because the cooling rate is high, diffusion of solute atoms is strongly restricted, and a supersaturated α-Al solid solution is formed. At the same time, Ti reacts with aluminum to generate numerous star-shaped $L1_2$-Al_3Ti primary particles, which slow down the advance of the solid–liquid front and gradually build up both compositional undercooling (ΔT_CS) and thermal undercooling (ΔT_therm).

3.3.3. Nucleation and growth of equiaxed grains

When the overall undercooling (ΔT_total) becomes larger than the nucleation undercooling (ΔT_n), the $L1_2$–Al_3Ti particles act as preferred sites for heterogeneous nucleation of α-Al. New equiaxed grains then form in front of

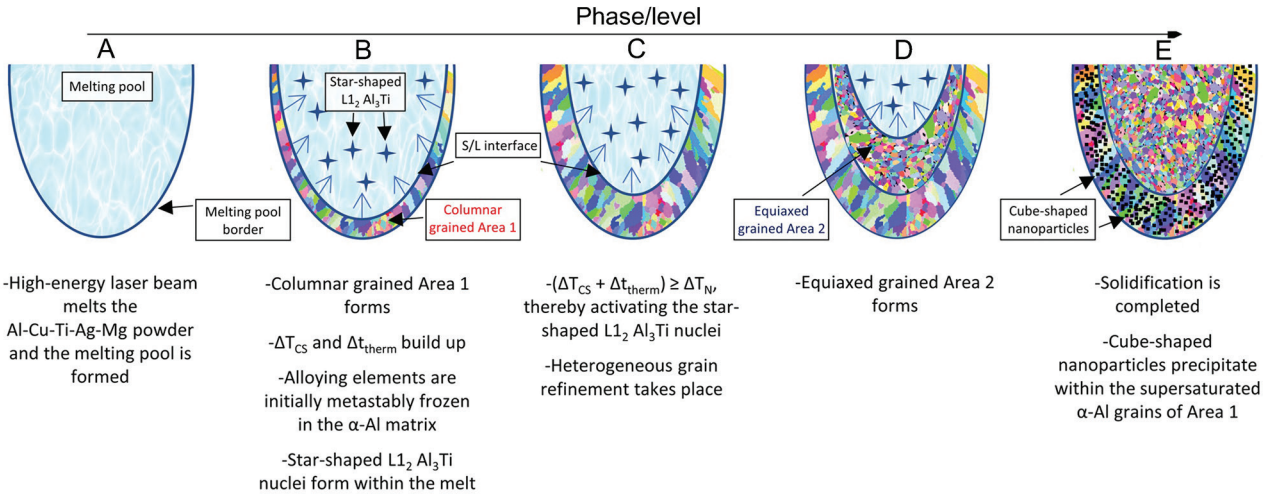

Figure 8. Schematic sequence of microstructural evolution in the melt pool. (A) Melt-pool formation; (B) columnar grains in Area 1; (C) heterogeneous nucleation and grain refinement; (D) equiaxed grains in Area 2 and (E) completed solidification with local nanoscale precipitates in supersaturated α-Al. Reproduced from Mair *et al.*[35]

the solid–liquid interface, and the grain size is refined (Figure 8C). A high level of Ti and Cu solute slows the advance of the solidification front and favors continuous precipitation of $L1_2$–Al_3Ti, so that these particles are more uniformly distributed in the melt pool. As freezing goes on, many small equiaxed grains develop, which makes the microstructure more homogeneous (Figure 8D). Finally, heat is removed through the already solidified columnar zone and the underlying material, and solidification gradually comes to an end.

3.3.4. Formation of nanoscale precipitates

During cooling, the supersaturated solute in the α-Al grains can form nanoscale precipitates in some local regions (Figure 8E). Their size is only a few tens of nanometers, and the spacing is small. However, only a limited amount of such precipitates is present, and most of the precipitation strengthening develops later during post-heat treatment.

In summary, the melt-pool microstructure is governed by the combined action of several interacting factors, which in turn shape the final microstructural state and mechanical response of the material.

3.4. Correlation between microstructure and mechanical properties

3.4.1. Relationship between microstructure and mechanical properties

The mechanical response of metals is strongly controlled by their microstructure. In this section, we summarize five key microstructural features that govern strength and toughness.

3.4.1.1. Grain size

Grain refinement can significantly improve the material's load-bearing capacity and resistance to fracture.[36] When the average grain size is reduced, the yield strength rises in accordance with the Hall–Petch relation. At the same time, a fine, equiaxed grain structure promotes more homogeneous plastic deformation, delays crack initiation and growth, and therefore allows strength and ductility to be improved together.

3.4.1.2. Phase constituents

Secondary particles and precipitates can strengthen the alloy. However, if these phases grow too large or are inhomogeneously dispersed, they may act as crack-initiation sites and reduce toughness.[37]

3.4.1.3. Grain morphology and orientation

Equiaxed grains usually give nearly isotropic mechanical behavior, whereas columnar grains and strong texture lead to marked anisotropy.[38] For LPBF parts, the elongation measured parallel to the build direction (longitudinal) is generally higher than that measured perpendicular to it (transverse), reflecting the preferred grain orientation and the distribution of grain boundaries.

3.4.1.4. Defects

Defects include dislocations and voids/cracks. Dislocations act as carriers of plastic deformation; a high dislocation density can induce work hardening, enhancing strength and hardness but reducing ductility.[39] Voids and cracks compromise material continuity and create stress concentration sites, significantly lowering fatigue strength and fracture toughness.

3.4.1.5. Substructure

Substructures can further refine grains at the mesoscale and strengthen the material.[40] The cellular structures produced by rapid LPBF solidification have cell walls enriched in solute and dislocations, subdividing grains to the submicron scale and thereby enhancing the material strength.

3.4.2. Experimental validation of the microstructure–property relationship

To complement the general discussion in Section 3.4.1, this section highlights representative experimental studies in which specific microstructural features are directly correlated with measured mechanical performance in LPBF-processed aluminum alloys.

3.4.2.1. Grain structure and orientation effects

Li *et al.*[41] studied four Al–Cu–Mg–Mn–Zr alloys with different compositions produced by LPBF, focusing on their microstructure and mechanical response. Figure 9 presents inverse pole figures, grain-size histograms, and (001) pole figures for alloys A–D. From A to D, the grain shape changes from columnar to equiaxed, the average grain size is progressively refined, and the grain-orientation distribution becomes increasingly uniform.

The tensile properties measured for these alloys are listed in Table 1. As the average grain size is reduced and the grains change from columnar to equiaxed, the alloys show higher yield and tensile strengths together with improved ductility.

3.4.2.2. Defect populations and defect type

Beyond grain structure, a growing body of work demonstrates that the mechanical performance of LPBF-processed aluminum alloys is often strongly limited by defect populations. Recent studies on LPBF AlSi10Mg have shown that different pore types—such as lack-of-fusion and keyhole-induced porosity—do not contribute equally to mechanical degradation. In particular, lack-of-fusion defects are more detrimental to elongation and fatigue life due to their irregular morphology and pronounced stress concentration, whereas spherical keyhole pores tend to have a less severe impact at comparable porosity levels.[22] These findings indicate that microstructural refinement

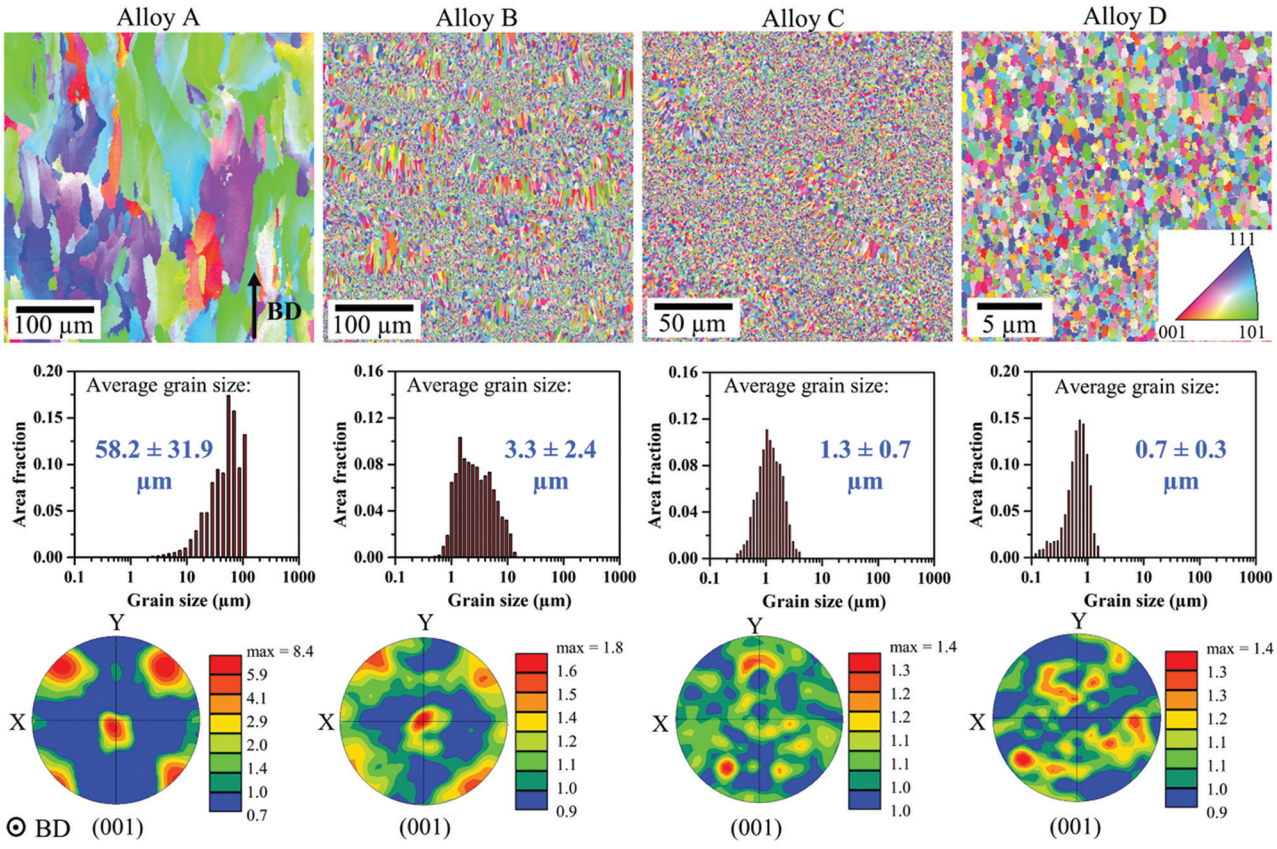

Figure 9. Inverse pole figures, grain-size distributions, and (001) pole figures for alloys A-D. Reproduced from Li *et al.*,[41] with permission from Elsevier. Copyright © 2021 Elsevier B.V.

alone may not yield meaningful performance gains unless defect type and distribution are simultaneously controlled.

3.4.2.3. Substructure and post-processing effects

At finer length scales, LPBF-processed aluminum alloys commonly exhibit characteristic cellular or subgrain structures formed during rapid solidification. In AlSi10Mg, for example, Si-rich cellular networks and dislocation-rich cell walls have been repeatedly observed in the as-built condition, and their stability has been linked to strength levels.[42] Experimental studies further show that post-processing treatments can modify or partially dissolve these substructures, leading to measurable changes in strength and ductility.[43] Such observations provide direct experimental evidence that mesoscale and subgrain-scale features, in addition to grain structure and defects, play an important role in determining the mechanical response of LPBF-processed aluminum alloys.

Taken together, these representative examples demonstrate that mechanical performance in LPBF-processed aluminum alloys arises from the combined effects of grain structure, defect populations, and substructural features.

4. Strengthening mechanisms for improved mechanical properties

In LPBF-processed aluminum alloys, improvements in mechanical properties through microstructural design still fundamentally rely on introducing obstacles to dislocation motion.[40] Building on the LPBF-specific microstructures outlined in the previous section, this section discusses the classical microstructure-based strengthening mechanisms that are most relevant to LPBF-processed aluminum alloys.

4.1. Grain boundary strengthening

LPBF-processed aluminum alloys generally exhibit much finer grains than conventionally cast alloys, owing to the extremely high cooling rates and steep thermal gradients.[8] In addition, the solidification conditions in LPBF often produce a mixed grain structure with columnar grains along the build direction and finer equiaxed grains in regions of enhanced nucleation.[35] In all of these cases, grain boundaries are key microstructural features that impede dislocation motion and thus contribute to strengthening.[44]

Table 1. Tensile properties of LPBF Al–Cu–Mg–Mn-based alloys A–D

Material	Elastic modulus (GPa)	Yield strength (MPa)	Ultimate tensile stress (MPa)	Elongation at fracture (%)
Alloy A	26±12	38±5	51±5	0.3±0.1
Alloy B	59±1	220±15	265±14	0.6±0.1
Alloy C	73±6	455±6	474±10	5.9±0.9
Alloy D	80±4	561±24	580±16	6.0±1.3

Notes: Reproduced from Li *et al.*,[41] with permission from Elsevier.

In polycrystalline materials, dislocations glide along the lattice under applied shear stress. When dislocations approach a grain boundary, the mismatch of slip plane orientations between adjacent grains prevents them from crossing the boundary, causing dislocations to "pile up" near the grain boundary (Figure 10). This pile-up means that a higher applied stress is needed for dislocations to pass through grain boundaries, which increases the yield strength and produces a grain-boundary strengthening effect.

Grain size directly influences the effectiveness of grain boundary strengthening.[45,46] In coarse-grained samples, dislocations traverse fewer grain boundaries, whereas in fine-grained samples, dislocations must cross more boundaries, leading to a more pronounced impediment effect. Therefore, grain refinement is a key approach to achieving grain boundary strengthening.

Grain-boundary strengthening is commonly expressed by the Hall–Petch relation.[45] Based on Hall and Petch's experiments, the macroscopic yield strength σ_{ys} of a polycrystal increases as the grain size decreases and can be written as Equation I:

$$\sigma_{ys} = \sigma_0 + Kd^{-1/2} \quad \text{(I)}$$

where σ_{ys} denotes the macroscopic yield strength (MPa), σ_0 represents the strength in the absence of grain boundaries (MPa), K is the Hall–Petch constant, and d is the average grain diameter (mm).

In LPBF-processed aluminum alloys, the presence of very fine grains suggests that grain-boundary strengthening is an important component of the overall strength. The

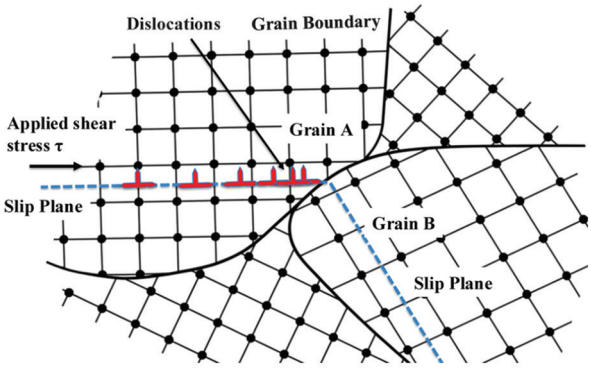

Figure 10. Schematic illustration of dislocation pile-up near a grain boundary. Image created by the authors.

extent of this contribution is governed by processing conditions and grain refiners, which control grain size and the development of substructure. Across LPBF-processed aluminum alloy families, grain-boundary strengthening is discussed with different emphases depending on alloy type and processing objectives. In Al–Si alloys, rapid solidification produces fine grains and sub-grain boundaries, and grain refinement is frequently invoked to rationalize the as-built strength.[47] For Al–Mg (5xxx) alloys, grain refinement is also commonly discussed, particularly in relation to processability and defect mitigation, where finer grains are associated with improved build integrity.[28] In high-strength wrought alloys (2xxx, 6xxx, and 7xxx), grain refinement is typically emphasized in the as-built condition, whereas post-build mechanical performance is more often interpreted through precipitation evolution after subsequent heat treatments.[48]

4.2. Solid solution strengthening

For LPBF-processed aluminum alloys, solid solution strengthening is an important contributor to the overall strength, especially in the as-built condition, where very high cooling rates can retain large amounts of solute in supersaturated solid solution.[49] In essence, solid solution strengthening is achieved by introducing solute atoms into the matrix lattice to form a solid solution, thereby inducing lattice distortion and generating dislocation fields. As a result, the alloy becomes stronger.

Depending on where the solute atoms sit in the lattice, solid solutions are usually described as substitutional or interstitial.[50] In a substitutional solid solution, solute atoms sit on the normal lattice sites of the matrix and replace the original atoms (Figure 11A). In an interstitial solid solution, small solute atoms stay in the spaces between matrix atoms instead of sitting on normal lattice sites (Figure 11B). These atoms distort the nearby lattice

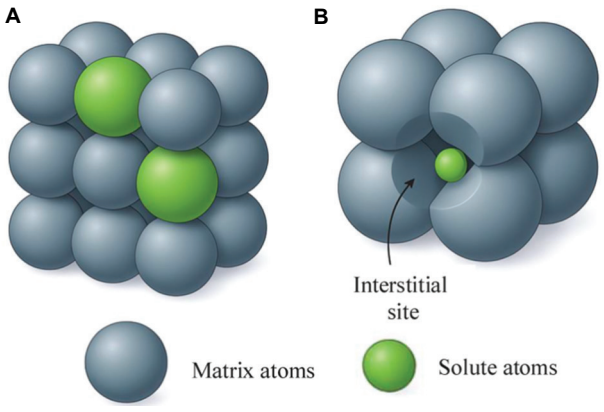

Figure 11. Schematic of solid–solution strengthening: (A) Substitutional and (B) interstitial distribution of solute atoms. Image created by the authors.

and make it harder for dislocations to move, thereby enhancing material strength.

Solid–solution strengthening is often expressed using a power–law relation between the increment in yield strength and solute concentration.[51-53] It can be approximated as Equation II:

$$\Delta\sigma_{ss} = \sum_i B_i X_i^n \quad \text{(II)}$$

where X_i is the atomic fraction of solute i, B_i is the strengthening coefficient reflecting size/modulus misfit, and n is typically in the range of 1/2–2/3 depending on the solute–dislocation interaction model.

In LPBF-processed aluminum alloys, solid solution strengthening is dominated by substitutional solutes. When aluminum atoms and solute atoms differ in atomic radius or shear modulus, the resulting strain fields can effectively hinder dislocation motion, thereby achieving solid–solution strengthening.[54] Table 2 summarizes how different solute elements strengthen binary Al–X systems through solid solution. The data indicate that Mg and Mn are typical solid solution strengthening agents under rapid solidification conditions.[55]

Solid–solution strengthening is interpreted differently across LPBF-processed aluminum alloy systems. In Al–Mg (5xxx) alloys, retained Mg in solid solution is frequently highlighted as a primary contributor to strength in the as-built condition, often in conjunction with high dislocation density.[28] In contrast, for high-

Table 2. Solid solubility of binary Al–X alloys at equilibrium and at a cooling rate of 10^6 K/s, together with the maximum misfit strain and the estimated solid–solution strengthening from first-principles calculations

Element	Misfit strain ε (%)	*$C_{max,e}$ (at%)	Δσ at $C_{max,e}$ (MPa)	*C_v at 10^6 K/s (at%)	*Δσ at C_v (MPa)
Mg	1.28	18.69	163	–	–
Mn	4.40	0.71	63	7.40	301
Fe	4.60	0.02	6	4.03	210
Cr	4.10	0.45	43	4.18	192
Ni	3.19	0.11	13	0.84	51
Si	0.87	1.50	21	1.95	24
Ti	1.42	0.78	22	0.96	25
V	3.11	0.34	27	2.88	114
Zr	1.35	0.08	5	1.99	39
Hf	1.05	0.18	6	4.00	48
Sc	1.38	0.20	8	2.51	46

Notes: Reproduced from Li *et al.*,[55] with permission from Elsevier. * Indicates first-principles values.

strength wrought alloys (2xxx, 6xxx, and 7xxx), rapid solidification during LPBF can trap alloying elements (*e.g.*, Cu, Mg, and Zn) in a supersaturated α-Al matrix; however, this state is commonly discussed as a precursor that enables subsequent precipitation strengthening during artificial aging rather than as a dominant long-term mechanism.[48,56] For Al–Si alloys, the contribution of solid-solution strengthening is generally described as limited, and strengthening discussions more often focus on substructure- and dislocation-related effects.[47]

4.3. Precipitation strengthening

4.3.1. Coherent versus incoherent precipitates

Precipitation strengthening refers to a strengthening mechanism in which fine, dispersed second-phase particles (precipitates) are formed within a metallic solid solution matrix.[57] These precipitates interact with dislocations and impede their motion, so the alloy becomes stronger and harder. For aluminum alloys produced by LPBF, two types of mechanisms are generally involved: coherent precipitation strengthening and incoherent precipitation strengthening. When solute atoms locally cluster within the lattice but still occupy matrix lattice sites, such that no distinct interface exists between the matrix and the precipitate, coherent precipitates are formed (Figure 12A). By contrast, when the precipitate loses coherency with the matrix lattice, incoherent precipitation strengthening occurs (Figure 12B).

4.3.2. Shearing versus bypassing

During LPBF, the very high cooling rate usually leaves the matrix as a supersaturated solid solution. During later heat treatment, the precipitates change from coherent to semi-coherent and finally to incoherent.[37] When coherent particles are dominant, moving dislocations cut through them, and the associated elastic strain fields provide the main strengthening. At later stages, incoherent particles become more important, and dislocations mainly bypass them by the Orowan looping mechanism. Thus, the contribution of precipitates to strength can be understood in terms of two basic interactions with dislocations: Shearing of particles and bypassing them by looping,[58] as shown in Figure 13.

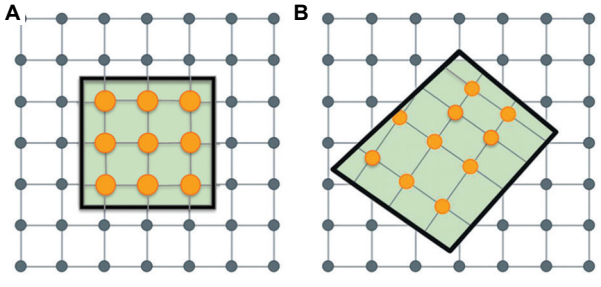

Figure 12. Schematic of two precipitation-strengthening modes: (A) Coherent and (B) incoherent. Image created by the authors.

For coherent and shearable ordered precipitates, dislocation cutting can create an anti-phase boundary (APB), giving rise to an APB-associated order-strengthening contribution. A commonly used simplified expression can be written as Equation III:[59]

$$\Delta\sigma_{ord} = 0.81M\frac{\gamma_{APB}}{2b}\left(\frac{3\pi f}{8}\right)^{1/2} \quad \text{(III)}$$

where f is the precipitate volume fraction, M is the Taylor factor, b is the magnitude of the Burgers vector of the matrix, and γ_{APB} is the APB energy of the precipitate.

4.3.3. Orowan strengthening

The Orowan bypass mechanism arises when dislocations encounter non-shearable second-phase particles during motion.[60] In this case, dislocations bow out between neighboring particles and eventually leave closed loops around them (Figure 14). These loops remain around the particles, blocking later dislocations and raising the shear stress needed for slip, so the alloy becomes harder to deform. In LPBF-processed aluminum alloys, this contribution is mainly controlled by the size, spacing, and distribution of relatively coarse, stable precipitates or dispersoids formed during and after the build.[61]

For non-shearable precipitates, the Orowan bypass mechanism gives a characteristic strengthening increment that scales with Gb/λ. A representative form of Orowan strengthening is given by Equation IV:[59,62]

$$\Delta\sigma_{Or} = M\frac{0.4Gb}{\pi\left(1-\nu\right)^{1/2}\lambda}ln\left(\frac{2r}{b}\right) \quad \text{(IV)}$$

where G is the matrix shear modulus, M is the Taylor factor, b is the Burgers vector, r is the precipitate radius, λ is the effective obstacle spacing on the active slip plane, and ν is Poisson's ratio.

4.3.4. Relevance across alloy systems

Precipitation strengthening is central to the discussion of heat-treatable LPBF-processed aluminum alloys, including 2xxx (Al–Cu), 6xxx (Al–Mg–Si), and 7xxx (Al–Zn–Mg–Cu) systems.[48] In these alloys, the as-built microstructure is typically characterized by a supersaturated solid solution with limited precipitation, whereas post-build T5 or T6 heat treatments activate precipitation-controlled strengthening responses.[56] By contrast, in non-heat-treatable Al–Mg (5xxx) alloys, precipitation strengthening is generally considered limited or undesirable, and strengthening

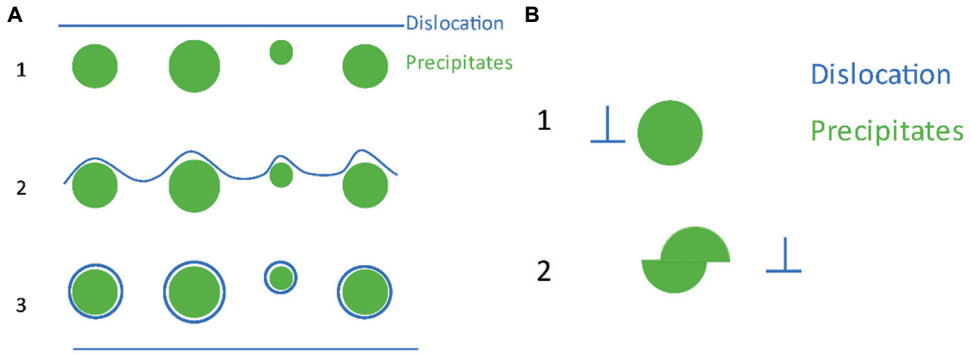

Figure 13. Schematic of dislocation–precipitate interactions in precipitation hardening: (A) Bypass by looping (Orowan mechanism); (B) shearing of precipitates by dislocations. Reproduced from Megahed *et al.*[58]

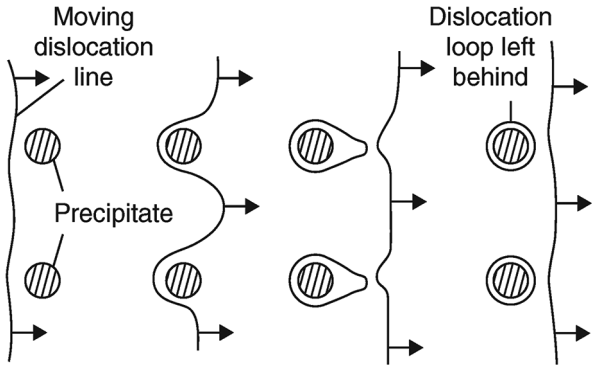

Figure 14. Orowan's strengthening mechanism. Reproduced from Smallman and Ngan,[60] with permission from Elsevier. Copyright © 2007 Elsevier Ltd.

is more often interpreted in terms of solid–solution and dislocation-based mechanisms.[28] Al–Si casting-type alloys similarly rely less on classical precipitation hardening, unless modified chemistries or tailored heat treatments are applied.[63]

4.4. Dislocation strengthening

In LPBF-processed aluminum alloys, dislocation-based mechanisms constitute an important part of the overall strengthening. In general, dislocation strengthening arises when a high density of dislocations interacts and forms a "dislocation forest," which impedes the motion of other dislocations and increases the flow stress.[64] The additional strength is commonly written as Equation V:

$$\Delta\sigma = M\beta Gb\sqrt{\rho} \quad \text{(V)}$$

where M denotes the Taylor factor, β the dislocation-interaction coefficient, G the shear modulus, b the Burgers vector, and ρ the dislocation density. In LPBF-processed aluminum alloys, dislocation strengthening is commonly discussed in terms of the total dislocation density, which can be separated into geometrically necessary dislocations (GNDs) and statistically stored dislocations (SSDs). In addition, LPBF-specific substructures can act as effective barriers and dislocation storage sites, further contributing to the dislocation-controlled strength.

4.4.1. GNDs

As the melt pool solidifies rapidly, thermally generated stresses give rise to heterogeneous plastic deformation within grains. Initially, equiaxed grains remain largely undeformed (Figure 15A). However, as thermal stress and plastic strain accumulate, grains gradually become misorient, leading to local voids or overlaps and thus heterogeneous strain distribution (Figure 15B). In regions with high strain gradients, large numbers of dislocations accumulate at grain and sub-grain boundaries to accommodate the deformation incompatibility, forming a network of GNDs (Figure 15C).

The amount of GNDs increases with the local plastic strain gradient.[65] The greater the strain inhomogeneity during LPBF, the more GNDs are required, resulting in higher dislocation density. The dense dislocation networks at grain and sub-grain boundaries effectively hinder the glide and transmission of other dislocations, thereby imparting a significant strengthening effect on the aluminum alloy.

4.4.2. SSDs

SSDs originate from dislocation multiplication and mutual interactions during plastic deformation that are not associated with a net strain gradient.[66,67] Unlike GNDs, which accommodate lattice curvature, SSDs accumulate through mechanisms such as dislocation glide, junction formation, and tangling, leading to a largely random spatial distribution within grains.[67,68]

In LPBF, steep thermal gradients and repeated layer-by-layer thermal cycling generate cyclic thermal stresses, which may locally exceed the yield strength and activate plastic accommodation within grains.[69] As a result,

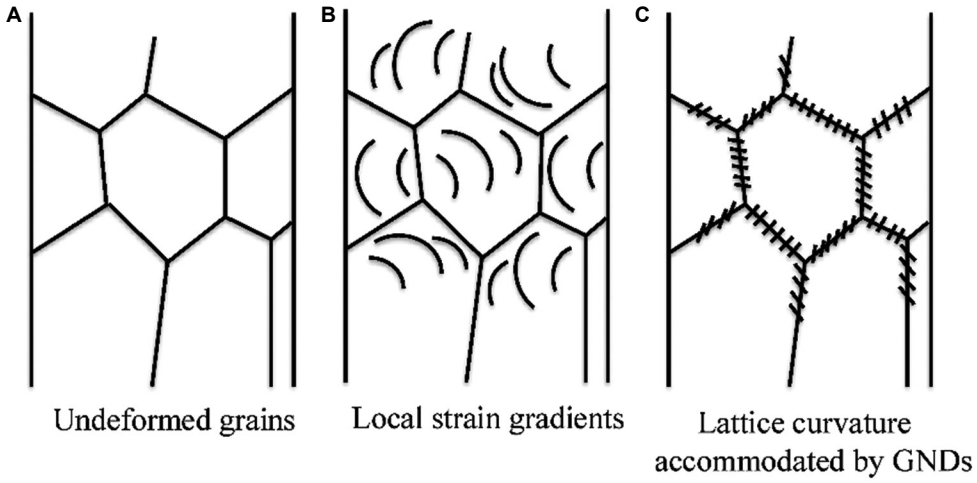

Figure 15. Schematic depicting the principle underlying GND formation. (A) Largely undeformed equiaxed grains. (B) Heterogeneous strain distribution induced by thermal stress and accumulated plastic strain. (C) GND network formed by dislocation accumulation at grain and sub-grain boundaries to accommodate deformation incompatibility. Image created by the authors.
Abbreviation: GND: Geometrically necessary dislocation.

dislocations can be repeatedly generated and rearranged during successive thermal cycles; in the dislocation-density framework commonly used for LPBF AlSi10Mg, such accumulated dislocation content is treated as part of the SSD population contributing to strength.[47]

4.4.3. Cellular strengthening

Strengthening associated with cellular structures originates from the network of sub-grain cells that develops inside the grains. In LPBF-processed aluminum alloys, the very rapid cooling largely freezes solute atoms in place, so elements such as Si and Mg have insufficient time to diffuse and precipitate, leaving a highly supersaturated solid solution in the α-Al matrix. As solidification proceeds, these solute atoms are pushed toward the subgrain cell walls, where they accumulate and form solute-enriched boundaries with dense dislocation arrays, giving rise to the characteristic cellular or subgrain cellular structures.[70]

Cellular structures strengthen the alloy mainly in two ways. First, the cell walls, which are enriched in solute atoms and dislocations, behave like sub-grain boundaries and hinder dislocation glides. Second, when dislocations move inside the relatively soft aluminum cell interiors and meet the harder solute-rich walls, they must bow around or cut through these walls, so a higher stress is needed for further motion. Because of these barriers and interactions, cellular structures increase the yield strength and hardness of LPBF-processed aluminum alloys and strongly affect their plastic-deformation behavior.

4.4.4. Relevance across alloy systems

Dislocation strengthening is widely discussed across LPBF-processed aluminum alloy systems due to steep thermal gradients and cyclic thermal stresses inherent to the process.[71] In Al–Si alloys, dislocation strengthening is frequently discussed together with cellular or sub-grain structures that act as effective dislocation storage sites.[47] In Al–Mg (5xxx) alloys, high dislocation density retained in the as-built condition is commonly invoked alongside Mg solid-solution strengthening to explain the measured strength.[28] For high-strength wrought alloys (2xxx, 6xxx, and 7xxx), dislocation strengthening is most often emphasized in the as-built or low-temperature-treated states, whereas post-heat treatments are reported to partially reduce dislocation density as precipitation strengthening becomes more prominent.[48]

4.5. Load-bearing strengthening

In load-bearing strengthening, stiff and strong phases are dispersed in a softer metal matrix. When the material is loaded, these hard particles carry part of the stress, so the matrix itself bears a lower effective stress. This requires good bonding at the particle–matrix interface; otherwise, the load cannot be transferred.[72] Because the particles usually have much higher strength and modulus than the surrounding metal, they behave like an internal skeleton that increases yield strength, stiffness, and the load-carrying ability of the composite.

Load-bearing strengthening in reinforced aluminum systems can be described using a simple load-sharing (rule-of-mixtures) framework. Under the iso-strain assumption, the composite flow stress can be approximated as Equation VI:[73]

$$\sigma_C \approx (1-V_r)\,\sigma_m + V_r\,\sigma_r \quad \text{(VI)}$$

where V_r is the reinforcement volume fraction, and σ_m and σ_r are the matrix and reinforcement stresses, respectively, evaluated at the same overall strain.

In LPBF-processed aluminum alloys, this mechanism is realized by adding ceramic or other rigid particles to the alloy. The problem is that these particles are brittle, and if their content is too high, cracks form easily, and the ductility drops. When designing the alloy, the type and amount of reinforcement therefore need to be chosen so that the gain in strength does not come with an unacceptable loss of toughness.

In LPBF-processed aluminum materials, load-bearing strengthening is typically discussed in composite-like architectures where a mechanically stiff phase is deliberately incorporated, and a load-transfer pathway can be established across the interface.[74] Reported routes include: (i) *ex situ* ceramic particle additions (*e.g.*, TiB_2, SiC, Al_2O_3) dispersed in an aluminum alloy matrix, where strengthening is interpreted in terms of load sharing together with interfacial integrity;[75] and (ii) *in situ* formation of rigid phases during processing (*e.g.*, reaction-derived borides/carbides), which can provide a more stable reinforcement distribution.[76] In these systems, load-bearing is often discussed alongside accompanying particle-enabled mechanisms such as thermal-mismatch–induced dislocations and Orowan-type bypassing.

4.6. Summary

Mechanical properties of LPBF-processed aluminum alloys are mainly improved by the combined action of five strengthening mechanisms, all of which operate by restricting dislocation motion through specific microstructural features. Because alloy chemistry and processing conditions vary from system to system, the weight of each mechanism is not the same, but together they still govern the overall strength.

5. Strengthening strategies for LPBF-processed aluminum alloys

For LPBF-fabricated aluminum parts, the mechanical behavior can be improved from three directions. One is to adjust the processing parameters so that the melt-pool shape and solidification are under better control. The second route is to design the alloy composition for microstructures that can carry higher loads. The third is to use post-build heat treatments to relax residual stresses and to modify precipitates and grain boundaries, so that strength and ductility are reasonably balanced. This section discusses these strategies, their mechanisms, and recent advances.

5.1. Optimization of processing parameters

In LPBF, choosing proper process parameters is a basic requirement for producing high-performance aluminum alloys. Among many parameters, volumetric energy density (VED) and scan strategy play a dominant role in determining the microstructure and properties.

5.1.1. VED

Laser power, scan velocity, hatch distance, and layer thickness act together to set the heat put into the melt pool and the corresponding cooling rate.[77] A commonly used lumped parameter is the VED (mathematically as E_v), defined as Equation VII:

$$E_v = \frac{P}{\upsilon h_D \mathrm{t}} \tag{VII}$$

where P denotes the laser power (W), υ the scan speed (mm/s), h_D the hatch spacing, and t the layer thickness (mm) (Figure 16).

VED significantly influences melt pool stability and pore formation, thereby indirectly affecting mechanical properties.[79-81] Low VED results in lack-of-fusion pores, whereas excessive VED can induce keyhole pores due to overmelting and vaporization.[82] At low VED, the melt lacks sufficient fluidity to adequately wet the underlying substrate or previously solidified layers; the melt track tends to narrow and undergo balling as the system minimizes surface energy, ultimately causing incomplete interlayer bonding and lack-of-fusion pores.[79] At the other extreme, when the energy input becomes very high, the local temperature within the melt depression may exceed the evaporation temperature, leading to intense evaporation and recoil pressure. The resulting vapor depression (keyhole) increases laser absorption through multiple internal reflections, establishing a positive

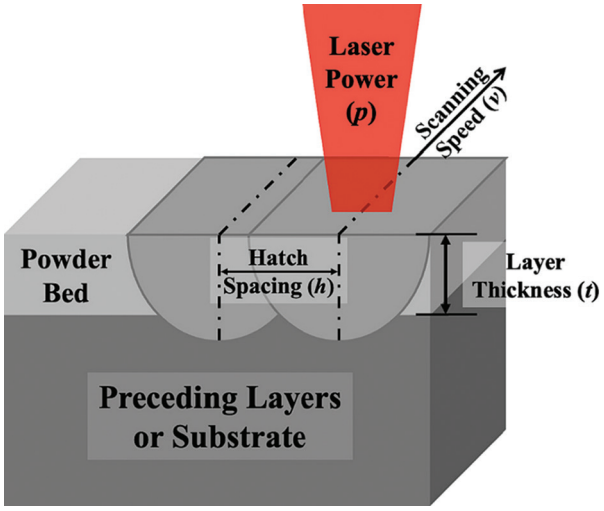

Figure 16. Laser powder bed fusion process parameters. Reproduced from Headley *et al.*,[78] with permission from Elsevier. Copyright © 2024 The Society of Manufacturing Engineers.

feedback loop that deepens the keyhole and promotes pore formation.[83]

Optimal energy input ranges yield maximum densification and superior tensile properties. For instance, Vaudreuil *et al.*[79] reported that AlSi7Mg0.6 exhibits optimal strength and modulus at 25–35 J/mm³ (Figure 17).

Subsequent studies show that the "optimal VED range" is not universal but depends on material and process conditions. Defanti *et al.*[80] found that in AlSi10Mg with fixed laser power (370 W) and layer thickness (60 μm), the best tensile performance occurs at 30–35 J/mm³, whereas Jatti *et al.*[81] observed an optimal VED of 86.81 J/mm³ under different conditions. These results suggest that the commonly used VED expression is only a rough indicator of the real energy input. In practice, it has to be corrected for the actual powder characteristics, layer thickness, and scanning pattern.

VED is related not only to porosity. It also controls the temperature gradient in the melt pool and thus the cooling rate.[84] High cooling rates and steep temperature gradients in LPBF shorten the time available for solute partitioning and long-range diffusion during solidification. As a result, microsegregation is suppressed, and solute can be retained in the α-Al matrix as a supersaturated solid solution;[11] meanwhile, the increased undercooling raises the nucleation rate and reduces the characteristic solidification length scales, promoting grain refinement and a finer cellular/dendritic substructure.[34] These features in turn support solid–solution, precipitation, and grain-boundary strengthening. By selecting an appropriate VED, defects can be reduced, the microstructure refined, and the mechanical response improved.

5.1.2. Optimization of scan strategy

In LPBF, besides VED, the scan strategy also influences the melt-pool thermal history and the final mechanical performance of aluminum alloys.[85,86] Commonly used scan strategies include parallel, bi-directional, island, and remelting modes (Figure 18). In the parallel strategy, the laser traces run back and forth in a single direction. In the bi-directional strategy, the scan vectors of successive layers are rotated by 90°. The island strategy divides the scanning plane into multiple isolated "islands," where each island is scanned locally, and consecutive layers are rotated by 37°, shortening the laser vector length and reducing heat accumulation. The remelting strategy involves performing a local remelt immediately after scanning each layer, with a 90° rotation between layers, which can improve surface density but may alter grain growth and precipitation behavior.

Zhang *et al.*[86] experimentally investigated the mechanical properties of Al–Mg–Sc–Zr specimens processed with different scan strategies. As shown in Figure 19, specimens processed with the island strategy exhibited the highest as-built tensile strength and maximum elongation, followed by the parallel and bi-directional strategies, whereas the remelting strategy resulted in a significant reduction in both strength and elongation.

Scan strategies influence the thermal history and solidification conditions of the melt pool, thereby affecting residual stress distribution, porosity formation, and grain morphology and size. These factors together dictate which strengthening mechanisms operate in the microstructure and what level of mechanical properties can be achieved. With a carefully chosen scan path, heat is less concentrated in one area, pores and cracks are reduced, and the grains become finer and more evenly distributed. The size and spacing of precipitates can also be better controlled, so solid–solution, grain-boundary, and precipitation strengthening work more effectively. Differences in properties between the various scan strategies are therefore mainly related to their influence on porosity and microstructural evolution; among them, the island strategy usually gives the most balanced combination of strength and ductility. Notably, Zhang *et al.*[86] further indicated that the property degradation in the remelting strategy was mainly associated with precipitation coarsening. Remelting promotes the formation of large $Al_3(Sc, Zr)$ precipitates that are difficult to shear by dislocations, thereby shifting the dislocation–precipitate interaction from precipitate

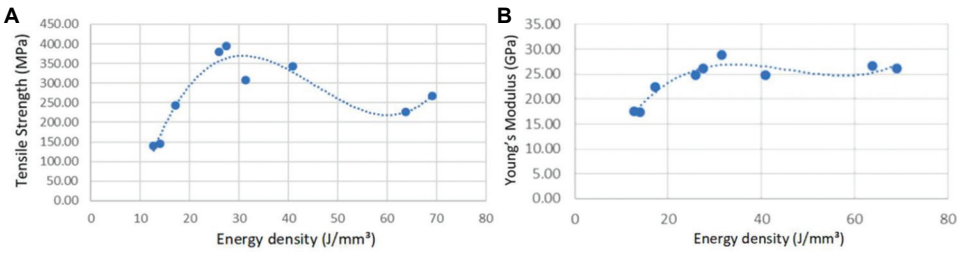

Figure 17. Variation of tensile properties with energy density for as-built parts: (A) Tensile strength (MPa); (B) Young's modulus (GPa). Reproduced from Vaudreuil *et al.*[79]

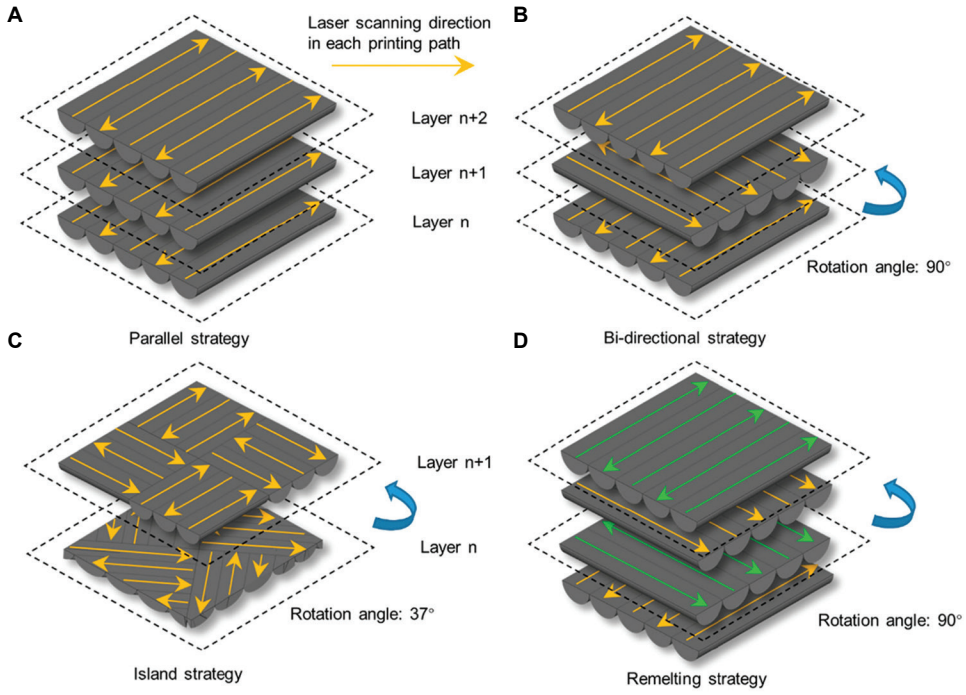

Figure 18. Schematic diagrams of different laser scan strategies: (A) Parallel, (B) bi-directional, (C) island, and (D) remelting. Reproduced from Zhang *et al.*,[86] with permission from Taylor & Francis. Copyright © 2022 The Author(s).

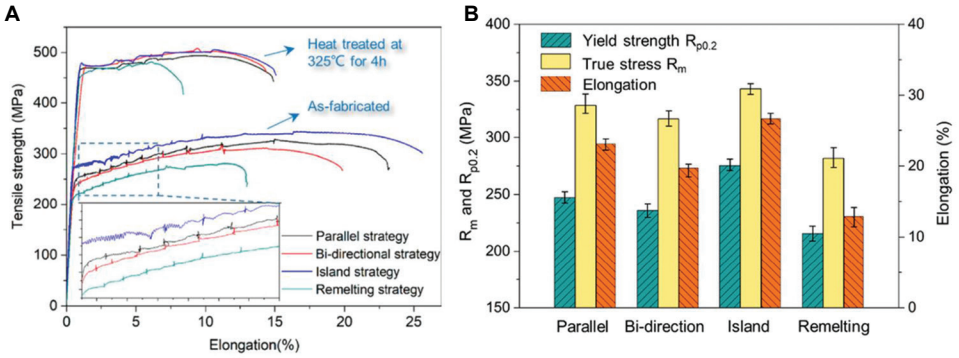

Figure 19. Effect of laser scanning strategy on the mechanical properties of Al–4.2Mg–0.4Sc–0.2Zr specimens: (A) Representative room-temperature tensile curves; (B) tensile parameters of as-built specimens for different scan strategies. Reproduced from Zhang *et al.*,[86] with permission from Taylor & Francis. Copyright © 2022 The Author(s).

shearing to Orowan bypassing. Meanwhile, coarsening increases the effective inter-precipitate spacing (*i.e.*, over-aging), which weakens the net precipitation-strengthening contribution and thus reduces both strength and ductility.

5.2. Alloy design

Rational alloy design is another important way to improve the mechanical performance of LPBF-processed aluminum alloys. LPBF is a highly non-equilibrium process; it allows the fabrication of high-alloy compositions that are not easy to obtain by conventional routes. Typical design options include adding primary elements, introducing several microalloying additions, and incorporating external reinforcement phases, as discussed in the following subsections.

5.2.1. Strengthening via principal alloying elements

5.2.1.1. Classification of principal alloying elements

In LPBF-processed aluminum alloys, the principal alloying elements include Si, Cu, Mg, and Zn.[1] (Table 3). High Si content improves melt pool fluidity and suppresses hot cracking, and after solidification, it forms an ultrafine eutectic network, thereby enhancing mechanical

Table 3. Roles and printability of principal alloying elements in LPBF-processed aluminum alloys[1]

Element	Representative system	Core function	LPBF printability	Remarks
Si	Al–Si	Eutectic network formation, improved processability, and crack suppression	Excellent	Medium strength; most widely used
Cu	Al–Cu (2xxx)	Precipitation and solid solution strengthening	Poor	High strength potential; prone to hot cracking
Mg	Al–Mg (5xxx), Al–Mg–Si (6xxx)	Solid solution and precipitation strengthening	Moderate	Improves strength and ductility; prone to evaporation
Zn	Al–Zn–Mg (7xxx)	Precipitation strengthening	Very poor	Highest strength; printing difficult

Abbreviation: LPBF: Laser powder bed fusion.

properties.[20] Cu and Zn can significantly increase strength but have poor printability;[12] Mg can enhance both strength and ductility, but its high vapor pressure may lead to evaporation.[27] Therefore, the selection of alloying elements must balance printability and performance. Among these, Al–Si systems, such as AlSi10Mg and AlSi12, are the most widely used in LPBF due to their superior fluidity, crack resistance, and reliability.[11]

5.2.1.2. Strengthening of Al–Si alloys

For Al–Si alloys, when the Si content exceeds its equilibrium solubility (~1.65%), LPBF's rapid, non-equilibrium solidification produces a highly supersaturated α-Al matrix. As the temperature rapidly decreases, the excess Si atoms redistribute along grain boundaries or sub-grain regions, forming ultrafine cellular or networked eutectic Si structures[87] (Figure 20). This morphology arises because the very high cooling rate limits long-range diffusion and conventional eutectic growth, causing Si to pile up at the solid–liquid front and be "frozen" into a refined, nearly continuous network. Meanwhile, the good fluidity of the liquid alloy improves melt-pool feeding and lowers the risk of hot cracking.

Kimura *et al.*[89] studied the mechanical properties of LPBF Al–xSi alloys with different Si levels (Figure 21). As Si content exceeded 4 wt%, both tensile and yield strengths increased steadily. Meanwhile, elongation decreased with higher Si content. (Samples with 1 wt% Si exhibited cracking, considered anomalous.)

As the Si content increases, both the tensile response and the yield stress of LPBF-processed aluminum alloys are significantly enhanced. Several factors are responsible for this hardening: (i) Load-bearing strengthening. Rigid crystalline Si, being much harder and more brittle than Al, can carry part of the external load and relieve the matrix; (ii) Dislocation strengthening. The eutectic Si network forms a cellular framework that pins and diverts dislocations; (iii) Solid–solution strengthening. Some Si atoms remain in supersaturated solid solution in the α-Al matrix, causing lattice distortion and making dislocation glide more difficult; (iv) Grain-boundary strengthening. High Si levels favor cellular or sub-grain microstructures with a high density of boundaries, which, according to the Hall–Petch relation, further restrict dislocation motion and thus increase strength.

However, higher Si contents are accompanied by a loss of ductility. This is mainly due to the discontinuity introduced by the hard Si particles, where interfaces act as crack initiation sites, resulting in decreased elongation at fracture.[34]

Furthermore, adding Mg provides an additional strengthening route. Mg interacts with Si to form a metastable phase sequence through solution treatment and aging, ultimately precipitating Mg_2Si, thereby achieving precipitation strengthening.[90]

5.2.1.3. Strengthening of other high-strength aluminum alloys

For Al–Mg alloys, Mg is the primary strengthening element and can simultaneously enhance strength and ductility, but its high vapor pressure at LPBF processing temperatures makes it prone to evaporation, spatter, and composition loss, which may degrade density and mechanical properties.[91] To address this issue, recent studies have optimized the process window (moderate energy density, adjusted scan speed and hatch spacing, and improved shielding-gas flow) and alloy composition (slightly increased nominal Mg content and/or additions of Sc and Zr) to compensate Mg loss and stabilize the microstructure.[92,93] Under these conditions, rapid solidification retains excess Mg in a supersaturated α-Al solid solution, giving a strong solid–solution strengthening effect, whereas subsequent heat treatments introduce additional precipitation strengthening.[94] As a result, LPBF-processed Al–Mg alloys containing Sc and/or Zr can reach yield stresses well above those of conventional wrought 5xxx alloys while still keeping reasonable ductility.[95]

For Al–Cu and Al–Zn–Mg alloy families, strength is mainly increased by the joint action of solid–solution hardening and age-hardening precipitates such as θ′-Al_2Cu and η′-$MgZn_2$ formed during ageing.[11] However, high

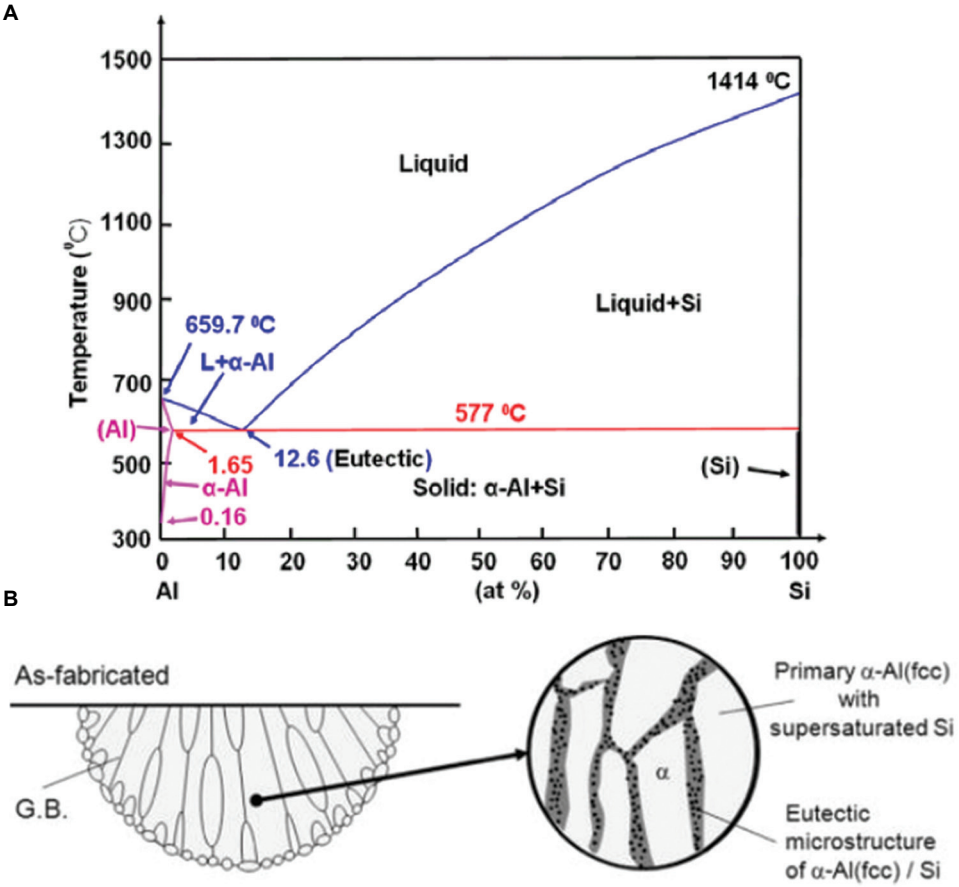

Figure 20. Al–Si phase relations and eutectic Si network morphology. (A) Al–Si phase diagram. Reproduced from Lin *et al.*[88] (B) Eutectic Si network. Reproduced from Takata *et al.*,[87] with permission from Elsevier. Copyright © 2017 Elsevier B.V.

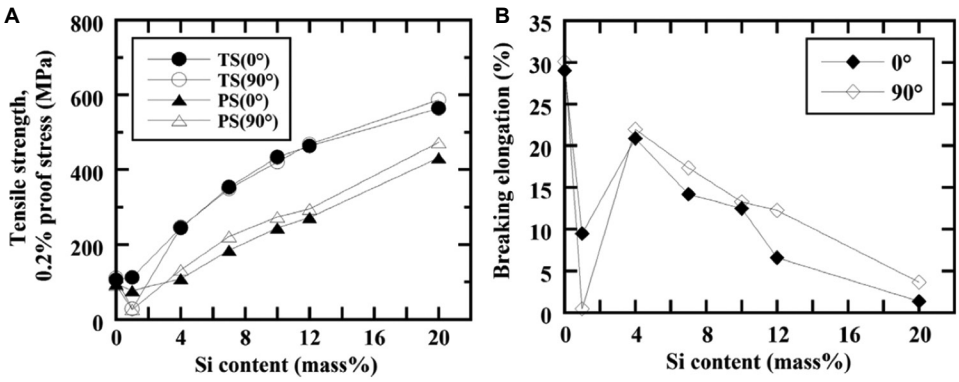

Figure 21. Tensile behavior of laser powder bed fusion-processed Al–xSi alloys: (A) Tensile strength and 0.2% proof stress; (B) breaking elongation. Reproduced from Kimura *et al.*,[89] with permission from Elsevier. Copyright © 2016 Elsevier B.V.

Cu/Zn contents significantly widen the solidification temperature range and deteriorate melt-pool fluidity, making LPBF processing more prone to hot cracking and other solidification defects, and thus leading to poor printability.[11] To overcome this issue, recent alloy-design strategies typically follow two routes. First, Cu and Zn are combined with eutectic-forming elements such as Si or Mg (*e.g.*, Al–Cu–Mg–Si or Si-modified 7xxx systems), so that the terminal eutectic liquid improves feeding and fluidity and reduces hot-cracking susceptibility.[96,97] Second, grain-refining elements or particles such as Zr, Sc, and TiB_2 are added to increase the growth-restriction

factor and provide potent heterogeneous nucleation sites, thereby promoting the formation of equiaxed grains and refining the overall grain structure, which helps to alleviate localized solidification shrinkage and suppress crack initiation.[98-101] When combined with appropriate process optimization, these approaches can largely reconcile high strength with good printability in LPBF-processed high-strength aluminum alloys.[101]

5.2.2. Micro-alloying element addition

5.2.2.1. Classification of micro-alloying elements

Besides the principal alloying elements, micro-alloying elements (<1 wt%) significantly influence the microstructure and mechanical behavior of LPBF-processed aluminum alloys. They affect nucleation and growth during solidification and precipitation during heat treatment, enabling performance beyond conventional alloys. Table 4 summarizes the key micro-alloying elements in LPBF-processed aluminum alloys, together with their main functions, purposes, and mechanisms.[102-104]

5.2.2.2. Solidification control and microstructural features of micro-alloying elements

Scandium (Sc) is a widely used micro-alloying element in LPBF-processed aluminum alloys. Its addition can produce both fine equiaxed grains (FG) and columnar grains (CG) at the microstructural level.[93,105-107] During the early stage of solidification, Al_3Sc precipitates first form along the MPB and act as potent nucleation sites for α-Al grains. At relatively low solidification rates, solute Sc has sufficient time to diffuse and segregate to these regions, producing an ultrafine equiaxed grain zone along the MPB. At high solidification rates and under steep thermal gradients, growth in the melt-pool center follows the heat-flow direction, leading to the formation of CG[108] (Figure 22).

Jia *et al.*[109] investigated Al–Mn–Sc alloys containing various amounts of Sc/Zr. They reported that when the Sc/Zr inoculant level was reduced, the area fraction of coarse CG rose sharply from 28.4% to 78.2%, the mean grain size increased from 0.92 μm to 3.14 μm, and the crystallographic texture became stronger (Figure 23).

5.2.2.3. Improvement in mechanical properties and strengthening mechanisms

This Sc/Zr-induced grain structure, composed of ultrafine FG and refined CG, not only achieves pronounced grain refinement but also markedly improves the mechanical properties. Qbau *et al.*[110] compared LPBF-fabricated AA6061 and AA6061–0.15Sc (Figure 24). The Sc-free AA6061 exhibited brittle fracture, whereas the addition of only 0.15 wt% Sc increased the 0.2% yield strength and ultimate tensile strength to about 300 MPa and 350 MPa, respectively, and raised the elongation to over 30%. For reference, cast AA6061 typically shows yield strength of 60–120 MPa, ultimate tensile strength of 150–250 MPa, and elongation of 12–15%; therefore, the present values are clearly much higher.

Adding Sc in LPBF makes use of the rapid solidification, producing metastable ultrafine microstructures and retaining a high solute level in the matrix, which gives a pronounced strengthening effect. The resulting high strength performance is mainly governed by three mechanisms:[111] (i) Grain-boundary strengthening arises from the ultrafine equiaxed grains (FG region) at the melt pool base, significantly enhancing strength according to the Hall–Petch relationship; (ii) solid–solution strengthening results from increased solubility due to rapid cooling, inducing local lattice distortions that impede dislocation motion; (iii) precipitation strengthening occurs through subsequent heat treatment, precipitating nanoscale, highly coherent $L1_2$ Al_3Sc dispersoids that are sheared by dislocations. Sc addition breaks the typical strength–ductility trade-off, providing both ultrafine grain regions for strength and coarse grain regions that contribute to work hardening and ductility.

5.2.2.4. Micro-alloying elements design trends

Although Sc-based microalloying is highly effective in enhancing the overall performance of LPBF-processed aluminum alloys, Sc itself is expensive and scarce, and the high cost of commercial powders such as Scalmalloy® is widely recognized as one of the main barriers to their large-scale structural use. Consequently, recent alloy-design strategies no longer simply pursue high Sc contents; instead, they reduce the Sc level and add small amounts of Zr, Er, and other minor elements, so that the alloy still

Table 4. Key micro-alloying elements in laser powder bed fusion-processed aluminum alloys[102-104]

Typical elements	Function	Purpose	Mechanism
Sc, Zr, Er	Grain refiners	Refine grains, improve strength and ductility	Promote heterogeneous nucleation; inhibit grain growth
	Precipitation optimizers	Enhance precipitation strengthening	Form coherent Al_3(Sc, Zr) precipitates; stabilize microstructure at high temperature

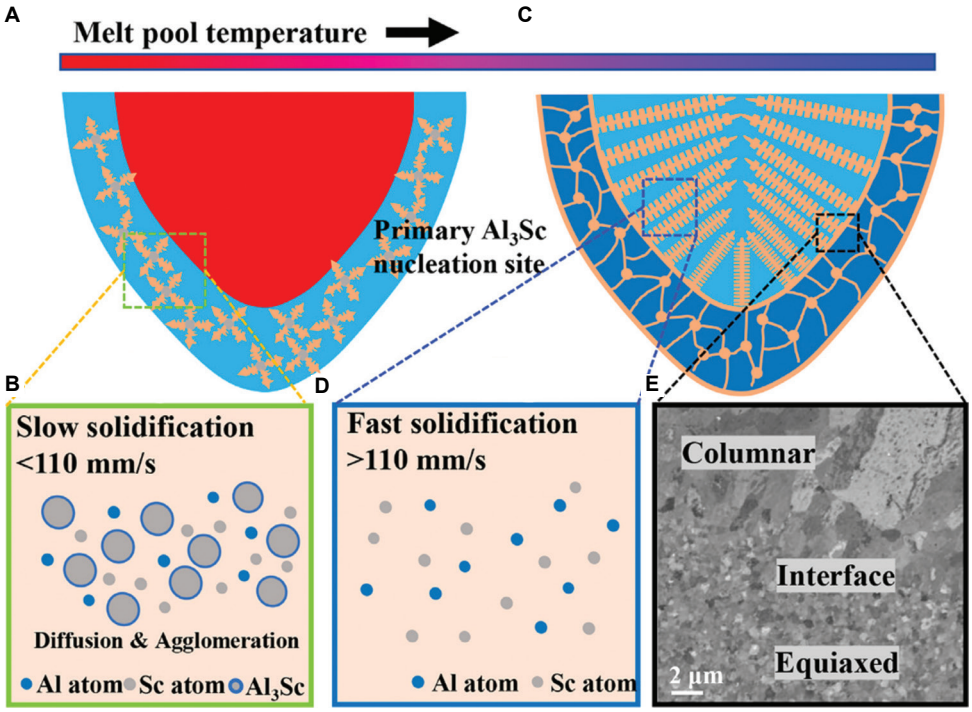

Figure 22. Schematic illustration of the effect of Al_3Sc on solidification in the laser powder bed fusion (LPBF) melt pool. Reproduced from He *et al.*,[108] with permission from Elsevier. Copyright © 2021 Acta Materialia Inc.

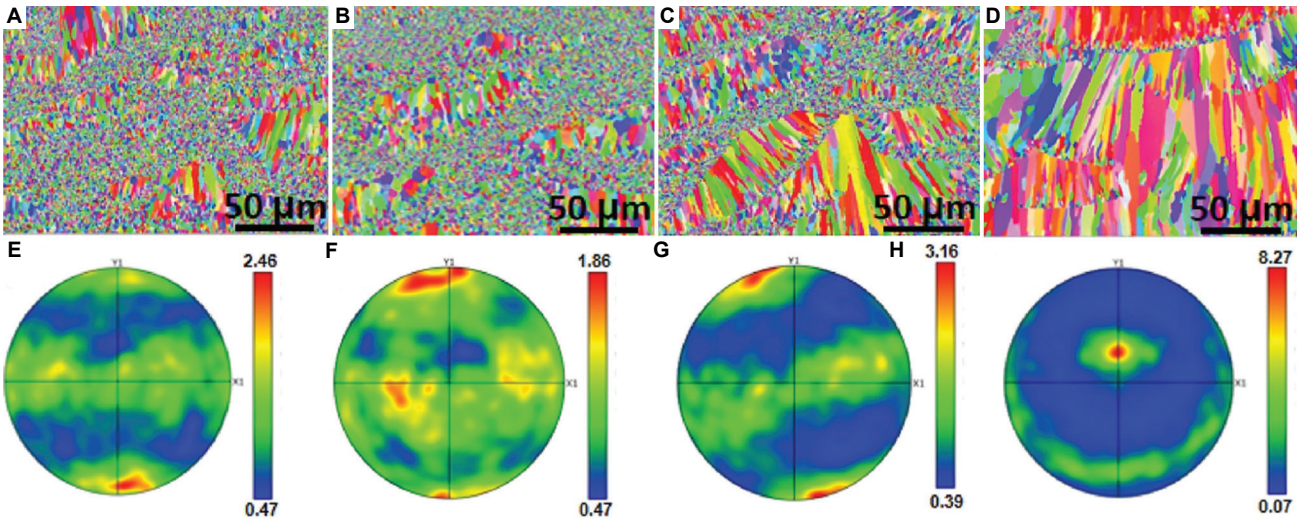

Figure 23. Microstructures of Al–Mn–Sc alloys fabricated using laser powder bed fusion (LPBF). From (A to D), the Sc and Zr contents decrease progressively. (E-H) Corresponding {100} pole figures for the microstructures shown in (a-d), respectively. Reproduced from Jia *et al.*,[109] with permission from Elsevier. Copyright © 2022 Elsevier B.V.

benefits from a fine bimodal grain structure and dispersoid hardening while lowering powder cost.[27,112]

5.2.3. Additives in LPBF-processed aluminum alloys

In the LPBF fabrication of aluminum alloys, the introduction of additives is an effective approach to improve mechanical properties. In recent years, researchers have commonly incorporated ceramic particles or composite additives into powders to achieve grain refinement, enhance strength, and, to some extent, improve toughness and ductility.

5.2.3.1. Overview of additive types and applications

The most frequently used additives include borides, carbides, nitrides, oxides, and hybrid/composite additives.

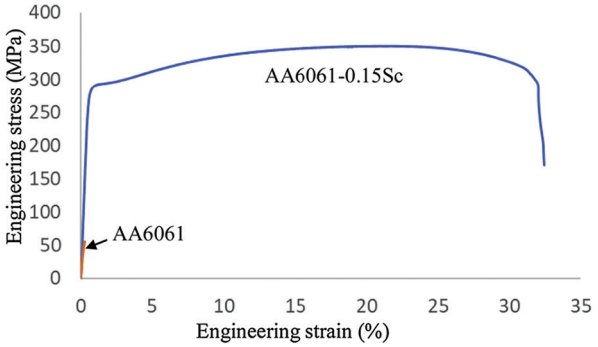

Figure 24. Stress–strain response of the base alloy and AA6061–0.15 scandium specimens. Reproduced from Qbau *et al.*,[110] with permission from Elsevier. Copyright © 2019 Published by Elsevier Ltd on behalf of The Society of Manufacturing Engineers.

Table 5 summarizes representative additives and primary property improvements.[113-125]

5.2.3.2. Strengthening mechanisms and representative additives

Grain-boundary strengthening. TiB_2, CaB_6, LaB_6, and TiN promote heterogeneous nucleation and hold grain boundaries in place, so that submicron grains are obtained, and the flow stress is raised.[113-115,118]

Orowan strengthening. Very fine TiC and SiC particles force dislocations to bow between them (Orowan looping), causing an increase in strength without sacrificing density.[116,117]

Load-bearing strengthening. High-modulus particles such as TiC and SiC can carry part of the applied load during deformation, so the composite shows higher strength and stiffness.[116,117]

Crack deflection/suppression. TiB_2, CaB_6, and Si_3N_4 tend to deflect and bridge growing cracks, lengthening the crack path and improving fracture resistance.[113,115,120]

5.2.3.3. Strategies for additive design

Low-content optimization. Many additives, such as LaB_6 and CaB_6, already give marked grain refinement and strength increases at 0.5–2 wt%, and, because particle clustering is limited, ductility remains acceptable.[114,115]

Nanoscale dispersion. For nanoparticles (TiC, SiC, AlN), good dispersion usually requires ball milling or careful tuning of process parameters; otherwise, they tend to cluster or form ring-like zones along the MPB.[116,117,119]

Composite synergy. Hybrid additions such as TiC+TiH_2 or Ti+B_4C can refine grains and reduce cracking at the same time, so high-strength grades like 2024 reach higher strength without a large loss of elongation.[124,125]

In situ reactions. In Ti–B_4C systems, TiB_2 and TiC are formed *in situ* and bond well to the matrix, but the process window must be controlled to avoid unwanted phases such as Al_4C_3.[127]

By choosing suitable additive types and levels, and combining low additions with nanoscale dispersion, hybrid systems and *in situ* reaction routes, LPBF-processed aluminum alloys can achieve high strength while keeping reasonable ductility. This makes them attractive for lightweight components in aerospace and other demanding applications.

5.3. Post-heat treatment

Besides process optimization and alloy design, post-build heat treatment is a key tool for improving LPBF-processed aluminum parts. Because of the very rapid solidification and steep thermal gradients, as-built material is far from equilibrium: Residual stresses are high, and the matrix contains a supersaturated solid solution, which strongly influences both strength and ductility. Suitable heat treatments can relax these internal stresses and, at the same time, control the formation and evolution of precipitates, so that a more favorable balance between strength and toughness is obtained.

5.3.1. Heat treatment of Al–Si alloys

Experimental studies on LPBF Al–Si alloys report a clear drop in mechanical properties after conventional solution treatment. This decrease is mainly linked to the loss of α-Al supersaturation, breakup of the eutectic Si network, and coarsening of Si particles.[48,128,129] To avoid these problems, alternative routes such as direct aging treatment (T5) and intermediate-temperature annealing are often used.

In the T5 condition, the supersaturated matrix produced directly by LPBF is used as the starting state, and artificial aging at relatively low temperatures is applied to introduce precipitation strengthening. The typical cellular microstructure of LPBF-processed Al–Si alloys is largely retained,[61,130] while both yield strength and ultimate tensile strength increase because of the precipitation of nanoscale Si or Mg_2Si phases.[131] If aging is continued for too long, over-aging occurs: precipitates coarsen, and a slight reduction in ductility is usually observed.[58,130]

Intermediate-temperature annealing, performed between the solutionizing and aging regimes, offers an effective approach to achieving a desirable balance between strength and ductility. Based on a study of an LPBF-processed Al–13.3 wt% Mg_2Si alloy annealed at 200–450°C, Yang *et al.*[132] reported that the as-built microstructure is composed of a nanoscale cellular eutectic Mg_2Si network combined with fine free particles, which collectively deliver robust cell-boundary and precipitation strengthening. When the alloy is annealed at intermediate temperatures,

Table 5. Classification and comparison of additives in LPBF-processed aluminum alloys

Category	Representative compounds	Main enhanced properties	Typical addition level
Borides	TiB_2,[113] LaB_6,[114] CaB_6[115]	Increased strength, improved elongation	TiB_2: 2 wt% (AlSi10Mg); LaB_6: 0.5 wt% (2024); CaB_6: 2 wt.% (2024).
Carbides	TiC,[116] SiC[117]	Higher strength and hardness, moderate ductility	TiC: 2 wt% (Al–Zn–Mg–Cu); SiC: 11.6 wt% (AlSi10Mg).
Nitrides	TiN,[118] AlN,[119,126] Si_3N_4[120]	Improved strength and toughness, crack suppression	TiN: 4 wt% (AlSi10Mg); AlN: 1 wt% (AlSi10Mg); Si_3N_4: 10 vol% (AlSi10Mg).
Oxides	Al_2O_3,[121] Y_2O_3,[122] ZrO_2,[123]	Enhanced strength and hardness	Al_2O_3: 0.25 wt% (AlSi10Mg); Y_2O_3: 0.5 wt% (AlSi10Mg); ZrO_2: 0.3 wt%(AlSi10Mg).
Hybrid/ Composite	Ti+B_4C,[124] TiC+TiH_2[125]	Balanced strength and ductility	Ti+B_4C: 2.5 wt% Ti+0.9 wt% B_4C (6061); TiC+TiH_2: 1 wt% TiC+1 wt% TiH_2 (2024).

Abbreviation: LPBF: Laser powder bed fusion.

this cellular network partly breaks down and additional fine particles precipitate, so the strength decreases slightly while ductility is greatly improved. At higher annealing temperatures, however, over-annealing causes the Mg_2Si particles to coarsen into polygon-like precipitates. As the strengthening effect weakens and stress concentrations increase, both strength and elongation decline (Figure 25).

To visually highlight the differences among post-processing routes for LPBF-processed Al–Si alloys, a comparative schematic is provided in Figure 26. The diagram contrasts the conventional solutionizing–quenching–aging (T6-type) pathway with two LPBF-adapted alternatives—direct aging (T5) and intermediate temperature annealing—while annotating the associated microstructural trends (network decomposition and precipitation) that underpin their distinct mechanical responses.

5.3.2. Heat treatment of other alloys

For non-Al–Si LPBF-processed aluminum alloys, the most common post-heat treatments are solution + aging treatment (T6) and T5, with the choice depending on alloy composition and the as-built microstructural features.

5.3.2.1. T6 treatment

This approach is suitable for alloy systems that require solution treatment to fully dissolve solute atoms into the matrix, followed by aging to precipitate strengthening phases, such as Al–Cu (2xxx) and Al–Zn–Mg (7xxx) alloys.

Al–Cu alloys (2xxx series). Wang *et al.*[133] studied an Al–3.5Cu–1.5Mg–1Si alloy whose as-built microstructure was mainly composed of α-Al and a quaternary Q phase (often reported as $Al_5Mg_8Cu_2Si_6$). After a T6 cycle (766 K for 1 h solution treatment followed by aging at 463 K for 10 h), fine needle-like $Al_2Cu(Mg)$ (S′/θ′) precipitates formed together with dispersed Mg_2Si. With this microstructural change, the yield strength rose from 223 MPa to 368 MPa, whereas the elongation remained at a similar level, changing only slightly from 5.3% to 6.2%.

Al–Zn–Mg alloys (7xxx series). Zhou *et al.*[134] examined a Si- and TiB_2-modified 7xxx alloy subjected to T6 treatment (solution at 490°C for 1 h plus aging at 120°C for 18 h). Following heat treatment, $MgZn_2$ precipitates together with TiB_2 and Si phases were identified, which jointly contribute to strengthening. The yield strength improved to 455 MPa, the ultimate tensile strength to 556 MPa, whereas elongation rose to 4.5%, versus ~350 MPa, ~450 MPa, and ~2.7% before treatment, respectively.

The strengthening mechanism of such alloys is as follows: During solution treatment, high temperatures dissolve solute atoms into a supersaturated solid solution; during aging, intermediate temperatures promote the formation of fine strengthening precipitates, significantly enhancing yield and tensile strength[135] (Figure 27).

5.3.2.2. T5 treatment

For some LPBF-processed aluminum alloys, the rapid solidification during fabrication already produces a highly supersaturated solid solution, making additional solution treatment unnecessary. These alloys can be directly strengthened via T5 aging, such as Al–Mg–Si (6xxx) and Al–Mg–Sc–Zr alloys.

Al–Mg–Si alloys (6xxx series). For an LPBF-processed Al–5Mg_2Si–2Mg alloy, Wang *et al.*[136] reported that a conventional solution treatment followed by aging produced little additional improvement, whereas direct aging at 180°C for 3.5 h yielded the best result. Under this condition, the tensile properties were improved to

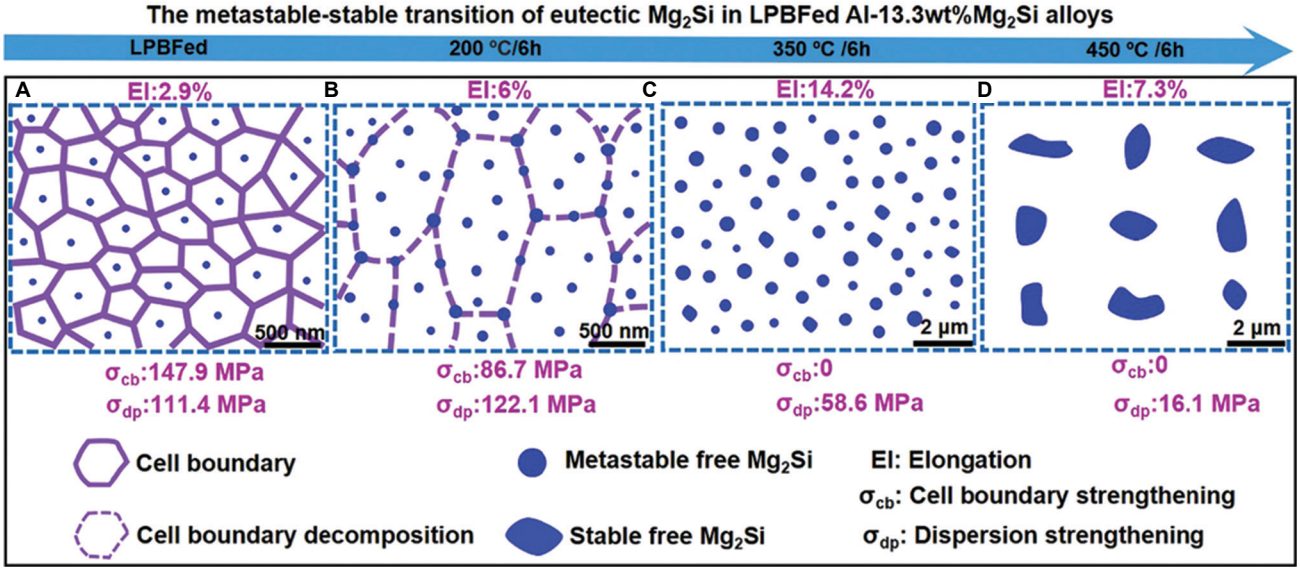

Figure 25. Illustration of the microstructural changes in LPBF-processed Al–13.3 wt% Mg_2Si under different annealing temperatures. Reproduced from Yang *et al.*,[132] with permission from Elsevier. Copyright © 2023 Elsevier B.V.
Abbreviation: LPBF: Laser powder bed fusion.

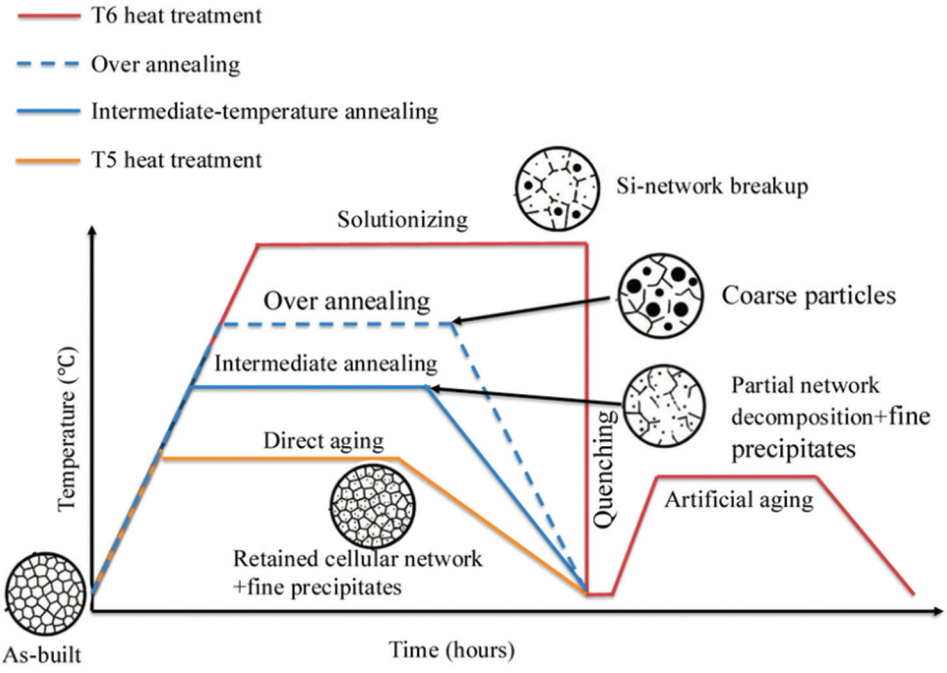

Figure 26. Comparative schematic illustrating typical post-heat-treatment pathways for laser powder bed fusion-processed Al–Si alloys. Image created by the authors.

377 MPa (from 295 MPa) in yield strength, 488 MPa (from 453 MPa) in ultimate tensile strength, and 9.6% (from 9.2%) in elongation.

Al–Mg–Sc–Zr alloys. Ma *et al.*[137] demonstrated that with aging, temperature increasing from 250°C to 350°C, the precipitation rate of Al_3(Sc, Zr) nanoparticles significantly accelerated, leading to continuous strengthening. The tensile strength improved from 362 MPa to 524 MPa, and yield strength from 336 MPa to 520 MPa, though elongation decreased from 11.2% to 3.1%, exhibiting a typical strength–ductility trade-off.

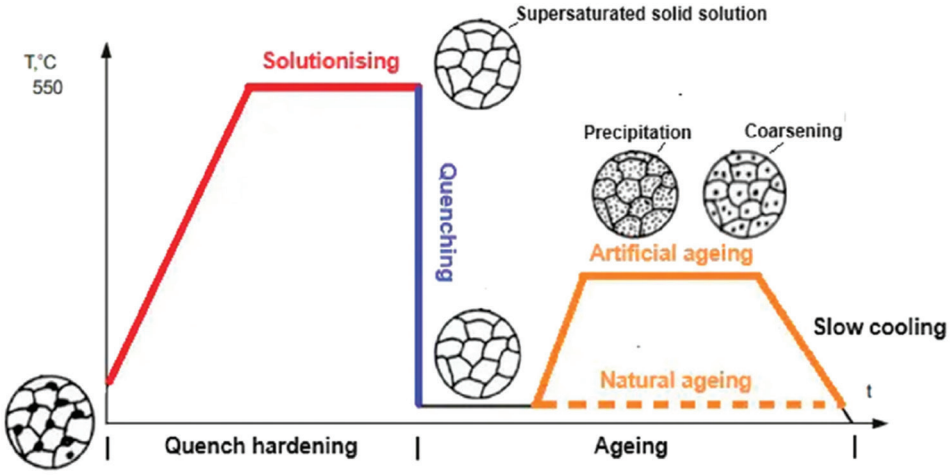

Figure 27. Schematic diagram of the solution and aging process in aluminum alloys. Reproduced from Patil *et al.*[135]

Table 6. Representative post-heat-treatment routes for non-Al–Si laser powder bed fusion -processed aluminum alloys

Alloy family	Representative alloy	Heat treatment route	Typical conditions	References
Al–Cu (2xxx)	Al–3.5Cu–1.5Mg–1Si	T6	Solution 766 K (493°C, 1 h) + aging 463 K (190°C, 10 h)	133
Al–Zn–Mg (7xxx)	Al–5.43Zn–2.65Mg–1.40Cu (Si/TiB_2 modified)	T6	Solution 490°C (1 h) + aging 120°C (18 h)	134
Al–Mg–Si (6xxx)	Al–5Mg_2Si–2Mg	T5	Direct aging 180°C (3.5 h)	136
Al–Mg–Sc–Zr	Al–4.0Mg–0.7Sc–0.4Zr–0.5Mn	T5	Direct aging 350°C (2 h)	137

Representative post-heat-treatment routes and typical temperature ranges reported for different non-Al–Si LPBF alloy families are summarized in Table 6.

5.4. Summary

In summary, high-strength LPBF-processed aluminum alloys can be improved on three levels:

(i) Process control. By tuning parameters such as VED and scan strategy, the solidification rate and thermal gradient can be adjusted, which in turn affect grain size, sub-grain cellular structures, and porosity, giving a tailored as-built microstructure.

(ii) Alloy design. Choosing suitable base compositions and small additions of elements such as Sc and Zr, or introducing ceramic phases (TiB_2, TiC, Al_2O_3, *etc.*), produces fine, well-distributed particles inside grains and along grain boundaries, improving load sharing, blocking dislocations, and refining the grain structure.

(iii) Post-heat treatment. Subsequent heat treatments modify the morphology, size, and distribution of secondary and grain-boundary precipitates, allowing strength and toughness to be adjusted together.

Taken together, these three routes—from processing, to composition, to heat treatment—provide a practical framework for tailoring LPBF-processed high-strength aluminum alloys and guide further alloy and process development.

6. Conclusion and outlook

6.1. Conclusion

This review discusses how melt-pool behavior and subsequent microstructural evolution in LPBF-processed aluminum alloys influence their mechanical performance. Five main contributions to strength are considered: grain-boundary, solid–solution, precipitation, dislocation, and load-bearing strengthening. Together, these mechanisms govern the attainable balance between strength and ductility in LPBF components.

On this basis, three practical classes of strengthening strategies are outlined: (i) Process optimization (*e.g.*, adjusting energy density and scanning strategy) to refine the microstructure and reduce defects; (ii) alloy design to make better use of solid–solution, precipitation, and load-bearing effects; and (iii) post-heat treatments to adjust precipitation behavior and relax residual stresses, so that strength can be increased without an excessive loss of ductility.

Overall, this review establishes a mechanism-based framework that links LPBF-specific microstructures to strengthening mechanisms and transferable strengthening strategies, providing a common reference for the design and manufacture of high-strength LPBF-processed aluminum alloys across different alloy families.

6.2. Outlook

With the deepening understanding of strengthening mechanisms in LPBF-processed aluminum alloys, future research may achieve further progress in the following two directions:

(i) Mechanism-oriented co-design of alloy, process, and heat treatment. Extensive work has already been carried out on microalloying and process-window optimization, but in many cases, the focus remains on "single element + local parameter tuning." Future studies could place more emphasis on mechanism-oriented co-design, in which grain refinement, precipitation strengthening, solid–solution strengthening, and load-bearing phases are treated as combinable "strengthening modules." Under constraints of printability and cost, alloy composition, laser processing parameters, and heat-treatment schedules should be optimized in an integrated manner. For example, the combination of thermodynamic/solidification calculations, precipitation, and microstructure-evolution simulations with targeted experiments may guide the screening and combination of multicomponent microalloying and particle-reinforcement strategies and allow systematic comparison of different strengthening routes. In this way, aluminum alloy systems with better cost–performance balance and process robustness, specifically tailored for LPBF, can be developed.

(ii) Integrated quantitative framework for "microstructure–mechanism–property" relationships. Although quantitative analyses of the five strengthening mechanisms have been reported for several typical alloy systems, they are often limited to case studies on a single material or a narrow process window, and a transferable, broadly applicable framework is still lacking. Building on the existing work, future research could combine *in situ* monitoring, advanced three-dimensional/high-resolution characterization, and mechanical testing to decompose and quantify the relative contributions of grain-boundary, solid–solution, precipitation, dislocation, and load-bearing strengthening across different alloy chemistries and process conditions. Coupling these measurements with multi-scale numerical simulations would enable a more rigorous description of the evolution of melt-pool morphology, grain structure, precipitation behavior, and residual stresses. Embedding such mechanism-resolved quantitative data into physics-informed, data-driven models is expected to yield more reliable "microstructure–strengthening mechanism–macroscopic property" prediction tools, providing computational and transferable guidance for performance optimization and rapid design of LPBF-processed aluminum components.

Acknowledgments

None.

Funding

None.

Conflict of interest

Xiaoming Wang serves as an Editorial Board Member of this journal, but was not in any way involved in the editorial and peer-review process conducted for this paper, directly or indirectly. Separately, other authors declared that they have no known competing financial interests or personal relationships that could have influenced the work reported in this paper.

Author contributions

Conceptualization: Yingming Zhang, Xiaoming Wang
Visualization: Yingming Zhang
Writing–original draft: Yingming Zhang
Writing–review & editing: Tianai Huang, Xin He, Xiaoming Wang

Ethics approval and consent to participate

Not applicable.

Consent for publication

Not applicable.

Availability of data

No new data or code were generated or analyzed in this study. All data supporting this review are available in the cited literature. Data sharing is therefore not applicable.

Further disclosure

During the preparation of this manuscript, the authors used a generative AI language model, ChatGPT (OpenAI), only to improve the readability and language of the text (*e.g.*, grammar checking and polishing of wording). The AI tool

was used under human supervision, and all scientific ideas, analyses, interpretations, and conclusions were developed and verified by the authors, who take full responsibility for the content of this publication.

References

1. Zhang J, Song B, Wei Q, Bourell D, Shi Y. A review of selective laser melting of aluminum alloys: Processing, microstructure, property and developing trends. *J Mater Sci Technol*. 2019;35(2):270-284.

   doi: 10.1016/j.jmst.2018.09.004

2. Gibson I, Rosen D, Stucker B, Khorasani M. Development of additive manufacturing technology. In: Gibson I, Rosen D, Stucker B, Khorasani M, editors. *Additive Manufacturing Technologies*. Cham: Springer International Publishing; 2021. p. 23-51.

3. Majumdar S, Sinha A, Das A, Datta P, Nag D. An insight view of evolution of advanced aluminum alloy for aerospace and automotive industry: Current status and future prospects. *J Inst Eng (India) Series D*. 2024.

   doi: 10.1007/s40033-024-00852-z

4. Zhang H, Ni DR, Xiao BL, Liu FC, Ma ZY. Recent progress of aluminum alloys and aluminum matrix composites produced via laser powder bed fusion: A review. *J Mater Sci*. 2024;59(22):9857-9891.

   doi: 10.1007/s10853-024-09368-z

5. Sharma SK, Grewal HS, Saxena KK, *et al*. Advancements in the additive manufacturing of magnesium and aluminum alloys through laser-based approach. *Materials (Basel)*. 2022;15(22):8122.

   doi: 10.3390/ma15228122

6. Aboulkhair NT, Simonelli M, Parry L, Ashcroft I, Tuck C, Hague R. 3D printing of aluminium alloys: Additive manufacturing of aluminium alloys using selective laser melting. *Prog Mater Sci*. 2019;106:100578.

   doi: 10.1016/j.pmatsci.2019.100578

7. Kotadia HR, Gibbons G, Das A, Howes PD. A review of laser powder bed fusion additive manufacturing of aluminium alloys: Microstructure and properties. *Addit Manuf*. 2021;46:102155.

   doi: 10.1016/j.addma.2021.102155

8. Zhao L, Song L, Santos Macías JG, *et al*. Review on the correlation between microstructure and mechanical performance for laser powder bed fusion AlSi10Mg. *Addit Manuf*. 2022;56:102914.

   doi: 10.1016/j.addma.2022.102914

9. Kumar Ramavajjala A, Dandekar TR, Khatirkar RK, Joshi C, Chouhan RN, Agnihotri A. A review on the correlation between microstructure, heat treatment and mechanical properties of additively manufactured AlSi10Mg by LPBF. *Crit Rev Solid State Mater Sci*. 2025;50(3):239-274.

   doi: 10.1080/10408436.2024.2414012

10. Liu Y, Li Y, Wang M, Chen Z. Review of laser powder bed fusion's microstructure and mechanical characteristics for Al-Ce alloys. *Materials*. 2024;17(20):5085.

    doi: 10.3390/ma17205085

11. Rometsch PA, Zhu Y, Wu X, Huang A. Review of high-strength aluminium alloys for additive manufacturing by laser powder bed fusion. *Mater Des*. 2022;219:110779.

    doi: 10.1016/j.matdes.2022.110779

12. Dixit S, Liu S. Laser additive manufacturing of high-strength aluminum alloys: Challenges and strategies. *J Manuf Mater Process*. 2022;6(6):156.

    doi: 10.3390/jmmp6060156

13. Qin H, Fallah V, Dong Q, Brochu M, Daymond MR, Gallerneault M. Solidification pattern, microstructure and texture development in laser powder bed fusion (LPBF) of Al10SiMg alloy. *Mater Charact*. 2018;145:29-38.

    doi: 10.1016/j.matchar.2018.08.025

14. Gong J, Wei K, Liu M, Song W, Li X, Zeng X. Microstructure and mechanical properties of AlSi10Mg alloy built by laser powder bed fusion/direct energy deposition hybrid laser additive manufacturing. *Addit Manuf*. 2022;59:103160.

    doi: 10.1016/j.addma.2022.103160

15. Wang X, Li A, Liu X. Fabrication of orientated micro porous metals: Control the melting process of powders by high scanning speed - ultra short hatch spacing scanning strategy. *Mater Lett*. 2023;335:133741.

    doi: 10.1016/j.matlet.2022.133741

16. Thijs L, Kempen K, Kruth JP, Van Humbeeck J. Fine-structured aluminium products with controllable texture by selective laser melting of pre-alloyed AlSi10Mg powder. *Acta Mater*. 2013;61(5):1809-1819.

    doi: 10.1016/j.actamat.2012.11.052

17. Ellendt N, Fabricius F, Toenjes A. Poreanalyzer-an open-source framework for the analysis and classification of defects in additive manufacturing. *Appl Sci*. 2021;11(13):6086.

    doi: 10.3390/app11136086

18. Leung CLA, Marussi S, Towrie M, *et al*. Laser-matter interactions in additive manufacturing of stainless steel SS316L and 13-93 bioactive glass revealed by *in situ* X-ray imaging. *Addit Manuf*. 2018;24:647-657.

    doi: 10.1016/j.addma.2018.08.025

19. Zhao C, Shi B, Chen S, *et al*. Laser melting modes in metal powder bed fusion additive manufacturing. *Rev Modern Phys*. 2022;94(4):045002.

    doi: 10.1103/RevModPhys.94.045002

20. Fan H, Hu J, Wang Y, *et al*. A review of laser additive manufacturing (LAM) aluminum alloys: Methods, microstructures and mechanical properties. *Opt Laser Technol*. 2024;175:110722.

doi: 10.1016/j.optlastec.2024.110722

21. Leis A, Weber R, Graf T. Process window for highly efficient laser-based powder bed fusion of AlSi10Mg with reduced pore formation. *Materials (Basel)*. 2021;14(18):5255.

doi: 10.3390/ma14185255

22. Kramer S, Wexel H, Purwitasari A, Jarwitz M, Schulze V, Zanger F. Impact of different pore types on the tensile and fatigue properties of AlSi10Mg parts produced by laser powder bed fusion. *Prog Addit Manuf*. 2025;10(12): 11305-11317.

doi: 10.1007/s40964-025-01288-x

23. Wang X, Zhang D, Li A, Yi D, Li T. A review on traditional processes and laser powder bed fusion of aluminum alloy microstructures, mechanical properties, costs, and applications. *Materials*. 2024;17(11):2553.

doi: 10.3390/ma17112553

24. Zhu Z, Hu Z, Ng FL, Seet HL, Nai SML. Extending the mechanical property regime of laser powder bed fusion Sc- and Zr-modified Al6061 alloy by manipulating process parameters and heat treatment. *Addit Manuf*. 2024;85:104164.

doi: 10.1016/j.addma.2024.104164

25. Liang Y, Han Q, Sui Z, *et al*. Laser powder bed fusion of high-strength crack-free Al7075 alloy with the in-situ formation of TiB2/Al3Ti-reinforced phases and nucleation agents. *Composites Part B Eng*. 2025;289:111940.

doi: 10.1016/j.compositesb.2024.111940

26. Yuan C, Ding R, Hou X, Guo Q, Gao X. Laser powder bed fusion of crack-free 6061Al alloy using nano-sized TiO2 modified powders. *Mater Sci Technol*. 2024;40(2):141-151.

doi: 10.1177/02670836231212808

27. Lu Y, Zhang H, Xue P, *et al*. Microstructural evaluation and tensile properties of Al-Mg-Sc-Zr alloys prepared by LPBF. *Crystals*. 2023;13(6):913.

doi: 10.3390/cryst13060913

28. Song CR, Dong BX, Zhang SY, *et al*. Recent progress of Al-Mg alloys: Forming and preparation process, microstructure manipulation and application. *J Mater Res Technol*. 2024;31:3255-3286.

doi: 10.1016/j.jmrt.2024.07.051

29. Trivedi R, Kurz W. Solidification microstructures: A conceptual approach. *Acta Metallurg Mater*. 1994;42(1): 15-23.

doi: 10.1016/0956-7151(94)90044-2

30. Chouhan A, Mädler L, Ellendt N. Modeling of rapid solidification in laser powder bed fusion processes. *Comput Mater Sci*. 2024;238:112918.

doi: 10.1016/j.commatsci.2024.112918

31. Morris LR, Winegard WC. The cell to dendrite transition. *J C Growth*. 1969;6(1):61-66.

doi: 10.1016/0022-0248(69)90093-1

32. Kim G, Takaki T, Shibuta Y, Sakane S, Matsuura K, Ohno M. A parametric study of morphology selection in equiaxed dendritic solidification. *Comput Mater Sci*. 2019;162:76-81.

doi: 10.1016/j.commatsci.2019.02.027

33. Rasch M, Heberle J, Dechet MA, *et al*. Grain structure evolution of al-cu alloys in powder bed fusion with laser beam for excellent mechanical properties. *Materials*. 2019;13(1):82.

doi: 10.3390/ma13010082

34. Van Cauwenbergh P, Samaee V, Thijs L, *et al*. Unravelling the multi-scale structure-property relationship of laser powder bed fusion processed and heat-treated AlSi10Mg. *Sci Rep*. 2021;11(1):6423.

doi: 10.1038/s41598-021-85047-2

35. Mair P, Braun J, Kaserer L, *et al*. Unique microstructure evolution of a novel Ti-modified Al-Cu alloy processed using laser powder bed fusion. *Mater Today Commun*. 2022;31:103353.

doi: 10.1016/j.mtcomm.2022.103353

36. Guan RG, Tie D. A review on grain refinement of aluminum alloys: Progresses, challenges and prospects. *Acta Metall Sin (Engl Lett)*. 2017;30(5):409-432.

doi: 10.1007/s40195-017-0565-8

37. Wang Q, Li Z, Pang S, Li X, Dong C, Liaw PK. Coherent precipitation and strengthening in compositionally complex alloys: A review. *Entropy (Basel)*. 2018;20(11):878.

doi: 10.3390/e20110878

38. Kube CM. Elastic anisotropy of crystals. *AIP Adv*. 2016;6(9):095209.

doi: 10.1063/1.4962996

39. Hull D, Bacon DJ. *Introduction to Dislocations*. Netherlands: Elsevier; 2011.

40. McElroy R, Szkopiak Z. Dislocation-substructure-strengthening and mechanical-thermal treatment of metals. *Int Metallurgr Rev*. 1972;17(1):175-202.

doi: 10.1179/imtlr.1972.17.1.175

41. Li G, Brodu E, Soete J, *et al*. Exploiting the rapid solidification potential of laser powder bed fusion in high strength and crack-free Al-Cu-Mg-Mn-Zr alloys. *Addit Manuf*. 2021;47:102210.

doi: 10.1016/j.addma.2021.102210

42. Zhang X, Zhang X, Liu W, Jiang A, Long Y. Towards understanding formation mechanism of cellular structures in laser powder bed fused AlSi10Mg. *Materials (Basel)*. 2024;17(9):2121.

doi: 10.3390/ma17092121

43. Eom YS, Park JM, Choi JW, *et al*. Fine-tuning of mechanical properties of additively manufactured AlSi10Mg alloys by controlling the microstructural heterogeneity. *J Alloys Compd*. 2023;956:170348.

doi: 10.1016/j.jallcom.2023.170348

44. Shen Z, Wagoner R, Clark W. Dislocation and grain boundary interactions in metals. *Acta Metallurg*. 1988;36(12): 3231-3242.

doi: 10.1016/0001-6160(88)90058-2

45. Hansen N. Hall-petch relation and boundary strengthening. *Scrip Mater*. 2004;51(8):801-806.

doi: 10.1016/j.scriptamat.2004.06.002

46. Lasalmonie A, Strudel J. Influence of grain size on the mechanical behaviour of some high strength materials. *J Mater Sci*. 1986;21(6):1837-1852.

doi: 10.1007/BF00547918

47. Snopiński P, Kotoul M, Petruška J, Rusz S, Żaba K, Hilšer O. Revealing the strengthening contribution of stacking faults, dislocations and grain boundaries in severely deformed LPBF AlSi10Mg alloy. *Sci Rep.* 2023;13(1):16166.

doi: 10.1038/s41598-023-43448-5

48. Fiocchi J, Tuissi A, Biffi CA. Heat treatment of aluminium alloys produced by laser powder bed fusion: A review. *Mater Des*. 2021;204:109651.

doi: 10.1016/j.matdes.2021.109651

49. Knoop D, Lutz A, Mais B, Von Hehl A. A tailored AlSiMg alloy for laser powder bed fusion. *Metals*. 2020;10(4):514.

doi: 10.3390/met10040514

50. Collings E. *Physics of Solid Solution Strengthening*. Berlin: Springer Science and Business Media; 2012.

51. Fleischer RL. Substitutional solution hardening. *Acta Metallurgica*. 1963;11(3):203-209.

doi: 10.1016/0001-6160(63)90213-X

52. Labusch R. A statistical theory of solid solution hardening. *Phys Status Solidi*. 1970;41(2):659-669.

doi: 10.1002/pssb.19700410221

53. Haché MJR, Cheng C, Zou Y. Nanostructured high-entropy materials. *J Mater Res*. 2020;35(8):1051-1075.

doi: 10.1557/jmr.2020.33

54. Zhu Z, Ng FL, Seet HL, *et al*. Superior mechanical properties of a selective-laser-melted AlZnMgCuScZr alloy enabled by a tunable hierarchical microstructure and dual-nanoprecipitation. *Mater Today*. 2022;52:90-101.

doi: 10.1016/j.mattod.2021.11.019

55. Li Q, Li G, Lin X, *et al*. Development of a high strength Zr/Sc/Hf-modified Al-Mn-Mg alloy using laser powder bed fusion: Design of a heterogeneous microstructure incorporating synergistic multiple strengthening mechanisms. *Addit Manuf*. 2022;57:102967.

doi: 10.1016/j.addma.2022.102967

56. Schuster M, De Luca A, Mathur A, Hosseini E, Leinenbach C. Precipitation in a 2xxx series Al-Cu-Mg-Zr alloy fabricated by laser powder bed fusion. *Mater Des*. 2021;211:110131.

doi: 10.1016/j.matdes.2021.110131

57. Keerthipalli T, Aepuru R, Biswas A. Review on precipitation, intermetallic and strengthening of aluminum alloys. *Proc Instit Mech Eng Part B J Eng Manuf*. 2023;237(6-7):833-850.

doi: 10.1177/09544054221111901

58. Megahed S, Bühring J, Duffe T, Bach A, Schröder KU, Schleifenbaum JH. Effect of heat treatment on ductility and precipitation size of additively manufactured AlSi10Mg. *Metals*. 2022;12(8):1311.

doi: 10.3390/met12081311

59. Ardell AJ. Precipitation hardening. *Metallur Trans A*. 1985;16(12):2131-2165.

doi: 10.1007/BF02670416

60. Smallman RE, Ngan AHW. Mechanical properties II - strengthening and toughening. In: Smallman RE, Ngan AHW, editors. *Physical Metallurgy and Advanced Materials Engineering*. 7th ed. Ch. 7., Oxford: Butterworth-Heinemann; 2007. p. 385-446.

61. Maeshima T, Oh-Ishi K, Kadoura H. Microstructural evolution and hardening phenomenon caused by aging of AlSi10Mg alloy by laser powder bed fusion. *Heliyon*. 2024;10(6):e28006.

doi: 10.1016/j.heliyon.2024.e28006

62. Chung H, Choi WS, Jun H, *et al*. Doubled strength and ductility via maraging effect and dynamic precipitate transformation in ultrastrong medium-entropy alloy. *Nat Commun*. 2023;14(1):145.

doi: 10.1038/s41467-023-35863-z

63. Kempf A, Hilgenberg K. Influence of sub-cell structure on the mechanical properties of AlSi10Mg manufactured by laser powder bed fusion. *Mater Sci Eng A*. 2020;776:138976.

doi: 10.1016/j.msea.2020.138976

64. Narutani T, Takamura J. Grain-size strengthening in terms of dislocation density measured by resistivity. *Acta Metallurgica Mater*. 1991;39(8):2037-2049.

doi: 10.1016/0956-7151(91)90173-X

65. Mughrabi H. On the current understanding of strain gradient plasticity. *Mater Sci Eng A*. 2004;387-389:209-213.

doi: 10.1016/j.msea.2004.01.086

66. Ashby MF. The deformation of plastically non-homogeneous materials. *Philos Magazine A J Theor Exp Appl Phys*. 1970;21(170):399-424.

doi: 10.1080/14786437008238426

67. Arsenlis A, Parks DM. Crystallographic aspects of geometrically-necessary and statistically-stored dislocation density. *Acta Materialia*. 1999;47(5):1597-1611.

doi: 10.1016/S1359-6454(99)00020-8

68. Nye JF. Some geometrical relations in dislocated crystals. *Acta Metallurgica*. 1953;1(2):153-162.

doi: 10.1016/0001-6160(53)90054-6

69. Hyer H, Zhou L, Park S, *et al*. Understanding the laser powder bed fusion of AlSi10Mg alloy. *Metallogr Microstruct Anal*. 2020;9(4):484-502.

doi: 10.1007/s13632-020-00659-w

70. Xiao Z, Yu W, Fu H, Deng Y, Wu Y, Zheng H. Recent progress on microstructure manipulation of aluminium alloys manufactured via laser powder bed fusion. *Virtual Phys Prototyp*. 2023;18(1):e2125880.

doi: 10.1080/17452759.2022.2125880

71. Liu H, Gu D, Xi L, *et al*. High-performance aluminum-based materials processed by laser powder bed fusion: Process, microstructure, defects and properties coordination. *Addit Manuf Front*. 2024;3(2):200145.

doi: 10.1016/j.amf.2024.200145

72. Yu Z, Tan Z, Xu R, *et al*. Enhanced load transfer by designing mechanical interfacial bonding in carbon nanotube reinforced aluminum composites. *Carbon*. 2019;146: 155-161.

doi: 10.1016/j.carbon.2019.01.108

73. Harris B. *Engineering Composite Materials*. India: Institute of Materials; 1999.

74. Minasyan T, Hussainova I. Laser powder-bed fusion of ceramic particulate reinforced aluminum alloys: A review. *Materials (Basel)*. 2022;15(7):2467.

doi: 10.3390/ma15072467

75. Ji X, Li S, Liu H, *et al*. Process optimization of sic-reinforced aluminum matrix composites prepared using laser powder bed fusion and the effect of particle morphology on performance. *Materials (Basel)*. 2024;17(5):1187.

doi: 10.3390/ma17051187

76. Sun T, Chen J, Wu Y, *et al*. Achieving excellent strength of the LPBF additively manufactured Al-Cu-Mg composite via *in-situ* mixing TiB2 and solution treatment. *Mater Sci Eng A*. 2022;850:143531.

doi: 10.1016/j.msea.2022.143531

77. Yang T, Liu T, Liao W, *et al*. Laser powder bed fusion of AlSi10Mg: Influence of energy intensities on spatter and porosity evolution, microstructure and mechanical properties. *J Alloys Compd*. 2020;849:156300.

doi: 10.1016/j.jallcom.2020.156300

78. Headley CV, Herrera Del Valle RJ, Ma J, *et al*. The development of an augmented machine learning approach for the additive manufacturing of thermoelectric materials. *J Manuf Process*. 2024;116:165-175.

doi: 10.1016/j.jmapro.2024.02.045

79. Vaudreuil S, Bencaid SE, Vanaei HR, El Magri A. Effects of power and laser speed on the mechanical properties of AlSi7Mg0.6 manufactured by laser powder bed fusion. *Mater (Basel)*. 2022;15(23):8640.

doi: 10.3390/ma15238640

80. Defanti S, Cappelletti C, Gatto A, Tognoli E, Fabbri F. Boosting productivity of laser powder bed fusion for AlSi10Mg. *J Manuf Mater Process*. 2022;6(5):112.

doi: 10.3390/jmmp6050112

81. Jatti VS, Saiyathibrahim A, Murali Krishnan R, Jatti AV, Suganya Priyadharshini G, Mohan DG. Investigating the effect of volumetric energy density on tensile characteristics of as-built and heat-treated AlSi10Mg alloy fabricated by laser powder bed fusion. *Adv Eng Mater*. 2025;27(4):2401924.

doi: 10.1002/adem.202401924

82. Shrestha S, Chou K. Formation of keyhole and lack of fusion pores during the laser powder bed fusion process. *Manuf Lett*. 2022;32:19-23.

doi: 10.1016/j.mfglet.2022.01.005

83. Shrestha S, Chou YK. A Numerical Study on the Keyhole Formation During Laser Powder Bed Fusion Process. In: *ASME Manufacturing Science and Engineering Conference (MSEC2019)*; 2019. Erie, PA, USA. Paper No. MSEC2019-2987.

doi: 10.1115/MSEC2019-2987

84. Wang J, Zhu R, Liu Y, Zhang L. Understanding melt pool characteristics in laser powder bed fusion: An overview of single- and multi-track melt pools for process optimization. *Adv Powder Mater*. 2023;2(4):100137.

doi: 10.1016/j.apmate.2023.100137

85. Dai D, Gu D, Zhang H, *et al*. Influence of scan strategy and molten pool configuration on microstructures and tensile properties of selective laser melting additive manufactured aluminum based parts. *Opt Laser Technol*. 2018;99:91-100.

doi: 10.1016/j.optlastec.2017.08.015

86. Zhang H, Gu D, Dai D. Laser printing path and its

influence on molten pool configuration, microstructure and mechanical properties of laser powder bed fusion processed rare earth element modified Al-Mg alloy. *Virtual Phys Prototyp*. 2022;17(2):308-328.

doi: 10.1080/17452759.2022.2036530

87. Takata N, Kodaira H, Sekizawa K, Suzuki A, Kobashi M. Change in microstructure of selectively laser melted AlSi10Mg alloy with heat treatments. *Mater Sci Eng A*. 2017;704:218-228.

doi: 10.1016/j.msea.2017.08.029

88. Lin CW, Hung FY, Lui TS. Microstructure evolution and microstructural characteristics of Al-Mg-Si aluminum alloys fabricated by a modified strain-induced melting activation process. *Metals*. 2018;8(1):3.

doi: 10.3390/met8010003

89. Kimura T, Nakamoto T, Mizuno M, Araki H. Effect of silicon content on densification, mechanical and thermal properties of Al-xSi binary alloys fabricated using selective laser melting. *Mater Sci Eng A*. 2017;682:593-602.

doi: 10.1016/j.msea.2016.11.059

90. Takata N, Liu M, Kodaira H, Suzuki A, Kobashi M. Anomalous strengthening by supersaturated solid solutions of selectively laser melted Al-Si-based alloys. *Addit Manuf*. 2020;33:101152.

doi: 10.1016/j.addma.2020.101152

91. Xi L, Li Z, Qi S, *et al*. Formation and influence mechanism of metal vapor on the powder spatter and denudation in laser additive manufacturing of Al alloys. *J Phys D Appl Phys*. 2025;58(24):245102.

doi: 10.1088/1361-6463/addad3

92. Wang D, Feng Y, Liu L, *et al*. Influence mechanism of process parameters on relative density, microstructure, and mechanical properties of low sc-content al-mg-sc-zr alloy fabricated by selective laser melting. *Chin J Mech Eng Addit Manuf Front*. 2022;1(4):100034.

doi: 10.1016/j.cjmeam.2022.100034

93. Spierings AB, Dawson K, Heeling T, *et al*. Microstructural features of Sc- and Zr-modified Al-Mg alloys processed by selective laser melting. *Mater Des*. 2017;115:52-63.

doi: 10.1016/j.matdes.2016.11.040

94. Belelli F, Casati R, Andrianopoli C, Cuccaro F, Vedani M. Investigation and characterization of an Al-Mg-Zr-Sc alloy with reduced Sc content for laser powder bed fusion. *J Alloys Compd*. 2022;924:166519.

doi: 10.1016/j.jallcom.2022.166519

95. Ekubaru Y, Gokcekaya O, Ishimoto T, *et al*. Excellent strength-ductility balance of Sc-Zr-modified Al-Mg alloy by tuning bimodal microstructure via hatch spacing in laser powder bed fusion. *Mater Des*. 2022;221:110976.

doi: 10.1016/j.matdes.2022.110976

96. Wang QZ, Kang N, Lin X, *et al*. On the Si-induced microstructure evolution, solidification cracking healing and strengthening behavior of laser powder bed fusion additive manufactured Al-Cu-Mg/Si alloys. *J Mater Process Technol*. 2023;313:117860.

doi: 10.1016/j.jmatprotec.2023.117860

97. Aversa A, Marchese G, Manfredi D, *et al*. Laser powder bed fusion of a high strength Al-Si-Zn-Mg-Cu alloy. *Metals*. 2018;8(5):300.

doi: 10.3390/met8050300

98. Mair P, Kaserer L, Braun J, Weinberger N, Letofsky-Papst I, Leichtfried G. Microstructure and mechanical properties of a TiB2-modified Al-Cu alloy processed by laser powder-bed fusion. *Mater Sci Eng A*. 2021;799:140209.

doi: 10.1016/j.msea.2020.140209

99. Yu W, Xiao Z, Zhang X, *et al*. Processing and characterization of crack-free 7075 aluminum alloys with elemental Zr modification by laser powder bed fusion. *Mater Sci Addit Manuf*. 2022;1(1):4.

doi: 10.18063/msam.v1i1.4

100. Yang T, Chen X, Liu T, *et al*. Crack-free high-strength AA-7075 fabricated by laser powder bed fusion with inoculations of metallic glass powders. *Mater Sci Eng A*. 2024;891:145916.

doi: 10.1016/j.msea.2023.145916

101. Uba CU, Ding H, Chen Y, Guo S, Raush JR. Enhancing the printability of laser powder bed fusion-processed aluminum 7xxx series alloys using grain refinement and eutectic solidification strategies. *Materials*. 2025;18(22):5089.

doi: 10.3390/ma18225089

102. Gao Z, Li H, Lai Y, Ou Y, Li D. Effects of minor Zr and Er on microstructure and mechanical properties of pure aluminum. *Mater Sci Eng A*. 2013;580:92-98.

doi: 10.1016/j.msea.2013.05.035

103. Spierings AB, Dawson K, Kern K, Palm F, Wegener K. SLM-processed Sc- and Zr- modified Al-Mg alloy: Mechanical properties and microstructural effects of heat treatment. *Mater Sci Eng A*. 2017;701:264-273.

doi: 10.1016/j.msea.2017.06.089

104. Zhang X, Le Q, Zhao D, *et al*. Research status and prospect of grain refinement in aluminum alloy. *J Mater Res Technol*. 2025;34:1880-1893.

doi: 10.1016/j.jmrt.2024.12.205

105. Shi Y, Yang K, Kairy SK, Palm F, Wu X, Rometsch PA. Effect of platform temperature on the porosity, microstructure and mechanical properties of an Al-Mg-Sc-Zr alloy fabricated by selective laser melting. *Mater Sci Eng A*. 2018;732:41-52.

doi: 10.1016/j.msea.2018.06.049

106. Jia Q, Rometsch P, Cao S, Zhang K, Wu X. Towards a high strength aluminium alloy development methodology for selective laser melting. *Mater Des*. 2019;174:107775.

doi: 10.1016/j.matdes.2019.107775

107. Wang Z, Lin X, Kang N, *et al*. Laser powder bed fusion of high-strength Sc/Zr-modified Al-Mg alloy: Phase selection, microstructural/mechanical heterogeneity, and tensile deformation behavior. *J Mater Sci Technol*. 2021;95:40-56.

doi: 10.1016/j.jmst.2021.03.069

108. He P, Webster RF, Yakubov V, *et al*. Fatigue and dynamic aging behavior of a high strength Al-5024 alloy fabricated by laser powder bed fusion additive manufacturing. *Acta Materialia*. 2021;220:117312.

doi: 10.1016/j.actamat.2021.117312

109. Jia Q, Lu C, Yan Y, *et al*. Tensile deformation behaviors of laser powder bed fusion fabricated Al-Mn-Sc alloy with heterogeneous grain structure. *Mater Sci Eng A*. 2022;849:143447.

doi: 10.1016/j.msea.2022.143447

110. Qbau N, Nam ND, Ca NX, Hien NT. The crack healing effect of scandium in aluminum alloys during laser additive manufacturing. *J Manuf Process*. 2020;50:241-246.

doi: 10.1016/j.jmapro.2019.12.050

111. Zhang H, Zhang LC, Liu H, *et al*. Strong and ductile Al-Mn-Mg-Sc-Zr alloy achieved in fabrication-rate enhanced laser powder bed fusion. *Virtual Phys Prototyp*. 2023;18(1):e2250769.

doi: 10.1080/17452759.2023.2250769

112. Guo Y, Wei W, Shi W, *et al*. Microstructure and mechanical properties of Al-Mg-Mn-Er-Zr alloys fabricated by laser powder bed fusion. *Mater Des*. 2022;222:111064.

doi: 10.1016/j.matdes.2022.111064

113. Xiao Y, Chen H, Bian Z, *et al*. Enhancing strength and ductility of AlSi10Mg fabricated by selective laser melting by TiB2 nanoparticles. *J Mater Sci Technol*. 2022;109:254-266.

doi: 10.1016/j.jmst.2021.08.030

114. Yao Z, Xie Z. Verification of the laser powder bed fusion performance of 2024 aluminum alloys modified using nano-LaB(6). *Materials (Basel)*. 2024;17(13):3367.

doi: 10.3390/ma17133367

115. Mair P, Goettgens VS, Rainer T, *et al*. Laser powder bed fusion of nano-CaB6 decorated 2024 aluminum alloy. *J Alloys Compd*. 2021;863:158714.

doi: 10.1016/j.jallcom.2021.158714

116. Liu X, Liu Y, Wang S, Du N, Yang S, Zhang B. Microstructure and mechanical properties of TiC-modified Al-Zn-Mg-Cu aluminum alloys fabricated by laser powder bed fusion. *Mater Sci Eng A*. 2025;944:148878.

doi: 10.1016/j.msea.2025.148878

117. Chen Y, Ren Y, Li K, Dang B, Jian Z. Laser powder bed fusion of oxidized microscale SiC-particle-reinforced AlSi10Mg matrix composites: Microstructure, porosity, and mechanical properties. *Mater Sci Eng A*. 2023;870:144860.

doi: 10.1016/j.msea.2023.144860

118. Gao C, Wu W, Shi J, Xiao Z, Akbarzadeh A. Simultaneous enhancement of strength, ductility, and hardness of TiN/AlSi10Mg nanocomposites via selective laser melting. *Addit Manuf*. 2020;34:101378.

doi: 10.1016/j.addma.2020.101378

119. Dai D, Gu D, Xia M, *et al*. Melt spreading behavior, microstructure evolution and wear resistance of selective laser melting additive manufactured AlN/AlSi10Mg nanocomposite. *Surf Coat Technol*. 2018;349:279-288.

doi: 10.1016/j.surfcoat.2018.05.072

120. Miao K, Zhou H, Gao Y, Deng X, Lu Z, Li D. Laser powder-bed-fusion of Si3N4 reinforced AlSi10Mg composites: Processing, mechanical properties and strengthening mechanisms. *Mater Sci Eng A*. 2021;825:141874.

doi: 10.1016/j.msea.2021.141874

121. Vasilev AA, Dzidziguri EL, Sivakova AO, *et al*. Laser powder bed fusion of AlSi10Mg alloy reinforced with Al2O3-CNF nanocomposite. *Ceram Int*. 2025;51(1):636-649.

doi: 10.1016/j.ceramint.2024.11.042

122. Zhang F, Zhang Z, Gu Q, *et al*. Microstructure and mechanical properties of nanoparticulate Y(2)O(3) modified AlSi10Mg alloys manufactured by selective laser melting. *Materials (Basel)*. 2023;16(3):1222.

doi: 10.3390/ma16031222

123. Sun M, Yang Z, Zhang J, *et al*. Effects of ZrO2 nanoparticles on the microstructure and mechanical properties of ZrO2/AlSi10Mg composites manufactured by laser powder bed fusion. *Ceram Int*. 2023;49(12):19673-19681.

doi: 10.1016/j.ceramint.2023.03.080

124. Rosito M, Vanzetti M, Padovano E, *et al*. Processability of A6061 aluminum alloy using laser powder bed fusion by *in situ* synthesis of grain refiners. *Metals*. 2023;13(6):1128.

doi: 10.3390/met13061128

125. Liu X, Liu Y, Zhou Z, Zhong H, Zhan Q. A combination strategy for additive manufacturing of AA2024 high-strength aluminium alloys fabricated by laser powder bed fusion: Role of hot isostatic pressing. *Mater Sci Eng A*. 2022;850:143597.

doi: 10.1016/j.msea.2022.143597

126. Pelevin IA, Ozherelkov DY, Nalivaiko AY, *et al*. AlSi10Mg/

AlN interface grain structure after laser powder bed fusion. *Metals*. 2022;12(12):2152.

doi: 10.3390/met12122152

127. Yi J, Zhang X, Rao JH, Xiao J, Jiang Y. *In-situ* chemical reaction mechanism and non-equilibrium microstructural evolution of (TiB2 + TiC)/AlSi10Mg composites prepared by SLM-CS processing. *J Alloys Compd*. 2021;857:157553.

doi: 10.1016/j.jallcom.2020.157553

128. Yaru L, Tiejun M, Tounan J, *et al*. Aging temperature effects on microstructure and mechanical properties for additively manufactured AlSi10Mg. *Mater Sci Technol*. 2023;39(10):1223-1236.

doi: 10.1080/02670836.2022.2164128

129. Ghio E, Cerri E. Work hardening of heat-treated AlSi10Mg alloy manufactured by selective laser melting: Effects of layer thickness and hatch spacing. *Materials*. 2021;14(17):4901.

doi: 10.3390/ma14174901

130. Fiocchi J, Biffi C, Colombo C, Vergani L, Tuissi A. Ad Hoc heat treatments for selective laser melted Alsi10mg alloy aimed at stress-relieving and enhancing mechanical performances. *Jom*. 2020;72(3):1118-1127.

doi: 10.1007/s11837-019-03973-z

131. Ghosh A, Pourkhorshid E, Rometsch P, Chen XG. Microstructure, processability, and strength of SiC-reinforced AlSi9Mg composite after laser surface remelting and post-heat treatment. *J Manuf Mater Process*. 2025;9(11):379.

doi: 10.3390/jmmp9110379

132. Yang F, Wang J, Wen T, *et al*. Manipulating microstructure and mechanical properties of laser powder bed fusion processed hypo-eutectic Al-13.3Mg2Si alloy via annealing. *J Alloys Compd*. 2023;967:171805.

doi: 10.1016/j.jallcom.2023.171805

133. Wang P, Gammer C, Brenne F, *et al*. Microstructure and mechanical properties of a heat-treatable Al-3.5 Cu-1.5 Mg-1Si alloy produced by selective laser melting. *Mater Sci Eng A*. 2018;711:562-570.

doi: 10.1016/j.msea.2017.11.063

134. Zhou S, Su Y, Wang H, Enz J, Ebel T, Yan M. Selective laser melting additive manufacturing of 7xxx series Al-Zn-Mg-Cu alloy: Cracking elimination by co-incorporation of Si and TiB2. *Addit Manuf*. 2020;36:101458.

doi: 10.1016/j.addma.2020.101458

135. Patil T, Washimkar D, Pawar A, Naidu MJ, Shinde S, Salunkhe S. Enhanced mechanical properties of AA7075 alloy through friction stir processing: A review. *Front Mech Eng*. 2025;11:1656081.

doi: 10.3389/fmech.2025.1656081

136. Wang J, Yang F, Yang H, *et al*. Effect of heat treatment on the microstructure and mechanical properties of an Al-5Mg2Si-2Mg alloy processed by laser powder bed fusion. *J Alloys Compd*. 2022;920:165944.

doi: 10.1016/j.jallcom.2022.165944

137. Ma R, Peng C, Cai Z, *et al*. Manipulating the microstructure and tensile properties of selective laser melted Al-Mg-Sc-Zr alloy through heat treatment. *J Alloys Compd*. 2020;831:154773.

doi: 10.1016/j.jallcom.2020.154773

ACCSCIENCE PUBLISHING

Engineering Science in Additive Manufacturing

PERSPECTIVE ARTICLE

Why semiconductor additive manufacturing is challenging—and what comes next

Ali Ghasemi* **and Swee Leong Sing***

Department of Mechanical Engineering, College of Design and Engineering, National University of Singapore, Singapore

Abstract

Semiconductors underpin modern electronics, optoelectronics, sensing, and energy technologies, yet their manufacturing remains dominated by centralized, tool-intensive, and largely planar process flows. Additive manufacturing (AM) offers a complementary pathway that can reduce material waste, accelerate prototyping, and unlock three-dimensional (3D) semiconductor architectures that are difficult to realize using conventional fabrication. However, AM of semiconductors is still in its infancy and has been demonstrated for only a limited set of materials and processes. This perspective synthesizes the current landscape of semiconductor AM by compiling reported 3D-printable semiconductor systems and mapping them to the corresponding AM techniques, including laser powder bed fusion, selective laser sintering, gas-phase reactive AM, inkjet printing, electrohydrodynamic redox printing, two-photon lithography, aerosol jet printing, extrusion-based AM, and laser-directed energy deposition. The key process-specific barriers are critically discussed—spanning feedstock limitations, densification and cracking, stoichiometry control and volatilization, texture and compositional heterogeneity, post-processing burdens, contamination, and scalability. On this basis, a length-scale–guided roadmap is proposed: laser powder bed fusion is positioned as the most promising route for cm–mm thermoelectric architectures, with advances in substrate/feedstock design, atmosphere control, and microstructure/defect engineering; ink-based and reactive approaches are highlighted for sub-mm to micro-scale functional devices through improved ink chemistry, 3D buildup, and multi-material integration; and electrohydrodynamic redox printing/two-photon lithography are identified as leading candidates for sub-micron to nanoscale fabrication, where material diversification, low-temperature conversion, residue mitigation, and hybrid integration with conventional microfabrication are essential. Collectively, this perspective clarifies terminology, consolidates the emerging evidence base, and outlines research priorities required to transition semiconductor AM from proof-of-concept demonstrations toward robust, application-relevant device manufacturing.

Keywords: Additive manufacturing; Three-dimensional printing; Semiconductor; Laser powder bed fusion; Ink-based printing; Two-photon lithography

***Corresponding authors:**
Ali Ghasemi
(ghasemia@nus.edu.sg)
Swee Leong Sing
(sweeleong.sing@nus.edu.sg)

Citation: Ghasemi A, Sing SL. Why semiconductor additive manufacturing is challenging—and what comes next. *Eng Sci Add Manuf.* 2026;2(1):026060003. doi: 10.36922/ESAM026060003

Received: February 7, 2026

Revised: February 26, 2026

Accepted: February 28, 2026

Published online: March 26, 2026

1. Introduction

Semiconductors are a broad family of materials that form the technological backbone of modern society. They are embedded in nearly every aspect of daily life, enabling devices and systems that individuals rely on routinely, often without noticing their presence. From everyday consumer products such as smartphones, smart televisions, wearable devices, and household appliances to more advanced technologies—including cloud computing infrastructure, navigation systems, and space technologies—semiconductors play a central role in shaping how information is processed, communicated, and utilized. Their widespread integration across consumer, industrial, and digital platforms underscores their fundamental importance to modern life.[1,2]

From an electrical conductivity perspective, materials are commonly classified into conductors, semiconductors, and insulators, with semiconductors occupying an intermediate position between the other two classes.[3] This distinction can be understood in terms of the valence and conduction bands (Figure 1A), separated by an energy gap that governs electrical behavior. In conductors, these bands overlap, enabling free electron movement and high conductivity. In insulators, a large band gap suppresses carrier excitation. Semiconductors possess a finite but smaller band gap, allowing electrons to be thermally, optically, or electrically excited into the conduction band, generating electron–hole pairs and enabling controlled charge transport.[4]

An intuitive way to visualize this behavior is to imagine two floors in a building: in conductors, the floors are connected by an open staircase, allowing people to move freely, while in insulators, the floors are separated by a high wall. Semiconductors lie between conductors and insulators, where a short staircase is present, enabling movement only when sufficient energy is provided. It is worth noting that in practical situations, the energy bands in semiconductors may locally shift or bend in response to external electric fields, interfaces, or charge accumulation, thereby modifying how easily charge carriers are generated and transported near surfaces or junctions.[5]

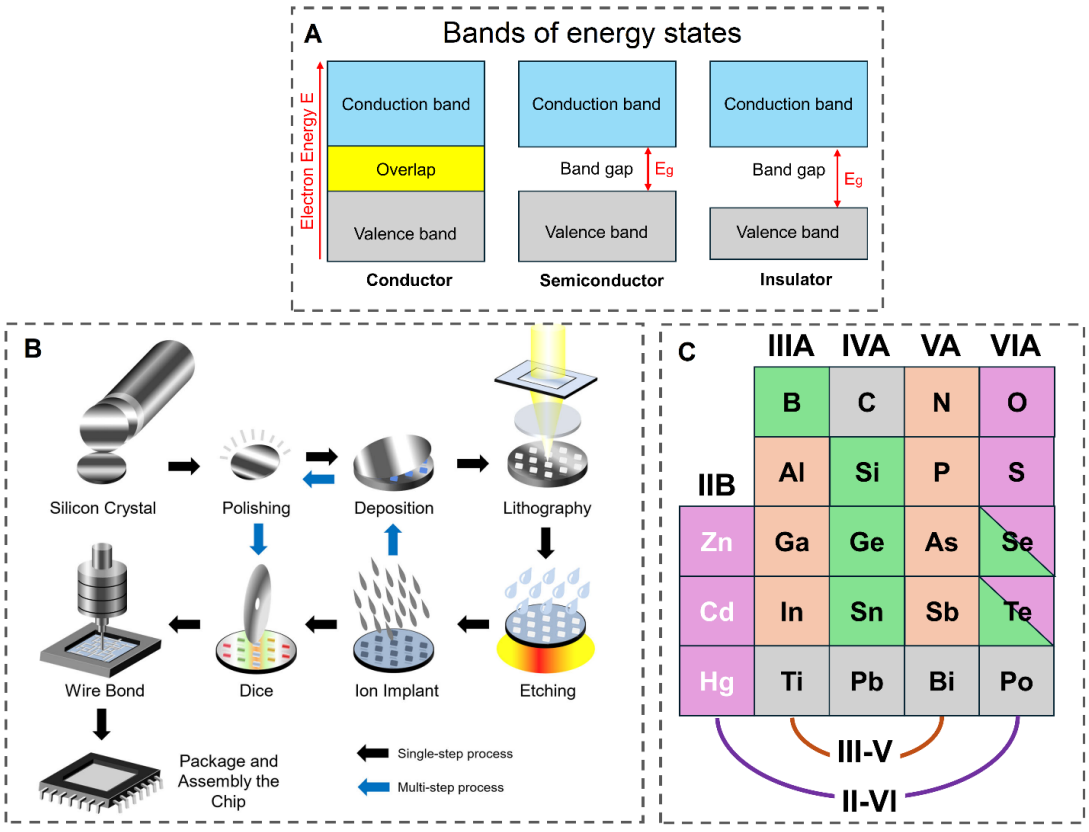

Figure 1. Overview of semiconductor fundamentals and conventional semiconductor manufacturing concepts. (A) Schematic comparison of electronic band structures in conductors, semiconductors, and insulators (created by the authors). (B) Simplified overview of conventional semiconductor manufacturing, from single-crystal growth and wafer processing to device fabrication and chip packaging (reproduced from Ref.[6]). (C) Simplified periodic table highlighting elemental groups relevant to compound semiconductor families (created by the authors).

The electrical properties of semiconductors can be tailored through doping, that is, the controlled introduction of trace impurity elements. Donor dopants increase free electron concentration (*n*-type), whereas acceptor dopants generate holes (*p*-type).[3] Rather than altering the fundamental band structure, doping introduces energy states that facilitate carrier excitation and enhance electrical conductivity. An intuitive way to visualize this effect is to imagine a city with bridges connecting two neighborhoods: adding dopants is similar to constructing shorter access roads that allow people to move between neighborhoods more easily, although the neighborhoods themselves remain in the same locations. Through controlled doping, the electrical response of semiconductors can be precisely tailored for a wide range of electronic, optoelectronic, and energy-related applications.

From a materials-chemistry perspective, semiconductor materials may be broadly classified into (i) elemental semiconductors (e.g., silicon [Si] and germanium); (ii) compound semiconductors, including III–V, II–VI, and IV–IV systems (e.g., gallium arsenide and zinc oxide [ZnO]); (iii) metal-oxide semiconductors (e.g., titanium dioxide [TiO_2] and stannic oxide); (iv) chalcogenide semiconductors (e.g., molybdenum disulfide and bismuth telluride); (v) organic semiconductors (e.g., pentacene and poly[3-hexylthiophene]); perovskite semiconductors (e.g., methylammonium lead iodide and cesium lead bromide); (vi) wide- and ultra-wide-band gap semiconductors (e.g., silicon carbide and gallium nitride [GaN]); and (vii) emerging semiconductor systems (e.g., two-dimensional materials and topological semiconductors).[1,7-16] Here, the Roman numerals in the III–V, II–VI, and IV–IV designations denote the corresponding column numbers of the constituent elements in the periodic table (Figure 1C), indicating the periodic-group elemental combinations that form these compound semiconductor families. These semiconductors underpin a wide range of technologies, including electronics, optoelectronics, photovoltaics, thermoelectrics (TEs), sensing, power conversion, quantum technologies, bioelectronics, radiation detection, and integrated photonics.[17]

Conventional semiconductor manufacturing is based on a sequence of highly controlled and well-established processing steps that have been refined over several decades to achieve the precision, reliability, and scalability required for modern electronic and optoelectronic devices. These conventional approaches, as shown in Figure 1B, rely on centralized fabrication facilities, sophisticated equipment, and multi-stage workflows to transform high-purity semiconductor materials into functional components using the following[18]:

(a) Crystal growth

The manufacturing process begins with the production of high-purity single-crystal semiconductor ingots, most commonly Si, which serve as the starting material for wafer fabrication. Si crystals are typically grown using the Czochralski crystal growth method, in which a seed crystal is drawn from molten Si under controlled thermal and rotational conditions to obtain a large, defect-minimized single crystal. Compound semiconductors may employ alternative crystal growth techniques.

(b) Wafer fabrication

The grown ingots are sliced into thin, circular wafers using precision cutting tools and subsequently polished to achieve ultra-smooth, mirror-like surfaces. Wafer thickness and surface quality are critical parameters that influence mechanical stability and downstream processing.

(c) Doping and carrier concentration control

Electrical properties are tailored by introducing controlled amounts of impurity atoms to create *n*-type or *p*-type regions within the semiconductor. Ion implantation is the predominant modern technique, offering high spatial accuracy and repeatability compared to earlier diffusion-based approaches.

(d) Photolithographic patterning

Geometric features are defined by transferring patterns from photomasks onto photosensitive resist layers deposited on the wafer surface. This step establishes the spatial arrangement and functional regions of semiconductor devices.

(e) Etching and material removal

Exposed regions of the wafer are selectively removed using chemical or plasma-based etching processes, enabling the formation of micro- and nanoscale device features.

(f) Oxide formation and surface passivation

Thin oxide layers are formed on the wafer surface to provide electrical insulation, chemical protection, and interface control. These layers are commonly produced through thermally activated or vapor-phase processes.

(g) Thin-film deposition

Additional conductive and insulating layers are deposited using techniques such as sputtering or chemical vapor deposition, allowing the construction of multilayer device architectures.

(h) Metallization and interconnection

Metal contacts and interconnects are formed to electrically link the semiconductor structures to external circuitry, completing the fabrication of functional semiconductor devices.

Despite remarkable advances in conventional semiconductor manufacturing—particularly in achieving nanoscale dimensional accuracy, high reproducibility, and efficient large-scale production—these approaches suffer from several inherent limitations. First, the highly optimized and tool-intensive nature of conventional fabrication workflows makes rapid prototyping and exploratory design iteration challenging, thereby slowing early-stage scientific discovery and technology development.[19] Second, conventional processes are often costly and time-consuming for customized or small-batch production, as design changes typically require new masks, tooling, or equipment reconfiguration, which is economically inefficient for personalized or application-specific electronics.[20] Third, semiconductor manufacturing relies heavily on hazardous chemicals and complex chemical processing steps, such as etching and cleaning, raising concerns related to worker safety, environmental impact, and waste disposal.[18]

In addition, while three-dimensional (3D) semiconductors and metal-oxide architectures have been shown to offer substantial performance enhancements, traditional fabrication techniques are largely restricted to planar or quasi-two–dimensional (2D) geometries, limiting access to fully 3D device designs.[21,22] This constraint is further compounded by the limited geometric flexibility of conventional methods, which favor relatively simple and repetitive layouts.[23] Finally, the subtractive nature of many fabrication steps leads to significant material waste, particularly during cutting and etching, thereby reducing overall material efficiency and sustainability.[24,25]

Additive manufacturing (AM), also known as 3D printing, has been proposed as a promising approach to address many of the limitations associated with conventional semiconductor manufacturing and to meet emerging technological demands. AM is widely regarded as a disruptive manufacturing paradigm that has already transformed several industries, with successful real-world adoption in sectors such as aerospace, automotive, tooling and die manufacturing, and turbine engineering.[26-29] Compared to subtractive manufacturing, AM offers a combination of compelling advantages, including a high buy-to-fly ratio that improves material efficiency and sustainability, reduced material waste and associated carbon dioxide emissions, and unparalleled geometric freedom.[28,30] Moreover, AM typically requires minimal or no tooling and molds, enabling rapid design iteration, cost-effective customization, and near-net-shape fabrication with limited post-processing.[31-33] The inherently layer-wise nature of AM further provides access to novel microstructures, functionally optimized architectures, and 3D designs that enable performance-driven components, which are difficult or impractical to realize using conventional manufacturing routes.

According to the International Organization for Standardization (ISO)/American Society for Testing and Materials (ASTM) 52900[34], AM is defined as "a process of joining materials to make parts from 3D model data, usually layer upon layer, as opposed to subtractive manufacturing and formative manufacturing methodologies." This standard classifies AM technologies into seven process categories: vat photopolymerization, material extrusion, material jetting, binder jetting, powder bed fusion (PBF), directed energy deposition, and sheet lamination. The capability of these AM approaches to fabricate polymeric, metallic, alloy, composite, and ceramic components has been extensively investigated and well documented in the literature. In contrast, semiconductors have received comparatively limited attention within the context of AM, despite their central role in modern technologies. This perspective article seeks to place AM of semiconductors under focused scrutiny by critically examining the current state of the art, identifying key technical and material limitations, and outlining future research directions needed to advance this emerging field.

For clarity and consistency, the term "additive manufacturing" is used in this article to describe fabrication processes that satisfy the following criteria: (i) material is added in a layer-by-layer manner; (ii) the process enables the construction of 3D objects with material buildup along the build (Z) direction; and (iii) 3D objects are built directly from a digital data file. Processes meeting these three requirements are referred to as AM in this work, regardless of whether they fall within the current ISO/ASTM classification framework or represent newly developed or emerging techniques. It is also important to note that, within the semiconductor literature, terms such as "printing" and "additive" are frequently used outside the strict context of AM, which can be a source of confusion for scholars in the field of AM. In many cases, these terms refer to 2D coating, deposition, or patterning processes, rather than true 3D fabrication. For example, multi-photon lithography is used to deposit planar semiconductor films or patterns on substrates[35]; however, when such a process is employed solely to produce thin films without volumetric buildup in the Z direction, it does not satisfy the criterion of 3D object formation and therefore should not be classified as AM technology. Such processes, while additive in nature, do not involve volumetric buildup and therefore should not be classified as AM technologies. In other words, all AM processes are additive, but not all additive or deposition-based processes qualify as AM.

Table 1. Summary of semiconductor materials fabricated by powder-bed laser additive manufacturing processes

Process	Material	Laser power (W)	Scan speed (mm/s)	Hatch spacing (mm)	Powder layer thickness (mm)	Maximum relative density (%)	Remarks	References
L-PBF	Sb_2Te_3	60, 100	200, 300	0.05	2	99.91	Mixed elemental Sb and Te powders were directly blended and deposited as a non-conventional 2 mm-thick powder layer on a stainless-steel substrate. Each layer was selectively laser-melted twice to enhance densification. The process was designed to fabricate dense thermoelectric ingots rather than thin-layer AM builds. Laser processing was carried out under high-purity Ar (1.5–2.0 KPa). A commercial continuous fiber-laser with a wavelength of 1,064 nm was used	24
	Bi_2Te_3	25	500	0.0375	0.15	88	Pre-alloyed Bi_2Te_3 powder was manually spread and flattened inside a thin stainless-steel ring acting as a powder-bed container, and the process was repeated for eight layers. Printing was conducted under an N_2 atmosphere with O_2 <4% to limit oxidation. The utilized laser was a 1,070 nm diode-pumped ytterbium fiber laser, operating in continuous wave mode	36
	$Bi_2Se_{0.3}Te_{2.7}$	25	NA	0.0375	0.15	77	Commercial melt-grown $Bi_2Se_{0.3}Te_{2.7}$ ingots were ball-milled and sieved to particle sizes below 75 μm. Powder layers were manually deposited and flattened using a stainless-steel roller, and L-PBF was carried out under an Ar atmosphere with O_2 <1%. A continuous YAG laser with a 1,070 nm wavelength was used for printing	37
	$Bi_{0.4}Sb_{1.6}Te_3$	NA	NA	NA	0.05	NA	Highly pure elemental Bi, Sb, and Te powders were first reacted via thermal explosion synthesis, followed by ball milling of the porous ingot to produce pre-alloyed powder (<400 mesh). The powder was dispersed in alcohol to form a slurry, spread onto the substrate, and dried prior to printing. A composition-matched spark-plasma-sintered substrate was used, and all printing was performed under a high-purity 95% Ar, 5% H_2 (0.5 atm) protective atmosphere to prevent oxidation. A commercial fiber laser with a wavelength of 1,064 nm was utilized for part fabrication	38
	$Bi_2Te_{2.7}Se_{0.3}$	1–13	NA	NA	0.05	NA	Elemental Bi, Te, and Se powders were mixed according to stoichiometry and dispersed in alcohol to form a slurry. During laser scanning, SHS occurred in situ, converting the elemental mixture into the thermoelectric compound. Printing was conducted under a mixed Ar/H_2 protective atmosphere. A commercial fiber laser with a wavelength of 1,064 nm was utilized for part fabrication	39
	$Bi_2Te_{2.7}Se_{0.3}$	3–10	50–500	0.05	0.03	NA	$Bi_2Te_{2.7}Se_{0.3}$ ingots were first synthesized by SHS, then ball-milled to produce pre-alloyed powder. The powder was mixed with alcohol to form a slurry and uniformly deposited onto the substrate prior to L-PBF. Printing was carried out under an Ar atmosphere at 0.5 atm. A commercial fiber laser with a wavelength of 1,064 nm was utilized for part fabrication	40

(*Cont'd...*)

doi: 10.36922/ESAM026060003

Table 1. *Continued*

Process	Material	Laser power (W)	Scan speed (mm/s)	Hatch spacing (mm)	Powder layer thickness (mm)	Maximum relative density (%)	Remarks	References
L-PBF	$Si_{80}Ge_{20}$	99–142	300–600	0.045	0.03	97.8	Pre-alloyed $Si_{80}Ge_{20}$ gas-atomized powder was printed directly onto an 430 stainless-steel substrate. To promote heat dissipation and improve densification, the laser jump speed between adjacent tracks was significantly reduced, and a unidirectional scan strategy was employed. Despite achieving high relative density, cracking was observed in all samples. Printing was carried out under an Ar atmosphere with O_2<1,000 ppm. A laser beam with a wavelength of 1,064 nm was utilized in this study (the laser source is not reported)	41
	$Si_{50}Ge_{50}$/ $Si_{80}Ge_{20}$	25–75	25–500	0.0375, 0.05	0.2	59	Pre-alloyed $Si_{50}Ge_{50}$ and $Si_{80}Ge_{20}$ materials were ball-milled from bulk granules and sieved to particle sizes below 75 μm. To avoid fusion with the substrate, the first powder layer thickness was increased to 400 μm, followed by rescanning using identical or modified parameters. In some cases, powders were HF-washed to remove surface SiO_2 prior to printing. Prior to laser processing, the enclosure was purged with Ar until an oxygen sensor sensed O_2<100 ppm. A continuous wave Nd-YAG laser with a wavelength of 1,070 nm was used in this study	42
	$Bi_2Te_{2.7}Se_{0.3}$	6	80	0.05	0.09	96	SHS-synthesized $Bi_2Te_{2.7}Se_{0.3}$ ingots were ball-milled and processed into an aqueous slurry. A dispenser-printing system was used to deposit uniform powder layers prior to L-PBF, with an optimized droplet spacing of 350 μm. This hybrid approach aimed at improving powder-bed quality. All experiments were carried out under a high-purity Ar atmosphere of 0.5 atm. A commercial fiber laser with a 1,064 nm wavelength was utilized for printing	43
	CP Si	80–100	300–1,800	0.09	0.03	98.5	Elemental silicon powders with purities of 99.61% and 99.87% were directly processed by L-PBF on a 316L stainless-steel substrate. High relative density was achieved, although cracking remained a concern. A high-purity Ar gas was flushed continuously inside the process chamber to minimize/avoid any possible oxidation. Nd: YAG laser was used for printing (the wavelength is not reported)	44
SLS	$Bi_{0.5}Sb_{1.5}Te_3$	30	3,200	0.05, 0.08	0.05	54	Pre-alloyed $Bi_{0.5}Sb_{1.5}Te_3$ powders were produced by ball milling bulk alloy ingots (100 mesh) and processed using a CO_2 laser (10.6 μm wavelength). Porous structures were intentionally fabricated to reduce thermal conductivity while maintaining acceptable electrical performance and mechanical strength	45

Abbreviations: AM: Additive manufacturing; Ar: Argon; Bi: Bismuth; CP: Commercially pure; Ge: Germanium; HF: Hydrofluoric acid; L-PBD: Laser powder bed fusion; NA: Not available; Nd-YAG: Neodymium-doped yttrium aluminum garnet; Sb: Antimony; Se: Selenium; SHS: Self-propagating high-temperature synthesis; Si: Silicon; Te: Tellurium; YAG: Yttrium aluminum garnet.

Table 2. Summary of semiconductor materials fabricated by other additive manufacturing techniques

Process	Material	3D-printing feedstock and process variables	Post-processing	References
GRAM	GaN	Liquid Ga was deposited from a molten Ga bath as a liquid-phase precursor onto *c*-plane sapphire substrates, followed by reactive conversion to GaN in a chamber under flowing N_2/NH_3 gas mixtures. Crystallization was carried out at 1,050 °C for 5–30 min, with N_2:NH_3 ratios between 1.25 and 50 controlled via NH_3 flow rate	NA	46
	GaN	Liquid Ga was deposited onto 2-inch *c*-plane sapphire wafers and subsequently crystallized to GaN in a vacuum chamber under flowing inert carrier gas and NH_3 (99.99%). Growth was conducted at 1,000 °C and 68–72 Torr, with delayed NH_3 introduction (0–10 min) and maintained during cooling to ensure N_2 overpressure	Wet etching was applied after each Ga deposition step to remove native Ga_2O_3 prior to subsequent growth	47
IJP	ZnO	A solid–gel zinc acetate ink (0.05 M in ethanol) was inkjet-printed onto Kapton® polyimide substrates using 10 pL droplets, a 10 μm drop spacing, and 10 print passes, with substrate temperatures of 40–60 °C	Immediately after printing, films were heated at 200 °C for 10 min to decompose the precursor, followed by furnace annealing at 400 °C for 1 h to sinter ZnO while preserving substrate integrity	48
	ZnO	A 50 mM zinc acetate–ethanol ink was inkjet-printed onto Si/SiO_2 substrates	The printed precursor layer was thermally decomposed on a hotplate at 200 °C for 10 min to form polycrystalline ZnO, followed by post-annealing in a quartz tube furnace at 250–350 °C for 30 min to further improve film quality	49
EHD-RP	Zn/ZnO	Zn was electrohydrodynamically printed using etched Zn wire anodes onto Au/Ti-coated Si substrates, with typical voltages of 110–130 V and a nozzle–substrate distance of 5–10 μm. Printing was conducted under an Ar atmosphere (<100 ppm O_2)	Post-print oxidation was performed by annealing at 325 °C for 6 h in air, converting deposited Zn to ZnO	50
TPL	ZnO	ZnO microstructures were fabricated using a zinc-ion–containing aqueous photoresin based on zinc nitrate, PEGDA, and DETC photoinitiator. Structures were written at 50 mW laser power and 1 mm/s scan speed on glass substrates with silicon chips as writing interfaces	Printed structures were calcined in air at 500 °C with controlled heating and cooling rates to form ZnO	23
AJP	ZnO	Water-based binder-free ZnO nanoparticle inks, including hybrid ZnO–TiO_2–Al_2O_3 dispersions, were deposited onto alumina substrates via ultrasonic AJP using a 150 μm nozzle and N_2 carrier/sheath gases, with platen temperatures up to 100 °C for in situ drying	Printed structures were densified by thermal sintering at 950 °C for 6 h	20
EAM	TiO_2	TiO_2 micropowders (1.5 μm) were processed via EAM using a polymer–wax binder system (e.g., LDPE, EVA, paraffin wax, stearic acid)	Printed parts underwent two-stage de-binding, including solvent de-binding in heptane at 40 °C and thermal de-binding at 500 °C, followed by sintering at 900 °C for 3 h to obtain dense TiO_2 structures	51
	PbTe	Binder-free colloidal PbTe inks composed of Na-doped (p-type) or Sb-doped (*n*-type) PbTe particles were extrusion-printed without organic rheological additives	Printed objects were dried and subsequently heat-treated at 1,073 K under N_2 atmosphere to consolidate the thermoelectric material	52
L-DED	Si	Metallurgical-grade Si powder (98% purity) was processed by L-DED using a 600 W pulsed laser (1 ms pulse duration, 50 Hz) and a *z*-stage build speed of 0.1 mm s^{-1}. Deposition was performed on a heated plate set to 25–980 °C	NA	53

Abbreviations: 3D: Three-dimensional; AJP: Aerosol jet printing; Ar: Argon; EAM: Extrusion-based additive manufacturing; EHD-RP: Electrohydrodynamic redox printing; EVA: Ethylene-vinyl acetate; Ga: Gallium; GaN: Gallium nitride; GRAM: Gas-phase reactive additive manufacturing; IJP: Inkjet printing; LDPE: Low-density polyethylene; L-DED: Laser directed energy deposition; NA: Not available; PbTe: Lead telluride; Si: Silicon; SiO_2: Silicon dioxide; Ti: Titanium; TiO_2: Titanium dioxide; TPL: Two-photon lithography; Zn: Zinc; ZnO: Zinc oxide; Au: Gold.

2. Additive manufacturing for fabricating semiconductors

To date, only a limited set of semiconductor materials has been successfully fabricated using AM, and these materials and their associated AM techniques are systematically summarized in Table 1 and shown in Figure 2, respectively. In the following subsections, each AM process is briefly introduced, along with its main advantages and inherent limitations when applied to semiconductor materials.

Although the present discussion has focused on AM routes, it is important to recognize that semiconductor processing shares conceptual overlap with the ceramic community, where powder-based consolidation techniques—such as pressureless sintering, hot pressing, and spark plasma sintering—have long been employed. Many oxide semiconductors are mechanically and thermally closer to ceramics than to ductile metals, and therefore their response to rapid thermal cycles during AM may resemble ceramic processing behavior. In this context, insights from conventional ceramic densification, such as diffusion-controlled neck growth, grain-boundary mobility, pore elimination kinetics, and thermal shock resistance, may provide a valuable framework for interpreting densification and cracking phenomena in semiconductor AM. Establishing clearer connections between ceramic processing science and AM could therefore accelerate the development of more robust processing strategies for brittle semiconductor systems in the future.

2.1. Laser powder bed fusion

Laser PBF (L-PBF), often referred to as selective laser melting, is an AM technique in which 3D components are fabricated through the successive consolidation of powder layers using a focused laser heat source[31] (Figure 2A). The process begins with the creation of a digital 3D model, which is computationally discretized into a series of 2D cross-sectional layers. During fabrication, a thin layer of powder is uniformly spread across a build platform, after which a scanning laser selectively irradiates predefined regions to locally melt or fuse the powder according to the corresponding digital slice. Once a layer is completed, the build platform is incrementally lowered, and a fresh powder layer is deposited. The laser scanning and fusion sequence is then repeated, enabling metallurgical bonding between adjacent layers and the gradual vertical buildup of the component.[28] Through this iterative layer-wise approach, L-PBF enables the production of geometrically complex structures with high spatial resolution.[58-62]

Selective laser sintering (SLS) follows the same fundamental layer-wise manufacturing principle as L-PBF, involving the sequential deposition of powder layers and selective laser scanning based on sliced digital data. The key distinction lies in the laser–matter interaction mechanism. SLS typically employs lasers with longer wavelengths and lower energy densities, such that the powder particles are not fully melted; instead, partial melting or surface softening occurs, leading to bonding via solid-state diffusion or viscous flow at particle interfaces.[63] As a result, consolidation in SLS is achieved primarily via sintering mechanisms rather than complete melting, which reduces thermal gradients and residual stresses but generally yields parts with lower density and resolution compared to L-PBF.[64]

Laser PBF has been predominantly explored for the fabrication of TE semiconductor materials (Table 1), which enable direct conversion of heat into electrical energy at elevated temperatures.[65] A typical TE module consists of interconnected *n*-type and *p*-type semiconductor legs.[66] Conventional manufacturing of such modules relies on powder mixing and alloying via high-energy ball milling, followed by consolidation through hot pressing or spark plasma sintering and subsequent dicing into the desired geometries.[66] Notably, it has been reported that the dicing step alone can account for up to 50% material loss, arising from chipping, cracking, and kerf losses.[67,68] In addition, dicing inherently restricts achievable geometries to simple planar shapes (e.g., rectangular or square legs), limiting design freedom. This geometric constraint is particularly problematic because practical heat sources and sinks are often curved, resulting in suboptimal thermal contact and reduced device efficiency.[41] These limitations have motivated increasing interest in L-PBF as a route to reduce material waste while enabling complex, conformal, and non-planar thermoelectric architectures.

Despite these potential advantages, L-PBF processing of TE semiconductors remains extremely challenging, primarily due to their intrinsic material characteristics. The first major challenge is the lack of suitable powder feedstock. Many TE materials are not commercially available as spherical powders, which are generally required for stable powder spreading in L-PBF. For example, several studies reported unsuccessful or manual layer deposition owing to the irregular morphology and agglomeration of non-spherical powders (Figure 3A).[37,66,69-71] These powders are usually manufactured through ball milling and sieving of the ingot of the semiconductor material. Although some reports demonstrated that irregular powders could be deposited, the resulting parts typically exhibited low densification, in part due to the use of low laser powers and insufficient volumetric energy densities imposed by equipment limitations. For example, a maximum relative

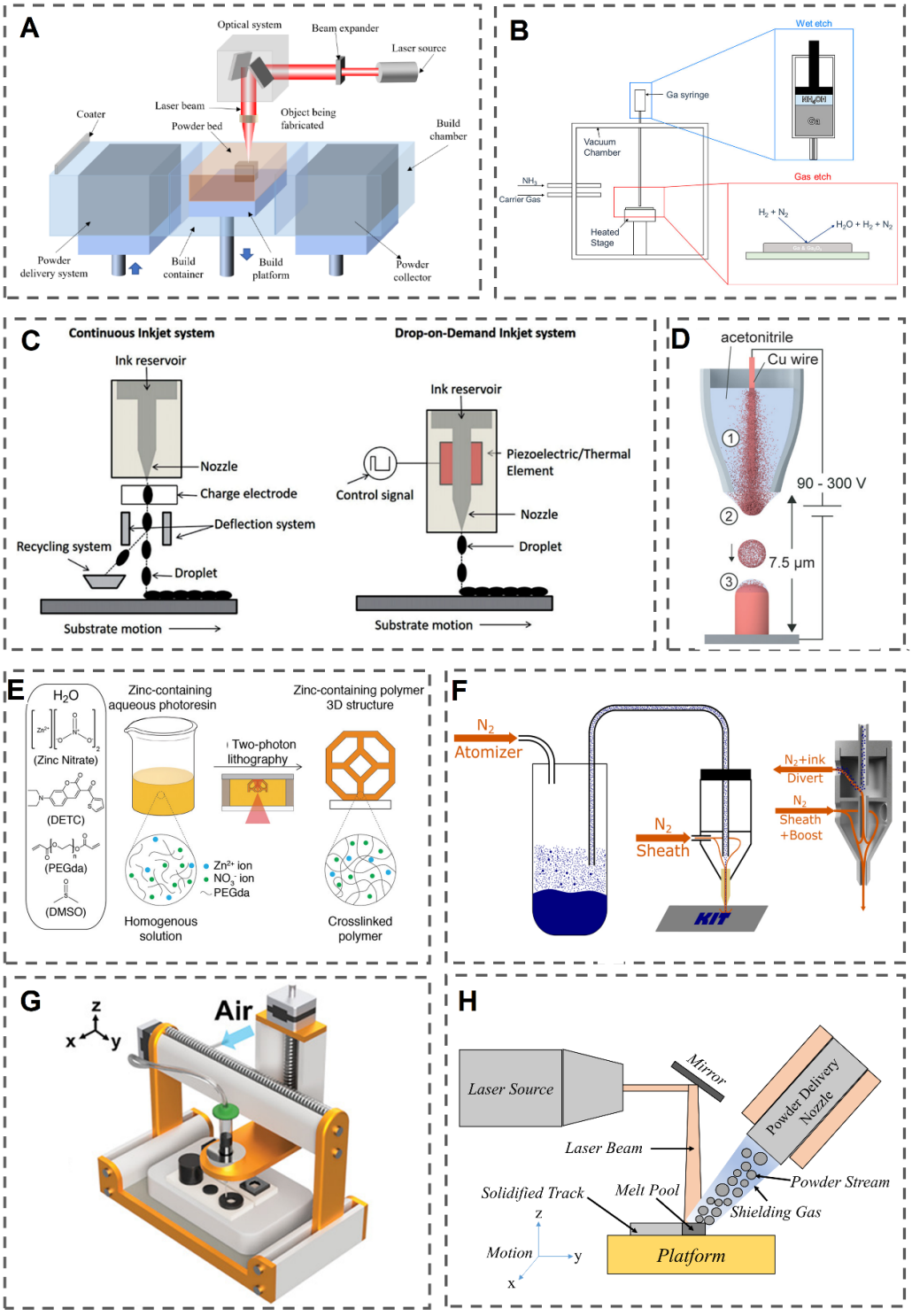

Figure 2. Schematic overview of additive manufacturing processes applied to semiconductor fabrication: (A) Laser power bed fusion (reproduced from Ref. 54), (B) gas-phase reactive additive manufacturing (reproduced with permission from Ref. 47, Copyright © 2024, American Chemical Society), (C) inkjet printing (reproduced from Ref. 55), (D) electrohydrodynamic redox printing (adapted from Ref. 56), (E) two-photon lithography (adapted from Ref. 23 with permission, Copyright © 2019, Wiley-VCH GmbH), (F) aerosol jet printing (adapted from Ref. 57), (G) extrusion-based additive manufacturing (reproduced from Ref. 52 with permission, Copyright © 2021, Wiley-VCH GmbH), and (H) laser directed energy deposition (created by the authors). Abbreviations: 3D: Three-dimensional; DETC: Diethyl thiophosphoryl chloride; DMSO: Dimethyl sulfoxide; PEGda: Poly(ethylene glycol) diacrylate.

density of only 77% (Figure 3B) has been reported for L-PBF-processed $Bi_2Se_{0.3}Te_{2.7}$[37] with cracks and porosities.

To address powder spreading issues, alternative strategies have been proposed, including gas atomization and the use of elemental powder blends dispersed in alcohol to form slurries, which can be uniformly deposited using a scraper. For the latter case, after deposition, the substrate is heated to evaporate the solvent prior to laser scanning.[38-40] Under appropriate processing conditions, self-propagating high-temperature synthesis, also referred to as in situ alloying, can occur during L-PBF, leading to the formation of the target TE compound.[39] While effective in improving layer uniformity, this approach introduces additional manual steps, increases processing time and cost, and may raise concerns regarding contamination and defect formation. In contrast, in situ alloying using dry elemental powder mixtures has also been demonstrated, notably for Sb_2Te_3[24], yielding homogeneous microstructures. Although this dry approach is more promising, suppressing compositional heterogeneity during in situ alloying remains a critical challenge, particularly given the stringent compositional control required for semiconductor performance.[37]

A second major challenge in L-PBF of TE semiconductor materials is crack formation induced by high thermal gradients and tensile residual stresses. Severe cracking has been reported in L-PBF-processed *n*-type $Si_{80}Ge_{20}$[41] and $Bi_2Se_{0.3}Te_{2.7}$ to a lesser extent (Figure 3B). However, the fundamental origins of cracking in TE materials have not yet been systematically investigated, highlighting the need for focused mechanistic studies in future work. In metallic L-PBF, cracking is commonly associated with mechanisms such as solidification cracking and liquation cracking at high temperatures, as well as solid-state phenomena, including strain-age cracking or cold cracking, particularly in martensitic steels.[31,72,73]

Cold cracking in such alloys is often linked to martensitic transformation-induced volumetric expansion and residual tensile stresses.[26] In contrast, many semiconductors and TE compounds are intrinsically brittle due to their predominantly covalent or partially ionic bonding, low fracture toughness, and limited dislocation mobility. As a result, classical hot or cold cracking phenomena established in metallic AM may not directly translate to semiconductor systems. Instead, cracking during semiconductor AM is expected to be dominated by thermal shock-induced fracture under steep thermal gradients, residual-stress–driven fracture in the absence of significant plastic strain accommodation (Figure 3B). This fundamental difference in deformation behavior suggests that defect mitigation strategies developed for metallic AM cannot be directly transferred to semiconductor AM without modification.

The third challenge concerns microstructural anisotropy and compositional heterogeneity in L-PBF–fabricated components. L-PBF of $Bi_2Se_{0.3}Te_{2.7}$, for example, resulted in highly textured columnar grains (Figure 3C).[37] The pronounced texture introduced strong anisotropy in thermoelectric properties, while nanoscale inclusions and elemental redistribution (Figure 3D) altered carrier transport behavior. In particular, tellurium-rich regions were observed along grain boundaries, and the combined effects of sparse inclusions and elemental segregation led to a transition from *n*-type to *p*-type conduction, indicating a shift in the dominant charge carriers from electrons to holes. In addition, short-range ordering, widely reported in complex ceramics and high-entropy systems, can influence local bonding environments and defect energetics in additively manufactured semiconductors. Although short-range ordering has not yet been systematically examined in semiconductor AM, its potential impact on carrier transport and phase stability merits future investigation.[74,75]

A fourth limitation arises from selective vaporization of volatile elements, especially under high volumetric energy densities. For Bi_2Te_3-based systems, it has been reported that a single-phase compound can be obtained at a relatively low energy density of approximately 20 J/mm^3.[40] However, increasing the energy density to 40 J/mm^3 results in the formation of secondary phases such as Bi_4Te_5, while further increases to 66.7 and 80 J/mm^3 lead to substantial vaporization of tellurium and selenium, reducing the stoichiometric ratio and promoting the formation of BiTe.[40] These observations highlight that excessive heat input causes compositional deviations, phase segregation, and degradation of thermoelectric performance. Consequently, the lowest laser energy density compatible with acceptable part quality should be employed to minimize volatilization of anion species.

The fifth challenge concerns the thermal conductivity of semiconductors. Thermal conductivity is a key material parameter governing melt-pool dynamics, temperature gradients, and overall printing quality in semiconductor L-PBF. Compared with most structural metals, many semiconductors, particularly TE compounds, exhibit relatively low intrinsic solid-state thermal conductivity. This limited heat dissipation leads to higher peak temperatures, steeper thermal gradients, and longer melt-pool lifetimes during laser processing. The resulting thermal stresses can exceed the fracture strength of brittle semiconductor materials, promoting microcracking and residual-stress–driven fracture. For example, in Bi_2Te_3-based systems processed by L-PBF, the inherently low and strongly temperature-dependent thermal conductivity of the solid

phase has been associated with pronounced temperature gradients and crack formation. It has been suggested that substrate preheating may reduce these gradients by increasing the temperature of previously solidified layers, thereby moderating thermal shock during subsequent laser passes.[76] More broadly, the temperature dependence of thermal conductivity in many semiconductors introduces an additional degree of freedom not typically dominant in metallic AM. Control of substrate temperature, laser pulse characteristics (e.g., repetition rate and pulse width), and heat-input modulation may enable the reduction of transient stress accumulation. Systematic management of heat flow and thermal boundary conditions is therefore critical for improving densification and mitigating cracking in semiconductor AM.

Finally, for Si-based systems, L-PBF inherently produces polycrystalline microstructures[44], whereas most semiconductor applications require single-crystal Si to ensure optimal electronic performance. This fundamental incompatibility further constrains the applicability of L-PBF for conventional semiconductor device fabrication.

2.2. Gas-phase reactive additive manufacturing

Gas-phase reactive AM (GRAM) is an emerging AM approach for the 3D fabrication of compound semiconductors that combines localized deposition of a liquid precursor with layer-wise gas–solid chemical reactions (Figure 2B).[47] Conceptually, GRAM is rooted in the principles of liquid-phase epitaxy[77], in which a molten elemental precursor serves as the source material for crystal growth while a reactive gas supplies the complementary element required for compound formation.

In the GRAM process, a liquid precursor (e.g., molten metals such as gallium or other low-melting constituents) is first deposited in a spatially controlled manner to define an individual layer on a substrate. Each deposited layer is subsequently exposed to a reactive gas atmosphere (e.g., ammonia or other nitrogen-containing gases) at elevated temperature, enabling localized chemical conversion before deposition of the next layer. Through this repeated sequence of deposition and reaction, 3D structures are progressively built.[46] This approach allows geometric definition to be governed by the printing step, while phase formation and crystallization are dictated by reaction kinetics rather than bulk melting. By avoiding the direct melting of compound semiconductor feedstocks and decoupling material placement from gas-phase transport, GRAM offers a flexible and potentially energy-efficient route for AM of semiconductors with complex geometries.

This approach is particularly well suited for applications requiring epitaxial thin films of high-melting-point semiconductors, such as GaN (Table 2). In such cases, reaction-based fabrication routes are favored over the direct use of GaN feedstock for several fundamental reasons. First, powder-based processing, analogous to L-PBF, inevitably yields polycrystalline microstructures, which are incompatible with the stringent crystallographic requirements of most compound semiconductor devices. Second, heating GaN powder to near-melting temperatures leads to nitrogen loss, stoichiometric imbalance, and defect formation, driven by the large disparity in vapor pressures between gallium and nitrogen. In addition, the melting point of GaN is exceptionally high (approximately 2,500 °C), whereas commercial reactive synthesis routes enable GaN formation at substantially lower temperatures (<1,200 °C), offering significant reductions in energy consumption and processing costs.[46]

Despite these advantages, the technique faces several notable limitations. These include limited spatial resolution and dimensional fidelity due to droplet spreading, volumetric changes during gas–liquid reactions, and the formation of native oxide layers (e.g., Ga_2O_3). Moreover, the process often results in pronounced surface roughness, while regions outside the printed features may become polycrystalline, likely due to wetting effects or contamination. Finally, the relatively low production rate restricts scalability, making this method more suitable for thin-film or 2.5D structures rather than fully 3D architectures.[47]

2.3. Inkjet printing

Inkjet printing (IJP) is a digitally controlled material deposition technique in which discrete liquid droplets are generated and selectively delivered to a target substrate (Figure 2C). Depending on the mechanism used to form and control droplets, IJP is generally divided into two main approaches: continuous IJP and drop-on-demand IJP. In continuous inkjet systems, droplets are produced continuously from a nozzle, and electric fields are used to steer individual droplets either toward the substrate or away from the printing region for recirculation. While this method enables high-throughput deposition, it is inherently less efficient in terms of material usage. Drop-on-demand IJP, by contrast, generates droplets only at prescribed locations, making it a more material-efficient approach. In this mode, droplet ejection is typically achieved through rapid thermal actuation or by mechanical displacement using a piezoelectric element.[78-81] Owing to its mask-less operation, precise spatial control, and compatibility with a wide range of functional inks, IJP has been widely explored in semiconductor-related applications, particularly for 2D coating[82,83] and patterning, although its extension to true 3D fabrication remains limited.

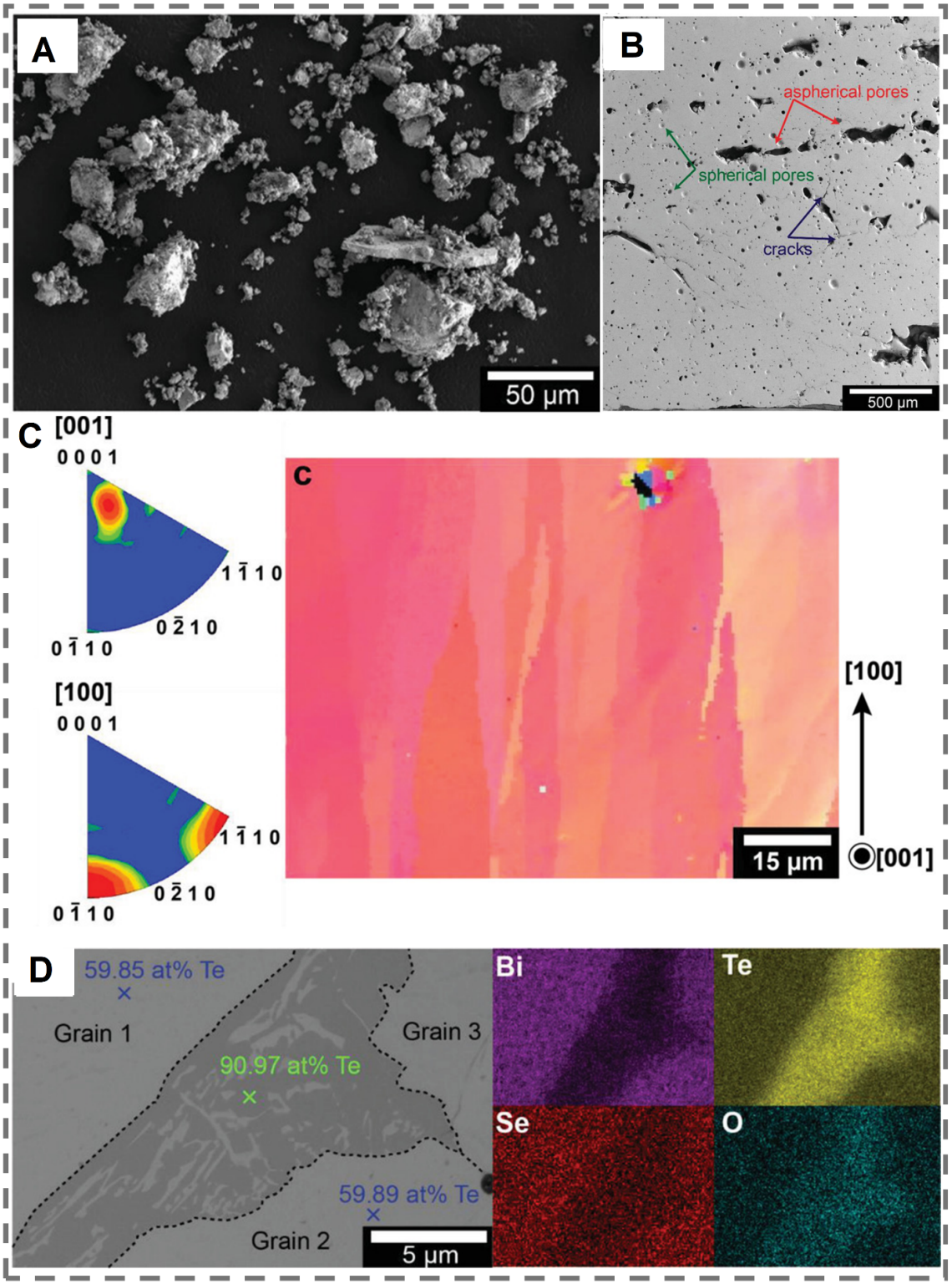

Figure 3. Microstructural challenges in laser powder bed fusion (L-PBF) of $Bi_2Se_{0.3}Te_{2.7}$ thermoelectric semiconductor: (A) irregular powder morphology (scale bar: 50 μm), (B) porosity and cracking in L-PBF fabricated part (scale bar: 500 μm), (C) strong texture (scale bar: 15 μm), and (D) elemental segregation (scale bar: 5 μm). Images adapted from Ref.[37]

Abbreviations: Bi: Bismuth; O: Oxygen; Se: Selenium; Te: Tellurium.

Although this technique has demonstrated encouraging performance for printing ZnO in sensor applications (Table 2), it is accompanied by several inherent limitations. First, the ink viscosity must be carefully controlled: excessively viscous inks can clog the nozzle, while low-viscosity formulations compromise dimensional accuracy; nozzle blockage is often associated with particle agglomeration within the orifice.[79] Second, residual precursor-related species, such as $Zn(OH)_2$, have been reported to persist after calcination, leading to shifts in the optical band gap of the resulting ZnO.[49] Third, the coffee-ring effect can induce non-uniform material distribution, producing uneven and inhomogeneous patterns that degrade printing resolution and spatial precision, particularly critical for miniaturized devices.[78] Fourth, internal stresses generated during post-print heat treatments may cause pattern distortion and surface wrinkling in the deposited films.[79] Finally, the presence of structural defects in the printed ZnO can further alter the electronic structure and adversely impact band-gap–related properties.

2.4. Electrohydrodynamic redox printing

Electrohydrodynamic redox printing (EHD-RP) is an electrochemical, high-resolution AM technique that enables the direct writing of dense metallic micro- and nanostructures through localized redox reactions (Figure 2D). In EHD-RP, metal ions are generated in situ by anodic dissolution of a sacrificial metal source within a liquid medium and are transported toward a conductive substrate by a strong electric field. Upon reaching the substrate, these ions are electrochemically reduced, forming a metallic deposit with sub-micron feature sizes.[84] Unlike many powder- or ink-based approaches, EHD-RP produces metallic structures directly during printing and therefore does not require post-deposition sintering or consolidation.[50] While the process inherently yields metals, semiconductor structures can subsequently be realized by controlled post-printing oxidation of the printed metallic features, converting them into their corresponding metal oxides.[50,85] Through this two-step route, namely electrochemical metal deposition followed by oxidation, EHD-RP provides an indirect yet highly precise pathway for fabricating semiconductor materials, particularly metal-oxide semiconductors.

This technique has been primarily applied to the fabrication of semiconducting materials for gas-sensing applications. EHD-RP offers a high printing throughput, reaching approximately 10 voxels/s with minimum voxel sizes of approximately 170 nm, outperforming other electrochemical printing approaches that typically achieve 1–3 voxels/s with comparable feature sizes.[86] A distinctive advantage of EHD-RP is its ability to dynamically control material chemistry during printing, enabling multi-metal deposition with chemical feature sizes below 400 nm. This capability arises uniquely from the in situ generation of metal ions from sacrificial anodes, which allows seamless switching between different metallic species within a single print.

The combination of high deposition speed and multi-material capability makes EHD-RP a promising platform for direct microscale fabrication. Moreover, the use of aqueous solvents provides substantial flexibility, as a wide range of metals can be dissolved and electrochemically redeposited. To date, copper and zinc have been successfully printed, which could subsequently be converted into their corresponding oxides through post-printing oxidation, yielding functional semiconductors. In principle, the compatibility of EHD-RP with aqueous systems could be extended to a broader range of metals. Furthermore, replacing sacrificial anodes with metal salt precursors may enable access to more noble metals that do not readily undergo corrosion in aqueous environments.[50]

Despite these advantages, several limitations currently restrict broader adoption. First, complete conversion of printed metals to oxides often requires prolonged oxidation times and elevated temperatures, and only partial oxidation has been done successfully to date. Second, thermal mismatch between the printed material and Si substrates during post-processing can lead to deformation, distortion, or fracture, undermining shape fidelity and structural integrity. Collectively, these challenges constrain the practical applicability of EHD-RP for robust semiconductor manufacturing.[50]

2.5. Two photon lithography

Two-photon lithography (TPL) is a high-resolution AM technique capable of producing complex 3D micro- and nanostructures through localized two-photon-induced photopolymerization (Figure 2E). In TPL, a tightly focused laser induces polymerization only at the focal volume via a nonlinear optical process, enabling feature sizes well below 1 μm and true 3D freeform fabrication.[35] For semiconductor-related applications, TPL is commonly combined with specially designed photoresins that contain metal-bearing species or inorganic building blocks. During printing, these photoresins are patterned into 3D polymer architectures that spatially define the desired geometry. Subsequent thermal treatment converts the printed structures into their corresponding inorganic or metal-oxide forms by removing the organic matrix and inducing oxide formation.[23] This indirect fabrication route allows TPL to overcome limitations associated with light scattering from solid particles and enables the creation of

monolithic semiconductor microstructures with arbitrary geometry and exceptionally high resolution. As a result, TPL-based AM has emerged as a powerful approach for fabricating 3D semiconductor and metal-oxide architectures that are difficult or impossible to realize using conventional lithographic or deposition techniques.

This technique demonstrates strong potential for fabricating 3D micro- and nanoscale structures, as evidenced by reports of nano-architected ZnO geometries with feature sizes down to approximately 250 nm (Figure 4). The presented slurry-free, photolithography-based approach for producing monolithic 3D ZnO architectures represents a substantial simplification compared with existing methods, while enabling structural designs and device concepts that were previously unattainable. An additional advantage of this process lies in its ability to control linear shrinkage during calcination through selective leaching of zinc ions, providing an effective secondary route for enhancing structural resolution, enabling size reductions of up to 70–90%. This capability marks a notable advancement beyond the current state of the art and opens a pathway toward the realization of previously inaccessible 3D piezoelectric microstructures.[23]

Despite these promising results, the applicability of this technique remains constrained. To date, its use has been largely limited to ZnO, with little information available on its extension to other semiconductor materials (Table 2). In addition, the process involves multiple fabrication and post-processing steps, and potential contamination introduced during processing may adversely affect semiconductor performance. Moreover, commonly used photoresists are liquid organic polymer systems with critical feature sizes typically limited to around 80–100 nm and with limited resistance to aggressive pattern-transfer conditions, making them unsuitable for many chip- and device-level applications.[87]

2.6. Aerosol jet printing

Aerosol jet printing (AJP) is a direct-write deposition technique that fabricates patterns by delivering an aerosolized stream of liquid ink onto a substrate with high spatial control (Figure 2F). In this approach, a liquid ink is first converted into fine droplets through an atomization process, forming an aerosol that is transported by a carrier gas toward the deposition nozzle. A secondary gas flow, commonly referred to as a sheath gas, surrounds and focuses the aerosol stream, effectively acting as a virtual nozzle that confines the material jet before it reaches the substrate. This gas-assisted focusing enables precise feature definition and reduces the likelihood of nozzle clogging compared with conventional IJP.[88-90] One of the key advantages of AJP is its broad ink compatibility, as it can accommodate a wide range of ink viscosities and material systems, including polymers, metals, and semiconductor-related inks. Owing to its mask-less operation, fine feature resolution, and flexibility in ink formulation, AJP has been widely explored for electronic and semiconductor applications, particularly for 2D patterning.[91] While aerosol jet/aerosol-gel printing is predominantly used for 2D and conformal 2.5D patterning, multiple studies have demonstrated true 3D, *Z*-directional buildup at the micro-scale (e.g., freestanding pillars, walls, and lattice-like microarchitectures) through layer-by-layer stacking and/or rapid curing/solidification mechanisms.[20]

Recent studies have demonstrated that the technique can be extended to produce complex 3D ZnO microlattice architectures and micropillars with intricate geometries (Figure 5A), suitable for applications such as cancer biomarker sensing. In addition, this process has shown promising potential for multimaterial 3D fabrication, including ZnO–TiO_2 systems (Figure 5B) and hybrid Al_2O_3–TiO_2–ZnO ceramic structures (Figure 5C), thereby highlighting its versatility for functional microarchitected materials.[20]

2.7. Extrusion-based additive manufacturing

Extrusion-based AM (EAM) is a material deposition technique in which a viscoelastic feedstock, typically formulated as a paste, slurry, or ink, is dispensed through a nozzle and deposited in a programmed, layer-by-layer manner to build 3D structures (Figure 5G). In this approach, functional powders are first dispersed within a liquid or polymeric binder to produce an extrudable ink with suitable rheological properties for continuous flow and shape retention after deposition. During printing, the ink is delivered from a reservoir or syringe through nozzles of defined diameter using pressure- or mechanically driven extrusion, while the motion of the print head or substrate defines the desired geometry. Following deposition, printed structures generally undergo drying to remove solvents and subsequent thermal treatment to eliminate organic constituents, promote particle bonding, and develop the final functional material properties. Owing to its simplicity, material versatility, and compatibility with highly loaded functional inks, EAM has been widely explored for the fabrication of ceramic, metallic, and semiconductor-related components, particularly where complex geometries and compositional flexibility are required.[51,52,92-94]

Using this approach, TiO_2 semiconductors for photocatalytic CO_2 reduction, as well as PbTe thermoelectric materials, have been successfully fabricated

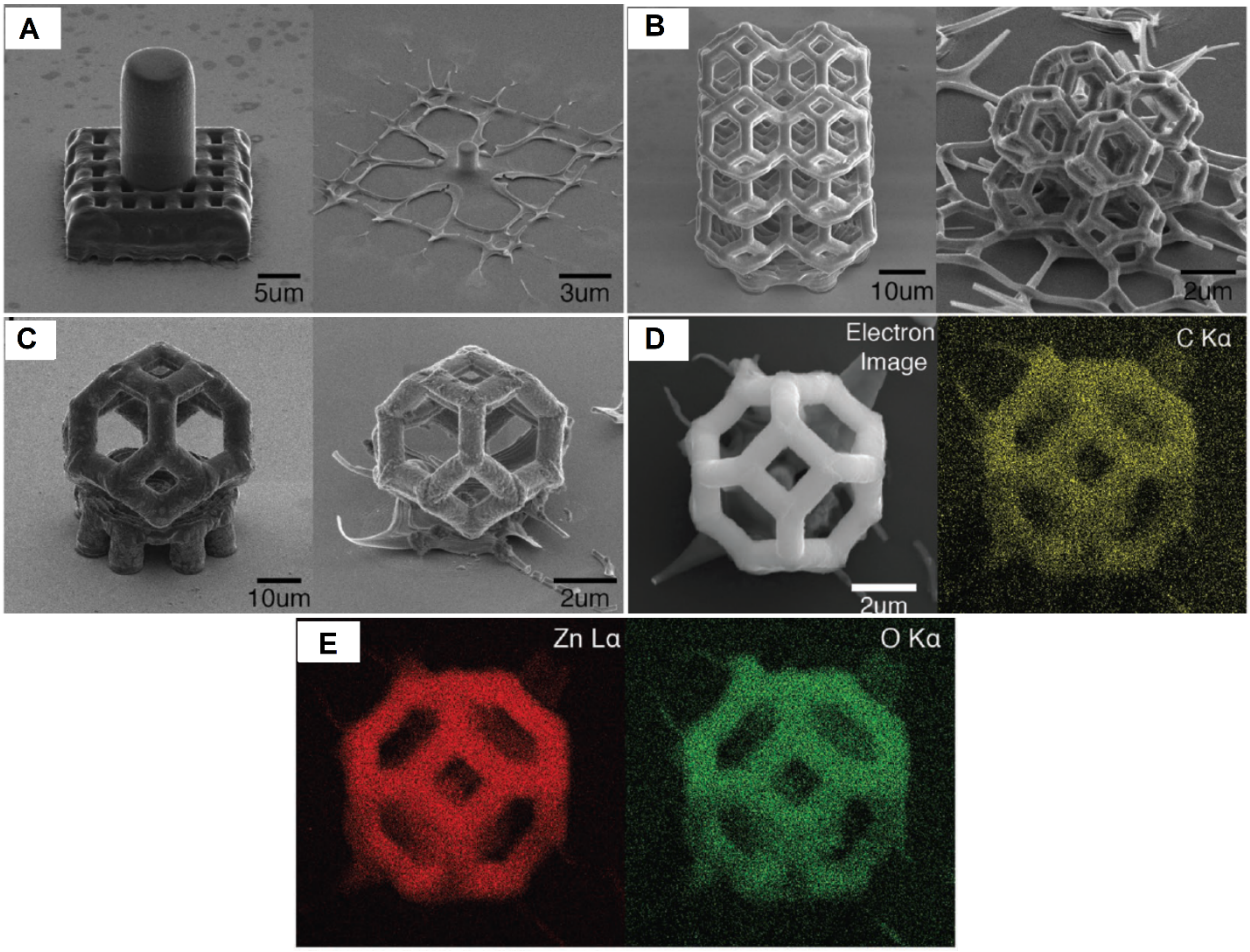

Figure 4. Representative scanning electron microscopy images showing: (A) a single cylindrical pillar (left: scale bar = 5 μm; right: scale bar = 3 μm), (B) a microlattice composed of tetrakaidecahedral units (left: scale bar = 10 μm; right: scale bar = 2 μm), and (C) an individual tetrakaidecahedron fabricated by two-photon lithography using an aqueous zinc ion photoresin (left: scale bar = 10 μm; right: scale bar = 2 μm), shown before (left) and after (right) calcination. All structures exhibit a uniform linear shrinkage of 87 ± 2% following calcination. (D, E) Energy-dispersive X-ray spectroscopy elemental maps of zinc (Zn), carbon (C), and oxygen (O) for a calcined tetrakaidecahedron unit cell. Images adapted from Ref.[23] with permission, Copyright © 2019, Wiley-VCH GmbH.

(Table 2).[51,52] Despite these encouraging demonstrations, the broader applicability of EAM to semiconductors remains limited. Inks or feedstocks suitable for many semiconductor materials are not readily available, and the process typically requires multiple post-processing steps (e.g., debinding and sintering), which can compromise dimensional fidelity and structural integrity. Furthermore, the achievable resolution and minimum feature size are generally on the order of hundreds of micrometers, rendering this technique unsuitable for applications demanding fine features, such as microelectromechanical systems and nanoelectronic devices.

2.8. Laser directed energy deposition

Laser-directed energy deposition (L-DED) is an AM process in which a concentrated energy source, most commonly a laser, is used in conjunction with a controlled material delivery system to fabricate 3D components (Figure 2H). In this technique, feedstock material, supplied in the form of powder or wire, is delivered directly into the laser–material interaction zone, where it is rapidly heated and melted.[31,95] The molten material is deposited onto a substrate or previously solidified layer, where it solidifies and forms a metallurgical bond. By moving the deposition head or substrate along predefined toolpaths, material is laid

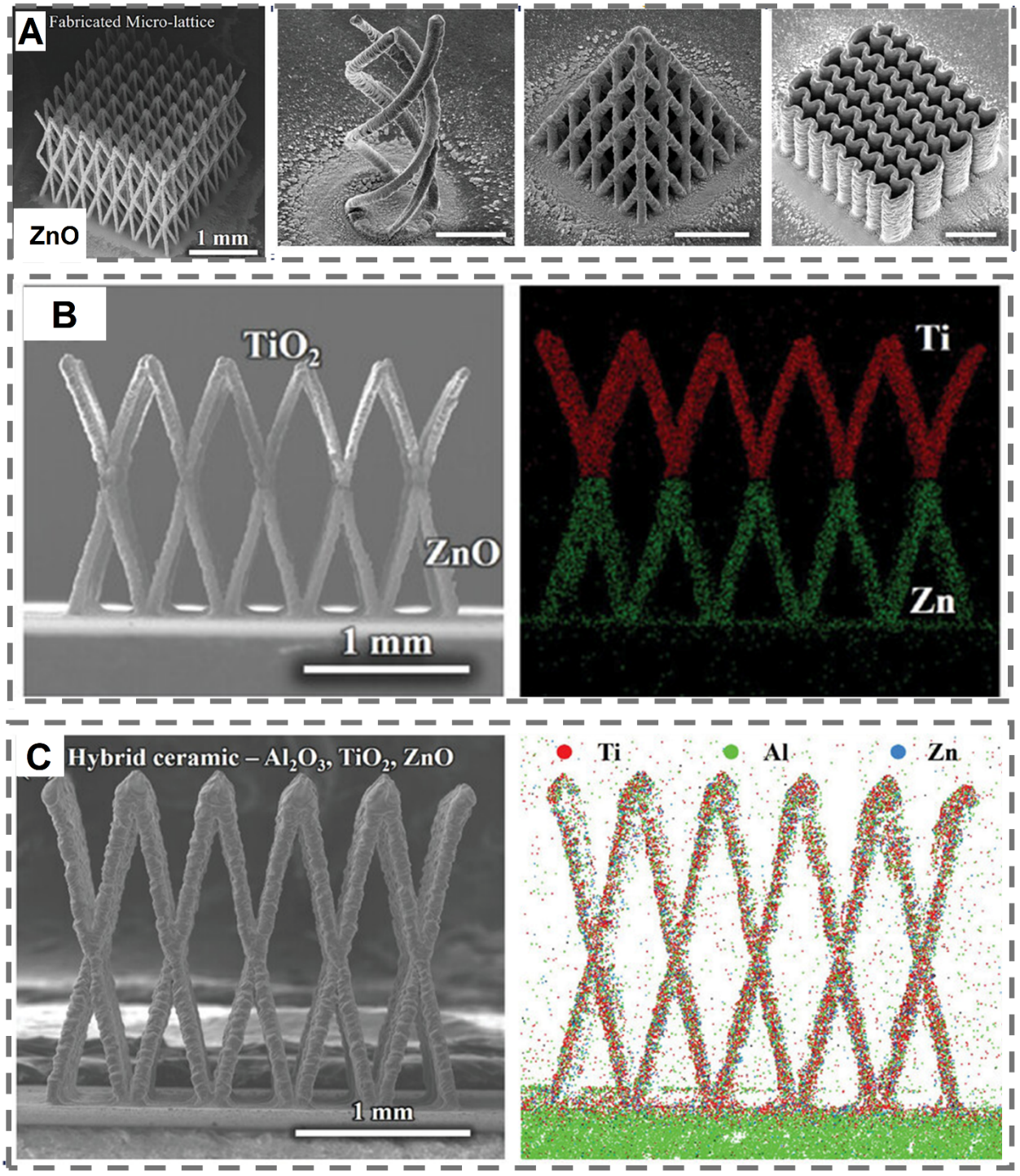

Figure 5. Monomaterial and multimaterial ceramic microarchitectures fabricated by aerosol jet printing demonstrating complex three-dimensional structures and spatially resolved compositional control. (A) Representative three-dimensional microarchitectures fabricated by aerosol jet printing, including ZnO microlattices (scale bar: 1 mm), multispiral structures (scale bar: 500 μm), pyramidal microlattices (scale bar: 500 μm), and wavy microwalls with nanoscale features (scale bar: 500 μm). (B) A bimaterial microlattice consisting of a TiO_2 upper region and a ZnO lower region, with EDX analysis confirming spatially resolved composition. (C) Hybrid ceramic microlattices composed of Al_2O_3, TiO_2, and ZnO, with EDX maps demonstrating a homogeneous distribution of Ti, Al, and Zn throughout the structure. Images adapted from Ref.[20]
Abbreviations: Al: Aluminum; Al_2O_3: Aluminum oxide; EDX: Energy-dispersive X-ray; Ti: Titanium; TiO_2:Titanium dioxide; Zn: Zinc; ZnO: Zinc oxide.

down in a track-by-track and layer-by-layer manner until the desired geometry is achieved.[96] Owing to its ability to deposit material precisely and dynamically, L-DED is well-suited for large-scale component fabrication, component repair, and the additive buildup of relatively complex 3D structures.

The application of L-DED to semiconductor fabrication remains extremely limited. To date, only a single study has reported the 3D printing of pillars from metallurgical-grade Si powder (98% purity) deposited onto Si substrates (Table 2).[53] This limited adoption is not unexpected, as L-DED is inherently optimized for high deposition rates and large-scale components, rather than the fine feature resolution and tight dimensional tolerances required in semiconductor manufacturing.[31] Consequently, L-DED is better suited for producing tooling, fixtures, or equipment components used in conventional semiconductor processing, rather than functional semiconductor devices themselves.

When applied to semiconductors, L-DED faces several fundamental challenges. These include insufficient dimensional accuracy, formation of inclusions during deposition, and crack formation driven by high thermal gradients in combination with the brittle nature of most semiconductor materials. Even for Si, severe interfacial cracking has been reported despite the use of substrate preheating up to 980 °C, underscoring the intrinsic difficulty of processing brittle semiconductors using this high-energy, melt-based technique.[53]

3. Future roadmap

3.1. Outlook for cm–mm-scale semiconductor fabrication by laser powder bed fusion

Collectively, it is evident that the AM of semiconductors is still at a nascent stage. To date, only a limited number of studies have been reported, many of which have struggled to produce defect-free, application-ready semiconductor components that can compete with their conventionally manufactured counterparts. Nevertheless, the progress achieved so far, particularly for thermoelectric materials, demonstrates significant promise. Building on the identified challenges, a roadmap for future research is outlined below.

For cm–mm-scale semiconductor components with sub-mm features, particularly in the context of thermoelectric materials, L-PBF remains the most promising AM technique. However, fully realizing its potential requires coordinated advances across materials, processing, and post-processing. Key research directions include:

(a) Development of compatible substrates

Laser PBF relies on depositing and melting powder layers onto compatible or compositionally matched substrates to ensure metallurgical bonding and to mitigate cracking. For many thermoelectric semiconductors, such substrates are currently unavailable. Future work should focus on producing composition-matched substrates via conventional routes such as liquid metallurgy, hot pressing, or spark plasma sintering.

(b) Production of L-PBF-grade semiconductor powders

High-quality powder feedstock is critical. Gas-atomized, spherical semiconductor powders with well-controlled particle size distributions must be developed. These powders should be systematically characterized in terms of flowability, packing density, laser absorptivity, oxygen content, and spreading behavior, parameters that remain largely unexplored for most semiconductor systems.

(c) Comprehensive process–structure–property–performance relationships

A systematic investigation of L-PBF process parameters across a wide range of semiconductors is required to optimize density, stoichiometric stability, control elemental evaporation, impurity levels, inclusions, surface quality, microstructural homogeneity, and crystallographic texture. These microstructural features must then be quantitatively correlated with electrical, thermal, mechanical, and thermoelectric performance.

(d) Post-build heat treatment and surface engineering

Tailored post-processing strategies, including heat treatments, annealing under controlled atmospheres, and surface finishing, are needed to refine microstructure, reduce defects, and achieve application-specific surface quality. Unlike metallic AM, where stress-relief and tempering treatments are routinely used to mitigate cracking and microstructural defects, the role of post-processing in semiconductor AM remains largely unexplored. Future research should systematically investigate whether controlled annealing can reduce residual stresses without inducing volatile element loss, dopant redistribution, phase segregation, or degradation of electronic properties. Establishing semiconductor-specific heat-treatment protocols represents a critical step toward defect mitigation and device reliability.

(e) Laser-based surface doping and modification

The feasibility of post-build laser surface doping or laser-assisted compositional modification within L-PBF platforms should be explored as a route to locally tune carrier concentration and functional gradients in semiconductor components.

(f) Geometric complexity beyond bulk ingots

Future studies should move beyond simple bulk or ingot-like geometries and exploit L-PBF's design freedom to fabricate complex, architected, and conformal semiconductor structures with functional advantages, such as improved thermal contact or enhanced transport properties.

(g) In situ alloying using elemental powder blends

The use of elemental powder mixtures for in situ alloying during L-PBF offers a flexible pathway for compound semiconductor fabrication. However, strategies to suppress compositional heterogeneity and phase segregation must be developed to meet the stringent requirements of semiconductor performance.

(h) High-temperature build platforms to mitigate cracking

Printing under elevated build-plate temperatures should be systematically investigated to reduce thermal gradients, mitigate residual stresses, and suppress cold cracking in brittle semiconductor materials.

(i) Atmosphere engineering during L-PBF

The development of controlled build atmospheres beyond inert Ar or N_2, including the use of anion-rich or semi-reactive atmospheres (e.g., Te- or Se-containing vapor overpressure), to suppress selective evaporation, stabilize stoichiometry, and mitigate phase segregation during L-PBF of volatile compound semiconductors.

(j) Texture and crystallographic orientation engineering

A systematic exploration of scan strategies, energy input modulation, and thermal gradients to deliberately control crystallographic texture and grain orientation, enabling alignment of anisotropic electrical and thermal transport properties with device-relevant directions in thermoelectric components.

(k) Defect and vacancy engineering as a functional design variable

A transition from defect suppression toward intentional control of point defects, antisite defects, and vacancy concentrations via L-PBF processing parameters, with the goal of tuning carrier concentration, phonon scattering, and overall thermoelectric performance.

(l) Hybrid L-PBF–solid-state transformation routes

The adoption of processing strategies in which L-PBF is used to fabricate near-net-shape, metastable bulk geometries, followed by controlled post-build solid-state transformations (e.g., ordering, precipitation, phase separation) to achieve the desired semiconductor phase constitution and functional properties.

(m) Functionally graded semiconductor architectures

The exploitation of L-PBF's spatial control to fabricate compositionally or dopant-graded semiconductor components, including graded n–p regions, thermal-expansion-matched interfaces, or property gradients within individual thermoelectric legs.

(n) Reliability, thermal cycling, and long-term stability assessment

A systematic evaluation of thermal fatigue, dopant diffusion, microstructural stability, and performance degradation under realistic service conditions to establish the long-term viability of L-PBF-fabricated semiconductor components.

3.2. Outlook for sub-mm to micro-scale semiconductor fabrication

At the sub-mm to micro-scale, AM processes (e.g., GRAM, IJP, AJP, and EAM) offer promising pathways for fabricating functional semiconductor structures and devices. However, further progress requires targeted advances in the following areas:

(i) Improved dimensional fidelity and resolution control: For GRAM and ink-based techniques, future work should focus on mitigating droplet spreading, wetting effects, and volumetric changes during reactions or drying, through optimized rheology, surface energy engineering, and substrate functionalization.

(ii) Expansion of printable semiconductor material libraries: The development of stable, printable inks or precursors for a broader range of semiconductors beyond ZnO, TiO_2, and PbTe is critical. This includes compound semiconductors, doped systems, and functional heterostructures with controlled composition.

(iii) Advanced ink and precursor chemistry design: Future efforts should emphasize binder-free or low-residue formulations, controlled decomposition pathways, and precursor systems that minimize residual phases, impurity incorporation, and band gap perturbations after post-processing.

(iv) Reduction of post-processing complexity and damage: Multi-step thermal treatments (e.g., calcination, debinding, and oxidation) should be streamlined or partially integrated into the printing process to reduce internal stresses, cracking, and loss of structural integrity.

(v) Controlled microstructure and phase formation: Systematic studies linking printing parameters to grain size, porosity, phase purity, and defect

density are needed to establish process–structure–property relationships at the micro-scale.

(vi) True 3D device architectures beyond 2D/2.5D patterning: While many ink-based techniques are currently used for planar or quasi-3D structures, future work should emphasize freestanding microstructures, vertical integration, and multilayer stacking, enabling functional 3D semiconductor devices.

(vii) Multimaterial and heterostructure integration: Building on early demonstrations (e.g., ZnO–TiO_2, hybrid oxide systems), research should explore spatially resolved multimaterial printing for junction formation, sensing platforms, and integrated device architectures.

(viii) Reliability and device-level validation: Beyond proof-of-concept structures, future studies must address long-term stability, thermal cycling, electrical reliability, and environmental robustness of sub-mm and micro-scale printed semiconductor devices.

3.3. Outlook for sub-micron to nanoscale semiconductor fabrication

For feature sizes below 1 μm, EHD-RP and TPL represent the most promising AM routes. At these length scales, the focus shifts from bulk fabrication to precision, functionality, and device-level integration.

(i) Broadening material diversity beyond metal oxides: To date, both EHD-RP and TPL have been demonstrated primarily for ZnO and a limited set of metal oxides. Future work should explore new semiconductor chemistries, including doped oxides, compound semiconductors, and mixed-anion systems.

(ii) Lower-temperature and faster post-conversion routes: For EHD-RP, strategies to achieve complete and uniform oxidation at reduced temperatures and shorter times are essential to prevent substrate damage and structural distortion. Similarly, TPL-derived structures would benefit from lower-temperature inorganic conversion routes.

(iii) Mitigation of thermal mismatch and substrate damage: At the nanoscale, thermal expansion mismatch between printed structures and substrates (e.g., Si) can cause distortion or fracture. Future work should explore buffer layers, compliant substrates, and low-stress conversion pathways.

(iv) Reduction of contamination and residue effects: In TPL, contamination arising from photoresist decomposition and residual organics remains a major concern. Development of inorganic-rich or hybrid photoresists with cleaner conversion chemistry is a critical research direction.

(v) Pushing resolution beyond current photoresist limits: Since conventional photoresists impose critical dimension limits (approximately 80–100 nm), future efforts should focus on novel resist chemistries, alternative photoinitiators, and shrinkage-engineering strategies to further enhance resolution.

(vi) Direct semiconductor printing without indirect conversion: A major long-term goal is to reduce reliance on indirect routes (metal → oxide or polymer → oxide) and enable the direct printing of functional semiconductors with controlled stoichiometry and electronic properties.

(vii) Integration with conventional micro/nanofabrication: Future research should emphasize hybrid fabrication workflows, combining EHD-RP or TPL with lithography, etching, and thin-film deposition to enable device-level integration rather than standalone structures.

4. Conclusion

Additive manufacturing of semiconductors remains in its infancy, yet the progress summarized in this perspective highlights its growing potential as a complementary fabrication paradigm, rather than a direct replacement for conventional semiconductor fabrication. By critically assessing current AM processes across relevant length scales, this perspective emphasizes that AM offers unique value, particularly in architected thermoelectric components, microstructured sensors, and nano-enabled functional devices, even as fundamental challenges persist. The proposed roadmap underscores that future success will rely on co-design of materials, processes, and device architectures, as well as tighter integration with established semiconductor manufacturing workflows. As these directions mature, AM is poised to expand the design space of semiconductor devices beyond planar constraints, enabling new functionalities that are inaccessible through traditional fabrication routes.

Acknowledgments

None.

Funding

None.

Conflict of interest

Swee Leong Sing is the Editor-in-Chief of this journal, but was not in any way involved in the editorial and peer-review process conducted for this paper, directly or indirectly. Separately, other authors declared that they have no known competing financial interests or personal relationships that could have influenced the work reported in this paper.

Author contributions

Conceptualization: All authors
Visualization: Ali Ghasemi
Writing – original draft: Ali Ghasemi
Writing – review & editing: All authors

Ethics approval and consent to participate

Not applicable.

Consent for publication

Not applicable.

Availability of data

Not applicable.

References

1. Sze SM, Li Y, Ng KK. *Physics of semiconductor devices*. 4th ed. Hoboken, NJ, USA: John Wiley & Sons; 2021.
2. Streetman BG, Banerjee S. *Solid state electronic devices*. 7th ed. New Jersey, USA: Prentice Hall; 2016. Available from: https://rrsdce.wordpress.com/wp-content/uploads/2018/07/sspd-eee-swapnil.pdf [Last accessed on 2026 Feb 06].
3. Askeland DR, Phulé PP, Wright WJ, Bhattacharya D. The science and engineering of materials. 2003. Available from: https://anupturnedworld.wordpress.com/wp-content/uploads/2016/06/askeland-the-science-and-engineering-of-materials.pdf [Last accessed on 2026 Feb 06].
4. Perez N. Physical Properties of Solids. In: Perez N, editor. *Materials Science: Theory and Engineering*. Berlin/Heidelberg, Germany: Springer Nature; 2024:739-788.
   doi: 10.1007/978-3-031-57152-7_14
5. Chen C-Y, Retamal JRD, Wu I-W, *et al*. Probing surface band bending of surface-engineered metal oxide nanowires. *Acs Nano*. 2012;6(11):9366-9372.
   doi: 10.1021/nn205097e
6. Yin Y, Yang Y. Sustainable Transition of the Global Semiconductor Industry: Challenges, Strategies, and Future Directions. *Sustainability*. 2025;17(7):3160.
   doi: 10.3390/su17073160
7. Peter Y, Cardona M. *Fundamentals of semiconductors: physics and materials properties*. Berlin/Heidelberg, Germany: Springer Science & Business Media; 2010.
   doi: 10.1007/978-3-642-00710-1
8. Pierret RF. *Semiconductor device fundamentals*. Boston, MA, USA: Addison-Wesley Publishing Company; 1996. Available from: https://s3-us-west-2.amazonaws.com/valpont/uploads/20151124213927/Semiconductor_Device_Fundamentals1.pdf [Last accessed on 2026 Feb 06].
9. Granqvist CG. *Handbook of inorganic electrochromic materials*. Amsterdam, The Netherlands: Elsevier; 1995.
   doi: 10.1016/B978-044489930-9/50001-5
10. Wang QH, Kalantar-Zadeh K, Kis A, Coleman JN, Strano MS. Electronics and optoelectronics of two-dimensional transition metal dichalcogenides. *Nat Nanotechnol*. 2012;7(11):699-712.
    doi: 10.1038/nnano.2012.193
11. Snyder GJ, Toberer ES. Complex thermoelectric materials. *Nature Mater*. 2008;7(2):105-114.
    doi: 10.1038/nmat2090
12. Poelking CR. *The (Non-) Local Density of States of Electronic Excitations in Organic Semiconductors*. Berlin/Heidelberg, Germany: Springer; 2017.
    doi: 10.1007/978-3-319-69599-0_7
13. Grätzel M. The light and shade of perovskite solar cells. *Nature Mater*. 2014;13(9):838-842.
    doi: 10.1038/nmat4065
14. Baliga BJ. *Fundamentals of power semiconductor devices*. Springer; 2018. Available from: https://link.springer.com/book/10.1007/978-3-319-93988-9 [Last accessed on 2026 Feb 06].
15. Hasan MZ, Kane CL. Colloquium: topological insulators. *Rev Mod Phys*. 2010;82(4):3045-3067.
    doi: 10.1103/RevModPhys.82.3045
16. Geim AK, Grigorieva IV. Van der Waals heterostructures. *Nature*. 2013;499(7459):419-425.
    doi: 10.1038/nature12385
17. Sze S. VLSI technology overviews and trends. *Jpn J Appl Phys*. 1983;22(S1):3.
    doi: 10.7567/JJAPS.22S1.3
18. Vaidya AA, Adithya R, Aravind Raj S. Additive Manufacturing for the Semiconductor Industry: An Automotive Perspective. In: *Metal Additive Manufacturing: Methods, Materials and Applications*. Berlin/Heidelberg, Germany: Springer; 2025:387-402.
    doi: 10.1007/978-981-96-8162-4_21
19. Craton MT, Konstantinou X, Albrecht JD, Chahal P,

Papapolymerou J. Additive manufacturing of a W-band system-on-package. *IEEE Trans Microw Theory Tech.* 2021;69(9):4191-4198.

doi: 10.1109/TMTT.2021.3076066

20. Hu C, Jahan S, Yuan B, Panat R. 3D-AJP: Fabrication of Advanced Microarchitected Multimaterial Ceramic Structures via Binder-Free and Auxiliary-Free Aerosol Jet 3D Nanoprinting. *Adv Sci*. 2025;12(15):2405334.

doi: 10.1002/advs.202405334

21. Lu LL, Lu YY, Xiao ZJ, *et al*. Wood-inspired high-performance ultrathick bulk battery electrodes. *Adv Mater*. 2018;30(20):1706745.

doi: 10.1002/adma.201706745

22. Lai W, Erdonmez CK, Marinis TF, *et al*. Ultrahigh-energy-density microbatteries enabled by new electrode architecture and micropackaging design. *Adv Mater*. 2010;22(20):E139-E144.

doi: 10.1002/adma.200903650

23. Yee DW, Lifson ML, Edwards BW, Greer JR. Additive manufacturing of 3D-architected multifunctional metal oxides. *Adv Mater*. 2019;31(33):1901345.

doi: 10.1002/adma.201901345

24. Shi J, Chen X, Wang W, Chen H. A new rapid synthesis of thermoelectric Sb2Te3 ingots using selective laser melting 3D printing. *Mater Sci Semicond Process*. 2021;123:105551.

doi: 10.1016/j.mssp.2020.105551

25. Gayner C, Kar KK. Recent advances in thermoelectric materials. *Prog Mater Sci*. 2016;83:330-382.

doi: 10.1016/j.pmatsci.2016.07.002

26. Narvan M, Ghasemi A, Fereiduni E, Kendrish S, Elbestawi M. Part deflection and residual stresses in laser powder bed fusion of H13 tool steel. *Mater Des*. 2021;204:109659.

doi: 10.1016/j.matdes.2021.109659

27. Balbaa M, Ghasemi A, Fereiduni E, Al-Rubaie K, Elbestawi M. Improvement of fatigue performance of laser powder bed fusion fabricated IN625 and IN718 superalloys via shot peening. *J Mater Process Technol.* 2022;304:117571.

doi: 10.1016/j.jmatprotec.2022.117571

28. Fereiduni E, Ghasemi A, Elbestawi M. Selective laser melting of aluminum and titanium matrix composites: recent progress and potential applications in the aerospace industry. *Aerospace*. 2020;7(6):77.

doi: 10.3390/aerospace7060077

29. Yu K, Yao Y, Zhang W, *et al*. Defects, monitoring, and AI-enabled control in soft material additive manufacturing: a review. *Virtual Phys Prototyp.* 2025;20(1):e2588456.

doi: 10.1080/17452759.2025.2588456

30. Wang YM, Voisin T, McKeown JT, *et al*. Additively manufactured hierarchical stainless steels with high strength and ductility. *Nat Mater.* 2018;17(1):63-71.

doi: 10.1038/nmat5021

31. DebRoy T, Wei HL, Zuback JS, *et al*. Additive manufacturing of metallic components–process, structure and properties. *Prog Mater Sci*. 2018;92:112-224.

doi: 10.1016/j.pmatsci.2017.10.001

32. Yu K, Zhang W, Lu L, *et al*. MG-LDM: A multimodal guided latent diffusion model with Mamba-based temporal encoding for inverse topological design of tissue engineering skin substitutes. *Adv Eng Inform.* 2026;71:104275.

doi: 10.1016/j.aei.2025.104275

33. Han C, Fang Q, Shi Y, Tor SB, Chua CK, Zhou K. Recent advances on high-entropy alloys for 3D printing. *Adv Mater*. 2020;32(26):1903855.

doi: 10.1002/adma.201903855

34. ISO. ISO/ASTM 52900:2021(en) Additive manufacturing-general principles-fundamental and vocabulary. Available from: https://www.iso.org/obp/ui/#iso:std:iso-astm:52900:ed-2:v1:en [Last accessed on 2026 Feb 06].

35. Cao C, Xia X, Shen X, *et al*. Ultra-high precision nano additive manufacturing of metal oxide semiconductors via multi-photon lithography. *Nat Commun.* 2024;15(1):9216.

doi: 10.1038/s41467-024-52929-8

36. Zhang H, Hobbis D, Nolas GS, LeBlanc S. Laser additive manufacturing of powdered bismuth telluride. *J Mater Res.* 2018;33(23):4031-4039.

doi: 10.1557/jmr.2018.390

37. Welch R, Hobbis D, Birnbaum AJ, Nolas G, LeBlanc S. Nano-and micro-structures formed during laser processing of selenium doped bismuth telluride. *Adv Mater Interfaces.* 2021;8(15):2100185.

doi: 10.1002/admi.202100185

38. Qiu J, Yan Y, Luo T, *et al*. 3D Printing of highly textured bulk thermoelectric materials: mechanically robust BiSbTe alloys with superior performance. *Energy Environ Sci*. 2019;12(10):3106-3117.

doi: 10.1039/C9EE02044F

39. Zhan R, Lyu J, Yang D, *et al*. Large-scale SHS based 3D printing of high-performance n-type BiTeSe: Comprehensive development from materials to modules. *Mater Today Phys.* 2022;24:100670.

doi: 10.1016/j.mtphys.2022.100670

40. Mao Y, Yan Y, Wu K, *et al*. Non-equilibrium synthesis and characterization of n-type Bi 2 Te 2.7 Se 0.3 thermoelectric material prepared by rapid laser melting and solidification. *Rsc Adv.* 2017;7(35):21439-21445.

doi: 10.1039/C7RA02677C

41. Baudry M, Savelli G, Roux G. 3D printing of bulk thermoelectric materials: Laser powder bed fusion of N-type silicon germanium. *Mater Sci Eng B*. 2023;298:116897.

doi: 10.1016/j.mseb.2023.116897

42. Welch R, Gubisch S, Leblanc S. Nano/microstructures and thermoelectric properties of silicon germanium manufactured using laser powder bed fusion. *J Mater Process Technol.* 2025;337:118749.

doi: 10.1016/j.jmatprotec.2025.118749

43. Wu K, Yan Y, Zhang J, *et al*. Preparation of n-type Bi2Te3 thermoelectric materials by non-contact dispenser printing combined with selective laser melting. *Phys Status Solidi (RRL)–Rapid Res Lett*. 2017;11(6):1700067.

doi: 10.1002/pssr.201700067

44. Lai Z, Guo T, Zhang S, *et al*. Selective laser melting of commercially pure silicon. *J Wuhan Univ Technol-Mater Sci Ed*. 2022;37(6):1155-1165.

doi: 10.1007/s11595-022-2647-3

45. Shi J, Chen H, Jia S, Wang W. 3D printing fabrication of porous bismuth antimony telluride and study of the thermoelectric properties. *J Manuf Process.* 2019;37:370-375.

doi: 10.1016/j.jmapro.2018.11.001

46. Gagnon JC, Presley M, Le NQ, Montalbano TJ, Storck S. A pathway to compound semiconductor additive manufacturing. *MRS Commun.* 2019;9(3):1001-1007.

doi: 10.1557/mrc.2019.114

47. Berkson MA, Pogue EA, Bartlett ME, *et al*. Evaluation and Mitigation of Impurities in Additively Manufactured Epitaxial Gallium Nitride. *Cryst Growth Des*. 2024;24(8):3149-3159.

doi: 10.1021/acs.cgd.3c01163

48. Tran V-T, Wei Y, Yang H, Zhan Z, Du H. All-inkjet-printed flexible ZnO micro photodetector for a wearable UV monitoring device. *Nanotechnology*. 2017;28(9):095204.

doi: 10.1088/1361-6528/aa57ae

49. Tran V-T, Wei Y, Du H. Influence of thermal treatment on electronic properties of inkjet-printed zinc oxide semiconductor. *Int J Smart Nano Mater.* 2022;13(2):330-345.

doi: 10.1080/19475411.2022.2084172

50. Nydegger M, Pruška A, Galinski H, Zenobi R, Reiser A, Spolenak R. Additive manufacturing of Zn with submicron resolution and its conversion into Zn/ZnO core–shell structures. *Nanoscale*. 2022;14(46):17418-17427.

doi: 10.1039/D2NR04549D

51. Oh H, Charles H, Im T, Khan H, Lee CS. Extrusion-based additive manufacturing of three-dimensional MoSe2-nanosheet-coated TiO2 hetero-structures for photocatalytic CO2 reduction. *Int J Adv Manuf Technol.* 2024;130(5):2731-2742.

doi: 10.1007/s00170-023-12869-x

52. Lee J, Choo S, Ju H, *et al*. Thermoelectric Generators: Doping-Induced Viscoelasticity in PbTe Thermoelectric Inks for 3D Printing of Power-Generating Tubes (Adv. Energy Mater. 20/2021). *Adv Energy Mater*. 2021;11(20).

doi: 10.1002/aenm.202170076

53. Le Dantec M, Abdulstaar M, Leistner M, Leparoux M, Hoffmann P. *Additive manufacturing of semiconductor silicon on silicon using direct laser melting*. Berlin/Heidelberg, Germany: Springer; 2017:104-116.

doi: 10.1007/978-3-319-66866-6_10

54. Yue W, Zhang Y, Zheng Z, Lai Y. Hybrid laser additive manufacturing of metals: a review. *Coatings*. 2024;14(3):315.

doi: 10.3390/coatings14030315

55. Vargas-Bernal R, He P, Zhang S. *Hybrid Nanomaterials: Flexible Electronics Materials*. BoD–Books on Demand; 2020.

doi: 10.5772/intechopen.83326

56. Menétrey M, Koch L, Sologubenko A, Gerstl S, Spolenak R, Reiser A. Targeted additive micromodulation of grain size in nanocrystalline copper nanostructures by electrohydrodynamic redox 3D printing. *Small*. 2022;18(51):2205302.

doi: 10.1002/smll.202270276

57. Gramlich G, Huber R, Häslich F, Bhutani A, Lemmer U, Zwick T. Process considerations for Aerosol-Jet printing of ultra fine features. *Flex Print Electron.* 2023;8(3):035002.

doi: 10.1088/2058-8585/ace3d8

58. Ghasemi A, Fereiduni E, Balbaa M, Elbestawi M, Habibi S. Unraveling the low thermal conductivity of the LPBF fabricated pure Al, AlSi12, and AlSi10Mg alloys through substrate preheating. *Addit Manuf.* 2022;59:103148.

doi: 10.1016/j.addma.2022.103148

59. Narvan M, Ghasemi A, Fereiduni E, Elbestawi M. Laser powder bed fusion of functionally graded bi-materials: Role of VC on functionalizing AISI H13 tool steel. *Mater Des.* 2021;201:109503.

doi: 10.1016/j.matdes.2021.109503

60. Ababneh M, Tarau C, Anderson W. 3D Printed Thermal Management System for the Next Generation of Gallium Nitride-Based Solid State Power Amplifiers. In: Proceedings of the 49th International Conference on Environmental Systems. 2019. Available from: https://ttu-ir.tdl.org/server/api/core/bitstreams/2344eb44-4812-4994-ad72-f7005f3f1dd3/content [Last accessed on 2026 Feb 06].

61. Park S, Lee J, Lee S, *et al*. Temperature Uniformity Control

of 12-Inch Semiconductor Wafer Chuck Using Double-Wall TPMS in Additive Manufacturing. *Materials*. 2025;18(1):211.

doi: 10.3390/ma18010211

62. Ye J, El Desouky A, Elwany A. On the applications of additive manufacturing in semiconductor manufacturing equipment. *J Manuf Process.* 2024;124:1065-1079.

doi: 10.1016/j.jmapro.2024.05.054

63. Joralmon D, Tang T, Jayant L, Yoo M, Li X. Recent Advances and Prospects in Selective Laser Sintering (SLS) and Melting (SLM) and Multiphoton Lithography for 3D Printing. In: *Laser-based Techniques for Nanomaterials: Processing to Characterization*; Cambridge, UK: Royal Society of Chemistry. 2024;185-217.

doi: 10.1039/9781837673513-00185

64. Kruth J-P, Wang X, Laoui T, Froyen L. Lasers and materials in selective laser sintering. *Assem Autom.* 2003;23(4):357-371.

doi: 10.1108/01445150310698652

65. Tritt TM, Subramanian M. Thermoelectric materials, phenomena, and applications: a bird's eye view. *MRS Bull.* 2006;31(3):188-198.

doi: 10.1557/mrs2006.44

66. El-Desouky A, Read AL, Bardet PM, Andre M, LeBlanc S. Selective laser melting of a bismuth telluride thermoelectric materials. 2015. 1043-1050. Available from: https://www.leblanclab.com/uploads/2/6/4/3/26439896/selective_laser_melting_of_a_bismuth_telluride_thermoelectric_material_eldesouky.pdf [Last accessed on 2026 Feb 06].

67. LeBlanc S, Yee SK, Scullin ML, Dames C, Goodson KE. Material and manufacturing cost considerations for thermoelectrics. *Renew Sustain Energy Rev.* 2014;32:313-327.

doi: 10.1016/j.rser.2013.12.030

68. LeBlanc S. Thermoelectric generators: Linking material properties and systems engineering for waste heat recovery applications. *Sustain Mater Technol.* 2014;1:26-35.

doi: 10.1016/j.susmat.2014.11.002

69. Carter MJ, El-Desouky A, Andre MA, Bardet P, LeBlanc S. Pulsed laser melting of bismuth telluride thermoelectric materials. *J Manuf Process.* 2019;43:35-46.

doi: 10.1016/j.jmapro.2019.04.021

70. El-Desouky A, Carter M, Mahmoudi M, Elwany A, LeBlanc S. Influences of energy density on microstructure and consolidation of selective laser melted bismuth telluride thermoelectric powder. *J Manuf Process*. 2017;25:411-417.

doi: 10.1016/j.jmapro.2016.12.008

71. El-Desouky A, Carter M, Andre MA, Bardet PM, LeBlanc S. Rapid processing and assembly of semiconductor thermoelectric materials for energy conversion devices. *Mater Lett*. 2016;185:598-602.

doi: 10.1016/j.matlet.2016.07.152

72. Panwisawas C, Gong Y, Tang YT, Reed RC, Shinjo J. Additive manufacturability of superalloys: Process-induced porosity, cooling rate and metal vapour. *Addit Manuf*. 2021;47:102339.

doi: 10.1016/j.addma.2021.102339

73. Ghoussoub JN, Tang YT, Dick-Cleland WJ, *et al*. On the influence of alloy composition on the additive manufacturability of Ni-based superalloys. *Metall Mater Trans A*. 2022;53(3):962-983.

doi: 10.1007/s11661-021-06568-z

74. Huang S, Zhang J, Fu H, *et al*. Irradiation performance of high entropy ceramics: A comprehensive comparison with conventional ceramics and high entropy alloys. *Prog Mater Sci*. 2024;143:101250.

doi: 10.1016/j.pmatsci.2024.101250

75. Wei S, Qureshi MW, Wei J, *et al*. Short-range order in high entropy carbides. *Nat Commun.* 2026.

doi: 10.1038/s41467-026-69095-8

76. Wu Y, Sun K, Yu S, Zuo L. Modeling the selective laser melting-based additive manufacturing of thermoelectric powders. *Addit Manuf*. 2021;37:101666.

doi: 10.1016/j.addma.2020.101666

77. Klemenz C, Scheel H. Crystal growth and liquid-phase epitaxy of gallium nitride. *J Cryst Growth*. 2000;211(1-4):62-67.

doi: 10.1016/S0022-0248(99)00831-3

78. Saengchairat N, Tran T, Chua C-K. A review: additive manufacturing for active electronic components. *Virtual Phys Prototyp.* 2017;12(1):31-46.

doi: 10.1080/17452759.2016.1253181

79. Tran VT. Inkjet-printed ZnO thin film semiconductor for additive manufacturing of electronic devices. Doctoral thesis. Nanyang Technological University; 2019. Available from: https://dr.ntu.edu.sg/entities/publication/81137943-8108-40fb-b814-07971ea64d83 [Last accessed on 2026 Feb 06].

80. Lesch A, Cortés-Salazar F, Bassetto VC, Amstutz V, Girault HH. Inkjet printing meets electrochemical energy conversion. *Chimia*. 2015;69(5):284-284.

doi: 10.2533/chimia.2015.284

81. Mattana G, Loi A, Woytasik M, Barbaro M, Noël V, Piro B. Inkjet-printing: A new fabrication technology for organic transistors. *Adv Mater Technol.* 2017;2(10):1700063.

doi: 10.1002/admt.201700063

82. Wu Y, Tamaki T, Volotinen T, Belova L, Rao KV. Enhanced photoresponse of inkjet-printed ZnO thin films capped with

CdS nanoparticles. *J Phys Chem Lett*. 2010;1(1):89-92.

doi: 10.1021/jz900008y

83. Akbari S, Kostov K, Lim J-K, *et al*. Fully printed ultrathin embedded electronics package for wide band gap power semiconductor devices using multimaterial inkjet additive manufacturing. *Prog Addit Manuf*. 2025:1-9.

doi: 10.1007/s40964-025-01040-5

84. Reiser A, Lindén M, Rohner P, *et al*. Multi-metal electrohydrodynamic redox 3D printing at the submicron scale. *Nat Commun*. 2019/04/23 2019;10(1):1853.

doi: 10.1038/s41467-019-09827-1

85. Hirt L, Reiser A, Spolenak R, Zambelli T. Additive Manufacturing of Metal Structures at the Micrometer Scale. *Adv Mater*. 2017;29(17).

doi: 10.1002/adma.201604211

86. Hengsteler J, Lau GP, Zambelli T, Momotenko D. Electrochemical 3D micro-and nanoprinting: current state and future perspective. *Electrochem Sci Adv*. 2022;2(5):e2100123.

doi: 10.1002/elsa.202100123

87. Jaiswal A, Rastogi CK, Rani S, Singh GP, Saxena S, Shukla S. Two decades of two-photon lithography: Materials science perspective for additive manufacturing of 2D/3D nano-microstructures. *iScience*. 2023;26(4):106374.

doi: 10.1016/j.isci.2023.106374

88. Hoey JM, Lutfurakhmanov A, Schulz DL, Akhatov IS. A review on aerosol-based direct-write and its applications for microelectronics. *J Nanotechnol*. 2012;2012(1):1-22.

doi: 10.1155/2012/324380

89. Wilkinson N, Smith M, Kay RW, Harris R. A review of aerosol jet printing—a non-traditional hybrid process for micro-manufacturing. *Int J Adv Manuf Technol*. 2019;105(11):4599-4619.

doi: 10.1007/s00170-019-03438-2

90. Binder S, Glatthaar M, Rädlein E. Analytical investigation of aerosol jet printing. *Aerosol Sci Technol*. 2014;48(9):924-929.

doi: 10.1080/02786826.2014.940439

91. Sun M. Micro-Additive Manufacturing of Metal-Oxide-Semiconductor Based Gas Sensors for Diabetes Detection via Breath Analysis. 2021. Available from: https://uwspace.uwaterloo.ca/items/742f212e-6152-4a14-8791-8532fef60ce8 [Last accessed on 2026 Feb 06].

92. Oh H, Im T, Pyo J, Lee J-s, Lee CS. Study of solid loading of feedstock using trimodal iron powders for extrusion based additive manufacturing. *Sci Rep*. 2023;13(1):4819.

doi: 10.1038/s41598-023-32095-5

93. Lakhdar Y, Tuck C, Binner J, Terry A, Goodridge R. Additive manufacturing of advanced ceramic materials. *Prog Mater Sci*. 2021;116:100736.

doi: 10.1016/j.pmatsci.2020.100736

94. Yu K, Gao Q, Yao Y, Lin Z, Zhang P, Lu L. Investigation of the humidity control in the printing space for the material extrusion of medical biodegradable hydrogel. *Addit Manuf*. 2024;93:104452.

doi: 10.1016/j.addma.2024.104452

95. Mueller B. Additive manufacturing technologies–Rapid prototyping to direct digital manufacturing. *Assem Autom*. 2012;32(2).

doi: 10.1108/aa.2012.03332baa.010

96. Alikhani AA, Ghasemi A, Pirjamadi A, Peng Z, Pouranvari M. Understanding microstructural evolution and metallurgical challenges in wire-arc directed energy deposition of 430 ferritic stainless steel. *Mater Charact*. 2025;219:114645.

doi: 10.1016/j.matchar.2024.114645

ACCSCIENCE PUBLISHING

Engineering Science in Additive Manufacturing

ORIGINAL RESEARCH ARTICLE

Understanding melt pool characteristics as a means for reducing build layout quality variations in laser-based powder bed fusion: An approach toward spatial parameter compensations

Jaivindra Singh[1], J. P. Oliveira[1], Hunter Taylor[2,3], Jesus Rivas[2*], Jorge Mireles[2], Oscar Garcia[2], and Ryan Wicker[2,4]

[1]CENIMAT/I3N, Department of Materials Science, NOVA School of Science and Technology, Universidade NOVA de Lisboa, Caparica, Portugal

[2]W.M. Keck Center for 3D Innovation, The University of Texas at El Paso, El Paso, Texas, United States of America

[3]Tailored Alloys LLC, Youngstown, Ohio, United States of America

[4]Department of Aerospace and Mechanical Engineering, The University of Texas at El Paso, El Paso, Texas, United States of America

***Corresponding author:**
Jesus Rivas
(jarivasescarce@utep.edu)

Citation: Singh J, Oliveira JP, Taylor H, Rivas J Mireles J, Garcia O, Wicker R. Understanding melt pool characteristics as a means for reducing build layout quality variations in laser-based powder bed fusion: An approach toward spatial parameter compensations. *Eng Sci Add Manuf*. 2026;2(1):025420029. doi: 10.36922/ESAM025420029

Received: October 15, 2025

Revised: November 11, 2025

Accepted: November 12, 2025

Published online: February 4, 2026

Abstract

This study investigates the impact of build platform location on melt pool variability during laser-based powder bed fusion of metals. The incident angle and gas flow are hypothesized to influence melt pool penetration and contribute to spatial variations in the melt pool. Results show that the typical build strategy using the same material-dependent processing parameters for all parts throughout the build chamber produces parts with location-dependent properties. An overarching goal of the present work was to attempt to fabricate similar parts at different locations within the build chamber by identifying processing parameters that produce similar melt pool depths at these locations. It was further hypothesized that by normalizing process parameters through similar melt pool depths, similar porosity counts could be achieved at these locations, thus mitigating process-induced variability. The study emphasizes the necessity of spatial parameter adjustments to minimize variability across different locations within the build platform, as well as the requirement for uniform gas flow across the build chamber, thereby eliminating gas flow-dependent variations from the analysis.

Keywords: Laser powder bed fusion; Build location; Test artifact; Surface roughness; Porosity

1. Introduction

Metal additive manufacturing (AM) is increasingly recognized as a potential complement and possible replacement in certain situations for traditional fabrication techniques across different industries due to its capacity for producing complex geometries, facilitating customization, and minimizing material waste.[1,2] Among the various AM technologies,

laser-based powder bed fusion of metals (PBF-LB/M) stands out for its superior design freedom and accuracy, surpassing alternatives such as directed energy deposition (DED) and electron beam powder bed fusion of metals (PBF-EB/M).[3] PBF-LB/M operates by melting a feedstock powder layer by layer, enabling the creation of intricate shapes that are often unachievable with conventional methods, when combined with computer-aided design (CAD).[4] Despite this, only a few hypoeutectic aluminum alloys, such as AlSi10Mg, exhibit reliable printability due to their narrow freezing ranges and favorable mechanical properties.[5] To drive the industrial application of PBF-LB/M with aluminum alloys, it is crucial to explore key process variables, including powder-laser interactions and potential defect formation mechanisms.

Qualification test artifacts (QTAs), specimens, and/or coupons enable systematic and quantitative evaluation of the capabilities and limitations of a metal AM process. In the literature, three distinct categories of test artifacts have been identified: geometrical benchmarks, process benchmarks, and mechanical benchmarks. These artifacts serve to ensure geometrical accuracy, optimal process parameters, and sound mechanical properties.[6-8] The quality of PBF-LB/M products is influenced by several factors, including gas flow dynamics, build orientation, build location, and laser power-to-scan speed ratio, all of which impact mechanical properties.[9-12]

Previous research has highlighted the importance of uniform gas flow and efficient byproduct removal in preventing pore formation.[13] Wang *et al.*[14] demonstrated that porosity decreased in AlSi10Mg when the gas flow velocity was increased from 1.0 m/s to 4.0 m/s. Bagasol *et al.*[15] showed a similar porosity reduction in Ti-6Al-4 V alloy parts associated with gas flow by increasing the distance of parts from the argon gas flow inlet. Weaver *et al.*[16] evaluated the melt pool depth of single-track laser scans. They found a reduction in melt pool depth for slow laser scan speeds on the build platform, particularly near the inlet nozzle, and when the laser scans were parallel to the gas flow direction. Similarly, another factor associated with the quality of PBF-LB/M products is the angle of incidence with respect to the powder layer.[17] Previous research has highlighted the effect of the angle of incidence on surface roughness.[18]

Sendino *et al.*[19] evaluated variations on surface roughness in INCONEL 718 parts with respect to the incident angle, obtaining different values between parts located in the centers and the outer border. In addition, melt-pool morphology can be affected by the incident angle. Li *et al.*[20] used numerical modeling to demonstrate that an increase in incident angle leads to a shallower melt pool and a width comparable to the beam size as a function of the incident angle. Others have explored methods to mitigate the effect of the incidence angle. Dowling *et al.*[21] evaluated adjusting the energy density (by changing the speed) as a function of the incident angle, obtaining more uniform mechanical properties among samples in different build locations. Other work has been conducted for PBF-LB/M in general, demonstrating the need for geometry-specific parameter modifications to normalize energy input between long and short vectors.[22] This is especially reinforced by Rivas *et al.*[23] who found that lattice regions were more susceptible to porosity because a parameter set optimized for bulk features was universally applied. Moreover, Valadez Mesta *et al.*[24] demonstrated that the dynamic limitations of a laser scanner can lead to variations in melt pool depths, particularly at corner features where steering mirrors must slow down to achieve the commanded geometry, resulting in increased energy being applied to those regions.

Although numerous studies have explored the individual influence of parameters such as gas flow dynamics, build orientation, and laser incident angle on part quality in PBF-LB/M, the combined and spatially dependent interactions among these factors remain poorly understood.[22,23] Most previous investigations have relied on localized analyses or simplified geometries, which fail to capture the complex coupling between gas flow distribution, laser energy absorption, and build platform position.[25,26] As a result, spatial variations across the build area are often overlooked, leading to potential inconsistencies in mechanical performance and reduced process reproducibility. This limitation highlights a critical research gap in establishing a systematic correlation between the location of the build platform and the resultant quality attributes through an integrated experimental framework. The present study addresses this gap by employing a melt pool study using both a 2D scan on a plate and the manufacture of a 3D component, through the recently developed QTA proposed by Taylor *et al.*[8] By utilizing this approach, the study aims to elucidate how variations in build position influence differences in localized laser penetration, thereby facilitating the optimization of process parameters and contributing to the development of consistent, high-quality PBF-LB/M components.

2. Experimental methods

2.1. Materials

The precursor material used in this study was the AlSi10Mg aluminum alloy, provided by Valimet, Inc. (Stockton, CA, USA), with its chemical composition being detailed in Table 1. The supplier specified a powder size distribution

Table 1. Chemical composition of the AlSi10Mg powder

Element	Al	Si	Fe	Zn	Cu	Mg	Mn	Ti
Powder sample (wt%)	Balance	9.0–11.0	0.40	0.10	0.03	0.25–0.45	0.15	0.15

Abbreviations: AL: Aluminum; Si: Silicon; Fe: Iron; Zn: Zinc; Cu: Copper; Mg: Magnesium; Mn: Manganese; Ti: Titanium.

with D90, D50, and D10 values of 52 μm, 34 μm, and 17 μm, respectively. Before printing, further analysis of the reused powder's size and morphology was conducted using a CamsizerX2 (Microtrac Retsch GmbH, Haan, Germany) and scanning electron microscopy (SEM) with a JEOL JSM–IT500LV SEM (JEOL Ltd., Tokyo, Japan). The analysis revealed a powder size distribution with a D90 of 60 μm, a D50 of 37 μm, and a D10 of 23 μm.

The PBF-LB/M experiments were conducted using an EOS M290 machine (EOS GmbH, Krailling, Germany) equipped with a 400 W Yb fiber laser. Beam measurements revealed a beam waist (D4σ) between 75 and 85 μm, with an astigmatism that caused a focal offset of approximately 1 mm between the X and Y axes. This study aimed to evaluate the PBF-LB/M process through the production of QTAs across distinct phases:

- An initial build of two QTAs at two build plane locations (top/extent and center) using identical process parameters
- A series of plate scans at three build plane locations (top/extent, center, and bottom) to assess the effects of gas flow and laser power
- A second build of two QTAs at two build locations (top/extent and center) with modified scanning parameters based on initial findings.

To determine location-dependent effects of laser power, beam incident angle, and gas flow, a series of plate melt experiments were conducted at three different locations on the build platform (center, top, and bottom) using AlSi10Mg plates (25 × 30 × 3.5 mm, initially fabricated from the base powder in the EOS machine) under controlled conditions to simulate real builds. Information on plate melt conditions is detailed in Figure 1A and Table 2, respectively, where the laser parameters are varied from the power-to-speed ratio (P/v) combination recommended by EOS for this material (ID No. 1). The flow conditions within the EOS M290, as described by Elkins *et al.*,[27] were used to help guide the selection of part locations in this study. The first phase involved producing two QTAs (Figure 1B), one at the platform's center and another near the edge on the inlet flow side (referred to as "top" for plate scans and "extent" for QTAs), where recirculating gas flow was expected to cause higher lack-of-fusion porosity. However, contrary to expectations, no significant increase in lack-of-fusion porosity was observed in the artifact located at the extent. Instead, the initial QTA fabrication demonstrated that the standard process parameters produced significant keyhole pores in the artifact built at the center of the build chamber. This led the team to perform a series of plate melts to determine appropriate process parameters for the artifacts to be fabricated at different locations with similar melt pool penetrations (and with melt pools expected to be better positioned within the optimal processing window for this machine and material, *i.e.*, using reduced laser powers and P/v). Based on the melt pool analysis, a second build with adjusted parameters was conducted and examined to determine if quality variations across build locations were minimized through prescribed melt pool depths.

3. Results and discussion

3.1. Single and hatch melt experiment

The primary objective of conducting single-line and hatch scans is to identify optimal P/v ratio values that minimize variations in melt pool depth at both the center and edge of the build platform during artifact manufacturing. By enabling similar properties and quality of artifacts at these locations, the plate scans effectively capture differences in the melt pool depth caused by factors such as gas flow and incident angle. To mitigate the effects of soot and spatter, single-line vectors were designed with a one-second delay between each vector. Significant differences in melt pool depths were observed between the top, center, and bottom positions (Figure 2), primarily attributed to fluctuations in energy density resulting from inconsistencies in shielding gas flow and laser incidence effects.

(A) Top plate single melt; (B) top plate hatch pad scan; (C) center plate single melt; (D) center plate hatch pad scan; (E) bottom plate single melt; (F) bottom plate hatch pad scan.

The results from the hatch scans revealed more pronounced melt pool depth differences, especially at high P/v configurations (above 0.25) compared to single-line scans (Figure 3A), particularly at the top, where gas flow issues are exacerbated by soot accumulation (Elkins *et al.*'s paper[27] for a detailed discussion of gas flow in the EOS M290). The laser power was systematically adjusted from 300 to 370 W to achieve consistent melt pool depths across the center and edges of the build platform, maintaining a constant scan speed of 1200 mm/s. A P/v ratio of 0.308 at the extent/top and 0.26 at the center of the platform yielded nearly identical melt pool depth, contrasting with the first P/v ratio iteration of 0.285 at both locations (Figure 3B).

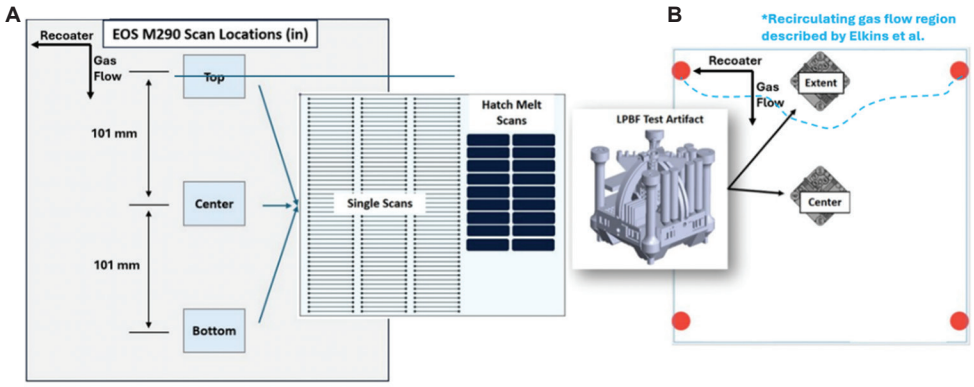

Figure 1. Schematic representation of the layout of plate scans (A) and the build location of the test artifact within two distinct gas flow regions described by Elkins *et al.*[27] (B)

Table 2. Parameters selected for single melt scan and hatch scan with justification

Melt pool ID no.	Power (W)	Scan speed (mm/s)	P/v ratio	Justification
1	370	1300	0.285	To elucidate the influence of different combinations of power and laser scan speed on melt pool depth while maintaining a constant P/v ratio
2	341	1200	0.284	
3	312	1100	0.284	
4	284	1000	0.284	
5	270	950	0.284	
6	256	900	0.284	
7	100	1000	0.100	To evaluate the parameter region more representative of the downskin conditions using relatively lower P/v ratios
8	200	1000	0.200	
9	75	750	0.100	
10	150	750	0.200	
11	125	1250	0.100	
12	250	1250	0.200	
13	300	1200	0.250	To identify the power required to achieve a similar melt pool depth at the center and extent (top) of the build platform
14	350	1200	0.292	
15	370	1200	0.308	
16	300	1600	0.188	To identify the risk for balling effects and unstable melt pool conditions
17	350	1800	0.194	
18	370	2000	0.185	

Abbreviation: P/v: Power-to-speed ratio.

The first build iteration of the QTA aimed to evaluate the performance of the PBF-LB/M machine by producing one QTA at the center of the build platform and another in a region characterized by recirculating gas flow, hypothesizing that the latter would exhibit increased lack-of-fusion porosity due to the interaction of the laser with ejecta and vapor plumes. In this first iteration, the downskin and contour parameters remain the same regardless of spatial location, despite each location experiencing differing laser incidence angles. In the second iteration, adjustments were made to the process parameters based on findings from plate scan experiments, which employed varying P/v ratios (0.308 at the extent/top and 0.26 at the center) while maintaining a constant speed of 1200 mm/s. Although there was a notable improvement of more than 20% in surface roughness, corresponding to a reduction in (Sa) between iterations at the 90° and 60° walls, the extent-fabricated artifact remained rougher than the center across both iterations (Figure 4). The elevated roughness in extent artifacts is likely due to variations in solidification

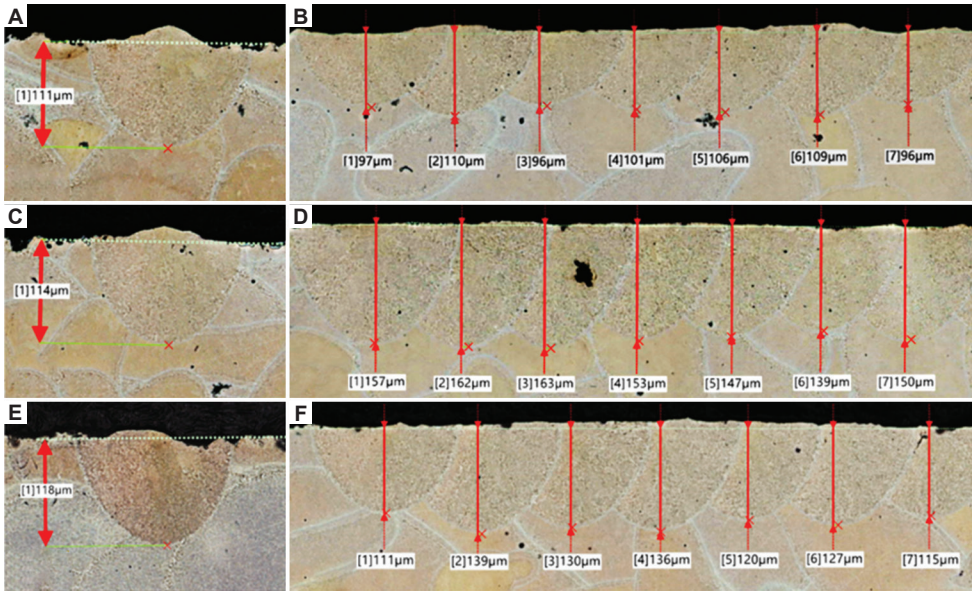

Figure 2. Melt pool depth of nominal EOS M290 AlSi10Mg scanning parameters. (A) Top plate single melt; (B) top plate hatch pad scan; (C) center plate single melt; (D) center plate hatch pad scan; (E) bottom plate single melt; (F) bottom plate hatch pad scan.

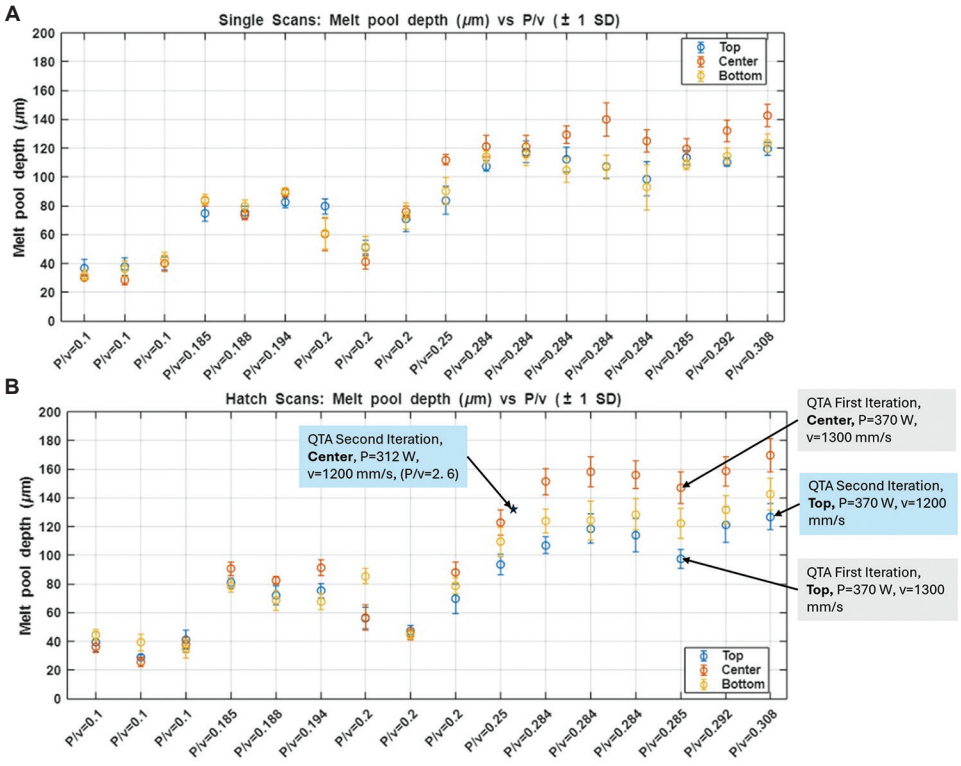

Figure 3. Variation in melt pool depth with P/v ratio (A) Single line scans, and (B) Hatch scans
Abbreviation: P/v: Power-to-speed ratio.

conditions stemming from differences in energy density (resulting from changes in spot size due to variations in incidence angle) and the presence of adhered powder particles, exacerbated by uneven gas flow within the build chamber. Future work is needed to effectively normalize gas flow conditions spatially. At this point, laser incidence effects can be isolated and compensated through improved scanning hardware or spatially variant scan strategies.

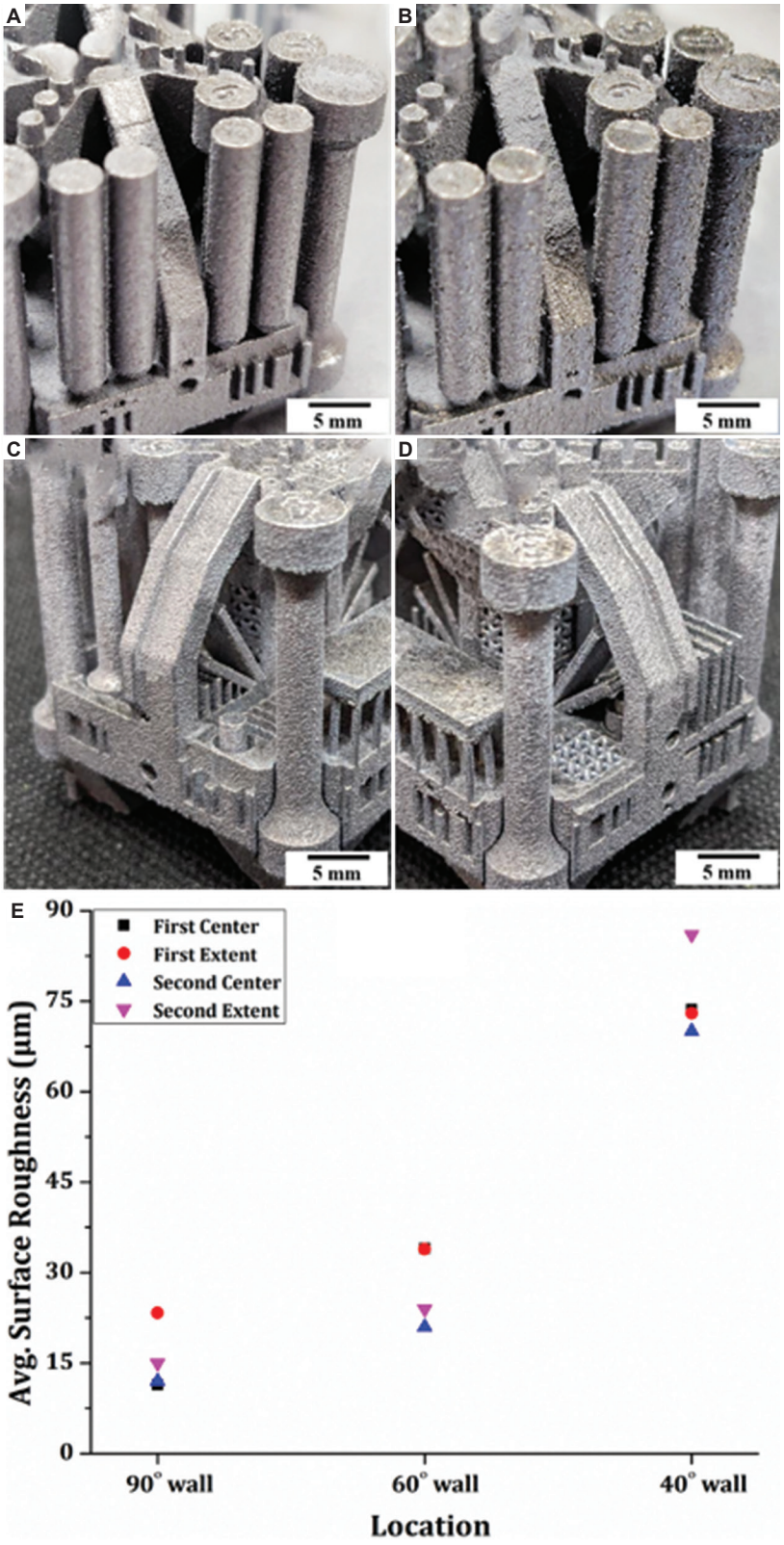

Figure 4. Surface roughness results. (A and B) Center and extent artifacts: first iteration; (C and D) center and extent artifacts: second iteration; (E) roughness comparison between iterations.

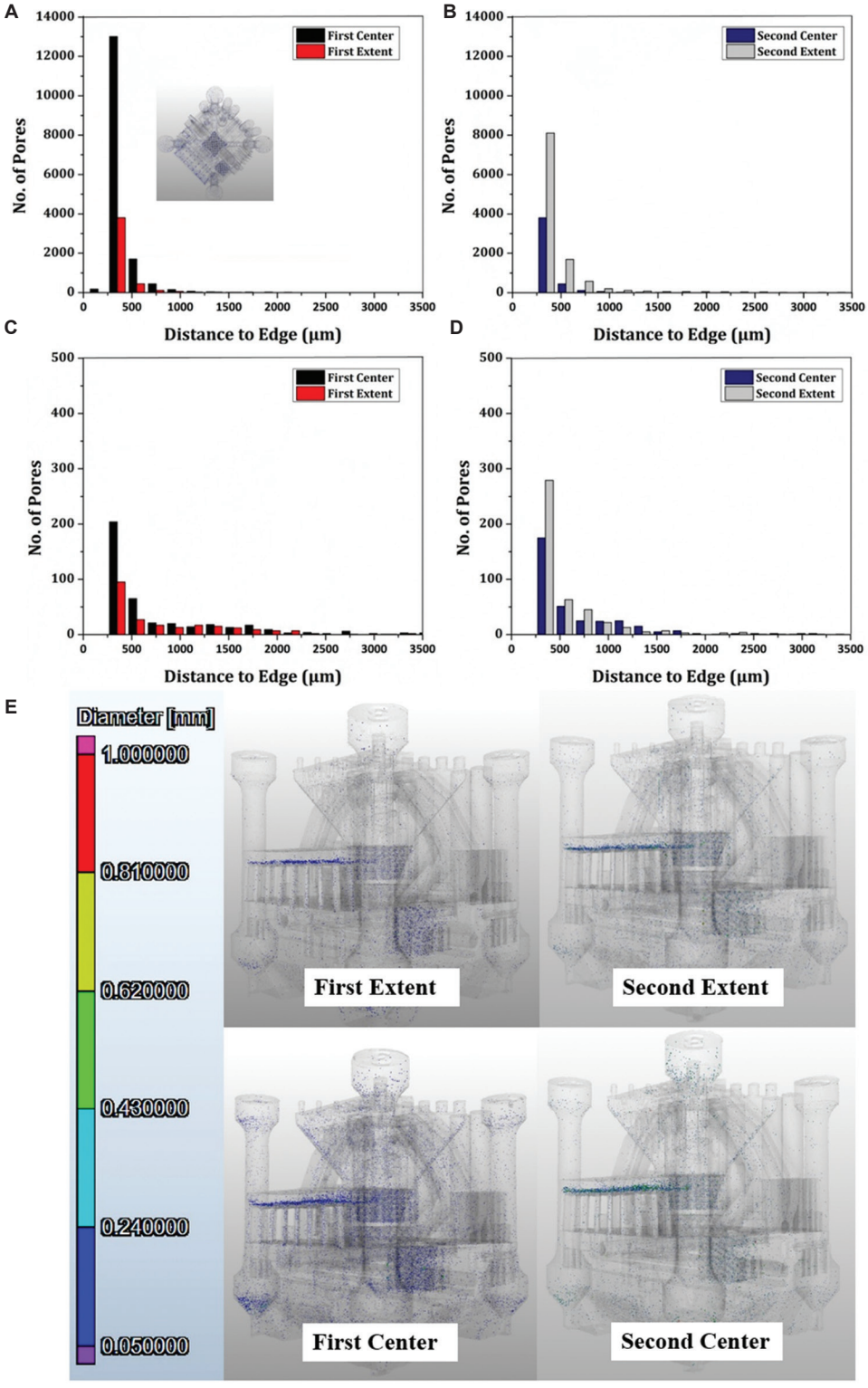

Figure 5. Porosity results of the bulk region from the first and second iterations. (A and B) CT scanning; (C and D) micrograph analysis (bulk region); (E) CT porosity, diameter, and distribution.
Abbreviation: CT: Computed tomography.

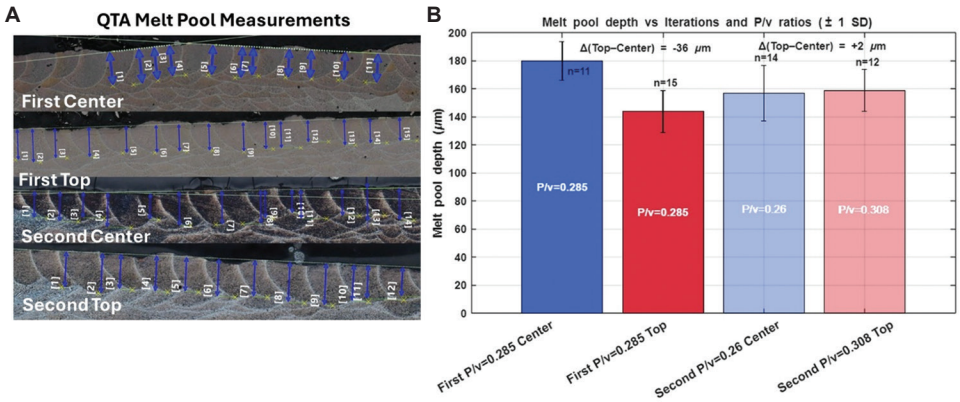

Figure 6. QTAs' melt pool measurements with P/v adjustments as a function of the build plate location to obtain uniform melt pool depths. (A) Cross-sectional view of QTAs' melt pools; (B) Melt pool depth results per P/v ratio and build plate location (Top, Center).
Abbreviations: P/v: Power-to-speed ratio; QTA: Qualification test artifact.

To further evaluate the quality of the QTAs, porosity was analyzed using CT and micrography (bulk region), specifically targeting pores located more than 750 µm from the part's edge to minimize contamination effects from contour parameters and geometric features. Achieving unidirectional and steady gas flow in the build chamber, as used in the EOS M290, is challenging, primarily due to the classic backward-facing step flow configuration described by Elkins *et al.*[27] While measuring porosity carries high uncertainty,[28-30] the analysis did show a noteworthy decrease between the first iteration and the second iteration, indicating that the effects of gas flow and laser incidence differences were minimized through parameter variations (Figure 5). In addition, most pores in all QTAs exhibited a sphericity of 0.8 or higher, indicating spherical shapes and reinforcing the keyhole behavior, particularly pronounced in the center (*i.e.*, additional iteration is required to provide parameters more confined to the optimum processing window). This suggests that further parameter refinement beyond what was done in this study is necessary to optimize part quality even more.

The porosity results described in the Figure 5 were further analyzed, considering the P/v variations among QTAs, which resulted in different melt pool depths (Figure 6). For the first iteration, this high energy density is likely the primary reason for the increased porosity observed at the center. For the second iteration, uniform melt pool depths were achieved between the center and top by adjusting the P/v as a function of the build location.

Although both artifacts demonstrated similar microstructural features, indicating minimal impact from build platform position, this conclusion may not generalize to other materials or alloys, as microstructural variability could be more significant in different contexts. Despite variations in energy density, no substantial differences in hardness or microstructure were found between iterations, highlighting the necessity for further exploration with other alloys that may reveal more pronounced differences across platform locations. Nonetheless, the existence of a non-negligible amount of porosity, depending on the platform location, is expected to impact both tensile and fatigue properties of the fabricated parts.

4. Conclusion

This study aimed to fabricate similar parts at various locations within the build chamber by identifying processing parameters that yield similar melt pool depths at these locations. Based on the results, the following conclusions are drawn:

(i) The effect of the build platform location significantly influences the melt pool depth. This variation can be normalized or minimized by adjusting the laser power and scan speed, leading to more consistent part quality in terms of porosity and surface roughness

(ii) A P/v ratio of 0.308 (370 W, 1300 mm/s) for the extent position produced a melt pool depth nearly identical to that of the center using P/v of 0.26 (312 W, 1200 mm/s), as shown in Figures 3 and 6, which underscored the importance of laser power and gas flow dynamics on melt pool characteristics. It is hypothesized that further improvements to improve quality throughout the build platform will require enhancements to the gas flow, making it unidirectional and more uniform. We believe that uniform gas flow will better assist in isolating the impact of laser incidence angle (through varying melt pool depths) on quality. This will be the focus of future work

(iii) The number of pores in all cases was deemed far too high, even though a marginal improvement was seen on the second iteration of artifacts. Thus, future work

will focus on first optimizing the gas flow to provide a more unidirectional and uniform flow across the build plate. Once the flow can be removed as a variable in the analysis, a more detailed study can be conducted to achieve equivalent melt pools at different locations within the build chamber, aimed at producing parts of much higher quality.

In conclusion, this study highlights the importance of location-specific processing parameters in maintaining consistent quality throughout the build chamber.

Acknowledgments

Jaivindra Singh and J. P. Oliveira acknowledge funding by national funds from FCT – Fundação para a Ciência e a Tecnologia, I.P., in the scope of the project's LA/P/0037/2020, UIDP/50025/2020, and UIDB/50025/2020 of the Associate Laboratory Institute of Nanostructures, Nanomodeling and Nanofabrication – i3N. The research described here was performed at The University of Texas at El Paso (UTEP) within the W.M. Keck Center for 3D Innovation (Keck Center). The authors are grateful to UTEP student Luis Tarango, who assisted in various aspects of the project. This work is based on research sponsored, in part, by award 70NANB21H006 from the U.S. Department of Commerce, National Institute of Standards and Technology (NIST). Additional support was provided by strategic investments through discretionary UTEP Keck Center funds and the Mr. and Mrs. MacIntosh Murchison Chair I in Engineering Endowment at UTEP.

Funding

The current work was funded by FCT – Fundação para a Ciência e a Tecnologia, I.P., in the scope of the project's LA/P/0037/2020, UIDP/50025/2020, and UIDB/50025/2020 of the Associate Laboratory Institute of Nanostructures, Nanomodeling, and Nanofabrication – i3N, and by award 70NANB21H006 from the U.S. Department of Commerce, National Institute of Standards and Technology (NIST). Additional support was provided by strategic investments through discretionary UTEP Keck Center funds and the Mr. and Mrs. MacIntosh Murchison Chair I in Engineering Endowment at UTEP.

Conflict of interest

J. P. Oliveira serves as an Editorial Board Member of this journal but was not in any way involved in the editorial and peer-review process conducted for this paper, directly or indirectly. Separately, other authors declared that they have no known competing financial interests or personal relationships that could have influenced the work reported in this paper.

Author contributions

Conceptualization: Hunter Taylor, Jorge Mireles
Data curation: Oscar Garcia, Jaivindra Singh
Funding acquisition: Ryan Wicker, J. P. Oliveira
Investigation: Hunter Taylor, Oscar Garciab
Methodology: Jorge Mireles, Hunter Taylor
Project administration: Jorge Mireles
Validation: Hunter Taylor
Visualization: Jesus Rivas
Writing–original draft: Jaivindra Singh, Jesus Rivas
Writing–review & editing: Jaivindra Singh, Ryan Wicker, Jorge Mireles, Jesus Rivas

Ethics approval and consent to participate

Not applicable.

Consent for publication

Not applicable.

Availability of data

The datasets presented in this article are not readily available due to technical/time limitations.

References

1. Moran TP, Warner DH, Soltani-Tehrani A, Shamsaei N, Phan N. Spatial inhomogeneity of build defects across the build plate in laser powder bed fusion. *Addit Manuf.* 2021;47:102333.

   doi: 10.1016/j.addma.2021.102333

2. Robinson DKR, Lagnau A, Boon WPC. Innovation pathways in additive manufacturing: Methods for tracing emerging and branching paths from rapid prototyping to alternative applications. *Technol Forecast Soc Change*. 2019;146: 733-750.

   doi: 10.1016/j.techfore.2018.07.012

3. de Formanoir C, Paggi U, Colebrants T, *et al*. Increasing the productivity of laser powder bed fusion: Influence of the hull-bulk strategy on part quality, microstructure and mechanical performance of Ti-6Al-4V. *Addit Manuf.* 2020;33:101129.

   doi: 10.1016/j.addma.2020.101129

4. Mussatto A, Groarke R, Vijayaraghavan RK, *et al*. Assessing dependency of part properties on the printing location in laser-powder bed fusion metal additive manufacturing. *Mater Today Commun*. 2022;30:103209.

   doi: 10.1016/j.mtcomm.2022.103209

5. Tradowsky U, White J, Ward RM, Read N, Reimers W, Attallah MM. Selective laser melting of AlSi10Mg: Influence of post-processing on the microstructural and tensile properties development. *Mater Des*. 2016;105:212-222.

doi: 10.1016/j.matdes.2016.05.066

6. Rebaioli L. A review on benchmark artifacts for evaluating the geometrical performance of additive manufacturing processes. *Int J Adv Manuf Technol*. 2017;93:2571-2598.

   doi: 10.1007/s00170-017-0570-0

7. Kotadia HR, Gibbons G, Das A, Howes PD. A review of laser powder bed fusion additive manufacturing of aluminium alloys: Microstructure and properties. *Addit Manuf*. 2021;46:102155.

   doi: 10.1016/j.addma.2021.102155

8. Taylor HC, Garibay EA, Wicker RB. Toward a common laser powder bed fusion qualification test artifact. *Addit Manuf*. 2021;39:101803.

   doi: 10.1016/j.addma.2020.101803

9. Anwar A Bin, Pham QC. Selective laser melting of AlSi10Mg: Effects of scan direction, part placement and inert gas flow velocity on tensile strength. *J Mater Process Technol*. 2017;240:388-396.

   doi: 10.1016/j.jmatprotec.2016.10.015

10. Philo AM, Sutcliffe CJ, Sillars S, Sienz J, Brown SGR, Lavery NP. A Study Into the Effects of Gas Flow Inlet Design of the Renishaw AM250 Laser Powder Bed Fusion Machine Using Computational Modelling. In: *Solid Freeform Fabrication. Proceedings of the 28th Annual International Solid Freeform Fabrication Symposium*, An Additive Manufacturing Conference, Austin, Texas, United states of America; 2017. p. 1203-1219.

11. Subramanian R, Rule D, Nazik, O. Dependence of LPBF Surface Roughness on Laser Incidence Angle and Component Build Orientation. In: Proceedings of the ASME Turbo Expo 2021. Turbomachinery Technical Conference and Exposition: Industrial and Cogeneration; Manufacturing Materials and Metallurgy. Virtual. Vol. 7; 2021.

    doi: 10.1115/GT2021-59755

12. Dowling L, Kennedy J, Shaughnessy SO, Trimble D. A review of critical repeatability and reproducibility issues in powder bed fusion. *Mater Des*. 2020;186:108346.

    doi: 10.1016/j.matdes.2019.108346

13. Ladewig A, Schlick G, Fisser M, Schulze V, Glatzel U. Influence of the shielding gas flow on the removal of process by-products in the selective laser melting process. *Addit Manuf*. 2016;10:1-9.

    doi: 10.1016/j.addma.2016.01.004

14. Wang J, Yin Q, Li H, Liu W, Shen S, Lv C. Influence of shielding gas flow on pore evolution in AlSi10Mg/In718 alloy by laser powder bed fusion. *J Mater Res Technol*. 2024;30:8774-8791.

    doi: 10.1016/j.jmrt.2024.05.194

15. Bagasol AJI, Kaschel FR, Ramachandran S, Mirihanage W, Browne DJ, Dowling DP. The influence of a large build area on the microstructure and mechanical properties of PBF-LB Ti-6Al-4 V alloy. *Int J Adv Manuf Technol*. 2023;125 (3-4):1355-1369.

    doi: 10.1007/s00170-022-10671-9

16. Weaver J, Schlenoff A, Deisenroth D, Moylan S. Assessing the influence of non-uniform gas speed on the melt pool depth in laser powder bed fusion additive manufacturing. *Rapid Prototyp J*. 2023;29(8):1580-1591.

    doi: 10.1108/RPJ-10-2022-0366

17. Fathi-Hafshejani P, Soltani-Tehrani A, Shamsaei N, Mahjouri-Samani M. Laser incidence angle influence on energy density variations, surface roughness, and porosity of additively manufactured parts. *Addit Manuf*. 2022;50:102572.

    doi: 10.1016/j.addma.2021.102572

18. Yogurtcuoglu V, Simsek U, Koc B. Effects of design parameters on surface roughness of additively manufactured thin-walled structures. *J Addit Manuf Technol*. 2023;2(1):692.

    doi: 10.18416/JAMTECH.2212692

19. Sendino S, Gardon M, Lartategui F, Martinez S, Lamikiz A. The effect of the laser incidence angle in the surface of l-pbf processed parts. *Coatings*. 2020;10(11):1-12.

    doi: 10.3390/coatings10111024

20. Li E, Shen H, Wang L, Wang G, Zhou Z. Laser shape variation influence on melt pool dynamics and solidification microstructure in laser powder bed fusion. *Addit Manuf Lett*. 2023;6:100141.

    doi: 10.1016/j.addlet.2023.100141

21. Dowling L, Kennedy J, Trimble D. Effect of a modified energy density equation to achieve a more uniform energy input during LPBF for improved repeatability. *J Manuf Process*. 2022;77:607-615.

    doi: 10.1016/j.jmapro.2022.03.045

22. Yeung H, Lane B. A residual heat compensation based scan strategy for powder bed fusion additive manufacturing. *Manuf Lett*. 2020;25:56-59.

    doi: 10.1016/j.mfglet.2020.07.005

23. Rivas J, Mireles J, Wicker RB. Scanner position accuracy, repeatability, and process anomalies correlation in PBF-LBM. *Addit Manuf Lett*. 2025;15:100326.

    doi: 10.1016/j.addlet.2025.100326

24. Valadez Mesta BL, Thome P, Lam MC, Tin S, Mireles J, Wicker RB. Impact of a typical scanner delay processing parameter on local microstructure in metallic laser-based powder bed fusion. *Addit Manuf Lett*. 2025;13:100273.

    doi: 10.1016/j.addlet.2025.100273

25. Aiza I, Baldi C, de la Vega FM, *et al*. Effects of

build orientation and inclined features on physical, microstructural and mechanical properties of powder bed fusion additively manufactured metallic parts. *Prog Mater Sci*. 2025;147:101357.

doi: 10.1016/j.pmatsci.2024.101357

26. Yang Y, Chen Z, Liu Z, Wang H, Zhang Y, Wang D. Influence of shielding gas flow consistency on parts quality consistency during large-scale laser powder bed fusion. *Opt Laser Technol*. 2023;158:108899.

doi: 10.1016/j.optlastec.2022.108899

27. Elkins CJ, Mireles J, Estrada HH, Morgan DW, Taylor HC, Wicker RB. Resolving the three-dimensional flow field within commercial metal additive manufacturing machines: Application of experimental Magnetic Resonance Velocimetry. *Addit Manuf*. 2023;73:103651.

doi: 10.1016/j.addma.2023.103651

28. Wilbig J, Wilson-Heid AE, Bernard L, Baptista J, Obaton AF. Comparison of porosity analysis based on X-Ray computed tomography on metal parts produced by additive manufacturing. *Appl Sci*. 2025;15(18):9876.

doi: 10.3390/app15189876

29. Rathore JS, King A, Le Bourdais F, Garandet JP. In-depth analysis of CT resolution impact on porosity evaluation in laser powder bed fusion additive manufacturing. *Tomogr Mater Struct*. 2025;8:100065.

doi: 10.1016/j.tmater.2025.100065

30. Holgado I, Ortega N, Yagüe-Fabra JA, Plaza S, Villarraga-Gómez H. Metrological evaluation and classification of porosity in metal additive manufacturing using X-ray computed tomography. *Mater Des*. 2025;254:114057.

doi: 10.1016/j.matdes.2025.114057

ACCSCIENCE PUBLISHING

Engineering Science in Additive Manufacturing

ORIGINAL RESEARCH ARTICLE

Dual-wavelength photoinhibition-aided vat photopolymerization (PinVPP) of bio-based polymers and functional hydrogels

Yousra Bensouda and Xiayun Zhao*

ZXY Intelligent Precision – Advanced Manufacturing (ZIP-AM) Laboratory, Department of Mechanical Engineering and Materials Science, University of Pittsburgh, Pittsburgh, Pennsylvania, United States of America

Abstract

Despite the widespread adoption of vat photopolymerization (VPP) in additive manufacturing, extending it to bio-based polymers and hydrogels remains challenging due to limited control over photopolymerization kinetics, which often leads to overcuring, surface roughness, and mechanically fragile structures—particularly in optically complex or highly fluidic materials. These issues arise largely from the intrinsic coupling of initiation and propagation in conventional single-wavelength exposure schemes. This work evaluates, for the first time, the feasibility and potential of dual-wavelength photoinhibition-aided VPP (PinVPP) as a strategy for two representative, yet fundamentally different, material classes. By spectrally decoupling visible-light initiation from UV-triggered inhibition, PinVPP enables independent regulation of radical generation and spatial confinement of curing. Using a lab-developed PinVPP platform, a bio-based polylactic acid/polyurethane acrylate (PLA–PUA) resin is investigated under independently controlled inhibition ratios, demonstrating suppression of excessive cure thickness and improved control over polymerization kinetics without compromising bulk integrity. Photo-differential scanning calorimetry, optical profilometry, and rheological analysis reveal that photoinhibition temporally redistributes polymerization, enhancing surface quality and mechanical consistency in a resin system prone to slow and uneven curing. Furthermore, applied to polyethylene glycol diacrylate (PEGDA)-based hydrogels, PinVPP reduces overcuring and shape distortion while improving surface smoothness and mechanical robustness under hydrated conditions. Raman spectroscopy quantifies local chemical conversion, and swelling, water uptake, and dimensional stability measurements confirm improved resistance to hydration-induced deformation. Overall, these results demonstrate that PinVPP expands the VPP processing envelope by introducing tunable kinetic control effective for traditionally challenging material systems, offering a scalable pathway for additive manufacturing of sustainable polymers and functional hydrogels with enhanced process stability and material performance.

Keywords: Vat photopolymerization; Photoinhibition; Bio-based polymer; Polymeric blend; Hydrogel; Digital light processing; Sustainable 3D printing

***Corresponding author:**
Xiayun Zhao
(xiayun.zhao@pitt.edu)

Citation: Bensouda Y, Zhao X. Dual-wavelength photoinhibition-aided vat photopolymerization (PinVPP) of bio-based polymers and functional hydrogels. *Eng Sci Add Manuf.* 2026;2(1):026080004. doi: 10.36922/ESAM026080004

Received: February 20, 2026

Revised: March 13, 2026

Accepted: March 16, 2026

Published online: March 31, 2026

1. Introduction

1.1. Bio-based polymers: Opportunities and challenges in vat photopolymerization

Polymeric blends have become integral to modern engineering due to their tunable properties and overall versatility. They combine two or more distinct materials to form a third one with enhanced properties, and can therefore offer superior properties, such as increased strength or reduced weight. With the recent advances in additive manufacturing technologies, the range of processable materials has expanded significantly to meet complex design and manufacturing needs.[1] Among these technologies, vat photopolymerization (VPP), particularly digital light processing (DLP), has emerged as a leading technique for fabricating high-resolution, functional components through light-induced curing of liquid resins.[2-5] This technology, along with others, has opened new possibilities in manufacturing, enabling the production of intricate and functional parts that are increasingly shaping the future of industries worldwide.[6,7] However, most commercially available resins are petrochemical-based, posing environmental and health concerns related to their non-biodegradability and end-of-life disposal. To address these issues, there is growing interest in developing sustainable, bio-based resins derived from renewable feedstocks such as cornstarch, which reduce fossil fuel dependence and environmental footprint.[8-10] The shift toward these materials aligns with global efforts to achieve a circular economy centered on resource efficiency, recyclability, and biodegradability.[11-14]

Polylactic acid (PLA) and polyurethane acrylate (PUA) are particularly promising candidates for sustainable photopolymer systems, owing to their eco-friendly nature, affordability, and lightweight. Together, they offer a unique blend of mechanical, thermal, and electrical properties, holding immense potential across multiple industries.[12] PLA is a well-known non-toxic crystalline biopolymer synthesized directly by condensation (step-growth polymerization) or catalytic ring opening of naturally produced lactic acid from materials such as wheat, biomass, and corn starch.[15] The sugar fermentation of corn and sugar canes allows for the acquisition of lactic acid (HO–CH_3–CH–COOH)—the base of PLA synthesis. When polymerized, it results in the formation of long-chain polymers constituting PLA.[6-8] A 2019 report predicted that the worldwide PLA market would experience a compound annual growth rate of 19.3% from 2018 to 2028.[16-19] The production of biodegradable plastics is projected to surpass 3.5 million tons by 2027, driven by significant advancements in polymers like PLA.[13] On the other hand, PUA is a versatile and durable polymer widely recognized for its broad range of applications. It is synthesized through a polyaddition reaction, where a diisocyanate reacts with a polyol, typically derived from petroleum or renewable sources like vegetable oils. This process forms long-chain polymers that result in the creation of PUA. The choice of diisocyanate and polyol, along with the inclusion of chain extenders or cross-linkers, allows for the customization of PUA's properties, making it suitable for various applications, from flexible foams to rigid plastics.[20] Combining PLA and PUA therefore yields a hybrid resin system that leverages the mechanical resilience of PUA with the biodegradability of PLA, creating a balanced, eco-friendly bio-based suspension suitable for high-resolution additive manufacturing.

Despite their promise, bio-based resins often face challenges in conventional single-wavelength VPP, including limited curing control, dimensional inaccuracies, and surface irregularities. These shortcomings arise largely from the inability to precisely modulate polymerization kinetics and spatial confinement during curing, which can lead to overcuring, reduced resolution, and poor surface finish, these complications are particularly problematic for DLP-based VPP, where precise light delivery is essential for achieving fine features and consistent curing. To date, reports on VPP of PLA-PUA suspensions remain scarce, and the combined use of this material system with advanced light modulation strategies has not been explored.[21]

To overcome these limitations, this study introduces a dual-wavelength photoinhibition-aided vat photopolymerization system (PinVPP) as a novel route to print bio-based polymer resins. PinVPP employs dual light sources, blue light to initiate polymerization and UV light to inhibit it, enabling dynamic control over cure thickness and crosslinking kinetics.[22,23] By dynamically balancing these two light inputs, the process provides tighter control over the polymerization front, enabling improvements in dimensional accuracy, surface smoothness, and mechanical performance of printed parts, thus expanding the printable design space of sustainable bio-based materials.

1.2. Hydrogels: Opportunities and challenges in vat photopolymerization

Vat photopolymerization (VPP) has also emerged as a powerful platform for fabricating soft, biocompatible hydrogel architectures with microscale precision, enabling applications in tissue engineering, drug delivery, and soft robotics.[24] Despite significant advances in materials and hardware, hydrogel-based VPP remains constrained by uncontrolled overcuring, degraded lateral fidelity, and poor vertical resolution. These limitations arise from the intrinsic optical complexity of hydrogels,[25-27] including

strong light scattering, refractive index mismatch, and broad radical diffusion that collectively widen the effective polymerization zone.[28-30] Conventional single-wavelength approaches struggle to spatially confine polymerization, leading to cure-through, blurred interlayer boundaries, and compromised feature definition, especially in formulations with higher water content that further reduce optical penetration depth. While absorbers and careful formulation design can partially mitigate these effects, they typically impose trade-offs in cure speed, mechanical performance, and optical transparency, and offer limited dynamic control over curing geometry.[30,31]

Photoinhibition offers a conceptual solution by dynamically modulating radical propagation in space and time. In particular, the use of a dual-wavelength PinVPP system can decouple radical generation and suppression by assigning distinct spectral bands to initiation and inhibition, therefore enabling tunable confinement of the polymerization window in both lateral and axial dimensions.[23,32-34] However, a systematic framework for harnessing dual-wavelength inhibition in hydrogel VPP that links inhibitor photochemistry, dose ratios, and hydrogel composition to print fidelity and functional performance remains underdeveloped.

To address this gap, we investigate PinVPP for hydrogel 3D printing using representative hydrogel formulations and accessible light sources.[24,35] Building on insights from the PLA-PUA system, we extend the framework to polyethylene glycol diacrylate (PEGDA) hydrogels, establishing protocols to quantify print fidelity, mechanical behavior, and swelling stability.

Overall, this work presents the first systematic experimental evaluation of PinVPP across two representative and fundamentally distinct material classes—bio-based polymers and hydrogels. While previous studies have primarily focused on demonstrating photoinhibition concepts in conventional photopolymer systems, this work extends the approach to materials that are traditionally challenging for VPP due to their optical complexity, curing instability, or high water content. Through the experimental examination of the influence of tunable photoinhibition on curing kinetics, dimensional fidelity, surface quality, and mechanical behavior, this study establishes a unified framework for understanding how dual-wavelength control can expand the VPP processing envelope. The results demonstrate that controlled photoinhibition enables reliable fabrication of materials that are otherwise difficult to print using conventional single-wavelength VPP approaches. The remainder of this work details the experimental systems, methods, and results.

The objective of this work is to investigate the feasibility and effectiveness of applying dual-wavelength PinVPP to fabricate PLA-PUA polymers—a material system not previously studied with this approach. The study aims to assess how dual-wavelength control can address the curing and resolution challenges while enabling tunable mechanical and structural properties. Moreover, building on the polymer printing results, this work further extends the PinVPP framework to hydrogel printing using a PEGDA-based formulation, and following a similar testing protocol. This extension allows assessment of the technique's adaptability to different resin chemistries and material systems that are difficult to print using traditional VPP.

The remainder of this paper is organized as follows: Section 2 (Materials and methods) describes the PinVPP system setup, resin formulations, printing process, and characterization methods. Section 3 (Results and discussion) evaluates the inhibition and curing process characteristics, as well as the structural and mechanical properties of both the polymers and hydrogels, with emphasis on the influence of photoinhibition. Drawing on multiple techniques, including optical microscopy, photo-differential scanning calorimetry (Photo-DSC), rheology characterization, and water uptake analysis, this work provides a comprehensive evaluation of the process-structure property relationships enabled by PinVPP across bio-based polymers and hydrogels.

2. Materials and methods

2.1. Dual-wavelength PinVPP system

The lab-built open-architecture dual-wavelength PinVPP system incorporates two light emitting diodes (LEDs) light sources (Prizmatix UHP-T- 460-DI at 460 nm and Prizmatix UHP-T-370-LA34 at 365 nm) delivered via Ø3 mm liquid light guides. These sources emit distinct beams: one for photopolymerization (blue light, 460 nm wavelength) and the other for photoinhibition (UV light, 365 nm wavelength). A 50/50 beam splitter is used to merge the orthogonal light paths passing through digital micro-mirror devices (DMDs) given a resolution of 1920×1080 pixels; tunable controls allow to tweak the light intensities emanating from them. The detailed system configuration was reported by Zhang *et al.*[36] Both light sources were positioned alongside a movable build platform equipped with a linear translation stage (LTS 150 from Thorlabs, NJ) for optimized print positioning. Both light sources were aligned as best as possible such that the dual-wavelength projections ensure maximum precision in inhibition and curing. The system configuration is illustrated schematically in Figure 1a, while the corresponding

real-life experimental setup is shown in Figure 1b. The underlying working principle of the PinVPP method is illustrated in Figure 1c.

This dual-light approach allowed for precise control over the resin's curing dynamics. Adjusting the intensity of both the blue and UV lights, an *inhibition ratio* I_{UV}/

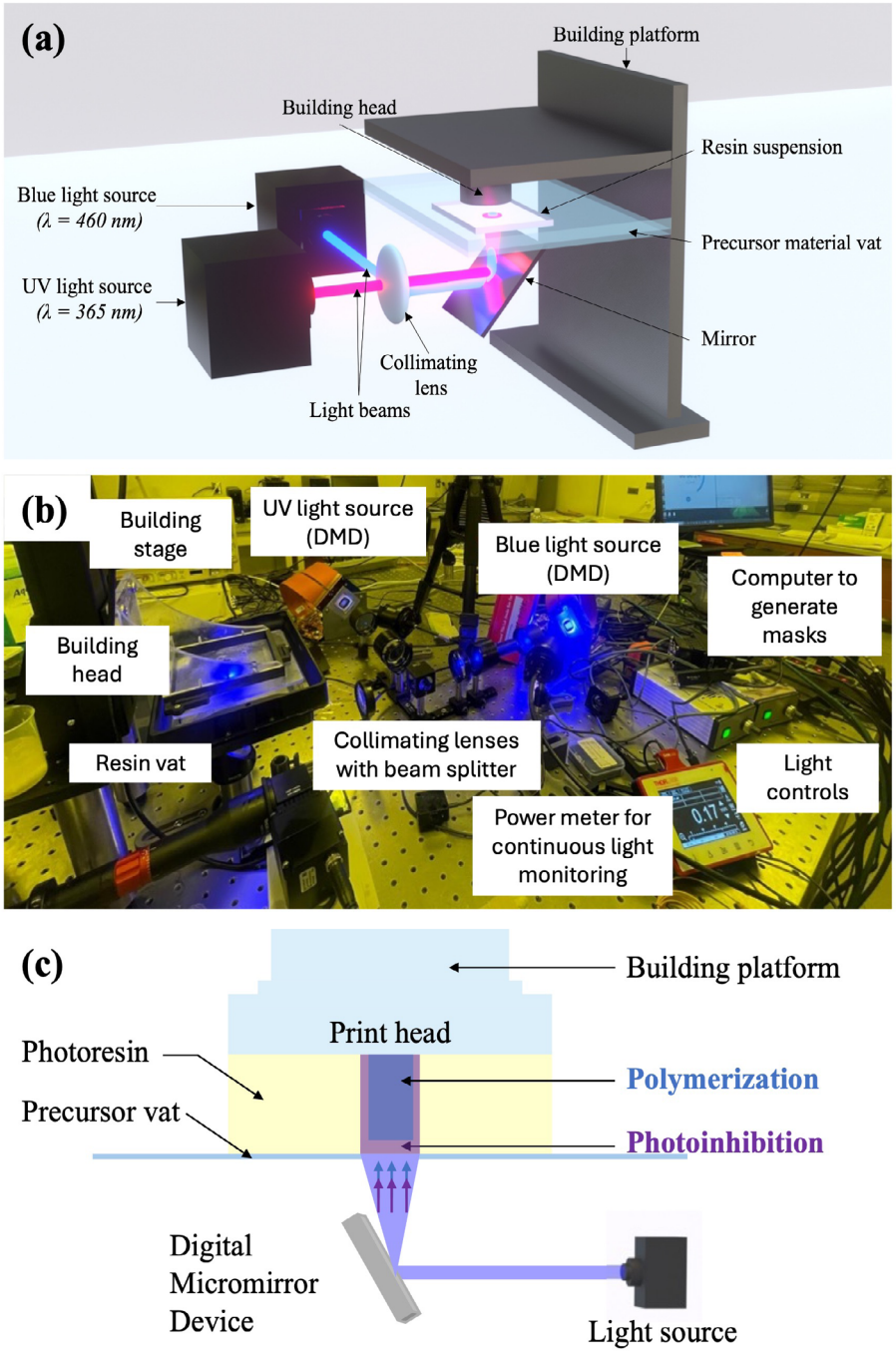

Figure 1. Concept overview and implementation of the printing system. (a) Simplified schematic of the lab-designed dual-wavelength PinVPP system setup for printing PLA-PUA polymers and hydrogels in this work. (b) Corresponding real-life printing system setup. (c) Simplified illustration of the dual-wavelength photopolymerization and photoinhibition mechanics and interactions.
Abbreviations: DMD: Digital micro-mirror device; PinVPP: Photoinhibition-aided vat photopolymerization; PLA: Polylactic acid; PUA: Polyurethane acrylate; UV: Ultraviolet.

I_{Blue} was established. This ratio defines the balance between photopolymerization (induced by blue light) and photoinhibition (induced by UV light) within the resin. Varying the inhibition ratio at different levels allowed for fine-tuning of the curing process, providing enhanced control over the material's structural and mechanical properties. The blue light intensity used was fixed at 21 mW/cm^2, while the UV light intensity ranged from 0 mW/cm^2 to 12.6 mW/cm^2 based on the corresponding I_{UV}/I_{Blue} ratio required. In this work, the projected masks form two overlapping circles with an equal diameter of 10 mm, measured via a digital caliper with a resolution of 0.01 mm. An optical power meter with a thermal surface absorber sensor (PM400, S405C, Thorlabs, NJ, USA) was used to measure light intensities frequently to ensure relatively stable light powers.

2.2. Material system and preparation

2.2.1. PLA-PUA polymeric blend resin system

The feedstock system used in this study is based on a PLA-PUA suspension adapted from the work reported by Feng *et al.*,[37,38] and tailored to suit the requirements of our PinVPP process through experiment trials for feasible blue-light-initiated curing and UV-induced inhibition. The monomer matrix comprises a 95:5 weight ratio of PUA to PLA, selected for its mechanical robustness and partial biodegradability. The system is initiated by visible light using 0.2 wt% camphorquinone (CQ), 0.5 wt% ethyl 4-(dimethylamino)benzoate (EDAB) serving as co-initiator and photoinhibiton is achieved via 3 wt% of 2-(2-chlorophenyl)-4,5-diphenylimidazole (o-Cl-HABI), which is UV-responsive. To validate the spectral compatibility of this dual-wavelength photoinitiator system, the UV/visible absorbance spectra of CQ, EDAB, and o-Cl-HABI were characterized and overlaid with the emission profiles of the UV and blue lights used in the printing setup, as seen in Figure 2. The emission spectra were reconstructed using the peak wavelength, peak spectral density, and baseline values reported by the manufacturer (Prizmatix) using a StellarNET EPP2000 spectrometer measurements, with intensity shown in recorded detector counts. The material spectral data were retrieved and adapted from the NIST Standard Reference Database and the Wiley Science Solutions Spectral Databases to ensure accurate spectral representation.[39] The plotted absorbance spectrums analysis demonstrates selective photoactivation: CQ exhibits strong spectral overlap with the blue emission (centered at 453.23 nm), enabling efficient radical generation for polymerization, while o-Cl-HABI shows dominant absorption in the UV region (centered at 369.03 nm), confirming its role in UV-triggered inhibition with minimal cross-activation by visible light. The clear spectral separation between the blue-activated initiator (CQ) and UV-activated inhibitor (o-Cl-HABI) is critical for achieving independent control over curing and inhibition zones, which is fundamental to the precision of the printing process.

A reactive diluent, triethylene glycol dimethacrylate (TEGDMA), was incorporated at 37.5 wt% to improve resin viscosity and reactivity. The total monomeric matrix (PLA-PUA) represents 58.8 wt% of the resin and is made by mixing PUA received in liquid form, with PLA powder. No fillers are used in this study. All materials, with the exception of PLA, were obtained from Sigma-Aldrich (St. Louis, MO, USA) and used as received without any additional modifications. PLA powder (100 mesh size grains, particle size ≈150 μm) was obtained from Magerial Science (Sheridan, WY, USA). The resin formulation involves a multi-step protocol to ensure consistent dispersion and photoreactivity. First, o-Cl-HABI is dissolved in tetrahydrofuran (THF) to form a 30 wt% stock solution, mixed for 20 min at 30 °C and 600 rpm on a magnetic stirring plate. CQ, EDAB, and the o-Cl-HABI solution are then added to TEGDMA to form the non-monomer base. This mixture was stirred again for 20 min under the same conditions. The PLA-PUA blend was subsequently introduced and mixed thoroughly to complete the resin formulation. Mixing follows each addition to ensure homogeneity. The shelf life of the prepared resin was 24 h, and fresh formulations were prepared before each printing session and stored in dark amber vials to prevent premature curing. For each exposure time tested, three replications were performed to assess repeatability and acquire statistically significant results.

2.2.2. Hydrogel resin preparation

The hydrogel matrix used in this section of the study consists of polyethylene glycol diacrylate (PEGDA, M = 700 Da, Sigma-Aldrich) and deionized water, with PEGDA comprising 40 wt% by mass. This composition was selected to achieve a balance between print fidelity, optical penetration, and network swelling suitable for photoinhibited hydrogel fabrication. The photoreactive system is identical to that used in the previously introduced PLA-PUA polymer formulation. CQ (0.2 wt%) serves as the visible-light photoinitiator, while EDAB (0.5 wt%) is the co-initiator and o-Cl-HABI (3 wt%) enables UV selective photoinhibition. All chemicals were used as received without additional purification. Resin preparation follows the same multi-step protocol described earlier. Briefly, o-Cl-HABI was first dissolved in THF to form a 30 wt% stock solution and stirred magnetically for 20 min at 30 °C and 600 rpm. CQ and EDAB were then added to

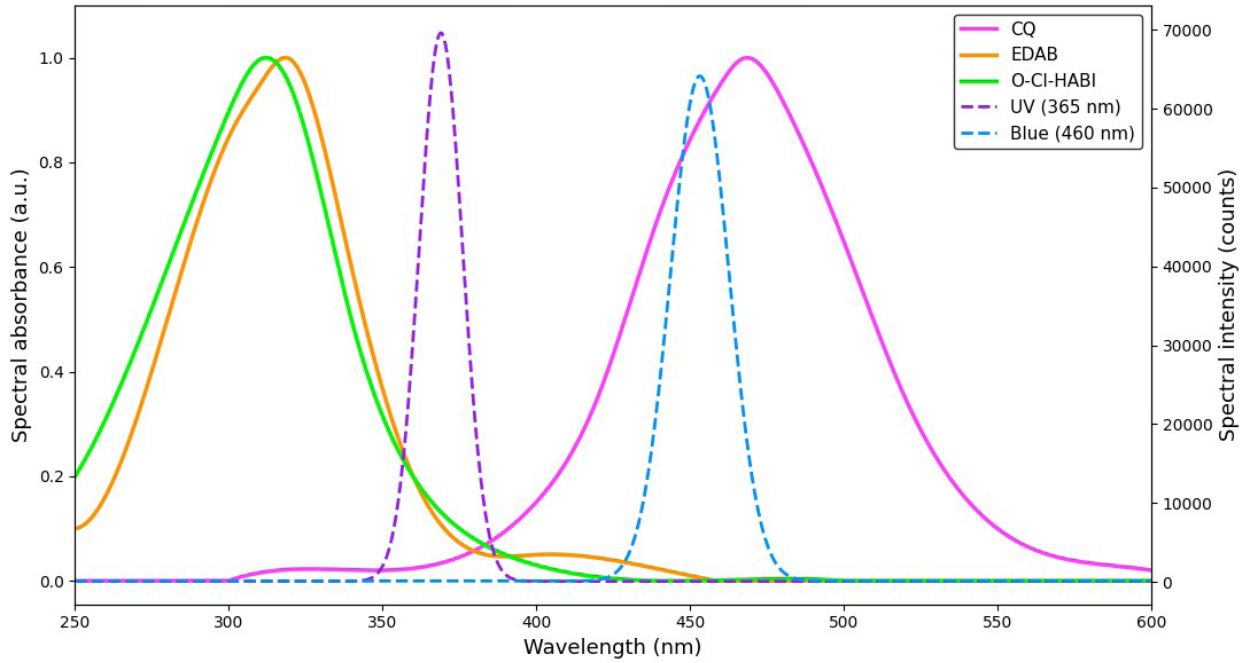

Figure 2. Spectral intensity for UV and blue light sources and material spectral absorbance of the resin's active species used in the PinVPP photopolymerization reaction. Light spectra were reconstructed using reported Prizmatix measurements. Material data retrieved and adapted from the NIST Standard Reference Database and the Wiley Science Solutions Spectral Databases.[39]
Abbreviations: CQ: Camphorquinone; EDAB: Ethyl 4-(dimethylamino)benzoate; o-Cl-HABI: 2-(2-chlorophenyl)-4,5-diphenylimidazole; PinVPP: Photoinhibition-aided vat photopolymerization; UV: Ultraviolet.

the PEGDA-water mixture, followed by the incorporation of the o-Cl-HABI solution. The complete formulation is mixed under identical conditions for an additional 20 min to achieve a homogeneous hydrogel resin. Three replicates were made for each printing condition.

2.3. Experiment design

A two-phase experimental design was developed to study the effects of photoinhibiton on the printing process and the resulting properties of the PLA-PUA polymeric blend. In Phase I, samples were printed at a fixed exposure time of 60 s under seven inhibition ratios, I_{UV}/I_{Blue} = 0, 0.1, 0.2, 0.3, 0.4, 0.5 and 0.6 (see Figure A1 in Appendix A). In Phase II, two inhibition ratios were selected for further investigation under varying exposure times to assess the interplay between radiant exposure and inhibition level. The control group I_{UV}/I_{Blue} = 0 samples were printed using blue light only, while the inhibited group I_{UV}/I_{Blue} = 0.3 samples represented a medium inhibition condition identified from the former experiments. Samples in this phase were printed at exposure times of 15, 30 and 45 s to evaluate dimensional accuracy and curing behavior changes with respect to increasing exposure durations (see Figure A2 in Appendix A for scans of the printed samples for both ratios). The selected inhibition ratios and exposure times were determined through extensive preliminary exposure trials aimed at identifying a stable processing window in which both photopolymerization and photoinhibition effects could be clearly observed without completely suppressing curing.

Building on insights from these experiments, hydrogel printing was subsequently conducted in a single phase. Preliminary exposure trials were used to identify an optimal exposure range, after which three representative exposure times were selected for testing. Printing was performed under two conditions as well, I_{UV}/I_{Blue} = 0 (pure blue light) and I_{UV}/I_{Blue} = 0.6 (see Figure B1 in Appendix B). This streamlined design enabled direct comparison of curing and inhibition behavior in the hydrogel system relative to the polymer formulation.

2.4. Characterization methods

Unless otherwise stated, all characterization procedures followed the standard operating protocols of the respective analytical instruments and widely accepted practices in photopolymerization and additive manufacturing characterization.

2.4.1. Photo differential scanning calorimetry (Photo-DSC)

Photo-differential scanning calorimetry (Photo-DSC) was employed to quantify the photopolymerization kinetics and curing behavior of the PLA-PUA resin under dual-wavelength exposure. The PinVPP printing light sources were coupled directly to a NETZSCH Photo-DSC 204 F1, enabling *in situ* characterization under irradiation profiles identical to those used during printing. Upon illumination, the photoinitiators dispersed in the resin generate reactive radical species that drive an exothermic crosslinking reaction.[40] The resulting heat flow, recorded in real time, provides a direct measure of the polymerization rate and total reaction enthalpy. Variations in peak intensity and position reflect differences in reaction kinetics and molecular structure associated with each inhibition condition. All experiments were conducted under a vacuum-tight, nitrogen-purged atmosphere (20 mL/min) to suppress oxygen inhibition, using identical irradiance levels to those employed during 3D printing. An isothermal temperature of 25 °C and a heating rate of 40 K/min were selected to replicate practical curing conditions. To ensure consistent thermal response, samples of equal mass (28 mg) were placed in standard aluminum crucibles, given that the measured enthalpy is proportional to the sample mass.[41] Photo-DSC runs were performed at selected inhibition ratios (I_{UV}/I_{Blue} = 0 and 0.3) and exposure times (15, 30, and 45 s) to evaluate the effect of UV-induced inhibition on polymerization rate and conversion. The instrument continuously measured the heat flow $q(t)$ from which the total polymerization enthalpy ΔH_{tot} and degree of conversion $\alpha(t)$ were calculated as follows by **Equations 1** and **2**:

$$\Delta H_{tot} = \frac{1}{m}\int_0^{t_{end}} q(t)\,dt \tag{1}$$

$$\alpha(t_i) = \frac{\int_0^{t_i} q(t)\,dt}{\int_0^{t_{end}} q(t)\,dt} \tag{2}$$

The curing rate, expressed as the time derivative of the conversion was obtained from the normalized heat flow expressed by **Equation 3**:

$$\frac{d\alpha}{dt} = \frac{q(t)}{\Delta H_{tot}} \tag{3}$$

Raw calorimetric data were processed using the Proteus software (NETZSCH, Germany). A linear baseline correction method was applied to remove instrumental drift before integration. The peak area corresponding to each sample was obtained by integrating the heat flow curve over time, and the degree of conversion, DoC ($\alpha(t)$), was derived from the ratio of partial to total reaction enthalpy.[42,43] The extracted kinetic parameters—including peak heat flow, total enthalpy and time-dependent conversion profiles—were used to assess the impact of photoinhibition on the curing process, fitted by the model described in **Equation 4**:

$$\frac{d\alpha}{dt} = \Lambda e^{\frac{-E}{RT}}(1-\alpha)^n(\alpha)^m \tag{5}$$

where Λ is the pre-exponential factor and $e^{\frac{-E}{RT}}$ is the temperature dependent Arrhenius factor. These two factors are often used to scale the rate of reaction $\frac{d\alpha}{dt}$. The concentrations of the monomer and the crosslinked product are denoted by $(1-\alpha)$ and α respectively. The scaling factors are taken as rate constants (k_1 and k_2) given the fixed temperature conditions; therefore, **Equation 4** can be rewritten as **Equation 5:**

$$\frac{d\alpha}{dt} = \left(k_1 + k_2(\alpha)^m\right)(1-\alpha)^n \tag{5}$$

2.4.2. Optical microscopy

A VR-3200 optical microscope (Keyence, Japan) was used to measure the PinVPP print geometry and surface. The measurement data provides basis for characterizing the PinVPP inhibition zone and geometrical properties. The system was equipped with 25× magnification objective lenses, enabling high-resolution imaging for preliminary topographical analysis. Scanning was conducted immediately following print completion to ensure accurate measurement of the cured layer thickness and minimize post-curing variations. The hydrogel samples were evaluated similarly.

2.4.3. Rheological behavior

The objective of this analysis was to elucidate how dual-wavelength PinVPP influences the mechanical performance of the PLA-PUA polymeric blend and the hydrogels, respectively, by examining their stress-strain behavior. In addition to conventional stress-strain characterization, the mechanical response was evaluated through the storage modulus (G') and loss modulus (G''), which describe the elastic energy stored in the polymer network and the viscous energy dissipated during deformation, respectively. Monitoring the evolution of G' and G'' as a function of shear strain provides insight into the stability of the crosslinked network, the onset of nonlinear behavior, and strain-induced structural rearrangement. In the small-strain regime, G' typically dominates G'', reflecting an elastic, network-dominated response, whereas deviations from this regime indicate

increasing chain mobility, network disruption, and a transition toward more dissipative deformation modes.

Quantifying the relationship between applied stress and resulting strain provides direct insight into how photoinhibition parameters, specifically the inhibition ratio and curing time, affect polymer crosslinking, stiffness and ductility. Uniaxial tensile tests were performed to characterize the deformation and failure behavior of the printed specimens. During testing, the applied load force was continuously recorded, and stress σ and strain ε were automatically calculated. Plotting stress-strain curves enables a detailed evaluation of the material's elastic and plastic behavior. The initial linear region corresponds to the elastic regime, where stress is proportional to strain. Beyond the elastic region, the deviation from linearity and the subsequent strain at fracture provide insight into the material's ductility and overall toughness.

All tensile tests were conducted using a modular compact rheometer (Anton Paar MCR-302e) operated in tensile mode, equipped with a 25.019 mm parallel plate and controlled via the RheoCompass software. The test chamber was equilibrated at 20 °C and a normal force of 5 N was applied prior to each run to ensure proper contact and alignment. Stress-strain data were continuously recorded and exported for quantitative analysis. During the sweeps, the instrument's active sensors feedback allowed to monitor and keep the force within range; if the force drifted below 5 N the gap was re-zeroed to compensate for small compliance changes in the sample.

2.4.4. Raman spectroscopy

Raman spectroscopy, based on the inelastic scattering of monochromatic light, provides detailed information about molecular vibrations and crystal structures. When incident photons interact with the sample, they can undergo either elastic (Rayleigh) or inelastic (Raman) scattering. The Raman shift is typically expressed in wave numbers and is a function of λ_i and λ_s, the wavelengths of incident and scattered light, respectively.

For a photopolymerization reaction, the DoC typically measures how far the chemical reaction has progressed, thus reflecting the conversion state of the crosslinking reaction achieved by the printed sample. Studying this parameter is therefore a crucial step in understanding the geometric, mechanical and macroscopic properties of any print. In this work, the degree of conversion of the printed hydrogels can be estimated from monitoring the intensity of the carbon-carbon double bond (C=C) stretching band (around 1605 cm^{-1}) and the carbon-hydrogen (C–H) deformation band (around 1450 cm^{-1}). Consequently, the DoC can be measured from the peak area decrease of the C=C peak around 1605 cm^{-1}, and the C–H peak used as standard for absorbance normalization around 1450 cm^{-1} relative to a reference peak given by **Equation 6**:

$$DoC\ (\%) = \left(1 - \frac{I_{c=c} / I_{ref}}{I^0_{C=C} / I^0_{ref}}\right) x100 \tag{6}$$

such that $I^0_{C=C}$ and I^0_{ref} are the initial intensities of the uncured resin, and $I_{c=c}$ and I_{ref} are their intensities after curing. Thus, the equation can be rewritten as **Equation 7**:

$$DoC(\%) = \left(1 - \frac{\left(A_{1605} / A_{1450}\right)_{cured\ sample}}{\left(A_{1605} / A_{1450}\right)_{liquid\ resin}}\right) x100 \tag{7}$$

such that A_{1605} and A_{1450} are the absorbance peaks areas for the corresponding wavelengths, while $\left(A_{1605} / A_{1450}\right)_{\text{cured sample}}$ is the peak areas ratio of the cured polymer and $\left(A_{1605} / A_{1450}\right)_{\text{liquid resin}}$ is the peak areas ratio of the liquid monomer (resin suspension).[44-48] To evaluate the structural and molecular characteristics of the cured samples, Raman spectroscopy was performed using a Horiba LabRAM Soleil Raman Microscope (HORIBA, France). Measurements were conducted on samples cured under varying exposure times of 30, 45, and 60 s for two inhibition ratios: pure blue I_{UV}/I_{Blue} = 0 and inhibited I_{UV}/I_{Blue} = 0.6. Spectra were acquired using a 50× ELWD BD objective under an episcopic illumination mode with a 532 nm excitation laser. The laser power was carefully adjusted to preserve sample integrity, ranging from 6.3% (5.3 mW) to 100% (84 mW). Each sample was scanned point by point with an acquisition time of 2 s and a confocal hole size of 200 µm. All spectra were collected under fixed laser power and integration time conditions to ensure comparability across formulations and inhibition ratios. The residual bond fraction was determined relative to the spectra of uncured resin, enabling quantitative evaluation of the DoC as a function of exposure time and inhibition ratio. Comparative analysis of the pure blue and inhibited samples provided insights into whether photoinhibition-induced resolution enhancement could be achieved without compromising polymerization efficiency. Finally, the Raman data were correlated with curing thickness measurements to establish the relationship between optical control and chemical conversion.

3. Results and discussion

3.1. PinVPP printing of bio-based PLA-PUA polymeric blends

3.1.1. Photo-DSC analysis of curing with and without photoinhibition

Following the method described in Section 2.4.1, the heat flow $q(t)$, the degree of conversion $\alpha(t)$ and the

curing rate $d\alpha/dt$ were evaluated to characterize the polymerization kinetics of the material system under dual-wavelength VPP, given two inhibition ratios, I_{UV}/I_{Blue} = 0 and 0.3. This aims to determine how the imposed inhibition ratio influences the onset of curing, the reaction rate and the total reaction enthalpy, thus providing direct thermal evidence of the interplay between blue light-driven initiation and UV-induced inhibition. As defined in **Equation 1**, all integrations were performed relative to the zero line of the baseline-corrected heat flow signal, meaning that the "area under the curve" refers specifically to the integral of $q(t)$ relative to that baseline. Figure 3a presents the baseline-corrected heat flow $q(t)$ traces for the two exposure conditions. Under pure blue irradiation, the heat flow signal increases rapidly and reaches a well-defined maximum within roughly 20 s, followed by a monotonic decay toward baseline within about one minute. Polymerization therefore begins immediately after the signal rises from the baseline. We should note that the exothermic peak does not denote the onset of curing but rather the point in time when the instantaneous curing rate $d\alpha/dt$ reaches its maximum, since $q(t)$ is proportional to $d\alpha/dt$ according to **Equation 3**. The peak time thus corresponds to the fastest network formation, while the peak magnitude reflects the highest energetic rate of radical propagation and therefore most rapid rate of conversion. Additionally, the total reaction enthalpy ΔH_{tot} is given by the full integrated area under the corrected differential scanning calorimetry (DSC) curve. The differences in ΔH_{tot} between the two inhibition conditions quantify the effect of UV-induced inhibition on overall conversion within the measurement window.

When UV inhibition is introduced via the ratio I_{UV}/I_{Blue} = 0.3, the heat flow profile changes in a manner consistent with photoinhibition. The exothermic peak shifts to later times, decreases in magnitude, and exhibits a more

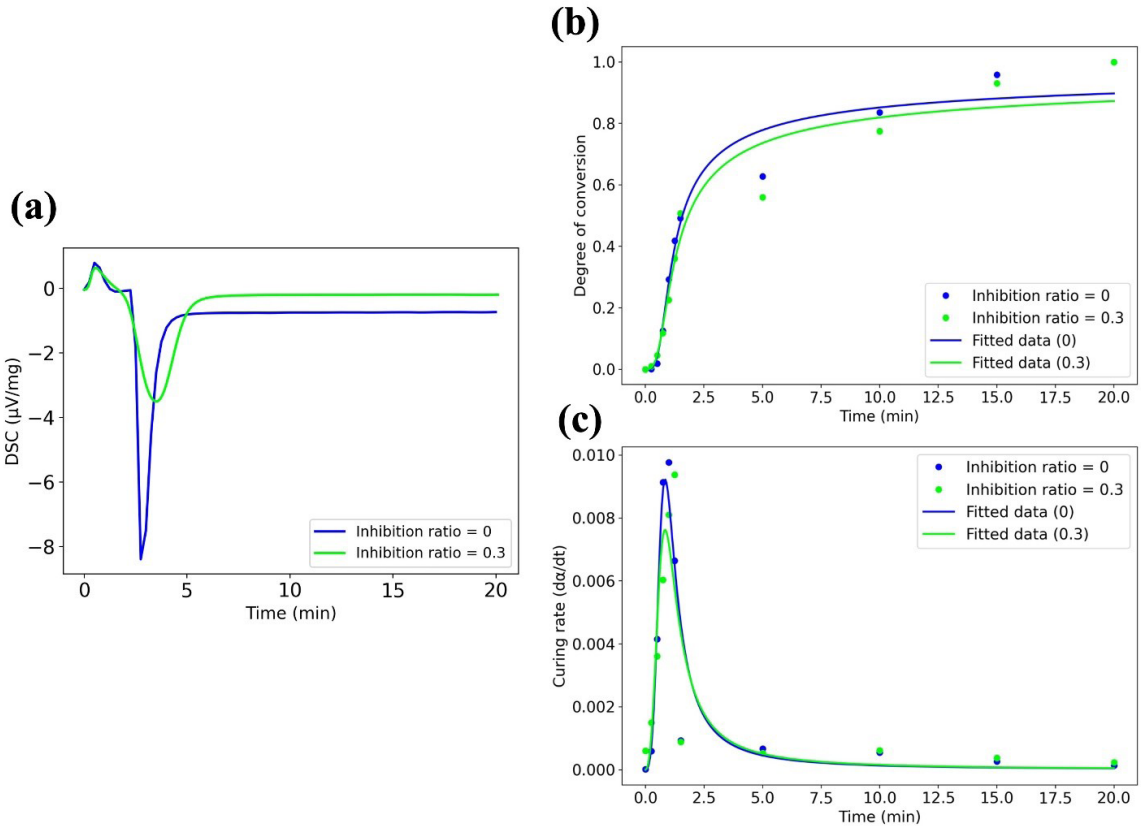

Figure 3. Effects of photoinhibition on polymerization kinetics. (a) Photo-DSC heat flow (μV/mg) versus time for pure blue light (inhibition ratio I_{UV}/I_{Blue} = 0) and under inhibition exposure (I_{UV}/I_{Blue} = 0.3). Plots compare the exothermic response and reaction kinetics under pure blue irradiation and an inhibiting irradiation regime, highlighting differences in polymerization behavior. (b) Overlay of the degree-of-conversion kinetics under pure blue light (I_{UV}/I_{Blue} = 0) and inhibition (I_{UV}/I_{Blue} = 0.3) exposures. (c) Curing rate profiles for the material system as functions of increasing exposure time under pure blue irradiation I_{UV}/I_{Blue} = 0, and photoinhibition I_{UV}/I_{Blue} = 0.3. The inhibited system shows a reduced and slightly delayed peak rate, consistent with transient UV-induced radical suppression in the PinVPP process.

Abbreviations: PinVPP: Photoinhibition-aided vat photopolymerization; Photo-DSC: Photo-differential scanning calorimetry; UV: Ultraviolet.

gradual rise compared to the pure-blue condition. These trends are consistent with the dual-wavelength mechanism of PinVPP: blue light excites the photoinitiators and drives radical generation, while UV light activates the inhibitor and produces persistent radicals that suppress propagation. Thus, UV light exposure does not assist nor accelerate curing; rather, it temporarily delays it by lowering the net concentration of propagating radicals. As the inhibition mechanism competes with blue-light-induced initiation, the polymerization rate decreases, resulting in: (i) a longer induction period, (ii) a delayed and lower exothermic peak, and (iii) reduced overall heat release within the measurement window. Once the concentration of inhibitory radicals diminishes, blue-initiated radicals dominate, allowing polymerization to proceed and producing the observed delayed peak.

The degree of conversion $\alpha(t)$ plots in Figure 3b were computed directly from the DSC thermogram following standard DSC methodology as defined by **Equation 2,** where the integrated area normalized by ΔH_{tot}, given the total reaction enthalpy at time t_i and the baseline corrected heat flow were used. Here the area under the curve before the peak indicates early-stage polymerization occurring at rates lower than the peak rate. In Figure 3b, the scattered points represent experimentally integrated conversion values at discrete times (*i.e.*, the cumulative heat released up to each measurement point), whereas the plots represent best-fit kinetic curves generated from the heat-flow data. Because the fits are continuous mathematical models and the data points are the result of numerical integration of measured heat flow, perfect overlap is not expected; minor deviations between the points and curves reflect experimental noise, DSC baseline uncertainty, and numerical differentiation. Data before ~2 min appear crowded because the reaction proceeds most rapidly early in the exposure, thus resulting in several closely spaced measurements over a short period. These early measurements correspond to low conversion values (<10%) but are essential for capturing the induction and acceleration phases of the reaction.

For both inhibition ratios I_{UV}/I_{Blue} = 0 and 0.3, rapid and early-stage growth was detected, followed by a gradual approach toward an asymptotic maximum. The pure blue case reaches a conversion of approximately $\alpha \approx 0.85$ within 20 min, while the inhibited system consistently trails below it, reflecting a reduced early-stage reaction rate as well as a modest reduction in the long-time conversion. The shape of the curves is characteristic of free-radical photopolymerization dynamics, and the deviation between the two experimental conditions directly reflects the inhibition induced suppression of propagation predicted by the DSC heat flow results earlier. Since photo-DSC is a dynamic characterization method that measures curing kinetics under illumination conditions rather than the cured state of printed parts, a value closer to $\alpha = 1$ indicates the practical upper limit of conversion achievable within the imposed exposure conditions for the material system. For photopolymer resins, final conversions in the range of 70–90% are common, and the plateau values observed here ($\alpha \approx 0.85$ for I_{UV}/I_{Blue} = 0 and slightly lower for I_{UV}/I_{Blue} = 0.3) fall within the typical range.

The curing rate profiles in Figure 3c further illustrate the effects of photoinhibition, and are expressed as time derivatives of the conversion given the normalized heat flow according to **Equation 3**. Under pure blue exposure (I_{UV}/I_{Blue} = 0), the curing rate exhibits a clear maximum near one minute at approximately $d\alpha/dt \approx 9.5 \times 10^{-3}\ s^{-1}$ consistent with the heat flow peak in Figure 3a. Under inhibition with I_{UV}/I_{Blue} = 0.3, the maximum rate decreases to roughly $d\alpha/dt \approx 8 \times 10^{-3}\ s^{-1}$ and occurs slightly later. This reduced and delayed maximum is directly attributed to the transient dominance of inhibitory radicals generated by UV light. Because inhibitory radicals compete directly with chain propagating species, they lower the net radical population available for curing. Once those species decay, the blue light initiators regain control of the reaction kinetics, and the polymerization accelerates toward its plateau. Beyond ~5 min, both systems exhibit similarly low reaction rates, indicating that the process transitions to a diffusion-limited regime where chemical inhibition no longer governs the reaction speed.

Together, the DSC heat flow, the DoC and the curing rate analyses provide a coherent picture of the curing kinetics under dual-wavelength PinVPP. Pure blue exposure yields rapid polymerization, a short induction period and a high maximum polymerization rate, while UV light exposure imposes a controlled photoinhibition step that transiently suppresses radical propagation, delays the rate maximum and reduces the total reaction enthalpy. These results confirm that the inhibition ratio provides a tunable handle on both temporal and energetic characteristics of photopolymerization in our material system, thereby enabling deliberate modulation of cure progression for applications requiring spatially controlled polymerization.

3.1.2. Inhibition zone depth

To characterize the effect of dual-wavelength exposure on vertical curing behavior, the cured layer depth and inhibition zone thickness were measured as functions of the inhibition ratio. The goal of this analysis is to determine whether the inhibition zone can be intentionally controlled to reduce surface roughness at the top layer while still

achieving sufficient cure thickness for mechanical support. Surface roughness and geometrical properties are addressed in the Section 3.1.3. Cure thickness was measured using the Keyence VR-3200 optical profilometer as outlined in Section 2.4.2, with scans collected immediately after printing to avoid any post-cure contributions. Figure 4a shows the measured cure thickness for samples printed at a 60 s exposure time across inhibition ratios from I_{UV}/I_{Blue} = 0 to 0.6. Under pure blue exposure, the resin cures to approximately 2500 µm. Increasing the inhibition ratio leads to a gradual but consistent decrease in cure thickness, reaching ~1600 µm at the highest inhibition ratio. This trend reflects the expected suppression of radical propagation when UV light induced inhibitor radicals compete with blue light-initiated chain growth during exposure.

The inhibition zone depth (thickness) was determined by subtracting the inhibited cure thickness from the fully cured reference depth obtained under I_{UV}/I_{Blue} = 0. As shown in Figure 4b, the inhibition depth increases almost linearly with inhibition ratio, from ~200 µm at I_{UV}/I_{Blue} = 0.1 to ~1100 µm at I_{UV}/I_{Blue} = 0.6. The fitted curve emphasizes the strong correlation between the imposed inhibition ratio and the inhibition depth. These results confirm that the inhibition zone is not a secondary or incidental effect but a controllable design parameter directly determined by powers of blue and UV lights, and consequently the inhibition ratio I_{UV}/I_{Blue}. This demonstrates that dual-wavelength VPP has the potential to enable fine control of polymerization depth.

3.1.3. Geometrical and surface properties

A key objective of this study is to assess whether dual-wavelength PinVPP can improve dimensional accuracy and surface finish relative to traditional VPP. This is particularly relevant to minimizing the common issues of excessive cure thickness overcuring, lateral overgrowth and surface defects that limit print resolution in conventional VPP systems. To systematically evaluate this capability, cured dimensions (depth and diameter) and surface roughness were quantified under varying exposure conditions for both uninhibited (I_{UV}/I_{Blue} = 0) and inhibited samples (I_{UV}/I_{Blue} = 0.3). Target dimensions of 10,000 µm in diameter (corresponding to the dimensions of the projected masks) and 3,000 µm (printing chamber height) in cure thickness were used as benchmarks for evaluating dimensional accuracy and process control. Figure 5 shows the variation in cure thickness as a function of radiant exposure, measured using the Keyence VR-3200 optical profilometer. Under pure blue light, the cure thickness increases slightly from 3,400 µm at 315 mJ/cm² exposure (15 s) to nearly 3,600 µm at 945 mJ/cm² (45 s). These values consistently exceed the 3000 µm target, indicating vertical overcuring regardless of exposure level. When photoinhibition is introduced at I_{UV}/I_{Blue} = 0.3, the cure thickness stabilizes between 2,700 µm and 3,000 µm across all exposures studied, thereby aligning much more closely with the target value. This demonstrates that dual-wavelength exposure effectively suppresses excessive polymerization overcuring while still achieving a continuous cured layer. The reduction in cure thickness is highly consistent across exposures, highlighting the reliability of photoinhibition in moderating penetration even as radiant exposure is increased.

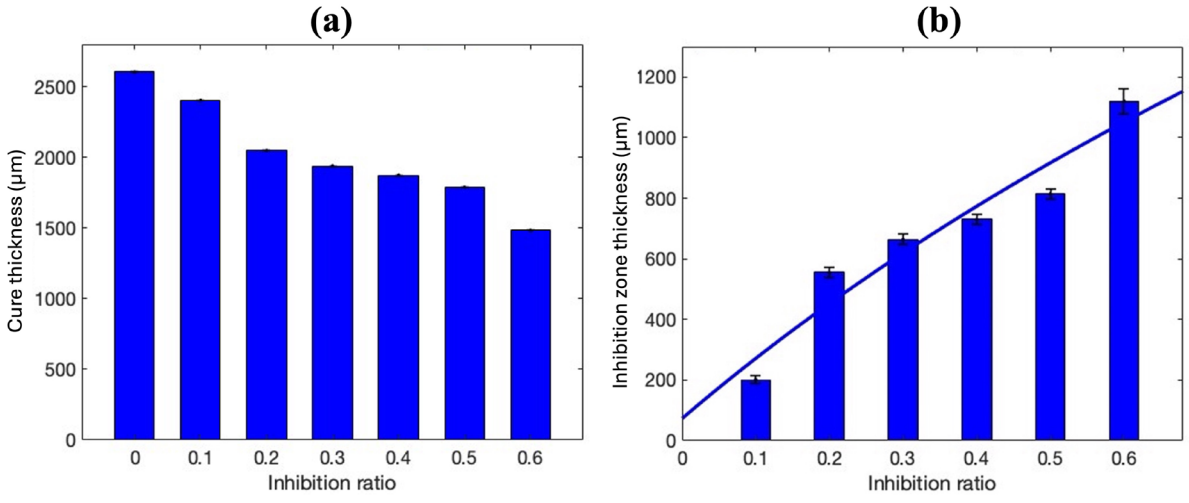

Figure 4. Effect of inhibition ratio on cure thickness and inhibition zone. (a) Average cure thickness vs. I_{UV}/I_{Blue} with corresponding relative standard errors. (b) Average inhibition zone variation with curve-fitted data for multiple inhibition ratios I_{UV}/I_{Blue} with corresponding relative standard errors. See Table A1 in Appendix A for detailed data on all replications and calculations.

The combined effects of exposure and inhibition on both cure thickness and lateral resolution are further illustrated in Figure 6. Without inhibition, the cure thickness increases monotonically with exposure time. By contrast, inhibited samples display a much narrower range, thus offering a more controlled way to cap cure thickness than adjusting exposure time alone. Lateral dimensional accuracy is also retained during inhibited curing. Across all exposure times, both inhibited and uninhibited samples achieve measured diameters between approximately 9000 and 10,500 μm, close to the target value of 10,000 μm. The inhibited samples tend to exhibit slightly smaller diameters (on the order of 5–10%), but these deviations remain modest and indicate reduced lateral overcuring without compromising resolution. This relatively small lateral effect is expected, as the current experiments employed only overlapping inhibition, rather than a deliberately patterned lateral inhibition strategy. If intentional lateral inhibition patterns are introduced, a more pronounced lateral confinement is anticipated, as demonstrated in previous work by our research group reported by Zhang *et al.*[34] The fact that the diameter remains stable across a range of exposure times further suggests that, under present experimental conditions, inhibition primarily influences depth-wise curing rather than in-plane propagation. Therefore, PinVPP can control cure thickness and limit lateral overcuring simultaneously, a valuable characteristic for layer-based fabrication where overcuring in one dimension worsens accuracy in the others.

Surface roughness is a critical quality metric in VPP directly influencing friction, and overall build performance. Typically, surface irregularities often arise due to the interaction between the build head and the substrate, which tend to destroy the fragile samples. Thus, PinVPP aims to limit such defects by preventing overcuring through inhibition, which acts as a buffer during layer separation, thereby reducing bumps or tearing at the cured sample boundary. To quantify top-surface quality, the arithmetic average roughness S_a was evaluated using profilometry scans, and computed similarly to our previous work.[23] This metric provides a representative measure of surface profile variation and is widely used in VPP literature as a benchmark for print quality. Figure 7 presents the S_a values for samples printed under both inhibition ratios (I_{UV}/I_{Blue} = 0 and 0.3) at various exposure times. Under pure blue light exposure, roughness reaches nearly 1,000 μm 15 s, indicative of a strongly perturbed interface where suction forces and partial curing likely contribute to surface damage. With photoinhibition applied roughness is significantly reduced to approximately 600 μm, demonstrating that inhibition's potential to effectively limit interfacial disruptions. As exposure time increases, roughness decreases for both systems. At 45 s, both inhibited and uninhibited samples exhibit improved smoothness with roughness values ranging from 200 to 250 μm. While the gap between inhibited and uninhibited

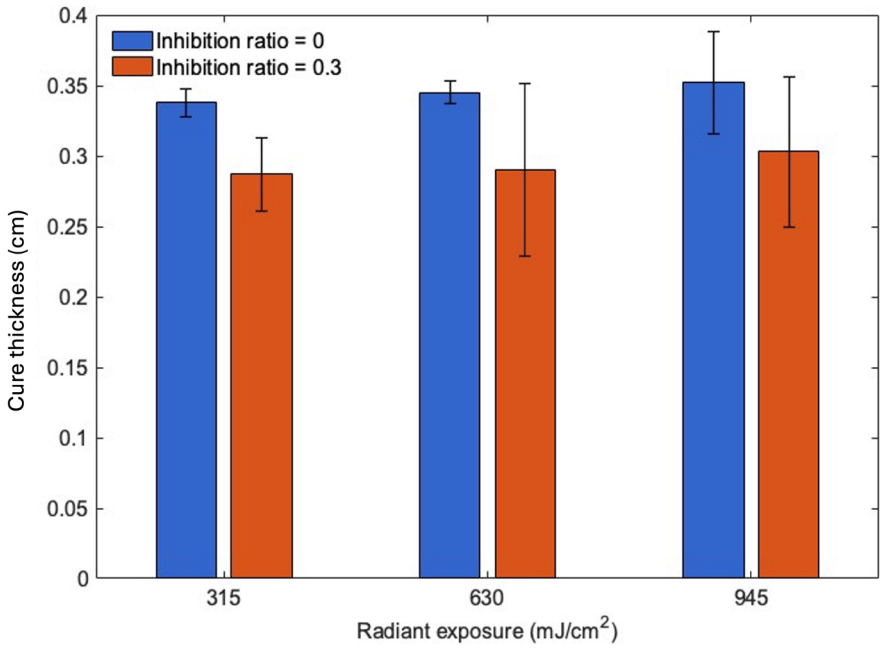

Figure 5. Cure thickness as a function of radiant exposure for samples printed under pure blue light exposure (I_{UV}/I_{Blue} = 0) and under photoinhibition (I_{UV}/I_{Blue} = 0.3). Data reflects measurements for samples cured for 15, 30 and 45 s for both experimental groups.

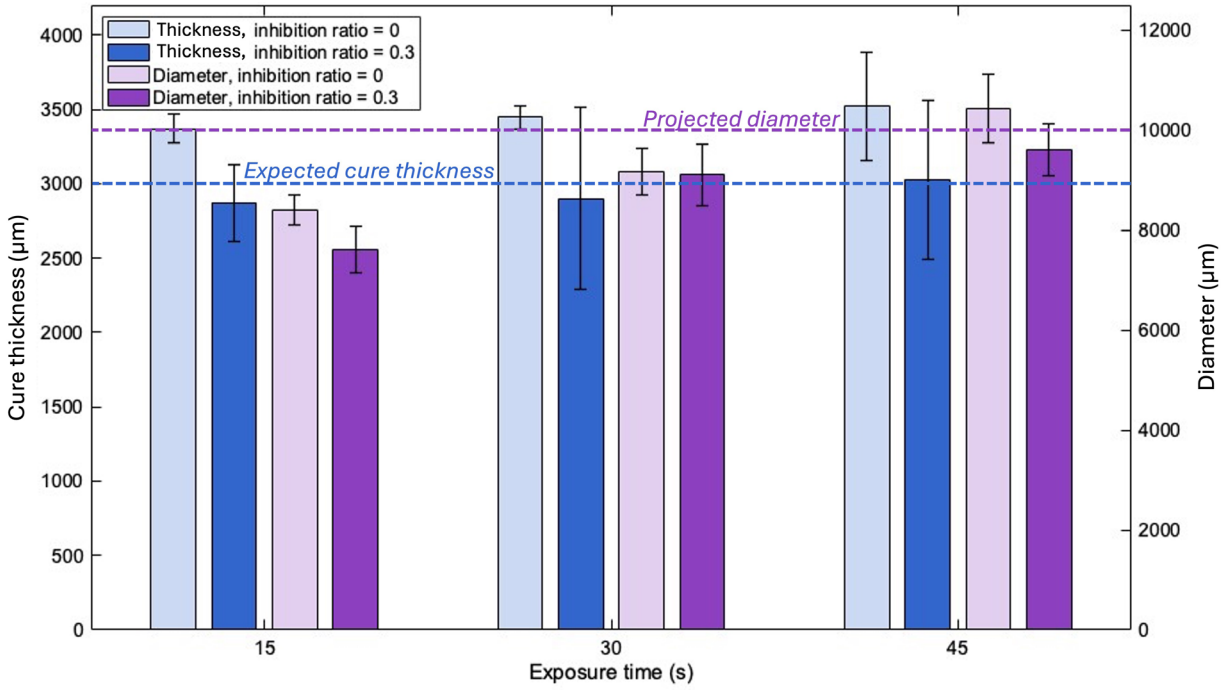

Figure 6. Effect of exposure time on cure thickness and lateral feature diameter for samples printed under inhibition ratios I_{UV}/I_{Blue} = 0 and 0.3 given varying exposure times. Bars indicate cure thickness (left y axis), while symbols show the measured diameter (right y axis) obtained from Keyence VR-3200 scans. All samples were printed under identical conditions except for the programmed changing exposure time.

samples narrows at higher exposures, inhibited samples consistently show equal or lower S_a values across all conditions. The error bars in Figure 7 further indicate that the variability in surface roughness is smallest at the higher inhibition ratio, suggesting that PinVPP provides a more robust route in producing smooth surfaces. In particular, the spread in surface roughness values under inhibited conditions is noticeably reduced across all exposure times, with the most pronounced reduction occurring at shorter exposures where process instabilities are typically strongest. At 15 s and 30 s, the uninhibited samples exhibit substantially larger scatter, reflecting the sensitivity of the process to interfacial forces and partial curing during layer separation. By contrast, the inhibited samples show tighter clustering of roughness values, indicating improved repeatability and reduced process variability. Photoinhibition appears able to mitigate interfacial forces during sample separation from print head, especially at shorter exposures when the cured sample is less robust and more vulnerable to defects; by creating a controlled inhibition region, dual-wavelength exposure reduces the mechanical stresses exerted and leads to smoother cured surfaces without compromising dimensional accuracy. The observations, coupled with the dimensional control demonstrated earlier, highlight the method's potential to produce high-quality parts with reduced post-curing requirements.

3.1.4. Dynamic mechanical properties characterization

A central question in PinVPP processing is whether the introduction of photoinhibition alters the mechanical integrity of the printed material, particularly given that UV inhibition intentionally slows early network formation during curing. This section evaluates how dual-wavelength curing influences the shear mechanical response and whether inhibited prints can ultimately achieve stiffness and strength comparable to, or exceeding, those obtained under conventional single-wavelength (pure only) exposure. Addressing this question is critical for determining whether the improved dimensional accuracy and surface quality enabled by PinVPP are achieved without compromising mechanical performance.

Figure 8a presents the shear stress-strain response of samples cured at exposure times of 15, 30, and 45 s under two inhibition ratios (I_{UV}/I_{Blue} = 0 and 0.3). For all conditions, the response exhibits the nonlinear behavior characteristic of crosslinked photopolymer networks. At small strains, stress increases approximately linearly with strain, corresponding to elastic deformation governed by network connectivity. As strain increases, deviations from

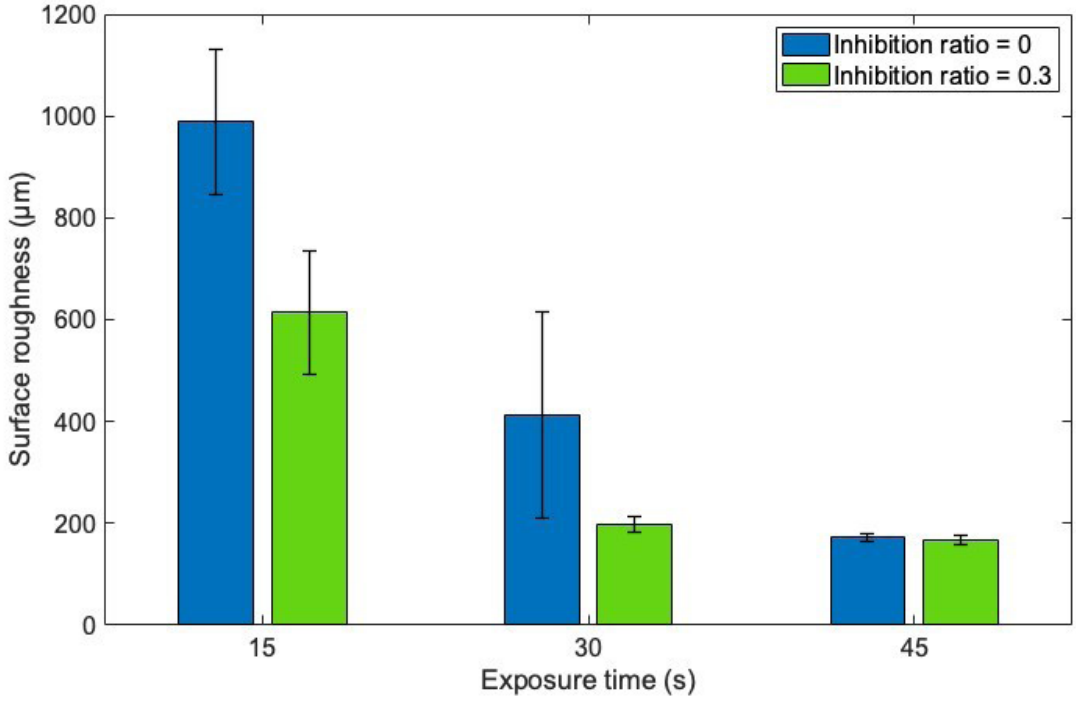

Figure 7. Inhibition effects on surface roughness of printed samples for ratios I_{UV}/I_{Blue} = 0 and 0.3, with exposure times of 15, 30 and 45 s

linearity emerge, followed by stress saturation or softening, reflecting strain-induced network rearrangement and progressive disruption of load-bearing chain segments. To interpret these results, it is important to clarify the mechanical metrics presented. The shear stress-strain curves in Figure 8a quantify the material's resistance to shear deformation under increasing strain. Higher shear stress at a given strain indicates greater resistance to deformation under applied shear. In contrast, the storage modulus G' shown in Figure 8b and 8c represents the elastic stiffness of the network in the small-strain regime, while the loss modulus G'' reflects viscous energy dissipation. Together, these quantities describe how the network balances elastic load-bearing and dissipative mechanisms during deformation.

In the absence of inhibition (I_{UV}/I_{Blue} = 0), shear stress increases systematically with exposure time. The 15 s samples display the lowest stress levels and reach an early stress plateau, indicative of an underdeveloped network with limited resistance to shear deformation. Increasing exposure to 30 s and 45 s results in higher peak stresses and delayed onset of softening, consistent with increased crosslink density and improved stress transfer within the polymer network. At 45 s, the uninhibited samples sustain elevated stresses over a broader strain range, indicating near-complete curing and mechanical stabilization. Introducing photoinhibition (I_{UV}/I_{Blue} = 0.3) modifies the mechanical response in a distinct manner. At 15 s, inhibited samples exhibit substantially higher stresses than their uninhibited counterparts throughout the strain range, despite the delayed curing kinetics. At 30 s and 45 s, inhibited samples maintain elevated stress levels over extended strain ranges and do not exhibit abrupt stress drops or premature yielding. This behavior indicates that UV-induced inhibition does not embrittle the material. Instead, the inhibited networks demonstrate improved strain accommodation and resistance to shear-induced softening.

The stress-strain behavior in Figure 8a is directly reflected in the strain-dependent viscoelastic properties shown in Figure 8b and 8c. For all samples, G' exceeds G'' in the small-strain regime, confirming that elastic deformation governs the initial mechanical response. In Figure 8b (I_{UV}/I_{Blue} = 0), the storage modulus decreases rapidly with increasing strain, particularly for shorter exposure times, indicating early network softening and limited resistance to strain-induced rearrangement. The accompanying rise in G'' at moderate strains reflects increased viscous dissipation as the partially developed network undergoes structural reorganization. Longer exposures shift the onset of modulus decay to higher strains, consistent with the higher stresses sustained in Figure 8a. In contrast, Figure 8c (I_{UV}/I_{Blue} = 0.3) shows that inhibited samples exhibit slightly lower initial storage moduli at longer exposures (notably

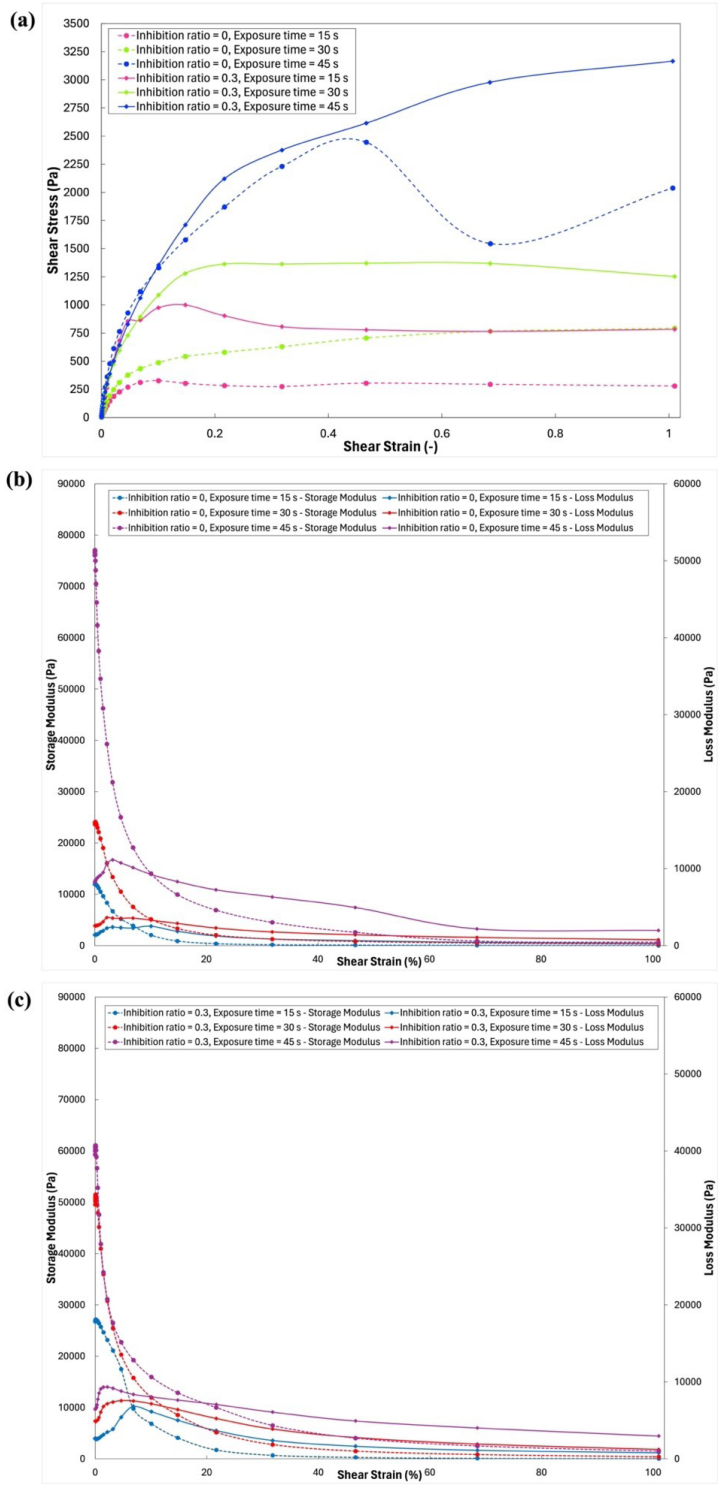

Figure 8. Mechanical response under uninhibited and inhibited curing. (a) Shear stress-strain response of samples cured under pure blue light (*IUV/IBlue = 0*) and dual-wavelength photoinhibition (*IUV/IBlue = 0.3*) at exposure times of 15, 30 and 45s. The plots reflect viscoelastic behavior obtained from amplitude sweep measurements. (b, c) Storage modulus (G') and loss modulus (G'') as functions of shear strain for samples cured under pure blue light (b) and photoinhibition (c), respectively. These measurements are obtained from amplitude sweeps and are used to evaluate the mechanical response and viscoelastic behavior of the printed materials. The results show compliant behavior with a stress plateau at higher strains, indicating a change in deformation response under increasing strain.

at 45 s), indicating reduced elastic stiffness consistent with delayed network formation and moderated crosslink density under photoinhibited conditions. However, despite this reduction in small-strain stiffness, inhibited samples sustain higher shear stresses at larger strains. This apparent divergence between shear stress and storage modulus indicates that photoinhibition redistributes polymerization temporally, altering the balance between stiffness and energy dissipation. Specifically, by slowing early radical propagation and delaying rapid network build-up, photoinhibition prolongs the period during which polymer chains retain mobility. This moderated network formation reduces internal stress concentration and promotes more uniform strain distribution during deformation. As a result, the inhibited networks exhibit lower initial stiffness but enhanced resistance to strain-induced softening, reflected by extended stress plateaus and delayed G' decay. The more gradual increase in G'' further suggests more progressive and distributed energy dissipation rather than abrupt structural failure. It is important to note that this behavior does not imply that inhibition enhances crosslink density or promotes polymer formation beyond conventional curing. Rather, it modifies the temporal evolution of network development, shifting the mechanical response from stiffness-dominated elasticity toward a more deformation-tolerant and dissipative behavior. The observed increase in shear stress at higher strains therefore reflects improved shear resistance through strain accommodation mechanisms, not an increase in elastic modulus.

As exposure time increases, the mechanical differences between inhibited and uninhibited samples diminish in both stress-strain and modulus responses. This convergence indicates that photoinhibition primarily delays early-stage network formation rather than limiting the final achievable stiffness or strength. With sufficient exposure, both curing strategies approach comparable structural stability, although inhibited samples retain a modest advantage in strain tolerance and resistance to softening.

Overall, the combined analysis of shear stress-strain behavior and strain-dependent viscoelastic moduli demonstrates that dual-wavelength photoinhibition does not compromise the shear mechanical integrity of PinVPP-printed parts. While UV-induced inhibition moderates early curing kinetics and slightly reduces initial elastic stiffness, it promotes improved strain accommodation and energy dissipation, enabling enhanced resistance to shear-induced softening. Consequently, PinVPP achieves improved dimensional control and surface quality while preserving mechanical robustness, and in some cases enhancing, deformation tolerance relative to conventional blue-only curing.

3.2. PinVPP printing of functional hydrogels

3.2.1. Curing characterization via Raman spectroscopy

Raman spectroscopy was employed to characterize the curing behavior of the printed hydrogels at the molecular scale, enabling direct evaluation of bond conversion as a function of exposure time and inhibition ratio. Unlike bulk mechanical measurements, which probe the emergent macroscopic response of the network, Raman analysis provides localized insight into the progression of polymerization through the evolution of characteristic vibrational modes. In this work, the DoC was quantified using a peak-area ratio approach, normalized to an internal reference band as introduced in Section 2.4.4, with all the values calculated relative to the uncured (liquid) resin. Although the aliphatic C=C stretching bond near 1638 cm^{-1} is commonly used to track conversion in methacrylate-based systems, this band was not suitable for quantitative analysis in our hydrogel formulation. In hydrated polymer networks, the spectral region around 1640 cm^{-1} is strongly influenced by the H_2O bending vibration (see Figure 9a–c). The water in the material system produces a weak broad feature that overlaps with the C=C band. Naturally, due to the water content of the hydrogel samples, this contribution dominated the spectral response in this region, resulting in a poorly reproducible signal by contrast to the band around 1605 cm^{-1}, which was consistently stronger across all exposure times and inhibition ratios. Additionally, a pronounced peak near 1700 cm^{-1} corresponding to the functional carbonyl stretching vibration (C=O), was also observed in all spectra. This band was however not accounted for, since not directly involved with the free-radical polymerization reaction, and consequently not tied to network formation and conversion. Nonetheless, the band persistence across curing conditions serves as an internal consistency check for spectral stability.

The Raman spectra of the uninhibited samples ($I_{UV}/I_{Blue} = 0$) are shown in Figure 9a. With increasing exposure time from 30 to 60 s, the relative intensity of the 1,600 cm^{-1} band decreases progressively, consistent with increasing bond conversion. The most pronounced spectral changes occur between 45 and 60 s, indicating that a substantial fraction of polymerization takes place at longer exposure times in this system. This behavior is reflected in the DoC values (illustrated in Figure 9c), which increase from 3.14% at 30 s to 6.37% at 45 s, and 25.68% at 60 s. This monotonic increase in DoC with exposure time is consistent with conventional photopolymerization behavior, where prolonged

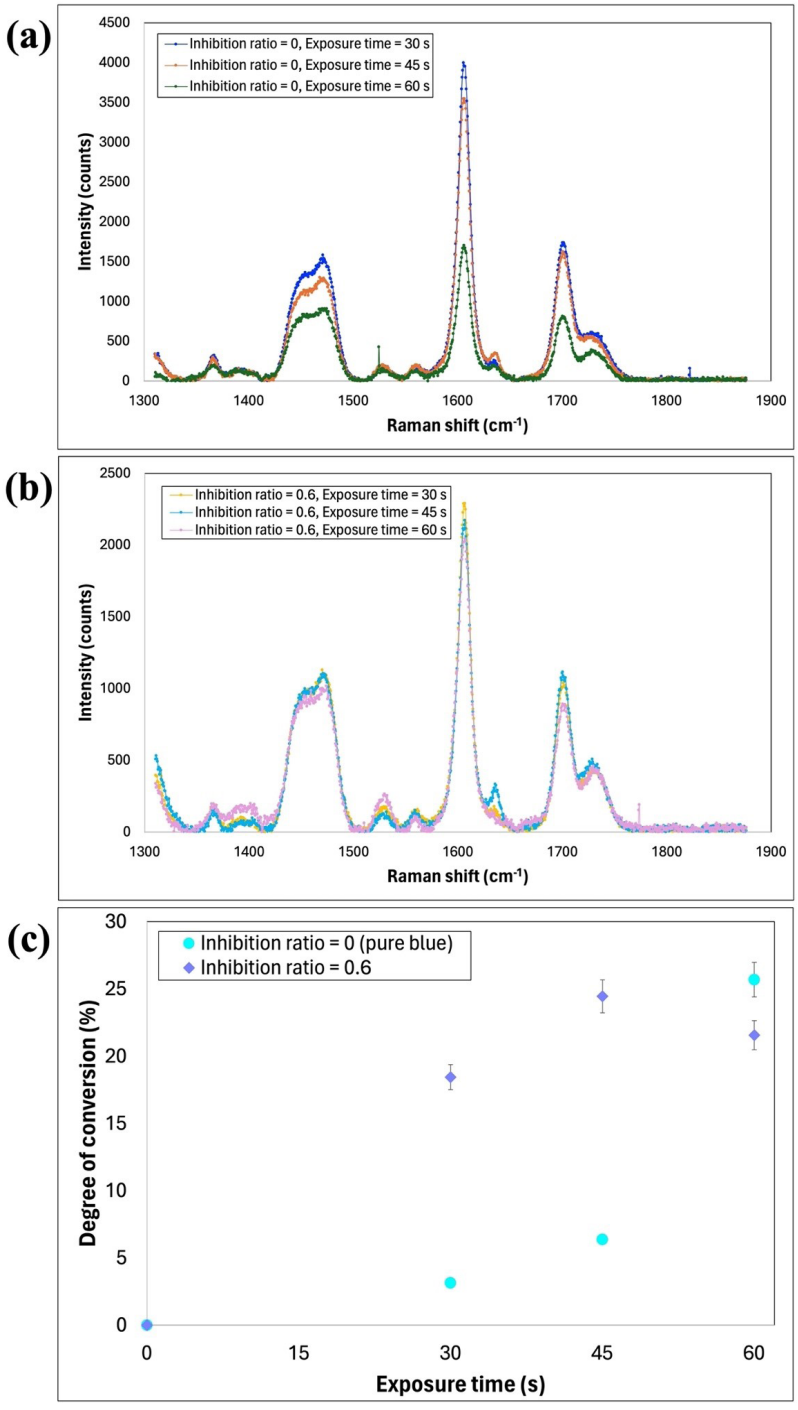

Figure 9. Raman spectra of hydrogels given exposure times of 30, 45 and 60 s: (a) samples cured under pure blue light ($I_{UV}/I_{Blue} = 0$); (b) samples cured under inhibition ($I_{UV}/I_{Blue} = 0.6$); (c) Raman-derived degree of conversion as a function of exposure time for both conditions. Uninhibited samples exhibit a monotonic increase in DoC with exposure time, while inhibited samples show elevated apparent conversion at short exposure times followed by saturation, highlighting the influence of photoinhibition on curing kinetics rather than final conversion extent. The reported values are normalized with respect to the measured signal and do not represent absolute conversion. Minor variations in the reference band intensity may arise from measurement conditions and sample heterogeneity. In particular, the samples are not perfectly uniform in size or geometry, and their surfaces are not ideally flat, which makes consistent Raman acquisition challenging and can introduce variability in the normalized values. The trends shown should therefore be interpreted qualitatively within the context of the experiments.

irradiation promotes continued radical propagation and crosslink formation. The corresponding spectra for the inhibited samples (I_{UV}/I_{Blue} = 0.6) are shown in Figure 9b. In contrast to the uninhibited case, the inhibited samples exhibit more modest changes in peak intensities with increasing exposure time, particularly between 45 and 60 s. The DoC values extracted are 18.44% at 30 s, 24.45% at 45 s, and 21.56% at 60 s (shown in Figure 9c). While the DoC initially increases with exposure time from 30 to 45 s, it does not continue to rise at 60 s, instead exhibiting a slight decrease. At first glance, this behavior appears counterintuitive, especially since the DoC values for the inhibited samples are higher than those printed under pure blue exposure, with the exception of samples acquired at 60 s, where the expected trend is recovered. However, several plausible mechanisms may explain these observations. Raman spectra were collected at multiple locations across the sample surfaces and averaged to obtain representative values, and the error bars shown in Figure 9c represent an estimated ±5% measurement uncertainty associated with Raman-based DoC measurements. First, the Raman-derived DoC reflects local chemical conversion at the probed surface rather than the global average conversion across the entire printed sample. In hydrogel systems, spatial heterogeneities in water content, oxygen diffusion and radical concentration can lead to localized variations in polymerization kinetics. Moreover, because Raman measurements rely on sufficient contrast between the sample and the background, imaging can be challenging. This limitation can further amplify local spectral variations and contribute to apparent deviations within the expected uncertainty range. Under photoinhibition, delayed curing may additionally promote enhanced chain mobility and radical diffusion at early stages, resulting in comparatively high conversion values at short exposure times. Second, prolonged exposure under inhibition may promote secondary processes such as radical recombination, or network rearrangement, which could reduce the apparent intensity contrast between the conversion-sensitive and reference bands. This could manifest as a plateau or slight decrease in the apparent DoC extracted from Raman ratios, even though crosslinking continues to evolve structurally. Importantly, this does not necessarily imply a true reduction in chemical conversion, but rather reflects the sensitivity of Raman metrics to local environment, scattering efficiency, and chain conformation. Lastly, the delayed polymerization induced by photoinhibition alters the competition between radical generation, network formation, and diffusion during curing. While inhibition reduces the instantaneous radical concentration, it also delays rapid network build-up and the associated mobility restrictions that normally limit further reaction. Traditionally, fast crosslink formation can quickly restrict radical and monomer diffusion, which limits additional conversion even while exposure continues. Under photoinhibited conditions, the reduced initial reaction rate prolongs the period during which the material remains mobile, allowing radicals and monomers to diffuse more effectively and continue reacting before the network becomes diffusion-limited. This extended mobility window can enable higher local conversion at early exposure times, even though the overall reaction is temporally delayed.

These results therefore indicate that photoinhibition primarily modifies the temporal evolution and spatial distribution of polymerization rather than simply suppressing the final extent of curing. Uninhibited samples exhibit slower early conversion but continue to polymerize significantly at longer exposure times. In contrast, inhibited samples show accelerated early-stage conversion followed by apparent saturation, consistent with delayed network formation, enhanced molecular mobility and redistribution of polymerization kinetics.

3.2.2. Dimensional and surface properties

A key objective of this section is to evaluate whether the benefits of dual-wavelength PinVPP observed in the PLA-PUA system extend to hydrogel printing, where excessive curing, dimensional and surface irregularities are particularly challenging due to the soft and highly hydrated nature of the material. Hydrogels are especially sensitive to overcuring and interfacial forces during layer separation, making them an ideal platform for assessing the effectiveness of photoinhibition in controlling cure thickness, feature fidelity, and surface quality. To this end, cure thickness, lateral feature diameter, and surface roughness were systematically quantified for hydrogel samples printed under pure blue light exposure (I_{UV}/I_{Blue} = 0) and under photoinhibition (I_{UV}/I_{Blue} = 0.6) across a range of radiant exposures and exposure times.

Figure 10 presents the variation in cure thickness as a function of radiant exposure for both curing conditions. Under pure blue exposure, the cure thickness increases steadily with increasing radiant exposure, rising from approximately 2,200 μm at 640 mJ/cm^2 to about 2500 μm at 1,280 mJ/cm^2. This monotonic increase reflects the unimpeded penetration of curing light and the cumulative nature of photopolymerization in the absence of photoinhibition. In contrast, when photoinhibition is introduced, the cure thickness is consistently reduced at all radiant exposures, remaining closer to 2,000–2,300 μm even as exposure is increased. This indicates that UV-induced inhibition effectively moderates depth-wise polymerization by limiting radical propagation beyond a

controlled inhibition zone. Most importantly, the inhibited samples still achieve continuous and mechanically stable layers, as demonstrated by the subsequent sections, reflecting how inhibition suppresses excessive penetration without completely preventing curing.

The combined influence of exposure time and inhibition on both vertical and lateral dimensions is further illustrated in Figure 11. For pure blue curing, the cure thickness increases substantially with exposure time, exceeding the expected target depth—defined by substrate and print head spacing—at longer exposures and indicating progressive vertical overcuring. In contrast, inhibited samples display a much narrower range of cure thickness across all exposure times studied, providing a more reliable means of reaching the desired layer depth—thickness—than exposure control alone. This stabilization is particularly advantageous for hydrogel printing, where excessive cure thickness can compromise layer definition and resolution.

Lateral dimensional fidelity shows a more nuanced trend. The projected mask diameter for these experiments was 10,000 μm, and the measured feature diameters for both inhibited and uninhibited samples fall within the same order of magnitude across the investigated exposure times.

However, deviations from the target dimension are observed, particularly at longer exposure times where overcuring becomes more pronounced. Inhibition consistently produces slightly smaller feature diameters than pure blue curing, indicating reduced lateral overgrowth even though the target diameter is not fully achieved under all conditions. In contrast, the cure thickness variations show a clearer benefit from inhibition. The desired cure thickness for these samples was approximately 2,000 μm, defined by the printing gap. Pure blue exposure ($I_{UV}/I_{Blue} = 0$) progressively exceeds this target with increasing exposure time, demonstrating vertical overcuring. The inhibited condition ($I_{UV}/I_{Blue} = 0.6$), however, achieves cure thicknesss much closer to the desired value and maintains a narrower variation across exposure times. Importantly, when overcuring occurs at longer exposures, it remains less severe under inhibited conditions than under pure blue curing.

The relatively modest lateral effect is expected because the present experiments employed overlapping inhibition rather than a deliberately patterned lateral inhibition strategy, as previously mentioned in Section 3.1.3. Under these conditions, photoinhibition primarily moderates depth-wise polymerization, while in-plane curing remains largely governed by the projected optical pattern. This decoupling of vertical and lateral control observed for the printed hydrogels presents an opportunity to control dimensional accuracy without requiring complex exposure

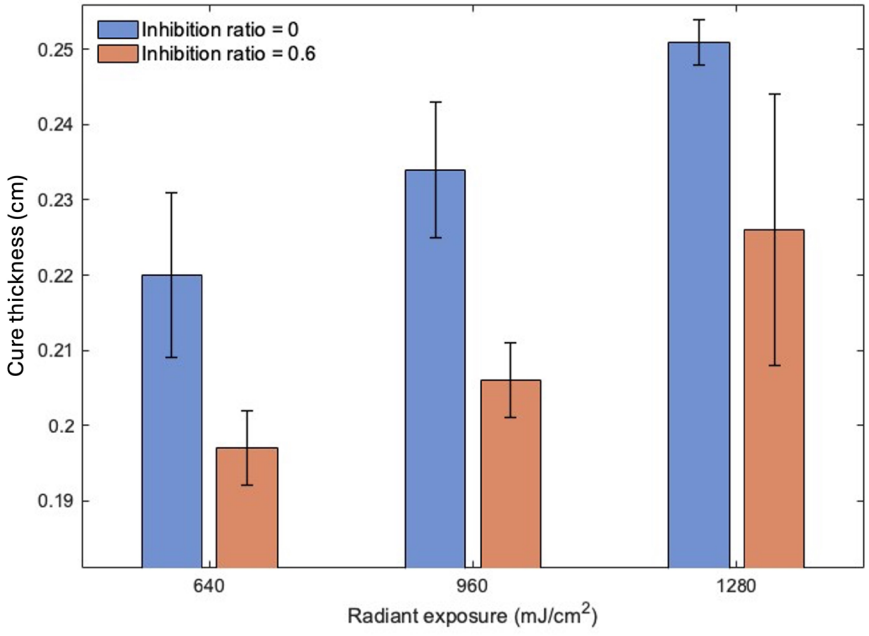

Figure 10. Cure thickness as a function of radiant exposure for hydrogel samples printed under pure blue light exposure ($I_{UV}/I_{Blue} = 0$) and under photoinhibition ($I_{UV}/I_{Blue} = 0.6$). Data reflects measurements for samples cured for 30, 45 and 60 s for both experimental groups.

tuning. Future work should therefore explore spatially patterned inhibition masks to intentionally control lateral polymerization and improve agreement with target feature dimensions.

Surface roughness measurements, summarized in Figure 12, further highlight the benefits of photoinhibition for hydrogel printing. Under pure blue light exposure, surface roughness is highest at the shortest exposure time, reaching values exceeding 300 μm at 30 s, accompanied by large variability. Such roughness is characteristic of fragile hydrogel layers that experience significant interfacial stresses during separation from the print window, thus leading to surface tearing and irregular deformation. When photoinhibition is applied, surface roughness is markedly reduced across all exposure times, with surface roughness consistently lower and exhibiting smaller scatter. At 30 s, inhibition reduces roughness by nearly half, indicating a substantial mitigation of interfacial stresses during layer detachment. As exposure time increases, surface roughness decreases for both conditions, reflecting improved structural robustness of the cured hydrogels. However, the inhibited samples maintain equal or lower roughness compared to uninhibited ones at all times, suggesting that the presence of an inhibition zone continues to play a protective role even as the material stiffens. Through the prevention of excessive curing, photoinhibition reduces suction forces and mechanical stresses during separation, thus resulting in smoother top surfaces and consistent surface quality.

3.2.3. Rheological behavior

Hydrogels present a fundamentally different mechanical landscape than rigid photopolymers due to their low crosslink density, high solvent content, and pronounced viscoelasticity. As a result, controlling network formation during VPP is especially critical for achieving mechanically uniform and deformation-tolerant structures. Due to these limitations, the use of dual-wavelength PinVPP presents an opportunity to test how UV-induced photoinhibition can be used to regulate polymerization kinetics and improve mechanical performance without compromising the intrinsic compliance of hydrogel networks. This section investigates the shear mechanical response of hydrogels printed at inhibition ratios of I_{UV}/I_{Blue} = 0 and 0.6 under exposure times of 30, 45, and 60 s, with the aim of clarifying how photoinhibition influences network development, stress response, and viscoelastic stability.

Figure 13a presents the shear stress-strain response of hydrogel samples cured under both inhibition conditions. For all samples, the stress-strain curves exhibit a strongly nonlinear response characteristic of soft networks, with an initially compliant regime followed by gradual stress

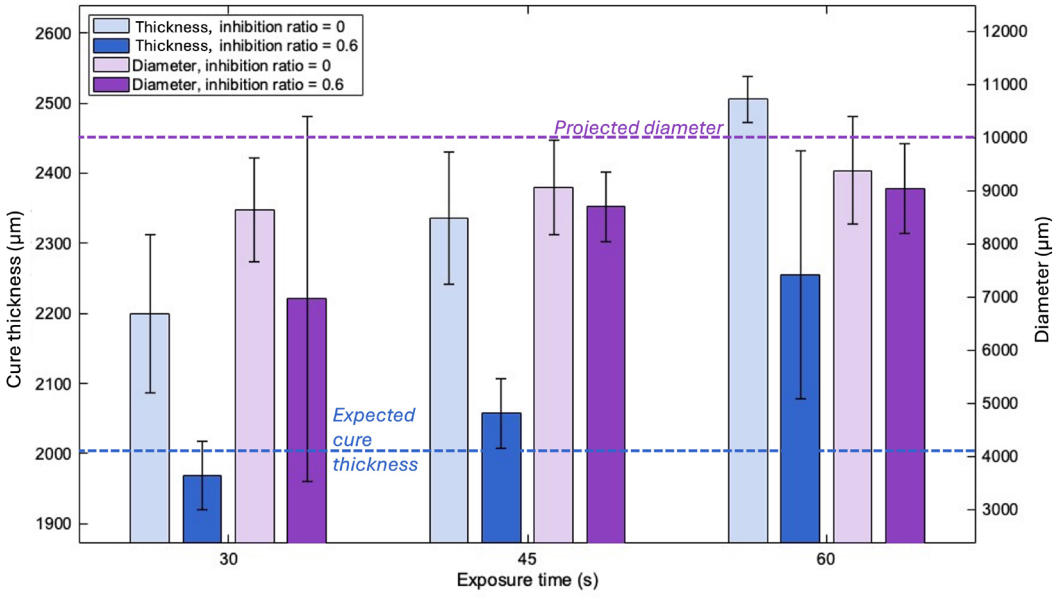

Figure 11. Effect of exposure time on cure thickness and lateral feature diameter for hydrogel samples printed under inhibition ratios I_{UV}/I_{Blue} = 0 and 0.6 at varying exposure times. Bars indicate cure thickness (left y axis), while symbols show the measured diameter (right y axis) obtained from Keyence VR-3200 scans. All samples were printed under identical conditions except for the programmed changing exposure time.

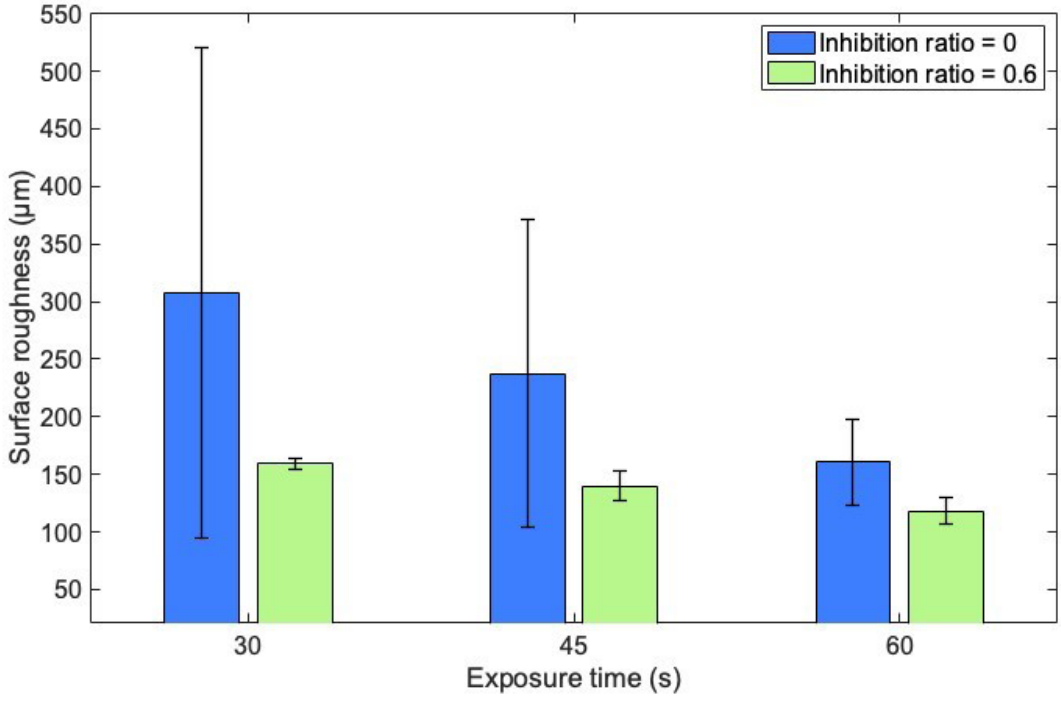

Figure 12. Hydrogel samples surface roughness evaluation for ratios I_{UV}/I_{Blue} = 0 and 0.6, printed under exposure times of 30, 45 and 60 s

buildup and extended strain accommodation. Unlike the polymer system discussed previously, the hydrogels do not exhibit sharp yielding or brittle failure, reflecting the dominance of elastic stretching and viscous dissipation within the swollen polymer network.

Under uninhibited curing (I_{UV}/I_{Blue} = 0), the shear stress increases with exposure time, indicating progressive network formation and increased crosslink density. The 30 s samples display the lowest stress levels and reach a shallow stress plateau at relatively low strains, consistent with an underdeveloped network. Increasing the exposure time to 45 s and 60 s results in higher stresses sustained over a broader strain range, reflecting enhanced capacity as network connectivity increases. However, even at the longest exposure, the stress growth remains gradual, underscoring the compliant nature of the hydrogel matrix.

Using inhibition (I_{UV}/I_{Blue} = 0.6) modifies the shear stress response of the hydrogels in a manner that is strongly dependent on exposure time and strain regime, rather than producing a uniform enhancement across all conditions. Inhibited samples do not consistently exhibit higher stresses than their uninhibited counterparts at equivalent strains. Instead, photoinhibition alters the shape of the stress-strain curves, particularly at intermediate and large strains, where differences in strain and stress saturation become apparent. At shorter exposure times, inhibited samples tend to show reduced stress buildup, consistent with delayed network formation. With increasing exposure, however, the inhibited networks develop more gradually and sustain continued stress growth over extended strain ranges, whereas some uninhibited samples exhibit earlier stress saturation or partial softening. This behavior suggests that photoinhibition primarily affects how the hydrogel network evolves under deformation, rather than simply increasing its stiffness or strength. Notably, none of the inhibited samples display abrupt stress drops or brittle-like failure, confirming that UV-induced inhibition does not induce embrittlement. Instead, the broader stress plateaus and smoother transitions observed in the inhibited curves indicate enhanced deformation tolerance and more progressive load redistribution within the swollen polymer network.

The strain-dependent viscoelastic behavior underlying these stress-strain trends is elucidated in Figure 13b and 13c, which show the storage modulus G' and loss modulus G'' as functions of shear strain for I_{UV}/I_{Blue} = 0 and 0.6, respectively. For all hydrogel samples, G' dominates G'' in the small-strain regime, confirming that elastic deformation governs the initial mechanical response. As expected for soft, water-swollen networks, the absolute magnitude of G' is substantially lower than that observed for the polymer systems, reflecting the lower crosslink density and greater chain mobility characteristic of hydrogels.

In Figure 13b (I_{UV}/I_{Blue} = 0), G' decreases rapidly with

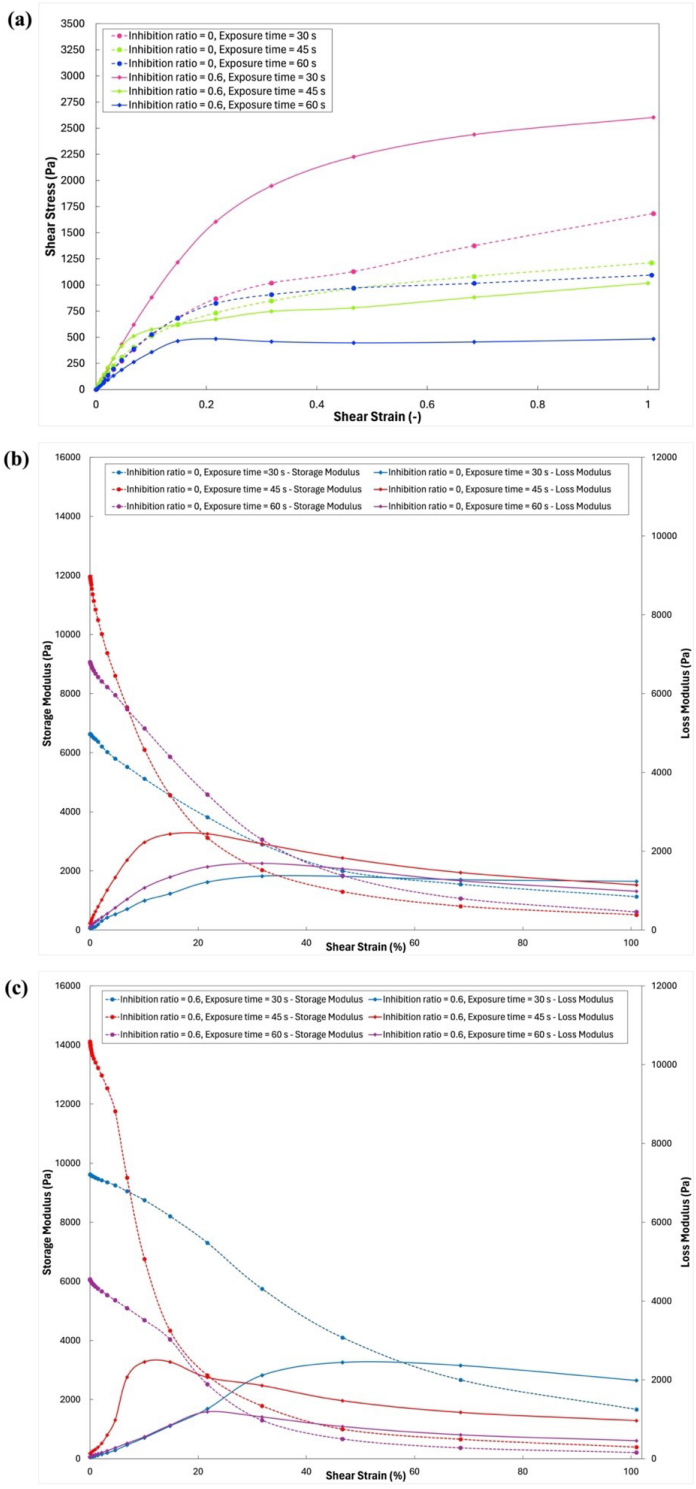

Figure 13. Mechanical response of hydrogel samples printed without and with inhibition. (a) Shear stress-strain amplitude response of hydrogel samples cured under pure blue light (*IUV/IBlue = 0*) and dual-wavelength photoinhibition (*IUV/IBlue = 0.6*) at exposure times of 30, 45, and 60 s. The plots reflect viscoelastic behavior obtained from amplitude sweep measurements. (b, c) Storage modulus (G') and loss modulus (G'') as functions of shear strain for samples cured under pure blue light (b) and photoinhibition (c), respectively. These measurements correspond to shear-based mechanical testing, with modulus values obtained from amplitude sweep experiments. The results show compliant mechanical behavior, with variations in response observed across exposure conditions and inhibition levels.

increasing strain, particularly for the samples cured in shortest exposure time, indicating early network softening and limited resistance to strain-induced rearrangement. This rapid decay of G' is accompanied by a pronounced rise in G'' at moderate strains, highlighting the increasing contribution of viscous dissipation as polymer chains slide, disentangle, and reorganize within the swollen matrix. Increasing exposure time delays the onset of modulus decay, consistent with the more sustained stress growth observed in Figure 13a.

In contrast, Figure 13c (I_{UV}/I_{Blue} = 0.6) shows that photoinhibition systematically alters the strain-dependent viscoelastic response. While the initial G' values are not uniformly higher than those of the uninhibited samples, the decay of G' with strain is generally more gradual, and the rise in G'' occurs more progressively. This indicates that inhibited networks undergo a more distributed and continuous rearrangement process under shear, rather than rapid strain-induced softening. The more gradual crossover between G' and G'' reflects a smoother transition from elastic-dominated to dissipation-dominated behavior, consistent with the broader stress plateaus and extended strain observed in Figure 13a. As exposure time increases, the mechanical differences between inhibited and uninhibited hydrogels diminish. With sufficient exposure, both curing strategies converge toward comparable stiffness levels; however, the inhibited samples consistently exhibit more gradual modulus decay and smoother stress evolution, suggesting improved resistance to strain localization and network heterogeneity.

Dual-wavelength PinVPP modifies hydrogel mechanics primarily by regulating how the network forms and reorganizes under deformation, rather than by simply increasing stiffness. By slowing early photopolymerization kinetics, photoinhibition promotes a more progressive and spatially uniform network development, leading to enhanced deformation tolerance. These findings confirm that PinVPP can be extended to soft hydrogel systems, enabling improved mechanical stability under large deformations while preserving the flexibility and compliance required for hydrogel-based applications, especially in the biomedical field.

3.2.4. Sample stability and shrinkage assessment

In order to assess the long-term dimensional fidelity of the printed structures and determine whether photoinhibition improves resistance to post-print shrinkage, the shrinkage and geometric stability of hydrogel samples were monitored through time-resolved diameter measurements immediately after printing and after two weeks of air storage. Figure 14 presents the evolution of sample diameter for structures printed under pure blue exposure given I_{UV}/I_{Blue} = 0 (see Figure 14a) and dual-wavelength PinVPP with I_{UV}/I_{Blue} = 0.6 (see Figure 14b), comparing the projected mask dimensions, post-print values, and measurements obtained after two weeks of air storage. Diameter was selected as the primary metric, as the sample weight remained comparatively stable over this time frame and did not provide additional insight into shrinkage measurement (see Figure B2 in Appendix B for sample scans). Shrinkage percentage was then calculated with regards to the projected mask dimension (10 000 μm).

For the uninhibited samples in Figure 14a, a clear reduction from the projected dimension to the post-print diameter is observed, reflecting polymerization-induced shrinkage associated with monomer-to-polymer conversion and network densification. This shrinkage decreases systematically with increasing exposure time, from 24.70% at 30 s to 19.72% at 45 s and 16.87% at 60 s. This trend is consistent with more complete network formation at longer exposures, which promotes earlier curing and reduces subsequent volumetric collapse. After two weeks, the corresponding values remain close to the post-print measurements (24.93%, 20.61%, and 17.69%, respectively), indicating that most of the dimensional contraction occurs during curing. Once formed, the network reaches a mechanically stable configuration that resists further deformation.

In contrast, the inhibited samples in Figure 14b exhibit a markedly different early-stage response. At 30 s, the post-print shrinkage is extremely large (69.94%), indicating insufficient early-stage network formation and poor structural integrity immediately after printing. This behavior is consistent with the delayed polymerization kinetics imposed by photoinhibition, which suppresses early radical propagation and postpones rapid network build-up. As discussed in the rheological analysis, photoinhibition shifts polymerization temporally rather than suppressing the final extent of curing. The network therefore remains more weakly developed immediately after printing, making it more susceptible to post-print densification and dimensional shrinkage as polymerization continues. However, as exposure time increases to 45 and 60 s, the post-print shrinkage decreases substantially to 20.63% and 19.42%, respectively, approaching the values observed for uninhibited samples. After two weeks, the inhibited samples show shrinkage values of 25.27%, 23.09%, and 20.75% for 30, 45, and 60 s, respectively. Importantly, the convergence between post-print and long-term dimensions at higher exposures indicates that photoinhibition does not compromise final geometric stability when sufficient curing is provided. Instead, inhibition primarily delays the

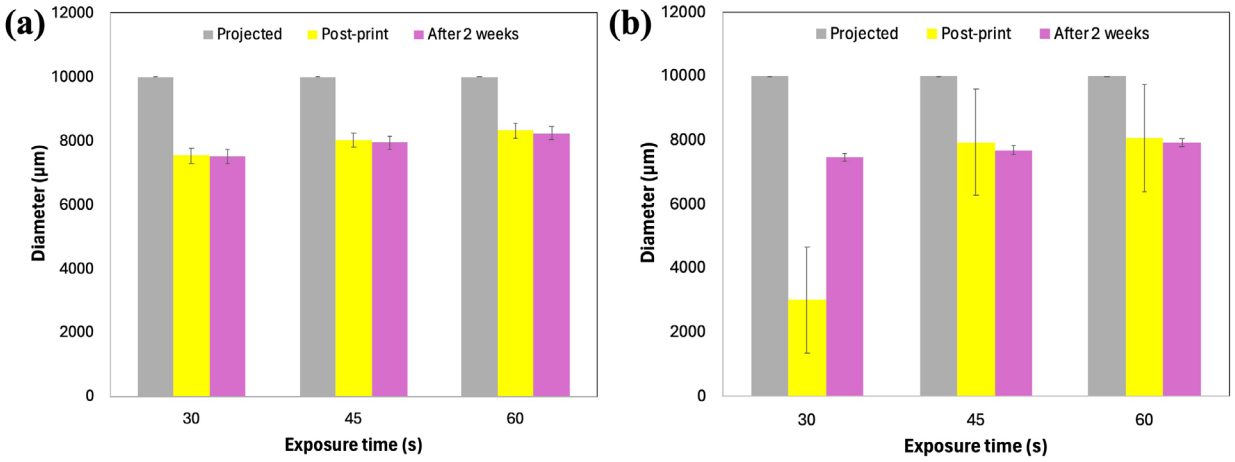

Figure 14. Diameter-based shrinkage and geometric stability of hydrogel samples printed under pure blue-light curing (I_{UV}/I_{Blue} = 0) (a) and dual-wavelength PinVPP (I_{UV}/I_{Blue} = 0.6) (b), shown relative to the projected mask dimensions, post-print state, and after two weeks of storage. The reduction from the projected dimension reflects curing-induced shrinkage, while convergence of post-print and long-term values at higher exposures indicates attainment of a stable final geometry. Abbreviation: PinVPP: Photoinhibition-aided vat photopolymerization.

onset of dimensional stabilization, allowing the network to evolve more gradually toward its final configuration.

These results demonstrate that shrinkage is strongly governed by both exposure time and inhibition ratio. Uninhibited samples polymerize rapidly, leading to faster network formation and earlier geometric stabilization. On the other hand, inhibited samples undergo a more progressive dimensional evolution due to delayed reaction kinetics, which can result in severe early contraction when exposure time is insufficient but ultimately converges toward similar final dimensions when adequately cured. While photoinhibition can suppress the overall degree of monomer conversion, the combined spectroscopic and rheo-mechanical evidence demonstrates that it simultaneously regulates radical generation, redistributes polymerization temporally, and promotes a more controlled and spatially organized polymer network architecture. Across these measurements, inhibition consistently produces a network that forms more gradually, exhibits reduced early stiffness, and stabilizes at later stages, ultimately reaching comparable long-term structural integrity once sufficient curing is achieved.

3.2.5. Swelling and water uptake variations

To evaluate the aqueous stability of the printed hydrogels and assess the influence of photoinhibition on post-print dimensional behavior, swelling and water uptake were quantified by immersing printed test specimens in deionized water at room temperature for predetermined time intervals of 2, 4, 6, 8 and 10 mins (Figure B3 in Appendix B). Sample mass and diameter were recorded at each time point using a precise balance and optical microscopy. Changes were expressed as percentage variations, enabling direct comparison across curing conditions. This approach allows isolation of curing-induced contraction from hydration-induced expansion and provides a quantitative basis for evaluating whether photoinhibition influences structural stability during aqueous exposure.

Figure 15 presents the weight evolution of the hydrogel samples during immersion for uninhibited (I_{UV}/I_{Blue} = 0) and photoinhibited (I_{UV}/I_{Blue} = 0.6) curing. For uninhibited samples, weight increases rapidly during the initial minutes of immersion, indicating fast water diffusion into the polymer network (see Figure 15a). This behavior is most pronounced at shorter exposure times, where the effective crosslink density is lowest. As exposure time increases from 30 to 60 s, the magnitude of water uptake decreases, reflecting the formation of a denser network with reduced free volume and lower permeability. This inverse relationship between hydration-induced mass uptake and crosslink density is characteristic of hydrogel systems.

On the other hand, the inhibited samples in Figure 15b exhibit more moderate and uniform weight swelling across all exposure times. Although photoinhibition delays early-stage polymerization, the final networks appear to be more homogeneous, leading to more controlled hydration behavior. The reduced and more gradual mass increase suggests suppression of large-scale network heterogeneities and a more uniform distribution of crosslinks. This

behavior is consistent with the smoother mechanical response and more progressive modulus decay observed in earlier sections.

The dimensional swelling trends shown in Figure 15c and 15d further corroborate these observations. For uninhibited samples in Figure 15c, the diameter increases substantially with immersion time, particularly at shorter exposure conditions. This pronounced expansion reflects a loosely crosslinked structure that readily accommodates solvent molecules. Note that the dimensional reduction observed at the 2 min time mark reflects a brief initial shrinkage driven by continued post-print network densification and rapid leaching upon immersion, before swelling becomes dominant and water uptake reaches equilibrium. As exposure time increases, swelling becomes more constrained, consistent with increased network density and reduced chain mobility. In Figure 15d, inhibited samples consistently show lower and more gradual dimensional expansion. Even at short exposure times, inhibited samples swell less than their uninhibited counterparts, indicating that delayed curing promotes a more uniform network architecture that resists osmotic expansion more effectively. This behavior aligns with the rheological results, which showed more progressive

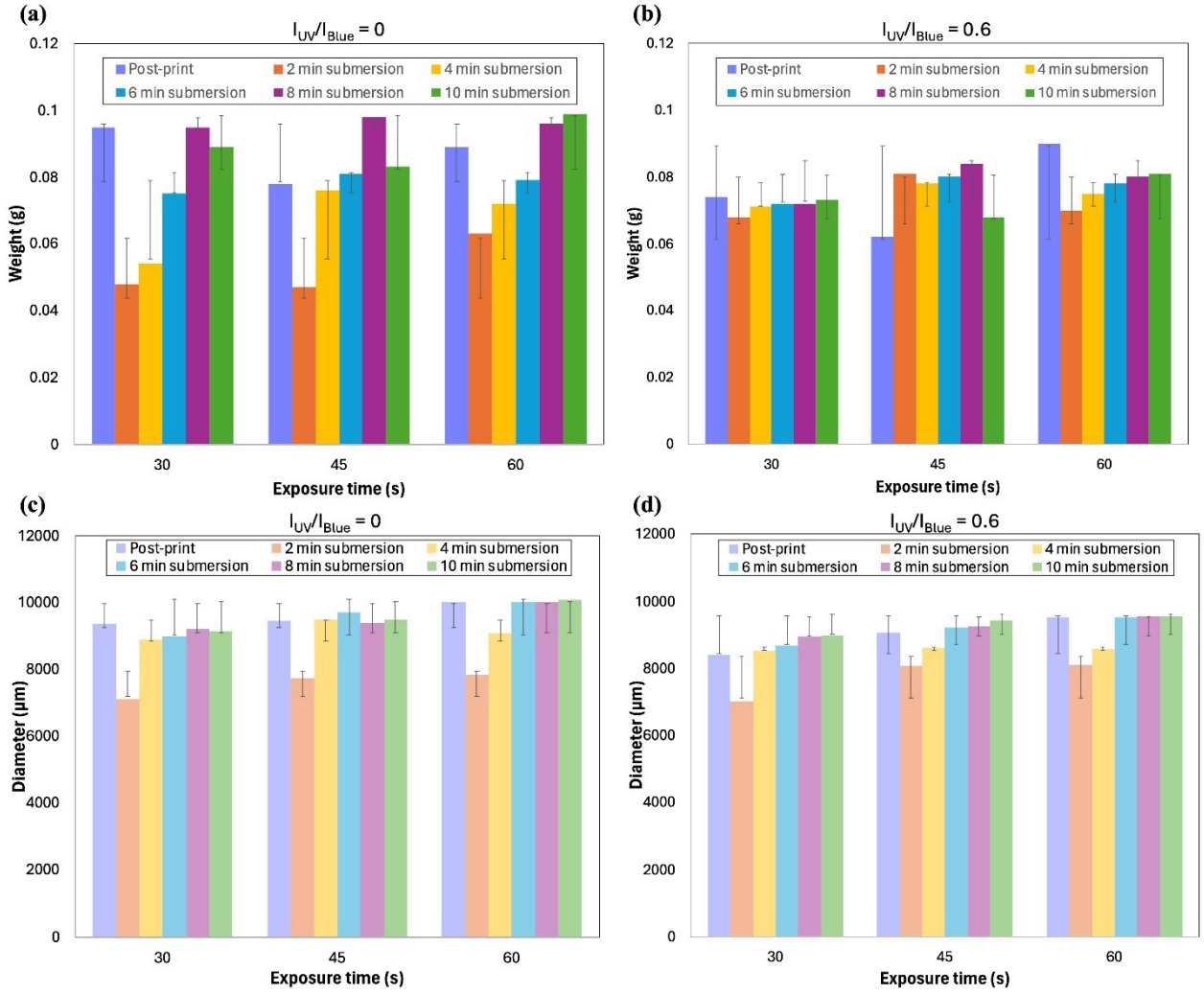

Figure 15. Swelling behavior of hydrogel samples printed without and with inhibition. (a, b) Water uptake of hydrogel samples printed under pure blue-light curing (I_{UV}/I_{Blue} = 0) (a) and dual-wavelength PinVPP (I_{UV}/I_{Blue} = 0.6) (b), quantified as weight increase relative to the dry state post-print samples as a function of exposure time. Uninhibited samples exhibit faster and larger early uptake, whereas inhibited samples show more moderate and uniform hydration behavior. (c, d) Swelling of hydrogel samples printed under pure blue-light curing (I_{UV}/I_{Blue} = 0) (c) and dual-wavelength PinVPP (I_{UV}/I_{Blue} = 0.6) (d), expressed as diameter increase relative to the post-print samples as a function of exposure time. Inhibited samples display a reduced and more gradual expansion.

Abbreviation: PinVPP: Photoinhibition-aided vat photopolymerization.

modulus decay and smoother stress redistribution under inhibited curing.

At longer immersion times (10 min), samples approach a swelling limit, beyond which fracture occurs. This indicates that the network has reached its maximum extensibility, where pressure and chain stretching can no longer be accommodated elastically. The fact that inhibited samples approach this limit more gradually further supports the hypothesis that photoinhibition enhances deformation tolerance and structural resilience. Overall, these results demonstrate that photoinhibition does not merely delay curing but actively modifies the pathway of network formation, resulting in structures that absorb water more uniformly and resist excessive expansion. This controlled hydration response is particularly advantageous for applications requiring long-term dimensional stability in aqueous environments, including biomedical implants, and soft wearable devices where uncontrolled swelling can lead to distortion and functional degradation.

4. Conclusion

This work presents a systematic and unified investigation of dual-wavelength photoinhibition-aided vat photopolymerization (PinVPP) as a potential strategy for improving print fidelity, curing control, and mechanical stability in both bio-based polymer systems and functional hydrogels. PinVPP introduces a new degree of freedom for regulating polymerization kinetics by decoupling radical generation and suppression. Across both material systems, photoinhibition was shown to modify the temporal pathways of radical generation and propagation, monomer crosslinking and network formation while limiting the final attainable extent of conversion. For the PLA-PUA polymeric blend, the analysis revealed measurable differences in DoC, indicating that inhibition alters curing progression and the evolution of crosslinking. In the hydrogel system, the changes in DoC were less pronounced due to the inherent experimental challenges associated with Raman measurements in water-rich networks. Nevertheless, the delayed polymerization pathway consistently altered how and when the network is developed. This manifests in the measured properties through reduced early-stage stiffness, more gradual modulus decay, enhanced resistance to strain-induced softening, delayed dimensional stabilization, and more controlled swelling behavior. Collectively, these results show that photoinhibition redistributes curing in time, leading to differences in stress development, defect formation, and hydration response even when the final conversion remains comparable at sufficient exposure.

The principal findings and contributions of this work are summarized as follows:

(i) **Controlled curing kinetics:** Photo-DSC measurements showed that photoinhibition delays the onset of rapid polymerization, reduces instantaneous reaction rates, and redistributes curing over extended time scales. This moderated temporal evolution suppresses excessive cure thickness, mitigates vertical overgrowth, and enables more predictable dimensional confinement, including improved control over lateral spreading and overall three-dimensional overcuring.

(ii) **Improved geometric fidelity and surface quality:** Inhibited samples consistently exhibited improved vertical accuracy and smoother surfaces relative to uninhibited counterparts, particularly at short exposure times where conventional VPP is most susceptible to dimensional instability.

(iii) **Preserved mechanical robustness:** Mechanical characterization confirmed that photoinhibition does not compromise structural integrity. In polymeric blends, inhibited samples sustained comparable or higher shear stresses over broader strain ranges and exhibited delayed softening. In hydrogel systems, inhibition shifted the response toward more progressive stress evolution, smoother modulus decay, and enhanced deformation tolerance.

(iv) **Temporal redistribution of network formation:** Photoinhibition modifies the timing and pathway of network development without suppressing ultimate network formation, thereby influencing stress evolution and structural stabilization rather than reducing crosslinking efficiency.

(v) **Controlled hydration and long-term dimensional stability:** Swelling and water uptake analyses revealed that photoinhibited hydrogels absorb water more gradually and exhibit reduced dimensional expansion compared to single-wavelength curing. Although inhibition delays early geometric stabilization, long-term dimensions converge when adequate curing is applied.

Building on these findings, several promising directions emerge for advancing the PinVPP framework and extending its impact across next-generation additive manufacturing systems. The demonstrated ability to regulate polymerization through tunable photoinhibition establishes PinVPP as a powerful strategy for tailoring material behavior to application-specific requirements without relying solely on static exposure conditions or extensive resin reformulation. Future research may explore the integration of real-time optical diagnostics to track

process dynamics during printing, enabling adaptive or closed-loop control of curing kinetics. Additional opportunities include spatially patterned inhibition for enhanced lateral confinement and feature resolution, as well as the extension of the approach to multi-material architectures and more complex functional resin systems. More broadly, treating photoinhibition as an active design parameter in the photopolymerization process opens new possibilities for engineering spatially and temporally controlled polymer networks. In this context, dual-wavelength PinVPP provides a versatile platform for expanding the material and performance envelope of vat photopolymerization, supporting the fabrication of sustainable structural polymers as well as soft, functional materials with programmable properties.

Acknowledgments

The authors would also like to thank Heyang Zhang for his work on the in-house system setup in the ZIP-AM research laboratory, and Professor Qihan Liu and his team for providing the rheology test equipment and assisting with the tests.

Funding

We acknowledge the fundings from the National Science Foundation under Faculty Early Career Development Award: CMMI-2238557. Any opinions, findings, and conclusions or recommendations expressed in this publication are those of the authors and do not necessarily reflect the views of the National Science Foundation.

Conflict of interest

The authors declare the following financial interests/personal relationships which may be considered as potential competing interests: Xiayun Zhao reports financial support provided by the National Science Foundation Faculty Early Career Development Program under Award ID CMMI-2238557. Xiayun Zhao is the inventor of a related patent (U.S. Patent No. 12,558,837; U.S. Application No. 17/437,343; International Application No. PCT/US20/21727), which covers aspects of two-wavelength digital light processing-based vat photopolymerization systems and methods described in this study.

Author contributions

Conceptualization: Yousra Bensouda, Xiayun Zhao
Data curation: Yousra Bensouda, Xiayun Zhao
Formal analysis: Yousra Bensouda, Xiayun Zhao
Funding acquisition: Xiayun Zhao
Investigation: Yousra Bensouda, Xiayun Zhao
Methodology: Yousra Bensouda, Xiayun Zhao
Project administration: Xiayun Zhao
Resources: Xiayun Zhao
Supervision: Xiayun Zhao
Validation: Yousra Bensouda
Visualization: Yousra Bensouda, Xiayun Zhao
Writing–original draft: Yousra Bensouda, Xiayun Zhao
Writing–review & editing: Yousra Bensouda, Xiayun Zhao

Ethics approval and consent to participate

Not applicable.

Consent for publication

Not applicable.

Availability of data

The data underlying this study are available from the corresponding author upon reasonable request.

References

1. Goh GD, Yap YL, Agarwala S, Yeong WY. Recent Progress in Additive Manufacturing of Fiber Reinforced Polymer Composite. *Adv Mater Technol*. 2018;4(1):1800271.

   doi: 10.1002/admt.201800271

2. Voet VSD. Closed-Loop Additive Manufacturing: Dynamic Covalent Networks in Vat Photopolymerization. *ACS Mater Au*. 2022;3(1):18-23.

   doi: 10.1021/acsmaterialsau.2c00058

3. Rasaki SA, Xiong D, Xiong S, Su F, Idrees M, Chen Z. Photopolymerization-based additive manufacturing of ceramics: A systematic review. *J Adv Ceram*. 2021;10(3):442-471.

   doi: 10.1007/s40145-021-0468-z

4. Sampson KL, Deore B, Go A, *et al*. Multimaterial Vat Polymerization Additive Manufacturing. *ACS Appl Polym Mater*. 2021;3(9):4304-4324.

   doi: 10.1021/acsapm.1c00262

5. Senthooran V, Weng Z, Wu L. Enhancing Mechanical and Thermal Properties of 3D-Printed Samples Using Mica-Epoxy Acrylate Resin Composites Via Digital Light Processing (DLP). *Polymers*. 2024;16(8):1148.

   doi: 10.3390/polym16081148

6. Li W, Mille LS, Robledo JA, Uribe T, Huerta V, Zhang YS. Recent Advances in Formulating and Processing Biomaterial Inks for Vat Polymerization-Based 3D Printing. *Adv Healthc Mater*. 2020;9(15):e2000156.

   doi: 10.1002/adhm.202000156

7. Pagac M, Hajnys J, Ma QP, *et al*. A Review of Vat Photopolymerization Technology: Materials, Applications, Challenges, and Future Trends of 3D Printing. *Polymers*.

2021;13(4):598.

doi: 10.3390/polym13040598

8. Weng Z, Zhou Y, Lin W, Senthil T, Wu L. Structure-property relationship of nano enhanced stereolithography resin for desktop SLA 3D printer. *Compos Part A Appl Sci Manuf*. 2016;88:234-242.

doi: 10.1016/j.compositesa.2016.05.035

9. Sealy MP, Avegnon KLM, Garrett A, Delbreilh L, Bapat S, Malshe AP. Understanding biomanufacturing of soy-based scaffolds for cell-cultured meat by vat polymerization. *CIRP Ann*. 2022;71(1):209-212.

doi: 10.1016/j.cirp.2022.04.001

10. Colucci G, Sacchi F, Bondioli F, Messori M. Fully Bio-Based Polymer Composites: Preparation, Characterization, and LCD 3D Printing. *Polymers*. 2024;16(9):1272.

doi: 10.3390/polym16091272

11. Ali W, Ali H, Gillani S, Zinck P, Souissi S. Polylactic acid synthesis, biodegradability, conversion to microplastics and toxicity: a review. *Environ Chem Lett*. 2023;21(3):1761-1786.

doi: 10.1007/s10311-023-01564-8

12. Tripathi N, Misra M, Mohanty AK. Durable Polylactic Acid (PLA)-Based Sustainable Engineered Blends and Biocomposites: Recent Developments, Challenges, and Opportunities. *ACS Eng Au*. 2021;1(1):7-38.

doi: 10.1021/acsengineeringau.1c00011

13. Balla E, Daniilidis V, Karlioti G, *et al*. Poly(lactic Acid): A Versatile Biobased Polymer for the Future with Multifunctional Properties-From Monomer Synthesis, Polymerization Techniques and Molecular Weight Increase to PLA Applications. *Polymers*. 2021;13(11):1822.

doi: 10.3390/polym13111822

14. Ortega F, Versino F, Lopez OV, Garcia MA. Biobased composites from agro-industrial wastes and by-products. *Emergent Mater*. 2022;5(3):873-921.

doi: 10.1007/s42247-021-00319-x

15. Li Y, Ren X, Zhu L, Li C. Biomass 3D Printing: Principles, Materials, Post-Processing and Applications. *Polymers*. 2023;15(12):2692.

doi: 10.3390/polym15122692

16. Ozaki T, Koto T, Nguyen TV, Nakanishi H, Norisuye T, Tran-Cong-Miyata Q. The roles of the Trommsdorff–Norrish effect in phase separation of binary polymer mixtures induced by photopolymerization. *Polymer*. 2014;55(7):1809-1816.

doi: 10.1016/j.polymer.2014.02.041

17. Joseph TM, Kallingal A, Suresh AM, *et al*. 3D printing of polylactic acid: recent advances and opportunities. *Int J Adv Manuf Technol*. 2023;125(3-4):1015-1035.

doi: 10.1007/s00170-022-10795-y

18. Román-Ramírez LA, Powders M, McKeown P, Jones MD, Wood J. Ethyl Lactate Production from the Catalytic Depolymerisation of Post-consumer Poly(lactic acid). *J Polym Environ*. 2020;28(11):2956-2964.

doi: 10.1007/s10924-020-01824-6

19. Ciriminna R, Pagliaro M. Biodegradable and Compostable Plastics: A Critical Perspective on the Dawn of their Global Adoption. *ChemistryOpen*. 2020;9(1):8-13.

doi: 10.1002/open.201900272

20. Duran MM, Moro G, Zhang Y, Islam A. 3D printing of silicone and polyurethane elastomers for medical device application: A review. *Adv Ind Manuf Eng*. 2023;7:100125.

doi: 10.1016/j.aime.2023.100125

21. Harris M, Potgieter J, Ray S, Archer R, Arif KM. Polylactic acid and high-density polyethylene blend: Characterization and application in additive manufacturing. *J Appl Polym Sci*. 2020;137(48):49602.

doi: 10.1002/app.49602

22. Van der Laan HL, Burns MA, Scott TF. Volumetric Photopolymerization Confinement through Dual-Wavelength Photoinitiation and Photoinhibition. *ACS Macro Lett*. 2019;8(8):899-904.

doi: 10.1021/acsmacrolett.9b00412

23. Bensouda Y, Zhang Y, Zhao X. Vat photopolymerization based Photoinhibition aided Ceramic additive manufacturing (PinCAM). *J Eur Ceram Soc*. 2024;44(13):7801-7824.

doi: 10.1016/j.jeurceramsoc.2024.05.080

24. Lu Z, Gao W, Liu F, *et al*. Vat photopolymerization based digital light processing 3D printing hydrogels in biomedical fields: Key parameters and perspective. *Addit Manuf*. 2024;94:104443.

doi: 10.1016/j.addma.2024.104443

25. Higgins CI, Killgore JP, DelRio FW, Bryant SJ, McLeod RR. Photo-tunable hydrogel mechanical heterogeneity informed by predictive transport kinetics model. *Soft Matter*. 2020;16(17):4131-4141.

doi: 10.1039/D0SM00052C

26. Fiedler CI, Aisenbrey EA, Wahlquist JA, *et al*. Enhanced mechanical properties of photo-clickable thiol-ene PEG hydrogels through repeated photopolymerization of in-swollen macromer. *Soft Matter*. 2016;12(44):9095-9104.

doi: 10.1039/C6SM01768A

27. Wendland RJ, Kolibaba TJ, Worthington KS, Killgore JP. A practical guide to hydrogel working curves for bioprinting. *Addit Manuf Lett*. 2025;14:100293.

doi: 10.1016/j.addlet.2025.100293

28. Madrid-Wolff J, Toombs J, Rizzo R, *et al*. A review of materials used in tomographic volumetric additive

manufacturing. *MRS Commun*. 2023;13(5):764-785.

doi: 10.1557/s43579-023-00447-x

29. Soullard L, Schlepp A, Buret R, *et al*. Towards the 3D printing of innovative hydrogel scaffolds through vat polymerization techniques using methacrylated carboxymethylcellulose aqueous formulations. *Prog Addit Manuf*. 2025;10(4):2177-2189.

doi: 10.1007/s40964-024-00744-4

30. Wieckowski HS, Erb RM. Tuning depth of cure in resins with photoabsorbing fillers for vat photopolymerization. *MRS Commun*. 2025;15(3):308-319.

doi: 10.1557/s43579-025-00713-0

31. Schwab A, Levato R, D'Este M, Piluso S, Eglin D, Malda J. Printability and Shape Fidelity of Bioinks in 3D Bioprinting. *Chem Rev*. 2020;120(19):11028-11055.

doi: 10.1021/acs.chemrev.0c00084

32. Wang B, Safari WSH, Hedayati SK, *et al*. Lateral Contrast Enhancement in Tomographic Volumetric 3D-Printing via Binary Photoinhibition. *arXiv*. Preprint posted online March 24, 2023.

doi: 10.48550/arXiv.2303.13941

33. De Beer MP, van der Laan HL, Cole MA, Whelan RJ, Burns MA, Scott TF. Rapid, continuous additive manufacturing by volumetric polymerization inhibition patterning. *Sci Adv*. 2019;5(1):eaau8723.

doi: 10.1126/sciadv.aau8723

34. Zhang Y, Zhang H, Zhao X. Exploring three-dimensional photoinhibition to enhance vat photopolymerization: A preliminary study. *Precis Eng*. 2024;90:176-190.

doi: 10.1016/j.precisioneng.2024.08.009

35. Ma C, Li W, Li D, *et al*. Photoacoustic imaging of 3D-printed vascular networks. *Biofabrication*. 2022;14(2):025001.

doi: 10.1088/1758-5090/ac49d5

36. Zhang H, Maier A, Mathews M, Hu J, Zhao X. Development of open-architecture two-wavelength grayscale digital light processing for advanced vat photopolymerization. *Addit Manuf*. 2025;107:104818.

doi: 10.1016/j.addma.2025.104818

37. Feng Z, Li Y, Xin C, Tang D, Xiong W, Zhang H. Fabrication of Graphene-Reinforced Nanocomposites with Improved Fracture Toughness in Net Shape for Complex 3D Structures via Digital Light Processing. *C*. 2019;5(2):25.

doi: 10.3390/c5020025

38. Feng Z, Li Y, Hao L, *et al*. Graphene-Reinforced Biodegradable Resin Composites for Stereolithographic 3D Printing of Bone Structure Scaffolds. *J Nanomater*. 2019;2019:9710264.

doi: 10.1155/2019/9710264

39. Talrose V, Yermakov AN, Leskin AN, *et al*. UV/Vis Database User's Guide. NIST Chemistry WebBook, SRD 69. Available from: https://webbook.nist.gov/chemistry/uv-vis/ [Last accessed on 2025 Oct 14].

40. Bachmann J, Schmölzer S, Ruderer MA, Fruhmann G, Hinrichsen O. Photo-differential scanning calorimetry parameter study of photopolymers used in digital light synthesis. *SPE Polym*. 2021;3(1):41-53.

doi: 10.1002/pls2.10063

41. Lynch JM, Corniuk RN, Brignac KC, *et al*. Differential scanning calorimetry (DSC): An important tool for polymer identification and characterization of plastic marine debris. *Environ Pollut*. 2024;346:123607.

doi: 10.1016/j.envpol.2024.123607

42. Drzeżdżon J, Jacewicz D, Sielicka A, Chmurzyński L. Characterization of polymers based on differential scanning calorimetry based techniques. *TrAC Trends Anal Chem*. 2019;110:51-56.

doi: 10.1016/j.trac.2018.10.037

43. Gill P, Moghadam TT, Ranjbar B. Differential Scanning Calorimetry Techniques: Applications in Biology and Nanoscience. *J Biomol Tech*. 2010;21(4):167-193.

44. Vallabh CKP, Zhang Y, Zhao X. In-situ ultrasonic monitoring for Vat Photopolymerization. *Addit Manuf*. 2022;55:102801.

doi: 10.1016/j.addma.2022.102801

45. Zhang Y, Zhang H, Zhao X. In-situ Interferometric Curing Monitoring for Digital Light Processing based Vat Photopolymerization Additive Manufacturing. *Addit Manuf*. 2024;81:104001.

doi: 10.1016/j.addma.2024.104001

46. Hoffmann GG. *Raman Spectroscopy, Volume I: Principles and Applications in Chemistry, Physics, Materials Science, and Biology*. Momentum Press; 2019.

47. Tu AT. *Raman Spectroscopy in Biology: Principles and Applications*. Wiley; 1982.

48. Lambrecht S, Biermann M, Kara S, Jopp S, Meyer J. A novel characterization technique for hydrogels – in situ rheology-Raman spectroscopy for gelation and polymerization tracking. *Mater Adv*. 2024;5(17):6957-6966.

doi: 10.1039/D4MA00543K

Appendix

Appendix A. Print samples and quantitative data characterization for PLA-PUA resin system across varying photoinhibition conditions

Figure A1. Representative PLA-PUA polymeric blend samples printed at a fixed exposure time of 60 s under seven inhibition ratios: I_{UV}/I_{Blue} = 0 (pure blue), and I_{UV}/I_{Blue} = 0.1, 0.2, 0.3, 0.4, 0.5 and 0.6
Abbreviations: PLA: Polylactic acid; PUA: Polyurethane acrylate.

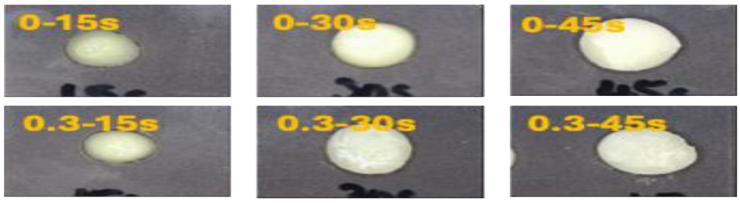

Figure A2. Representative PLA-PUA polymeric blend samples printed with and without inhibition for pure blue light (I_{UV}/I_{Blue} = 0) and a chosen inhibition ratio (I_{UV}/I_{Blue} = 0.3) across three exposure times: 15, 30 and 45 s
Abbreviations: PLA: Polylactic acid; PUA: Polyurethane acrylate.

Table A1. Cure thickness and inhibition zone depth changes for PLA-PUA polymeric blend samples with varying I_{UV}/I_{Blue} ratios under a fixed exposure time of 60 s

Inhibition ratio	Replication	Cure thickness (μm)	Average cure thickness (μm)	Relative standard error (RSE)	Inhibition depth (μm)	Average inhibition depth (μm)	Relative standard error (RSE)
0	R1	2679	2604.33	2.96	0	0	0
	R2	2609			0		
	R3	2525			0		
0.1	R1	2466	2403.00	2.37	213	201.33	13.62
	R2	2388			221		
	R3	2355			170		
0.2	R1	2015	2049.33	1.55	664	555.00	17.87
	R2	2078			531		
	R3	2055			470		
0.3	R1	1904	1940.00	1.78	775	664.00	16.78
	R2	1943			666		
	R3	1973			552		
0.4	R1	1821	1874.33	2.64	858	730.0	17.26
	R2	1883			726		
	R3	1919			606		
0.5	R1	1717	1789.67	3.53	962	814.67	16.77
	R2	1819			790		
	R3	1833			692		
0.6	R1	1028	1483.67	26.62	1651	1120.00	41.33
	R2	1693			916		
	R3	1730			795		

Abbreviations: PLA: Polylactic acid; PUA: Polyurethane acrylate.

Appendix B. Supplementary hydrogel printing results for inhibition characterization, shrinkage and submersion analysis under photoinhibition

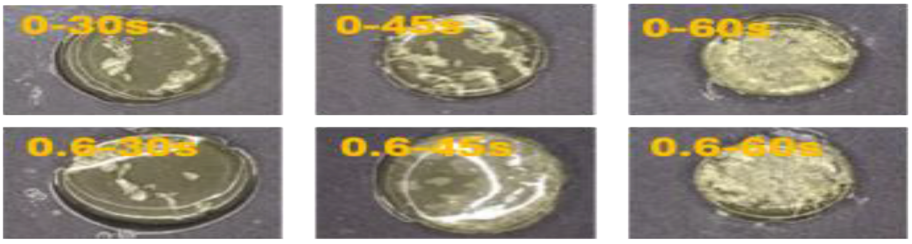

Figure B1. Hydrogel samples printed with and without inhibition for pure blue light (I_{UV}/I_{Blue} = 0) (top row) and a chosen inhibition ratio (I_{UV}/I_{Blue} = 0.6) (bottom row) across three exposure times: 30, 45 and 60 s

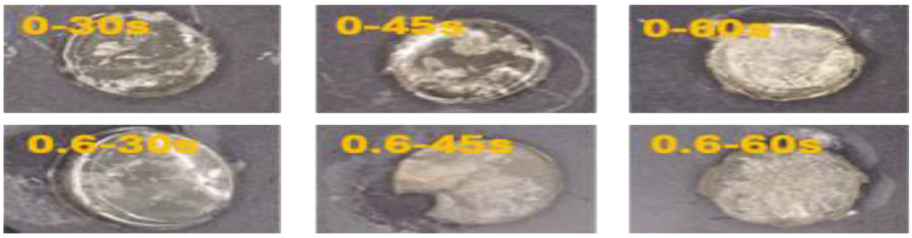

Figure B2. Shrinkage scans of hydrogel samples two weeks post-print at I_{UV}/I_{Blue} = 0 (top row) and I_{UV}/I_{Blue} = 0.6 (bottom row) across three exposure times: 30, 45 and 60 s

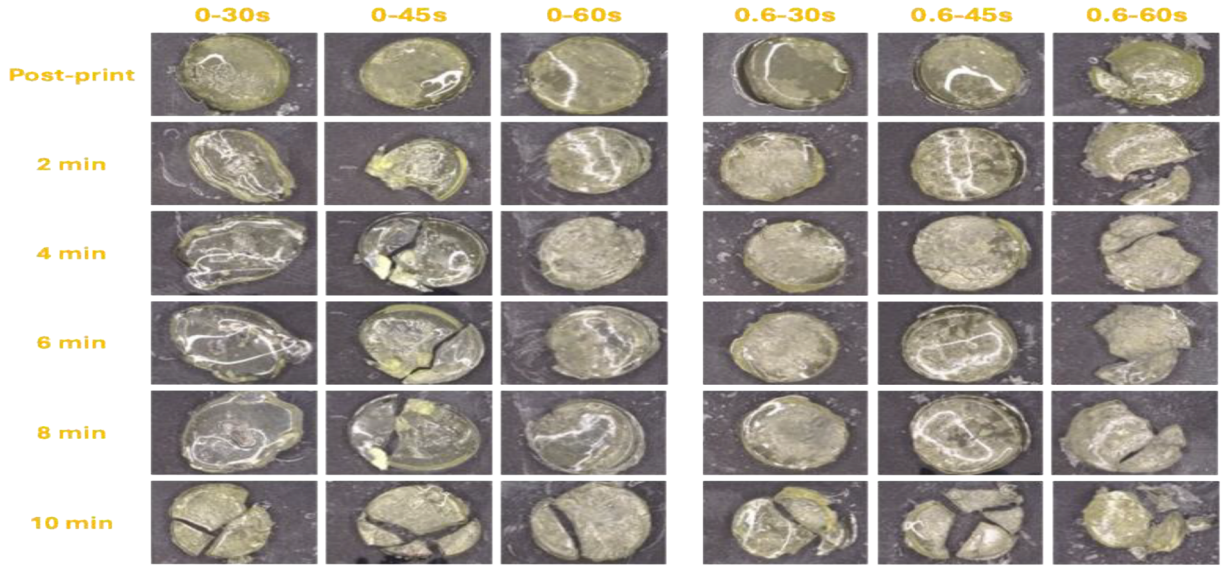

Figure B3. Post-print submersion scans of hydrogel samples at I_{UV}/I_{Blue} = 0 (left three columns) and I_{UV}/I_{Blue} = 0.6 (right three columns) across three exposure times: 30, 45 and 60 s. Fracture limit reached at 10 min.

ACCSCIENCE PUBLISHING

OUR JOURNALS

Materials Science in Additive Manufacturing (MSAM) aims to bridge the cutting-edge research between additive manufacturing and the entire spectrum of materials science. The journal covers all applied and fundamentals of processing, synthesis, structure, composition, properties and performance of materials designed or manipulated for additive manufacturing. The journal covers a wide scope of innovative techniques, processes, methods, and applications. Topics of particular interest include, but are not limited to:

- Theory and modelling
- Artificial intelligence
- Polymers
- Metals and alloys
- Ceramics
- Composites
- Magnetic materials
- Smart materials
- Nano-materials
- Materials for electronics
- Characterization techniques

International Journal of AI for Materials and Design is an international, peer-reviewed open-access journal that aims to bridge the cutting-edge research between AI and materials, AI and design. In recent years, the tremendous progress in AI is leading a radical shift of AI research from a mainly academic endeavor to a much broader field with increasing industrial and governmental investments. The maturation of AI technology brings about a step change in the scientific research of various domains, especially in the world of materials and design. Machine learning (ML) algorithms enable researchers to analyze extensive datasets on material properties and accurately predict their behavior in different conditions. This subsequently impact the industry to leverage on big data and advanced analytics to build scientific strategies, scale operational performance of processes and drive innovation.

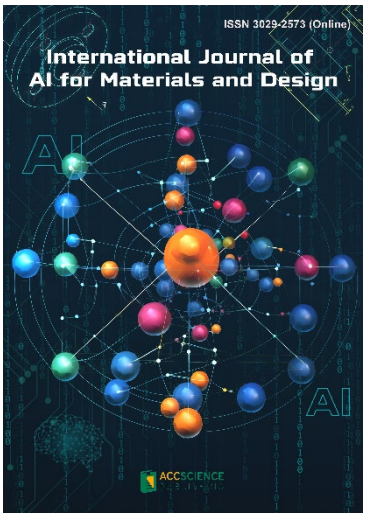

International Journal of AI for Materials and Design covers the following topics: AI or machine learning for material discovery, AI for process optimization, AI and data-driven approaches for product or systems design, application of AI in advanced manufacturing processes such as additive manufacturing, IoT, sensors, robotics, cloud-based manufacturing, intelligent manufacturing for various applications, autonomous experiments, material intelligence, energy intelligence, and AI-linked decarbonization technologies.

Start a new journal

Write to us via email if you are interested to start a new journal with AccScience Publishing. Please attach your CV, professional profile page and a brief pitch proposal in your email. We shall inform you of our decision whether we are interested to collaborate in starting a new journal.

Contact: info@accscience.com

https://accscience.com/journal/ESAM

Contact
www.accscience.com
2 Venture Drive, #07-06 Vision Exchange,Singapore 608526
Email: editorial@accscience.com
Phone: +65 8182 1586